

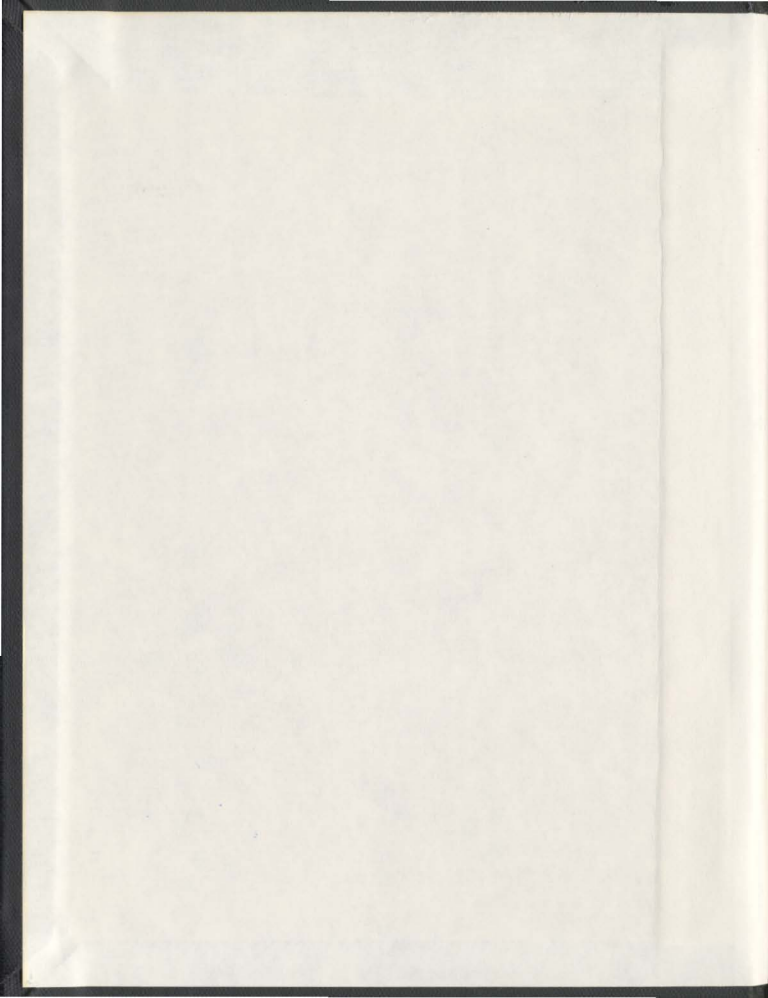
NON-DESTRUCTIVE EVALUATION OF CRACKING IN
TUBULAR T-JOINTS USING VIBRATION PROCEDURES

CENTRE FOR NEWFOUNDLAND STUDIES

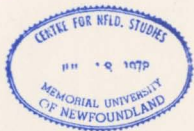
**TOTAL OF 10 PAGES ONLY
MAY BE XEROXED**

(Without Author's Permission)

SHUMIN CHENG



001311



INFORMATION TO USERS

This manuscript has been reproduced from the microfilm master. UMI films the text directly from the original or copy submitted. Thus, some thesis and dissertation copies are in typewriter face, while others may be from any type of computer printer.

The quality of this reproduction is dependent upon the quality of the copy submitted. Broken or indistinct print, colored or poor quality illustrations and photographs, print bleedthrough, substandard margins, and improper alignment can adversely affect reproduction.

In the unlikely event that the author did not send UMI a complete manuscript and there are missing pages, these will be noted. Also, if unauthorized copyright material had to be removed, a note will indicate the deletion.

Oversize materials (e.g., maps, drawings, charts) are reproduced by sectioning the original, beginning at the upper left-hand corner and continuing from left to right in equal sections with small overlaps. Each original is also photographed in one exposure and is included in reduced form at the back of the book.

Photographs included in the original manuscript have been reproduced xerographically in this copy. Higher quality 6" x 9" black and white photographic prints are available for any photographs or illustrations appearing in this copy for an additional charge. Contact UMI directly to order.

UMI

A Bell & Howell Information Company
300 North Zeeb Road, Ann Arbor MI 48106-1346 USA
313/761-4700 800/521-0600

NON-DESTRUCTIVE EVALUATION OF CRACKING IN TUBULAR T-JOINTS USING VIBRATION PROCEDURES

by

©Shumin Cheng, B. Eng., M. Eng.

A thesis submitted to the School of Graduate Studies
in partial fulfillment of the requirements for
the degree of Ph.D.

Faculty of Engineering and Applied Science
Memorial University of Newfoundland
January 1998

St. John's

Newfoundland

Canada

TO MY PARENTS

ABSTRACT

This thesis presents an experimental and analytical study of the initiation and growth of cracks in tubular T-joint members of the type used in some off-shore platforms. Cracks were developed experimentally under fatigue loading conditions.

The early stages of formation and growth of the cracks have been studied by fracture surface analysis, using scanning electron microscopy. Their growth has also been followed by modal testing. It has been shown that a number of significant changes occur in the static and dynamic response characteristics of the T-joints, as cracks initiate and grow. In particular, it has been shown that strain gauge modal testing provides a means of detecting cracks at a much earlier stage of formation than has been possible using alternative techniques.

The modal analysis methods developed in this thesis rely on the use of strain/acceleration frequency response functions to detect the presence of growing cracks. Three parameters were found to be significant in detecting the presence of cracks, and these include: a) response in the quasi-static region; b) response in the anti-resonant region; and c) non-linearity in the frequency response functions. The factors contributing to the observed changes are discussed.

In addition, measured (static) strains and stresses were also found to provide good indications of the presence of growing fatigue cracks. Abrupt changes in strain gauge outputs were observed consistently as small thumb-nail cracks, present in the early stages of crack growth, coalesced to form single cracks of much longer length.

Parametric equations were developed to relate the fatigue life of the tubular specimen to the strains/frequencies measured at the various strain gauge locations. In addition equations were also developed to relate the crack size to the strains/frequencies

measured at various locations. These equations could be utilized to predict the remaining life of the joint as well as the probable crack size at the critical location near the gauge.

Finite element analysis was used to predict the modal response of crack-free and cracked structures to dynamic excitation. Excellent agreement was observed between experiment and theory in all cases.

A lumped mass model has been developed to simulate the behavior of the fatigue cracks during dynamic testing. It has been shown that the structure in the vicinity of the cracks exhibits non-linear stiffness and compliance as the fatigue cracks open and close.

ACKNOWLEDGMENTS

I must first express my gratitude to my supervisor, Dr. A. S. J. Swamidas, for his guidance and support throughout my Ph.D. program at Memorial University of Newfoundland. His patience, experience and helpful suggestions guided me throughout my Ph.D. studies. I would also like to express my gratitude to my supervisory committee members, Dr. G. Sabin and Dr. M.R. Haddara. Furthermore, many thanks are due to Mr. Austin Bursey, Mr. Jim Andrews and Mr. Humphrey Dye for providing technical services from the manufacturing of the experimental setup to the end of the experiment. I also thank the manager and staff of the Center for Computer Aided Engineering for their support during the computational portion of my thesis.

I must acknowledge the great support of my parents who have been looking after my son during these four years of my study in Canada so that I can devote myself wholly to research. I am deeply indebted to my son, Haochao Jiang, who spent the formative years of his life — from two to six years old — without his mother's care. He is making his own contributions to society in his own unique ways.

Portions of this research investigation were sponsored and funded by the NSERC Strategic Grant program of my supervisor. I would also like to thank the Memorial University of Newfoundland and Faculty of Engineering and Applied Science, for the additional fellowship and teaching assistantship provided during this period.

Contents

Abstract	i
Acknowledgements	iii
List of Tables	x
List of Figures	xiii
List of Symbols	xxii
1 Introduction	1
1.1 Non-destructive Evaluation of Defects	1
1.2 Purpose of the study	4
1.3 Scope of Research	5
1.4 Organization of the Thesis	6
2 Literature Review	7
2.1 Conventional Methods	8
2.2 Methods Using Vibration Procedures	12
2.2.1 Defect Indicators	13
2.2.2 Modeling of the Crack	15
2.2.3 Crack/Damage Detection Methods	20

2.3	Conclusions	39
3	Theoretical Background for Analysis and Experiment	41
3.1	Introduction	41
3.2	Modal Analysis and Vibration Theory	42
3.2.1	Modal Analysis	42
3.2.2	Vibration Theory General Description	44
3.2.3	Governing Equations of Motion	45
3.2.4	Random Vibration	50
3.2.5	Strain Frequency Response Functions	52
3.3	Finite Element Method	54
3.3.1	Shell Element	54
3.3.2	Solution Procedure	54
3.3.3	Line Spring Element	55
3.4	Fatigue and Fracture Mechanics	60
3.5	Summary	62
4	Tubular Joint Fabrication, Experimental Setup, Instrumentation, Calibration, and Measurement of Responses	64
4.1	Introduction	64
4.2	The Fabrication of Tubular T-Joints	67
4.3	Characteristic Stresses Developed in Tubular T-joints	69
4.4	Geometric Properties of Tubular T-Joints	71
4.5	Experimental Setup	71
4.6	Instrumentation	73
4.6.1	Command Signals and the Function Generator	78
4.6.2	Exciter	78

4.6.3	Transducers	81
4.6.4	Load Cell	82
4.6.5	Analyzer	83
4.6.6	Actuator	83
4.6.7	Controller	83
4.6.8	STAR Software	84
4.7	Calibration of Transducers	84
4.7.1	Calibration of the Load Cell in Exciter for Modal Analysis	84
4.7.2	Calibration of Accelerometer	86
4.7.3	Calibration Factors for Other Transducers	87
4.8	Location of Strain Gauges and Accelerometers	87
4.8.1	Strain Gauge Arrangement	87
4.8.2	Marking of the Strain Gauge Location	91
4.8.3	Accelerometer Arrangement	91
4.9	Determination of Fatigue Load on the Tubular T-Joint	101
4.10	Signal Processing	104
4.11	Curve Fitting	107
4.12	Procedure for Testing	111
4.13	Conclusions	112
5	Experimental Studies and Salient Findings	113
5.1	Introduction	113
5.2	Crack Profile Determination	115
5.3	Fracture Surface Analysis	118
5.4	Description of Crack Growth	129
5.5	Static Response During Fatigue Crack Growth	138

5.5.1	Static Strains	138
5.5.2	Static Principal Stresses	140
5.6	Natural Frequencies and Damping	160
5.6.1	Natural Frequency Variations	160
5.6.2	Damping Ratio Variations	162
5.7	Salient Features of Dynamic Response	181
5.7.1	Introduction	181
5.7.2	Quasi-Static Components in Frequency Response Functions	182
5.7.3	Response in the Anti-Resonant Region	186
5.7.4	Nonlinearity in Frequency Response Functions	187
5.8	Conclusions	189
6	Results of Finite Element Analyses	205
6.1	Introduction	205
6.2	Finite Element Model	207
6.2.1	Element Selection	207
6.2.2	Simplifications	208
6.2.3	Mesh Generation and Simulation of Boundary Conditions	209
6.2.4	Length of Line Spring Elements	212
6.3	Matching of Finite Element Results to Experimental Results	213
6.4	Mode Shapes	222
6.5	Conclusions	230
7	Response of a Structure With an Opening and Closing Crack	239
7.1	Introduction	239
7.2	Response of a Structure Containing an Opening and Closing Crack	240
7.3	Continuously Opening and Closing Crack Model	243

7.4	Establishment of a Two-Degrees-of-Freedom Model of a Tubular T-Joint with "Opening and Closing" Crack	244
7.5	Results and Discussions	251
7.6	Conclusions	253
8	Conclusions, Contributions and Recommendations for Further Investigation	258
8.1	Review of Original Objectives	258
8.2	Major Observations and Contributions	259
8.3	Recommendations for Further Research	262
	References	264
	Appendices	273
A	Finite Element Analysis Basic Theory	273
A.1	General Equations of Elasticity	273
A.2	Shape Functions for Six-Noded Triangular and Eight-Noded Rectangular Elements	275
A.2.1	Six-Noded Triangular Elements	275
A.2.2	Eight-Noded Rectangular Elements	277
A.3	Shell Element	279
A.3.1	Element Geometry	279
A.3.2	Displacement Field	280
A.3.3	Definitions of Strains and Stresses	282
B	Detailed Structural Drawings of Tubular T-Joint	287
C	Specifications for Welding Procedures	291

D Equations for Static Strains and Stresses	296
D.1 Static Strains	296
D.2 Static Principal Stresses	306
E Natural Frequencies and Damping	312
E.1 Natural Frequency Variations	312
E.2 Damping Ratio Variations	320
F Equations Derived by Piecewise Cubic Spline Approach	328
F.1 Static Strains	328
F.2 Static Principal Stresses	332
F.3 Natural Frequencies	334

List of Tables

4.1	T-joint Geometry	72
4.2	Strain Gauge Properties	81
4.3	Accelerometer Features	82
4.4	Calibration of Load Cell	86
4.5	Calibration Factors for Accelerometers	86
4.6	Calibration Factors for Other Transducers	87
4.7	Computation of Fatigue Load	105
4.8	Characteristics of Fatigue Loads	105
5.1	Fatigue Cycles and Measured Crack Parameters	118
5.2	Fatigue Cycles and Measured Crack Parameters	123
5.3	Fatigue Cycles and Measured Crack Parameters	124
5.4	Fitting Constants for Crack Growth Curves	136
5.5	Static Strains for Specimen 1	141
5.6	Static Strains for Specimen 1	142
5.7	Static Strains for Specimen 2	143
5.8	Static Strains for Specimen 2	144
5.9	Static Strains for Specimen 3	145
5.10	Static Strains for Specimen 3	146
5.11	Equation Constants	146

5.12 Static Principal Stresses for Specimen 1	151
5.13 Static Principal Stresses for Specimen 1	152
5.14 Static Principal Stresses for Specimen 2	153
5.15 Static Principal Stresses for Specimen 2	154
5.16 Static Principal Stresses for Specimen 3	155
5.17 Static Principal Stresses for Specimen 3	156
5.18 Static Principal Stresses for Intact Specimens	157
5.19 Natural Frequencies for Specimen 1 (mode 1 – 4)	163
5.20 Natural Frequencies for Specimen 1 (mode 5 – 8)	164
5.21 Natural Frequencies for Specimen 1 (mode 9 – 12)	164
5.22 Natural Frequencies for Specimen 1 (mode 13 – 16)	165
5.23 Natural Frequencies for Specimen 1 (mode 17 – 20)	165
5.24 Natural Frequencies for Specimen 2 (mode 1 – 4)	166
5.25 Natural Frequencies for Specimen 2 (mode 5 – 8)	167
5.26 Natural Frequencies for Specimen 2 (mode 9 – 12)	168
5.27 Natural Frequencies for Specimen 3 (mode 1 – 4)	168
5.28 Natural Frequencies for Specimen 3 (mode 5 – 8)	169
5.29 Natural Frequencies for Specimen 3 (mode 9 – 12)	169
5.30 Damping (%) for Specimen 1 (mode 1 – 4)	172
5.31 Damping (%) for Specimen 1 (mode 5 – 8)	172
5.32 Damping (%) for Specimen 1 (mode 9 – 12)	173
5.33 Damping (%) for Specimen 1 (mode 13 – 16)	174
5.34 Damping (%) for Specimen 1 (mode 16 – 20)	174
5.35 Damping (%) for Specimen 2 (mode 1 – 4)	175
5.36 Damping (%) for Specimen 2 (mode 5 – 8)	176
5.37 Damping (%) for Specimen 2 (mode 9 – 12)	177

5.38 Damping (%) for Specimen 3 (mode 1 – 4)	177
5.39 Damping (%) for Specimen 3 (mode 5 – 8)	178
5.40 Damping (%) for Specimen 3 (mode 9 – 12)	178
6.1 Static Principal Stresses for Finite Element Model and Experimental Specimen 3	215
6.2 Natural Frequencies of Experimental Specimens and Finite Element Model	217
6.3 Natural Frequencies of Experimental Specimens and Finite Element Model	217
6.4 Natural Frequencies of Experimental Specimens and Finite Element Model	218
6.5 Natural Frequencies Obtained from Finite Element Model	218
6.6 Natural Frequencies Obtained from Finite Element Model	219
6.7 Natural Frequencies Obtained from Finite Element Model	219
6.8 Crack Profiles Predicted by Finite Element Model	232

List of Figures

3.1	(a) Rayleigh damping; (b) Mass- and stiffness- proportional damping	47
3.2	Line spring element	58
3.3	Single edge notch specimen	58
3.4	Line spring elements used with shell elements	59
3.5	Schematic of crack closure	63
3.6	Schematic load-displacement curve (Bäcklund, 1981, Newman, 1988)	63
4.1	Tubular T-joint under test	65
4.2	Tubular T-joint under modal test	68
4.3	Tubular T-joints	70
4.4	Tubular T-joint under fatigue test	74
4.5	Test bed	75
4.6	The connection between the specimen and actuator	75
4.7	Test specimen support	76
4.8	The stiffening ring on the end plate	77
4.9	The connection between the specimen and support	77
4.10	Instrument setup	79
4.11	Instrument flow chart	80
4.12	Sine sweep signal	80
4.13	Calibration flow chart for load cell	88

4.14	Calibration flow chart for accelerometers	88
4.15	Strain gauges on the chord (cracking side) for specimen 1	92
4.16	Strain gauges on the chord (noncracking side) for specimen 1	92
4.17	Strain gauges on the brace (front view) for specimen 1	93
4.18	Strain gauges on the brace (top view) for specimen 1	93
4.19	Traditional strain gauge locations (Wardenier et al. 1991)	93
4.20	Strain gauge channels on the chord (cracking side) for specimen 1	94
4.21	Strain gauge channels on the chord (noncracking side) for specimen 1	94
4.22	Strain gauge channels on the brace for specimen 1	95
4.23	Strain gauges on the chord (cracking side) for specimens 2 and 3	95
4.24	Strain gauges on the chord (noncracking side) for specimens 2 and 3	96
4.25	Strain gauges on the brace (front view) for specimens 2 and 3	96
4.26	Strain gauges on the brace (top view) for specimens 2 and 3	97
4.27	Strain gauge channels on the chord (cracking side) for specimens 2 and 3	97
4.28	Strain gauge channels on the chord (noncracking side) for specimens 2 and 3	98
4.29	Strain gauge channels on the brace for specimens 2 and 3	98
4.30	Cable connections on the chord (cracking side) for specimen 3	99
4.31	Cable connections on the chord (noncracking side) for specimen 3	100
4.32	Aliasing of signal	108
4.33	Signal leakage	108
4.34	Hanning window reduces leakage	109
4.35	Overlap averaging procedure	109
5.1	Photo of crack profile for specimen 1, side 1	117
5.2	Photo of crack profiles for specimen 2, side 1	117

5.3	Photo of crack profiles for specimen 2, side 2	117
5.4	Photo of crack profile for specimen 3, side 1	119
5.5	Photo of crack profile for specimen 3, detail left	119
5.6	Photo of crack profile for specimen 3, detail right	119
5.7	Traced crack profile for specimen 1, side 1	120
5.8	Traced crack profiles for specimen 2	121
5.9	Traced crack profiles for specimen 3, side 1	122
5.10	The presence of thumb-nail or elliptical cracks, as indicated by ink staining, along the weld toe of specimen 2 from left to right: (a) a single surface crack in half elliptical shape; (b) joining of two elliptical cracks; (c) three smaller thumb-nail cracks in the left of the coalesced crack	130
5.11	A closer look of the three individual thumb-nail cracks: (a) the one in the left; (b) the one in the middle; (3) the one in the right, as shown in Figure 5.10 c	131
5.12	Fracture surface features of (a) the trough area showing the texture and (b) the elevated area which has been pounded flat	132
5.13	A crack initiation site near the surface of the weld toe	133
5.14	Secondary cracking perpendicular to the direction of crack growth though the thickness	133
5.15	Fatigue striations in some trough areas (a) and (b) all in specimen 3 .	134
5.16	Flattened areas showing the evidence of crack closure (a) in specimen 2 (b) in specimen 3	135
5.17	Experimental observations (*) of crack width as a function of the number of cycles in fatigue for specimen 3. The line represents the interpolation of LEFM	137

- 5.18 Experimental observations (*) of crack depth as a function of the number of cycles in fatigue for specimen 3. The line represents the observed behavior. $N = 1.4 \times 10^5 + 6.25 \times 10^4 b$ 137
- 5.19 The observation of static strain (at gauge 1) as a function of the number of cycles in fatigue ("*" specimen 1; "o" specimen 2, "Δ" specimen 3). The lines are obtained from Equation , with the parameter values in Table ("-" specimen 1; "- ." specimen 2, "- ." specimen 3). 147
- 5.20 The observation of static strain (at gauge 4) as a function of the number of cycles in fatigue. ("*" specimen 1; "o" specimen 2, "Δ" specimen 3). The lines are obtained from Equation , with the parameter values in Table ("-" specimen 1; "- ." specimen 2, "- ." specimen 3). 147
- 5.21 The observation of static strain (at gauge 10) as a function of the number of cycles in fatigue. ("*" specimen 1; "o" specimen 2, "Δ" specimen 3). The lines are obtained from Equation , with the parameter values in Table ("-" specimens 1, 2 and 3). 148
- 5.22 (a) Maximum static principal stress σ_1 at gauge 1, specimen 1 (—), specimen 2 (- -), & specimen 3 (-.); (b) Minimum static principal stress σ_2 gauge 1, specimen 1 (—), specimen 2 (- -), & specimen 3 (-.) . . . 158
- 5.23 (a) Maximum static principal stress σ_1 at gauge 4, specimen 1 (—), specimen 2 (- -), & specimen 3 (-.); (b) Minimum static principal stress σ_2 at gauge 4, specimen 1 (—), specimen 2 (- -), & specimen 3 (-.) . . 158
- 5.24 (a) Maximum static principal stress σ_1 at gauge 10, specimen 1 (—), specimen 2 (- -), & specimen 3 (-.); (b) Minimum static principal stress σ_2 at gauge 10, specimen 1 (—), specimen 2 (- -), & specimen 3 (-.) . 159

- 5.25 (a) Natural frequency change with cycles for mode 1, specimen 1 (—), specimen 2 (- -), & specimen 3 (-.); (b) Natural frequency change with cycles for mode 2, specimen 1 (—), specimen 2 (- -), & specimen 3 (-.) 170
- 5.26 (a) Natural frequency change with cycles for mode 3, specimen 1 (—), specimen 2 (- -), & specimen 3 (-.); (b) Natural frequency change with cycles for mode 4, specimen 1 (—), specimen 2 (- -), & specimen 3 (-.) 170
- 5.27 (a) Natural frequency change with cycles for mode 5, specimen 1 (—), specimen 2 (- -), & specimen 3 (-.); (b) Natural frequency change with cycles for mode 6, specimen 1 (—), specimen 2 (- -), & specimen 3 (-.) 171
- 5.28 (a) Natural frequency change with cycles for mode 7, specimen 1 (—), specimen 2 (- -), & specimen 3 (-.); (b) Natural frequency change with cycles for mode 8, specimen 1 (—), specimen 2 (- -), & specimen 3 (-.) 171
- 5.29 (a) Damping changes with cycles for mode 1, specimen 1 (—), specimen 2 (- -), & specimen 3 (-.); (b) Damping changes with cycles for mode 2, specimen 1 (—), specimen 2 (- -), & specimen 3 (-.) 179
- 5.30 (a) Damping changes with cycles for mode 3, specimen 1 (—), specimen 2 (- -), & specimen 3 (-.); (b) Damping changes with cycles for mode 4, specimen 1 (—), specimen 2 (- -), & specimen 3 (-.) 179
- 5.31 (a) Damping changes with cycles for mode 5, specimen 1 (—), specimen 2 (- -), & specimen 3 (-.); (b) Damping changes with cycles for mode 6, specimen 1 (—), specimen 2 (- -), & specimen 3 (-.) 180
- 5.32 (a) Damping changes with cycles for mode 7, specimen 1 (—), specimen 2 (- -), & specimen 3 (-.); (b) Damping changes with cycles for mode 8, specimen 1 (—), specimen 2 (- -), & specimen 3 (-.) 180

5.33 Strain frequency response functions at gauge 2, channel 6, for specimen 2 at 0, 350,000, 500,000, 800,000, 962,500,000, 1120,000 and 1426,250 fatigue cycles	192
5.34 Acceleration frequency response functions at accelerometer 2 for specimen 2 at 0, 350,000, 500,000, 800,000, 962,500,000, 1120,000 and 1426,250 fatigue cycles	192
5.35 Strain FRF at gauge 1, channel 8, of specimen 2	193
5.36 Strain FRF at gauge 5, channel 13, of specimen 2	194
5.37 Strain FRF at gauge 12, channel 33, of specimen 1	195
5.38 Acceleration frequency response functions at accelerometer #5 for specimen 1	196
5.39 Acceleration frequency response functions at accelerometer #2 for specimen 2	197
5.40 Strain FRF at gauge 6, channel 20, of specimen 2 at 0, 650,000, 800,000 cycles	198
5.41 Strain FRF at gauge 3, channel 10, of specimen 2 at 0, 500,000, 650,000 cycles	198
5.42 Strain FRF at gauge 1, channel 9, of specimen 2 at 0, 500,000, 800,000 cycles	199
5.43 Strain FRF at gauge 8, channel 31, of specimen 2 at 0, 650,000, 800,000 cycles	199
5.44 Acceleration frequency response functions at accelerometer #1, of specimen 3 at 0, 557,000,765,000 cycles	200
5.45 Acceleration frequency response functions at accelerometer #5, of specimen 3 at 0, 557,000,765,000 cycles	200

5.46	Strain FRF at gauge 1, channel 8, of specimen 2 at 0, 800,000, 962,000, 1120,000 cycles	201
5.47	Strain FRF at gauge 4, channel 16, of specimen 3 at 0, 350,000, 765,000, 872,000 cycles	201
5.48	Strain FRF at gauge 9, channel 35, of specimen 2 at 0, 500,00, 800,000. 962,000 cycles	202
5.49	Strain FRF at gauge 15, channel 40, of specimen 2 at 0, 500,00, 800,000, 1120,000 cycles	202
5.50	Strain FRF at gauge 10, channel 23, of specimen 2 at 0. 500,00, 800,000. 1120,000 cycles	203
5.51	Strain FRF at gauge 16, channel 1, of specimen 2 at 0, 500,00, 800,000, 1120,000 cycles	203
5.52	Acceleration frequency response functions at accelerometer #1, of specimen 2 at 0, 650,000, 800,000, 1120,000 cycles	204
5.53	Acceleration frequency response functions at accelerometer #4, of specimen 2 at 0, 650,000, 800,000, 1120,000 cycles	204
6.1	Finite element model of tubular T-joint	206
6.2	Line spring elements and the connected elements	210
6.3	Strain FRFs obtained from FE model (- -) and crack free experimental model (-): Gauge 1 of specimen 3	223
6.4	Strain FRFs obtained from the FE model (- -) and the experimental model (-) at the first crack stage: Gauge 1 of specimen 3. The experimental data for the crack-free specimen are indicated by (-) . .	223

- 6.5 Strain FRFs obtained from the FE model (- -) and the experimental model (-) at second crack stage: Gauge 1 of specimen 3. The experimental data for the crack-free specimen are indicated by (-.) 224
- 6.6 Strain FRFs obtained from the FE model (- -) and the experimental model (-) at third crack stage: Gauge 1 of specimen 3. The experimental data for the crack-free specimen are indicated by (-.) 224
- 6.7 Strain FRFs obtained from FE model (- -) and crack-free experimental model (-): Gauge 4 of specimen 3 225
- 6.8 Strain FRFs obtained from FE model (- -) and the experimental model (-) at first crack stage: Gauge 4 of specimen 3. The experimental data for the crack-free specimen are indicated by (-.) 225
- 6.9 Strain FRFs obtained from FE model (- -) and the experimental model (-) at second crack stage: Gauge 4 of specimen 3. The experimental data for the crack-free specimen are indicated by (-.) 226
- 6.10 Strain FRFs obtained from FE model (- -), experimental model (-) at third crack stage: Gauge 4 of specimen 3. The experimental data for the crack-free specimen are indicated by (-.) 226
- 6.11 Strain FRFs obtained from FE model (- -) and crack-free experimental model (-): Gauge 7 of specimen 3 227
- 6.12 Strain FRFs obtained from FE model (- -), experimental model (-) at first crack stage: Gauge 7 of specimen 3. The experimental data for the crack-free specimen are indicated by (-.) 227
- 6.13 Strain FRFs obtained from FE model (- -), experimental model (-) at second crack stage: Gauge 7 for specimen 3. The experimental data for the crack-free specimen are indicated by (-.) 228

6.14	Strain FRFs obtained from FE model (- -), experimental model (-) at third crack stage: Gauge 7 of specimen 3. The experimental data for the crack-free specimen are indicated by (-)	228
6.15	Crack profiles from finite element model compared to specimen 3 . . .	229
6.16	(a) Mode shapes 1 and (b) 2 of the tubular T-joint	233
6.17	(a) Mode shapes 3 and (b) 4 of the tubular T-joint	234
6.18	(a) Mode shapes 5 and (b) 6 of the tubular T-joint	235
6.19	(a) Mode shapes 7, (b) 8, (c) 9 and (d) 10 of the tubular T-joint . . .	236
6.20	(a) Mode shapes 11, (b) 12, (c) 13 and (d) 14 of the tubular T-joint .	237
6.21	(a) Mode shapes 15, (b) 16, (c) 17 and (d) 18 of the tubular T-joint .	238
7.1	Load (P) - displacement (u) relations and the derived stiffness(k) for a crack under cyclic loading: a) an ideal crack, b) a fatigue crack under vibrational load, $F_0 e^{i\omega t}$, with $F_0 > P_{op}$ and (c) a fatigue crack under vibrational load with $F_0 < P_{op}$	255
7.2	Sine sweep forcing function	256
7.3	Response time history	256
7.4	Fourier transform	257
A.1	Node points for quadratic approximation in triangular element	285
A.2	Node points for quadratic approximation of serendipity class	285
A.3	Shape function, quadratic approximation of serendipity class	285
A.4	8 noded quadrilateral and 6 noded triangular elements	286
A.5	(a) Global coordinate system and displacements (b) Nodal coordinate system at node i and curvilinear coordinates	286
A.6	Local coordinate system	286

List of Symbols

a	Maximum depth of a semi-elliptical crack
$[C]$	Damping matrix
C_{ij}	Complementary energy
d	Brace diameter
D	Chord diameter
$[D]$	Elasticity matrix
E	Young's Modulus
$\{f\}$	Force vector
f^*	Nondimensional natural frequency
F	Force magnitude
F_x, F_y, F_z	x, y, z, direction force in force vector $\{f\}$
G	Energy release rate
$H_{jk}(\omega)$	Components in frequency response function
$H(\omega)$	Frequency response function
$H^e(\omega)$	Strain frequency response function
K_I	Stress intensity factor
$[K]$	Stiffness
l_i, m_i, n_i	Directional cosines along x, y, z direction

l	Half-length of a semi-elliptic crack
L	Maximum possible length of a crack
$[M]$	Mass matrix
N_i	Shape function
$\{Q\}$	Mass and mode shape modified force magnitude
r	Modal coordinate
$R_{uu}(\tau)$	Displacement autocorrelation function
$R_{ff}(\tau)$	Force autocorrelation function
$R_{uf}(\tau)$	Displacement and force cross correlation function
$R_{fu}(\tau)$	Force and Displacement cross correlation function
s	Nondimensional crack severity
$s_{1,2}$	Eigenvalues
$S_{uu}(\omega)$	Displacement power spectral density
$S_{ff}(\omega)$	Force power spectral density
$S_{uf}(\omega)$	Displacement and force cross spectral density
$S_{fu}(\omega)$	Force and displacement cross spectral density
t	Time
t	Thickness of the brace
T	Thickness of chord
t_1	Maximum crack depth
\bar{T}_i	Boundary area force

$T(\dot{u})$	Kinetic energy
u	Displacement
\bar{u}	Boundary displacement
U, V, W	x, y, z direction displacement component in vector u
$U(\epsilon_{mn})$	Strain energy
\dot{u}	Velocity
\ddot{u}	Acceleration
W	Nonconservative work
x, y, z	Global coordinate
x_i, y_i, z_i	Nodal coordinate
x'_i, y'_i, z'_i	Local coordinate
α	Real scalar in mass proportional damping component
β	Real scalar in stiffness proportional damping component
γ	Coherence function
$\gamma_x, \gamma_y, \gamma_z$	Shear strain components in x, y, z direction in strain vector
$\{\epsilon\}$	Strain vector
$\epsilon_x, \epsilon_y, \epsilon_z$	Strain components in x, y, z direction in strain vector $\{\epsilon\}$
ϵ^*	Nondimensional strain
ζ_r	Damping ratio of mode r
ζ^*	Nondimensional damping ratio
σ	Stress

σ_a	Tensile stress
σ_1	Maximum principal stress
σ_2	Minimum principal stress
σ^*	Nondimensional stress
τ	Time
ϕ	Mode shape
ϕ	Strain mode shape
Λ	Diagonalized mass normalized stiffness matrix
ν	Poisson's ratio
ξ, η, ζ	Curvilinear coordinates
ψ	Eigenvector
ω	Frequency
ω_r	Natural frequency of mode r
Ω_c	Complementary energy

Chapter 1

Introduction

1.1 Non-destructive Evaluation of Defects

Tubular members are widely used in off-shore structures because of their geometric simplicity, good hydrodynamic property and the omnidirectional (in cross-section) uniformity of stiffness and strength. The intersections of tubular members are joined by welding them together. The stress distributions around these welded joints are quite complex. Large stress concentrations and consequent plastic deformations occur in these regions and lead to cracking. Most of the failures that occur in off-shore structures are due to the growth of these small cracks into larger ones that may finally result in a catastrophic loss of strength and failure.

Defects may be formed in off-shore structures during any one of several manufacturing operations such as a) rolling and forming of the sheet steel to produce tubular products, b) welding of the tubes to produce three dimensional structures and c) assembly of these welded sub-assemblies to produce large platforms. The defects occurring during these stages of manufacture and assembly can generally be detected using conventional NDI (non-destructive inspection) techniques, and remedial measures taken. Defects, or more correctly cracks, may also be formed once the structures have entered service, and may be the result of environmental damage due to fatigue

(caused by cyclic loading), corrosion, or stress corrosion cracking (due to high static loads in a corrosive environment). These forms of damage are difficult to detect, and especially if they occur in parts of the structure that are submerged.

The presence of defects lowers structural integrity and reduces the strength. Even though all structures are designed to withstand the expected environmental loads, they are not immune to damage from overloads or repeated small amplitude fatigue loads leading to cracks. If these cracks are allowed to become large so as to impair the operational efficiency of these structures, human lives may be lost along with the possibility for loss of tremendous revenues. Hence to avoid such danger to the lives of crew members operating these structures and the consequent lost revenues, detection and monitoring of defects in structures at an early stage becomes an important task for all off-shore structural operators.

During the past fifty years, many methods have been developed for non-destructive evaluation of these defects and damage. They can be classified into two groups, viz., (i) one group, called conventional methods, consists of procedures that are now used invariably under all situations and are well developed; and (ii) the other, called recent, consists of procedures that are undergoing development and hence are not accepted as readily as others.

Many well-established non-destructive evaluation methods are already in use for detecting flaws and cracks in structures. These methods include magnetic particle inspection, dye penetrant, ultrasonic detection, radiography, eddy current, alternating current field measurement, and acoustic emission. Most of these procedures, however, need diver assistance and regular inspection of critical areas. With some of these techniques, such as ultrasonics and radiography, the whole surface must be scanned. So they are time consuming and expensive.

Some newer and emerging methods are based on dynamical procedures such as

vibration crack detection, wave propagation, laser interferometry, reflective laser techniques, etc. Dynamic defect/crack detection methods have advantages compared to the conventional methods, especially when cracks exist in large structures that are not easily accessible to human probing. In dynamical methods, the presence of defects in a structure can be recognized through the use of a number of remotely located sensors/transducers and the subsequent analysis of data obtained from them. These transducers can be used for continuous monitoring. In the monitoring methodology, digital data from transducers and sensors will be continuously transferred to computers. Any changes in the monitored parameters can be identified much faster by this means; consequently defect size will be determined by the intelligent processing of experimental data. Wholesale screening of the structure (as required by many of the earlier NDE techniques) is not necessary with dynamical methods; the inconvenience of access to the structure during testing can be overcome through the use of dynamic monitoring techniques. Also frequent diver assistance is not necessary. Thus vibration measurements offer an effective, inexpensive and fast means of non-destructive evaluation of structures.

The vibration methods for detecting defects may be broken into two subgroups: frequency monitoring and modal analysis methods. In frequency monitoring methods, various methods such as the sensitivity method and the relative natural frequency change method have been developed to detect the change of natural frequencies due to cracking. In the modal analysis method, many procedures have been developed for monitoring the location and extent of defects/cracks, which include monitoring frequency response functions, modal sensitivity functions, strain energy and displacement/curvature mode shapes. These procedures are being developed by ongoing studies so that they can form the basis of the dynamic non-destructive evaluation methodology using vibration techniques. Similar developments are taking place in all

the other dynamical methods mentioned above such as wave propagation technique, laser interferometry, reflective laser technique, etc. Moreover, instead of the conventional curve-fitting techniques used to identify the parameters, recently the use of neural network concepts and expert systems have been introduced in non-destructive evaluation.

1.2 Purpose of the study

A number of methods have been developed during the past twenty years, based on dynamic structural behavior. Initially the developments were mainly focused on rotating machines and beams. However, the dynamic properties and health monitoring of rotating machines beams and civil engineering structures are totally different. The work on beams has been summarized recently by Rytter (1993), and will be discussed in Chapter 2. Intense efforts to detect the damage/cracking in civil engineering structures have been made only during recent years. Difficulties have been encountered for crack detection in civil engineering structures because the changes in natural frequencies and modal magnitudes are too small to be identified as being due to cracking alone. No general theory or method is available for crack detection. **The aim of this investigation is to develop procedures that would accurately detect and predict the initiation and propagation of fatigue cracks in tubular T-joints or in any other similar structure. A specific goal is to lay the experimental and theoretical ground-work for an NDI method that can detect cracks in an off-shore structure, while in service and without diver assistance.** The dynamic behavior of tubular T-joints with a crack (or cracks) is investigated using the experimental facilities available in the Strength Laboratory of the Faculty of Engineering and Applied Science, Memorial University of Newfoundland.

Under applied cyclic fatigue loads, the cracks present in the structure will open and close. This leads to nonlinearity of stiffness, dynamic response and the frequency response functions. The "opening and closing" of cracks, during modal testing, has been considered earlier for a cantilever beam specimen (Ismail et al. 1990); but no results have been reported for tubular T-joint specimens. The nonlinearities associated with the crack opening and closing during the modal testing of structures have been investigated in detail in this study.

1.3 Scope of Research

In order to develop procedures for crack detection in tubular T-joints, and hence a general structure, relevant experiments and theoretical developments have been carried out in this study. Specifically, the scope of the study includes the following major tasks:

1. Design and develop the physical infrastructure for fatigue testing of tubular T-joint specimens, including the load application system, the load reaction system, the instrumentation, and the test control and data acquisition systems.
2. Completion of experimental studies on fatigue crack initiation and growth in the tubular T-joint specimens, and the development and application of modal testing techniques to monitor the development of fatigue damage, and especially the formation of cracks, in the structures.
3. Undertake the development of both phenomenological and mathematical models of the damage accumulation processes, and of the influence of this damage on the dynamic response characteristics of the structures. This testing was designed specifically to provide a theoretical basis for the development of a

practical experimental technique for detecting and locating cracks in tubular T-joint structures in service, or in related structures used in off-shore platforms.

4. The mathematical modelling is to include the use of finite element methods, and is to cover both the prediction of the fatigue crack growth processes (i.e crack shapes and sizes) and the dynamic response characteristics of the structure.

1.4 Organization of the Thesis

The contents of the thesis are organized according to the following format:

- Chapter 2 gives a literature review to provide an overview of the procedures developed for crack detection and identification. Chapter 3 gives the required theoretical background for dynamic structural modeling, modal analysis, experimental testing, and finite element analysis.
- Chapter 4 describes the experimental setup, instrumentation, calibration, and experimental procedures used for the dynamic tests. Chapter 5 gives the experimental results and analysis. Furthermore, relevant equations are developed for crack characterization in tubular T-joints. This chapter also includes the results of a fracture surface examination, performed using scanning electron microscopy.
- Chapter 6 presents the results of the finite element analysis carried out for cracked tubular T-joints. A general two-degree-of-freedom mathematical model is developed for crack opening and closing, and solved in Chapter 7.
- The concluding chapter, Chapter 8, summarizes all the findings in the research and gives additional recommendations for future research.

Chapter 2

Literature Review

A large number of studies have been carried out on conventional and the more recent, dynamical methods of non-destructive evaluation. The conventional methods have been well developed and implemented in widely-marketed equipment, whereas the dynamical methods are still under development and are implemented in a limited manner in some equipment. While these equipment detect the presence of very large cracks, the available methodologies are still not sufficiently precise to detect small or medium size cracks.

A detailed survey of available technical literature, and reviews from selected experts working in the field of damage-detection (using modal analysis procedures) was presented by Richardson (1980). The survey focused on structural integrity monitoring for nuclear power plants, large civil engineering structures, rotating machinery, and off-shore platforms, with by far the largest amount of literature associated with rotating machinery. The author stated that while monitoring of overall vibration levels for rotating machinery had become commonplace, attempts at relating structural damage to measured modal changes were still in their primitive stages. Several doctoral theses and dissertations that address structural damage detection and related issues were published recently. Each thesis/dissertation contained a literature

survey and development of the theory relevant to its scope; these include those of Rytter (1993), Hemez (1993), Kaouk (1993), and Doebling (1995). Mottershead and Friswell (1993) presented a survey of literature related to dynamic finite element model (FEM) updating, which was being used extensively for structural damage detection; their review contained a number of references on the topic of model updating. Bishop (1994) reviewed the literature in the field of neural networks: since neural networks were used extensively to solve inverse problems such as damage identification, the papers reviewed by Bishop were also relevant to the scope of this document.

The literature review given below highlights some of the developments in conventional non-destructive evaluation procedures and then outlines in detail the various developments that are taking place in the vibrational crack detection methodology.

2.1 Conventional Methods

The available conventional NDE methods are Visual, Dye Penetrant, Magnetic Particle Inspection, Ultrasonic Inspection, Radiographic, Eddy Current, Acoustic Emission and Optical Holographic techniques.

Visual Inspection and Dye Penetrant Inspection: Since man was created, the unaided eye has been used to inspect articles, to observe symptoms, and to detect abnormalities. Methods of aiding human visual perception using optical imagery and magnification have been developed; examples of visual inspection include endoscopy, real-time video/photoelectric imaging, dye penetrant and magnetic particle methods. They can only be used for detecting surface flaws, and cannot be used for detecting sub-surface flaws. Visual inspection using video imaging can be used for the undersea environment, whereas the conventional dye penetrant method cannot be used in such an environment; recent developments use a dye penetrant which does not react with

water during underwater usage. For subsea use of video or dye penetrant techniques, the surface of the structure must be cleaned for close inspection.

Magnetic particle detection is one of the most widely used and oldest visual non-destructive evaluation methods. It can be used in large and complex structures made of ferromagnetic material. It can be used effectively for surface and near-surface defect detection. The basic concept is that surface or near-surface discontinuities in magnetized material will distort the magnetic field. This will cause a leakage field to be formed that extends beyond the surface of the material. The defect is identified visually by a dense line of magnetic particles along its edge. In the detection procedure, test structures must be magnetized so that defects are transverse to the magnetic flux orientation (Bray et al. 1992).

Ultrasonic Inspection: Ultrasonic inspection is also widely used for crack detection. It can detect defects in metallic and nonmetallic materials. Defects can be located and measured in very thick materials. In many cases, it has a greater sensitivity than radiographic inspection to volumetric flaws. The ultrasonic technique has rapid testing capabilities and portable instrumentation is available for field use. There are two basic principles of ultrasonic testing. The first is based on the attenuation of the ultrasonic beam due to absorption by the flaw. This is sometimes referred to as the shadow method. The second principle of ultrasonic testing is based on the reflection of energy from a flaw or interface (Bayliss et al. 1988, Bray et al. 1992, Kobayashi et al. 1993).

Radiography: Radiography is an effective method for detecting defects in structures. The radiation pattern can be made visible with photographic film, fluorescent screens, or digitized images displayed on television or computer screens. A radiographic image is essentially a two dimensional shadow display or picture. Radiography provides a visual picture of discontinuities in structures. It can be used for many

forms of metallic and nonmetallic materials. It can assess a wide range of material thickness levels, radiograph complex shapes and provide a permanent record to the user (Bayliss et al. 1988, Bray et al. 1992).

Eddy Current Method: "Eddy currents are those currents caused to flow in an electrical conductor by the time and/or space variation of an applied magnetic field". Discontinuities affect the magnitude and phase of the induced eddy current. A flaw will change the magnitude of the eddy current in the metal sample, and this will be shown as a change in the voltage of the test coil due to its change of impedance. Because eddy current detection is effective only on the surface and near the surface, it may be necessary to use ultrasonics or radiography to supplement eddy current assessments (Bayliss et al. 1988, Bray et al. 1992).

A variation of this eddy current technique is carried out (using a pachometer) to detect the depth of concrete cover provided, for steel reinforcements, in concrete structures (Emmons, 1993).

A combination of eddy current principles (measuring the variation of resistance, impedance, capacitance, reactance, voltage, etc.) and injected electric current effect, of the magnetic flux leakage method, is called the ACFM (Alternating Current Field Measurement) method. This method has become very popular and is invariably used on off-shore steel structures. Initially the method started as a contact measurement of minute voltage variations developed in electrically conductive materials, when a constant current field was set up in the cracked specimen. Now the procedure has been developed as a near source non-contact procedure. The procedure can use both direct current and alternating current techniques to measure the flaws developed in the specimen under test.

Acoustic Emission: Acoustic emission (AE), or stress wave emission, is defined as "transient mechanical vibrations generated by the rapid release of energy from a

localized source within a material". It can be used for structural integrity monitoring. Stress or some other stimulus is required to release or generate emission. The method requires the use of several transducers placed on the structure and their outputs must be correlated in time to establish the position of the source of emission. There are two basic problems, viz., (i) measurement of the difference in time of arrival of pulses with sufficient accuracy; and (ii) recognition of the same pulse when it has traveled different distances, in different directions, in the material, and suffered attenuation and distortions. In general, acoustic emission monitoring systems are passive devices. They listen for and analyze sounds generated by crack initiation or growth. For large structures, acoustic emission is used to locate the crack and radiography or ultrasonic methods are used for detailed inspection. Non-propagating cracks cannot be detected by this method (Bray et al. 1992).

Optical Holographic Techniques: Holography is used as a non-destructive technique for inspecting materials. It uses the regenerated image of an object as a template to measure any deviation in shape or dimension. Optical holography uses certain unique characteristics of light waves such as wave phenomena, diffraction, interference and interferometry to accurately measure the flaws in a material by making and recording measurements under unstressed and stressed conditions. The process involves the recording of a complete wave front so that all information about a surface is retained and retrieved subsequently. The method of holography applies to all waves such as x-rays, light waves, microwaves and acoustic waves. The holographic techniques have been further developed to study the interference effects of waves; these interference effects have been widely used in the non-destructive examination of flaws in structural components. When holograms are reconstructed, they show characteristic patterns of the flawed surfaces; these are interpreted to quantify and characterize flaws. Holographic interferometry has used laser sources to provide

continuous sources of coherent light; two techniques used in the non-destructive examination are the time-lapse interferometry and real-time interferometry, depending on the type of laser sources utilized. A recent addition to this field is electronic speckle pattern interferometry.

Electronic speckle pattern interferometry (ESPI) is a kind of video-based speckle interferometry method. It can be used for non-destructive evaluation (NDE) of structures. The basic principle for speckle pattern interferometry is coherent light beam interference. In the detection procedure, a coherent laser beam is split into two branches. One is used as the reference beam; while the other is used to illuminate the test object. The coherent light scattered from a diffusely reflecting test object is made to interfere with the reference beam. The resulting interference speckle pattern is collected. Two speckle patterns are recorded. The second records a slightly different surface shape for the object (typically caused by stressing the object). The defects are found by comparing the two recorded interference speckle patterns. Since the deformation of the body is different near the discontinuity of the crack, the fringe pattern tends to be more closely spaced there (Bray et al. 1992, Kobayashi et al. 1993).

2.2 Methods Using Vibration Procedures

When a structure develops a crack, the stiffness and damping properties of the structure are changed; in addition the inertial behavior of the structure is also modified. This results in a structural response which is different from that of the crack free structure. Vibrational methods use the change of modal properties such as natural frequencies, mode shapes, damping, modal response, etc. to detect the presence of a crack.

2.2.1 Defect Indicators

Natural Frequencies: Any change of stiffness of the structure, caused by cracks, will change both the eigenvalues and eigenvectors; consequently, the natural frequencies and mode shapes of the structure will change. Therefore, natural frequencies can be regarded as one type of dynamical defect/crack indicator. Actually, many studies in non-destructive evaluation have been carried out by considering natural frequencies alone. Since natural frequency is indicative of the global behavior of a structure, it can be measured at any place and will remain the same. However, using natural frequency alone, it is difficult to locate and size a defect/crack. Also, natural frequency changes in a large structure, due to a crack, are too small to detect cracks reliably. Furthermore, a similar crack at a different place may cause the same change of natural frequencies. Any change in the non-structural mass (e.g., the mass on the top deck in an off-shore platform) of any structure will also be reflected in the change of natural frequencies (Rytter, 1993); hence care needs to be exercised in attributing the change in frequencies to any particular defect or crack.

Mode Shapes: The stiffness change due to a crack will also cause the change of eigenvectors. Hence mode shape can also be used as an indicator of a defect/crack. Mode shapes appear as local and global characteristics of the structure. When a defect/crack is introduced, the modal values at that particular location will change; but over the whole structure the changes will become dominant only when the defect/crack is quite large. There are many types of mode shapes which can be used as indicators of a defect/crack. The most widely used mode shapes are the displacement, curvature and strain mode shapes. Some values derived from them are also used, such as modal assurance criterion (MAC) (Allemang and Brown 1982, Fox 1992) and coordinate modal assurance coordinate (COMAC) (Lieven and Ewins 1988). Recent

investigations show that a defect/crack can be clearly identified by curvature and strain mode shapes. Displacement mode shapes and MAC or COMAC values based on displacement mode shapes are not very sensitive indicators of a defect/crack.

Damping: Theoretically, damping is a sensitive indicator of a defect/crack. Rytter (1993) reported damping increases up to 70 times were found due to a crack. However, damping is greatly influenced by environmental factors. It is very difficult to apply damping as a defect/crack indicator in real structures.

Other Indicators: An anti-resonance frequency indicator has been hypothesized by Afolabi (1987). In his study, a cantilever beam was modelled by a three-degrees-of-freedom lumped mass system. A crack was assumed by reducing the mass or the stiffness of a spring by 20 % to 50 %. It was shown that there was an anti-resonant frequency shift in some cases when there were large resonance frequency shifts in displacement frequency response functions. Hence, his indicator wasn't a successful one. However, this crack assumption could never represent a real crack.

Transmissibility, RDD-signatures (the Random Decrement signature), unexpected resonance frequencies, sub-/super-harmonic peaks in the spectra and probability density functions are also indicated as defect/crack indicators (Rytter, 1993).

A review of published literature shows that other works have detected cracks which are large with respect to the total load bearing cross sectional area of the beam or structure. In this study, a term

$$\text{normalized crack size} = \frac{\text{cracking area}}{\text{load-bearing area}}$$

is defined to describe a crack size. Typically the smallest detectable **normalized crack size** would be 0.125 (Gomes, 1990).

Rytter's (1993) work dealt mainly with large cracks. The change of resonant amplitude with frequency change becomes obvious when the normalized crack size

is much larger, when nearly 60 to 70 % (sometimes 80 - 85 %) of the fatigue life of the structure would have been spent in generating the crack. Damping increases become noticeable only when the crack depth is very large; in addition the damping changes indicated by Rytter seem to be too large. Mode shape changes are not significant unless the crack is very deep. The changes in MAC or COMAC values are also very small unless the normalized crack size is large. The subharmonic and superharmonic responses present in the frequency domain dynamic signatures, due to the opening and closing of a crack, seem to have potential for identifying the presence of a small/large crack; however even they seem to be dominant only for large normalized crack sizes. Hence, there is a need to identify parameters that will detect the presence of small normalized cracks in the structure. Unless the presence of small cracks can be detected, the usefulness of the vibration method as a NDT tool will be very much limited. Consequently, in this study, attention will be focused on the initiation and early stages of crack growth in typical tubular T-joint structures.

2.2.2 Modeling of the Crack

In order to carry out theoretical analysis, it is important to establish a crack model. The model generally reflects the change in stiffness caused by cracking. It is almost impossible to establish a model to reflect the change of damping; this is due to the fact that damping is quite sensitive to environmental conditions such as temperature, treatment of steel, etc. The modeling of a crack due to change of stiffness can be divided into open (always open) and breathing (open and close) crack models. Breathing or fatigue (open and close) cracks develop when cyclic loads are applied to a structure; the crack opens when the load produces a tensile strain around the crack zone, and closes in the reverse direction of the load cycle. These conditions are slightly modified when a static/dynamic, tensile/compressive, load acts in the

plane of the whole cross-section. Most researchers use open crack models to find relationships among modal parameters. Very few researchers have considered the breathing crack model. However the crack model utilized in the analysis will have varying degrees of influence on modal parameters. It has been observed from the earlier studies (Ismail et al. 1990) that the use of an open crack model to estimate breathing cracks would underestimate the severity of cracks.

2.2.2.1 Open Crack Model

A number of analytical/conceptual models have been developed to investigate the loss of stiffness in a structure due to an (always) open crack. They can be grouped as short beam, linear spring, reduced Young's modulus, reduced moment of inertia, and fracture mechanics models.

Short Beam Model: Cracks in a structure will decrease the cross-sectional areas resisting deformation and increase the stresses around those areas. Many researchers have isolated the cracked region and considered the region as a short beam. This model was probably the most commonly used model until the mid-seventies. With this model, an analytical solution is easily established and finite element analysis could be easily carried out (Rytter, 1993). Thomson and Madison (1949) used short beam models to determine the effect of a narrow groove or crack on flexural, longitudinal and torsional vibration of a slender bar. In their method, however, they pointed out that the size of an equivalent slot varied with the width and depth of the cut and must be established by experiment. Springer et al. (1987) developed an analytical expression that related the short beam length and the depth of a symmetric discontinuity and its location along a longitudinally uniform beam.

However, this idealized model is not a practical one for real crack detection. The

stress distribution is quite different from the real situation; consequently errors will be very large in the detection methodology, depending on crack sizes.

Linear Spring Model: The presence of a crack reduces the structural stiffness. The reduced stiffness, in a cracked portion, can be idealized by a linear spring. Haisty et al. (1985) investigated longitudinal vibration of a uniform beam containing two symmetric discontinuities by substituting the cracks with two linear springs. They used fracture mechanics concepts to obtain the equivalent spring stiffness. They also developed spring stiffnesses for (axial) tensile, bending and torsional loadings, of a beam containing a double-sided open crack (Haisty and Springer, 1988). Papadopoulos and Dimarogonas (1988) modeled the coupled bending and longitudinal vibration of a stationary cracked shaft with an open crack by tension and rotation springs. Gomes and Silva (1991) used a flexural spring model to investigate the changes in natural frequencies due to the presence of cracks.

The linear spring method has always been found to be useful in the crack simulation procedure. However, it must be realized that it is only an idealized model. The damping influence and stress distribution in the vicinity of a crack cannot be properly reflected in this model.

Reduced Young's Modulus and Moment of Inertia Models: In finite element analysis, it is very easy to assign material properties to elements. Because a crack decreases the local stiffness EI (of a beam), it is convenient from a modeling point of view to assume a change in Young's modulus so as to represent the presence of a crack (Yuen 1985, Pandey et al. 1991). Young's modulus is a material property and would not be measured in a specimen containing a crack. Any change in stiffness due to a crack, might be presented as an apparent change in modulus, but it is not a true change in modulus. This method requires only a simple modification in the finite element analysis and no new element is required. Moment of inertia reduction

reflects the removal of a local portion of the structure; in this way, local stiffness of a structure is varied (Salawu and Williams, 1994). This is similar to the short beam model where a certain length of beam is considered to act as a separate short beam.

Fracture Mechanics Models: According to Saint-Venant theory, the stress field is affected only in the vicinity of the crack. Hence, special stiffness matrices and equations are established by fracture mechanics theory for cracked elements using: (i) stress intensity factors (Rytter, 1993); (ii) singularity property (Shen and Pierre, 1990); (iii) strain energy theory at crack tip (Sekhar and Prabhu, 1992). This kind of model is always used in analytical and finite element formulations.

In the stress intensity factor consideration, the relationship between J integral and stress intensity factors for a linear elastic body is given by

$$J = \frac{\beta}{E}K_I^2 + \frac{\beta}{E}K_{II}^2 + \frac{1+\nu}{E}K_{III}^2 \quad (2.1)$$

where ν is Poisson's ratio, E is the modulus of elasticity, K_I , K_{II} , and K_{III} are the stress intensity factors for modes I, II and III, respectively, and

$$\beta = \begin{cases} 1 & \text{plane stress} \\ 1 - \nu^2 & \text{plane strain} \end{cases}$$

The flexibility caused by a crack is given by

$$\alpha_{ij} = \frac{1}{E} \int_0^{A_c} \frac{\partial^2}{\partial P_i \partial P_j} [\beta K_I^2 + \beta K_{II}^2 + (1 + \nu) K_{III}^2] dA \quad (2.2)$$

where K_I , K_{II} and K_{III} are the three stress intensity factors, P_i is force and A_c is the crack surface area.

In strain energy consideration, the local flexibility matrix due to a crack is given by

$$[C_c] = \frac{1}{F_0} \begin{bmatrix} \bar{C}_{11}R & & & \\ 0 & \bar{C}_{22}R & & \\ 0 & 0 & \bar{C}_{33}/R & \\ 0 & 0 & \bar{C}_{43}/R & \bar{C}_{44}/R \end{bmatrix} \quad (2.3)$$

where E is Young's modulus, $F_0 = \pi ER^2/(1 - \nu^2)$, $R = D/2$ and $\nu = 0.3$. C_{ij} are dimensionless compliance coefficients and D is the diameter of the structure (Sekhar and Prabhu, 1992).

2.2.2.2 Breathing Crack Model

Breathing cracks are produced when a cracked structure is subjected to a cyclic load, causing alternate opening and closing of the crack. Very few studies have considered the effects of actual opening and closing of cracks on the stiffness and dynamic response of a structure. Some studies have considered opening and closing crack in non-linear and bilinear crack models. Examples are the works of Lin and Ewins (1990), Huang and Gu (1993), Manson et al. (1993), Feldman and Braun (1995), Crespo et al. (1996), Actis and Dimarogonas (1989), Shen and Chu (1992), Chu and Shen (1992), Krawczuk and Ostachowicz (1992), Prime and Shevitz (1996). In the nonlinear crack model, the crack nonlinearity is considered to be produced by stiffness nonlinearities, higher order effects in the random structural response, higher order perturbation terms (using Volterra series for formulation) and a higher order analytic signal (using Hilbert transform). In the bilinear crack model, the remaining solid material in the plane of the crack is assumed to have two characteristic stiffnesses; one having a larger value when the crack is closing and the other having a smaller value when the crack is opening. Bilinearity in stiffness due to crack opening and closing will generate subharmonic and superharmonic response, in the frequency domain in a beam (Friswell, 1992).

Actual crack opening and closing is a continuous process wherein the structural stiffness changes continually from a lower value (when the crack is fully open) to a higher value (when the crack is fully closed).

Nonlinear Models: The frequency response function exhibits nonlinear character-

istics when a crack opens and closes. Side peaks are noticed in frequency response functions for closing and opening cracks (Ibrahim et al. 1987, Ismail et al. 1990). The presence of side peaks reveals nonlinear features, while linear behavior is observed for open cracks. The reason why the nonlinear behavior of the crack produces side peaks wasn't explained in his study. Open cracks produce larger changes in the natural frequencies of the structure compared to the breathing cracks; but for the same change of natural frequencies, the crack depth is much larger for a "opening and closing" crack. It is shown that reliance on the drop in the natural frequencies alone, especially for the higher modes, may lead to a serious underestimation of size of the crack. A very dangerous situation will result if the actual crack is much deeper.

Even though crack opening and closing leads to a nonlinear behavior, these nonlinearities have still not been properly modeled and quantified in the available literature. Further research is necessary to model and quantify the crack effects properly in order to fully evaluate crack influence.

Fracture Mechanics Models: Collins et al. (1992) presented a fracture mechanics formulation of a breathing crack model. Longitudinal vibrations of a cantilever bar, with a transverse crack, were investigated in their study. A quantity Λ was used in their analytical equation to express the opening and closing of a crack. However, due to cyclic loading, the crack progresses gradually from the closed state to the open state, and at any point in time it may be only partially open or partially closed. A model is needed that is able to deal with these partial degrees of crack opening/closing, as well as with the two extreme cases of fully open and fully closed.

2.2.3 Crack/Damage Detection Methods

The presence of a crack changes the natural frequencies, modal damping, modal vectors and the associated orthogonal/nonorthogonal properties associated with them.

Hence, methods used for the detection and sizing of these cracks could focus on any one of the above parameters and a mathematical procedure could be prescribed for achieving the same. In addition to the above, there may be advantages in considering non-linear effects, while the use of neural networks might facilitate the analysis.

2.2.3.1 Crack Detection by Frequency Monitoring

The stiffness changes occurring in a structure due to the presence of a crack will change the eigenvalues and hence the natural frequencies. The reason for selecting natural frequency to detect defects/cracks is that it can be measured or monitored from any place of the structure due to its global characteristics. The frequency monitoring method is defined as the method which uses frequency changes, without using modal shapes, to detect crack location and size. It can be divided into analytical and experimental investigations.

Early papers considered only the change of vibration frequencies to detect damage. Even today, much literature utilizing this method is published. The observation that changes in structural properties cause changes in vibration frequencies gave the impetus for using modal methods for damage identification and health monitoring. But it has significant practical limitations since only small changes in global vibration frequencies occur, even for large cracks. Moreover, in off-shore platforms, damage-induced frequency shifts are difficult to distinguish from shifts resulting from increased deck mass or subsea marine growth or underwater corrosion or erosion of the structure. In addition, as pointed out by several authors, there is often an insufficient number of frequencies with significant enough changes to determine the location of the damage uniquely (Doebbling et al. 1996).

There are numerous papers that deal with frequency monitoring for crack detec-

tion. The procedures and methodologies presented in these papers can be mainly categorized into sensitivity methods, natural frequency monitoring methods and strain-energy-based methods. Besides these methods, presented in the papers of Adams et al. (1978), Gomes and Silva (1990), and Sekhar and Prabhu (1992), which will be discussed in detail below, there still exist many others who have used the theory outlined in these papers, but have used different methodologies and derived different equations and procedures, viz., nomograms (Rytter 1993, Dimarogonas et al. 1980) or natural frequency change manipulations (Cawley and Adams, 1979).

Sensitivity Method: When sensitivity equations or other techniques are developed, and used in conjunction with frequency monitoring, defects could be located properly. In the frequency monitoring procedure developed for a bar by Adams et al. (1978), analytical equations for simple structures were combined suitably to find the crack severity. For one-dimensional systems, neglecting damping, natural frequency changes would also indicate the location of a crack.

The linear spring model, mentioned earlier in section 2.2.2, was used in the study by Adams et al. The spring had a varying stiffness K_x , which represented the damage in the structure. To know the position and severity of damage, the crack position x and K_x should be determined. So two modes should be considered. Considering the p th and q th modes, the relationships between K_x and direct receptances of the left side of the bar at the position x , β_{xx} , and right side of the bar at x , γ_{xx} , were given by

$$\frac{1}{K_x} = -(\beta_{xx} + \gamma_{xx})_{\omega=\omega_p-\Delta\omega_p} = -(\beta_{xx} + \gamma_{xx})_{\omega=\omega_q-\Delta\omega_q} \quad (2.4)$$

where the receptances were determined at the corresponding frequencies.

A graph superposing $-(\beta_{xx} + \gamma_{xx})_{\omega=\omega_p-\Delta\omega_p}$ and $-(\beta_{xx} + \gamma_{xx})_{\omega=\omega_q-\Delta\omega_q}$, plotted against x , gave the possible damage site(s) and the associated values of K_x at the

intersection of the curves. For a straight bar the relationship between K_x , x , and natural frequency was given by

$$\frac{EA}{K} = \frac{1}{\lambda} [\cot \lambda x + \cot \{\lambda(l - x)\}] \quad (2.5)$$

where $\lambda = \omega \sqrt{\rho/E}$. The possible damage site was given by the intersections of the curves of Eqn. 2.5 for different modes.

Experimental investigations, carried out for this purpose, reported a very satisfactory agreement between the predicted and actual damage sites. But when the damage was very severe, it was not possible to locate or size the damage; only one damage in a structure could be located properly. It was also shown that the minimum amount of damage which could be detected by this method was equivalent to the removal of about 1 percent of the cross-sectional area (Adams et al. 1978).

For symmetric structures, this method could not identify the crack location exactly; an extra location where no crack was present was also identified as crack location. In order to establish this methodology on a firm foundation, a proper relationship connecting K and crack size needs to be developed. Further, for more complex structures and loading conditions, it was hard to establish the relationship between crack severity K_x and crack location x .

Stubbs et al. (1990) identified the changes in resonant frequencies with the changes that occur in member stiffness, using a sensitivity approach. The authors mentioned that this sensitivity method had difficulty when the number of modes was much fewer than the number of damage parameters required to be identified.

Methods Based on Relative Natural Frequency Changes: The relationship existing between natural frequencies, crack locations, and their depths was investigated by Gomes and Silva (1990); springs which represented the bending stiffnesses at the crack locations were used in the analysis.

When a crack occurred in a beam, the relationship between the i th natural frequency for the uncracked beam ω_i and the cracked beam ω_{ci} could be expressed as follows:

$$Q_i = \frac{\omega_{ci}}{\omega_i} \quad R_i = \frac{\Delta\omega_i}{\omega_i} = \frac{\omega_i - \omega_{ci}}{\omega_i} = f_i(L_i, P) \quad (2.6)$$

where the ratio R_i (or Q_i) was a function of the location L_i and depth P of the crack.

Experimental studies were carried out on beams with slots and real line cracks. The results obtained with cracked beams were similar to the ones obtained with slotted beams. But changes of natural frequencies tended to be higher for cracked beams than for slotted beams; the discrepancies might be due to the fact that it was impossible to exactly control the manner in which the crack propagated under actual fatigue loading.

This method showed the relationship between frequency reduction, crack depth and location. However, when the frequency changes were small, it was not easy to detect the presence of a crack. Also, a similar crack at a different location could cause the same changes in natural frequencies.

Hearn and Testa (1991) developed a damage detection method by observing the ratio of changes between two natural frequencies $\Delta\omega_i$ and $\Delta\omega_j$. The authors summarized a two-step procedure, which was both qualitative and quantitative, for correlating changes in measured frequency ratios with damage locations.

Salawu (1995) proposed a global damage integrity index, based on a weighted ratio of damaged natural frequency to undamaged natural frequency, to detect and size the crack. When damage was indicated by any preliminary assessment procedure, local integrity indices could be calculated to locate the defective areas.

Skjaerbaek et al. (1996) developed an iterative method to estimate the average stiffness loss based on smoothed frequencies and mode shapes of the structure.

Strain-Energy-Based Method: The formation of a crack would change the local flexibility due to strain energy concentration in the vicinity of the crack tip. This method, which derived the flexibility matrix for a cracked element using the finite element method, could be used to investigate the influence of cracking on the dynamic response of structures (Sekhar and Prabhu 1992, Qian et al. 1990, Papadopoulos and Dimarogonas 1987).

The element matrix, except for the cracked element, was regarded as unchanged under a certain limitation of element size, since the crack affects only the stress field adjacent to it. By using strain energy, flexibility coefficients for an element without a crack were obtained as

$$[C_0] = \begin{bmatrix} \frac{l^3}{3EI} & & \text{sym} \\ 0 & \frac{l^3}{3EI} & \\ 0 & -\frac{l^2}{2EI} & \frac{l}{EI} \\ \frac{l^2}{2EI} & 0 & 0 & \frac{l}{EI} \end{bmatrix} \quad (2.7)$$

The local flexibility matrix due to the presence of the crack was given as

$$[C_c] = \frac{1}{F_0} \begin{bmatrix} \tilde{C}_{11}R & & \text{Sym} \\ 0 & \tilde{C}_{22}R & \\ 0 & 0 & \tilde{C}_{33}/R \\ 0 & 0 & \tilde{C}_{43}/R & \tilde{C}_{44}/R \end{bmatrix} \quad (2.8)$$

The total flexibility matrix for the cracked section was given as

$$[C] = [C_0] + [C_c] \quad (2.9)$$

where EI was the bending stiffness, l the element length, $F_0 = \pi ER^2/(1 - \nu^2)$, $R = D/2$ (for a circular shaft) and $\nu = 0.3$. C_{ij} were computed from the derivations given in the cited reference (Papadopoulos and Dimarogonas, 1987).

The normalized eigenfrequency change due to a crack in a shaft was given by (Sekhar and Prabhu, 1992),

$$\Delta\omega/\omega = f\{L/D, X/L, a/D\} \quad (2.10)$$

where ω was the natural frequency, L the length of the shaft, X crack location, a the crack depth and $\Delta\omega$ the change of natural frequency. Based on changes in natural frequencies, the crack position and depth were determined.

However, since natural frequency changes were very small, it was not easy to locate cracks or find their depth exactly by this method.

2.2.3.2 Modal Analysis Method

Since the occurrence of cracks in a structure would change its damping, stiffness and mode shape characteristics, the modal analysis method has been widely used in crack evaluation; in the modal analysis all the three effects could be combined under a single umbrella.

Mode Shape Change: West (1984) developed the first systematic use of mode shape information, viz., modal assurance criteria (MAC) for the location of structural damage. The change in MAC across the different matrix partitions was used to localize the structural damage.

Srinivasan and Kot (1992) found that the changes in mode shapes of a shell structure indicated damage better than the changes in resonant frequencies.

Salawu and Williams (1994) demonstrated that the relative mode shape changes did not indicate the damage efficiently, using experimental data. They stated that the selection of modes used in the analysis was the most important factor. They further showed that the MAC values could be used to indicate which modes were affected the most by damage (Salawu and Williams, 1995).

Frequency Response Function Method: The frequency response function has been widely used for crack evaluation. Frequency response relates the applied force and resulting structural displacement, acceleration, strain, etc. In this method, damage

is detected by comparing the frequency response functions of damped uncracked and cracked structures. Researchers working in the area have developed many methods which are described below selectively.

- Sensitivity Function Method

Some modal characteristics were generally not very sensitive to defects in structures, but there existed a sensitive frequency range in transfer or response functions around resonance which could be used for crack identification (Wang, 1987). The sensitivity analysis for crack diagnosis of structures, using vibration techniques, was based on this most sensitive frequency range.

From the above study, it was found that for light to medium damped structures ($\zeta < 0.707$), natural frequency, displacement, velocity and acceleration were not sensitive to changes of mass, stiffness and damping.

However, when frequency response functions were considered, sensitivity functions η for a single degree of freedom system, became (Wang, 1987)

$$\eta(H/k) = -\frac{1}{1 - \bar{\omega}^2 + j2\zeta\bar{\omega}} \quad (2.11)$$

$$\eta(H/m) = \frac{\bar{\omega}^2}{1 - \bar{\omega}^2 + j2\zeta\bar{\omega}} \quad (2.12)$$

$$\eta(H/c) = -\frac{j2\zeta\bar{\omega}}{1 - \bar{\omega}^2 + j2\zeta\bar{\omega}} \quad (2.13)$$

where $\bar{\omega} = \omega/\omega_n$ was the frequency ratio, H the displacement frequency response function, and k, m, c the modal stiffness, mass and damping, respectively.

The peak value of $|\eta(H/k)|$ or $|\eta(H/m)|$ was $1/2\zeta\sqrt{1-\zeta^2}$. So for small values of ζ , the peak in the sensitivity function was higher; and the sensitive range around the peak was distinct. The peak value of $|\eta(H/c)|$ was 1.

For an n degree of freedom system, the sensitivity functions were:

$$\eta(|H_{rs}|/k_{ij}) = -\frac{Re(H_{r1}H_{j2}H_{rs}^*)}{|H_{rs}|^2} k_{ij} \quad (2.14)$$

$$\eta(|H_{rs}|/m_{ij}) = \omega^2 \frac{\text{Re}(H_{ri}H_{js}H_{rs}^*)}{|H_{rs}|^2} m_{ij} \quad (2.15)$$

$$\eta(|H_{rs}|/c_{ij}) = \omega \frac{\text{Im}(H_{ri}H_{js}H_{rs}^*)}{|H_{rs}|^2} c_{ij} \quad (2.16)$$

The probable maximum values of η were $1/2\zeta_l\sqrt{1-\zeta_l^2}$ ($l=1,2,\dots,n$); and for the n -degrees-of-freedom system, the shapes of the sensitivity curves were similar to those of the single-degree-of-freedom system near the modal frequencies. There were multi-sensitive resonant frequency ranges in FRF; in addition, there also existed sensitive ranges near the anti-resonance frequencies. According to the above study, crack detection could be carried out in the sensitive ranges of FRF, both near the resonant and anti-resonant frequencies.

A series of frequency points in the sensitive ranges of $H_{rs}:\omega_1,\omega_2,\dots,\omega_N$ were chosen and the corresponding equations at each point were solved. This method could be used to find approximate crack locations; through the use of this method, it was also possible to find more than one crack. But it cannot be used to evaluate the size of the crack. Moreover a large number of computations had to be used for crack detection.

There are other papers that deal with crack diagnosis, e.g., that of Gu et al. (1989). This paper also used the frequency response function as the parameter for crack diagnosis. They adopted the least square identification method, using Kalman filtering and an adaptive filtering method, to diagnose structural defects. The numerical results were found to agree with experimental test results.

Li et al. (1992) also used a sensitivity method for crack defect detection. They only measured FRF of one or a few points as the observation signals. It was found that the extreme values of $\eta(|H_{ii}|/k_{ii})$ occurred at the frequencies of half power points.

Their calculation model for crack detection was given by

$$\Delta|H_{rs}| = - \sum_{L=1}^N \frac{\Delta P_L}{|H_{rs}|} \text{Re}([H_{ri}][A_L]\{H_{js}\}\bar{H}_{rs}) \quad (2.17)$$

where $[A_L] = \frac{\partial}{\partial P_L}[k_{ij}]$, $L = 1, 2, \dots, N$, and N was the number of modes considered in the study. ΔP_L denoted the change of parameter P_L caused by damage. To verify this method, an artificial crack occurring in an element of a modeled off-shore structure was considered. The crack was located successfully. The severity was known from the change of k_{ij} . The method only provided the model for crack location and severity; crack profiles could not be obtained by the model.

Law et al. (1992) developed a sensitivity equation based on the change in the FRF at any point, not just the resonance. A least squares fit was used to determine the change in the physical parameters.

• Strain Modal Analysis Method

Recently, many researchers have considered the use of strain modal analysis using strain gauges (Tsang 1990, Bernasconi and Ewins 1989, Li et al. 1989, Chen 1996). In a vibrating structure, strain was found to be more sensitive to cracks and convenient to measure; therefore, it provided a more accurate method for carrying out crack evaluation using strain modal analysis. Moreover, stresses and strains were more basic parameters that would characterize the local behavior in a much better manner than displacements/velocities/accelerations. In the paper on the modal behavior of a tripod tower platform due to crack growth, Swamidas and Chen (1992) detected cracks by monitoring natural frequencies and strain FRFs using strain gauges, accelerometers and a LVDT (linear variable displacement transducer). A 1/50 th scale model of a 340.0 m tall tripod tower platform, made of acrylic plastic, was used in their study. Simulated saw cuts were made on the platform and at each saw cut, which simulated a certain depth of crack, measurements of strains, accelerations and

displacements were made and the transfer functions computed. While acceleration and displacement transfer functions were not influenced much by the crack development and growth, the strain transfer function changed by around 60% when the crack grew through the thickness.

The governing equation for experimental strain measurements was given by (Tsang, 1990).

$$(-\omega^2[G] + [H])\{\epsilon(\omega)\} = \{F(\omega)\} \quad (2.18)$$

A theoretical expression of the strain responses was given by (Li et al. 1989)

$$\epsilon = [\psi^\epsilon][\Lambda]^{-1}[\phi]\{F\} = [H^\epsilon]\{F\} \quad (2.19)$$

where $[H^\epsilon]$ is the strain transfer function, ψ^ϵ the strain mode shape, and ϕ the displacement mode shape. From the analytical and experimental results, it could be stated that strain FRFs had larger changes as the crack size increased; similar changes were observed to be much smaller for acceleration and displacement FRFS. Hence the use of strain FRFs as a crack size and location estimator was an attractive concept that would require more detailed theoretical and experimental investigations.

Flexibility Changes: Pandey and Biswas (1994) detected and located the damage by using changes in flexibility of the structure. Their numerical and experimental results showed that the estimates of the damage condition and the location of the damage could be obtained from just the first two measured modes of the structure. Mayes (1995) measured flexibility from the results of a modal test on a bridge to locate damage.

Modal Sensitivity Function Method: When cracks occurred in a structure, mass, stiffness and damping distributions were affected; this caused a change in mode shapes and modal frequencies. So the sensitivity function for mass, stiffness and damping could also be used to evaluate cracks. The method derived the physical and modal

properties for the cracked structure in terms of the same property of the uncracked structure. plus an incremental change (Mannan and Richardson 1990, Richardson and Mannan 1991).

For classical or proportional damped structures, stiffness, mass and damping sensitivity equations could be obtained, respectively, as:

$$\begin{aligned} & \{U_i + dU_i\}^T [dK] \{U_i + dU_i\} + 2\{dU_i\}^T [K] \{U_i\} + \{dU_i\}^T [K] \{dU_i\} \quad (2.20) \\ & = \omega_{1i}^2 - \omega_{0i}^2 \end{aligned}$$

$$\begin{aligned} & \{U_i + dU_i\}^T [dM] \{U_i + dU_i\} + 2\{dU_i\}^T [M] \{U_i\} + \{dU_i\}^T [M] \{dU_i\} \\ & = (2\{dU_i\}^T [K] \{U_i\} + \{dU_i\}^T [K] \{dU_i\} - (\omega_{1i}^2 - \omega_{0i}^2)) / \omega_{1i}^2, \quad (2.21) \end{aligned}$$

$$\begin{aligned} & \{U_i + dU_i\}^T [dC] \{U_i + dU_i\} + 2\{dU_i\}^T [C] \{U_i\} + \{dU_i\}^T [C] \{dU_i\} \\ & = 2(d_{1i}^2 - d_{0i}^2) \quad (2.22) \end{aligned}$$

$$i = 1 \dots m \text{ modes}$$

where U_i is the mode shape matrix, ω_{0i} and ω_{1i} the natural frequencies without and with a crack, and d_{0i} and d_{1i} the damping coefficients without and with a crack.

For a small change the local stiffness changes could be written, using Equation (2.21), as

$$\sum_i \sum_j (U_{ik}^2 + U_{jk}^2 - 2U_{ik}U_{jk}) dk_{ij} = \omega_{1k}^2 - \omega_{0k}^2 \quad k = 1 \dots m \text{ modes} \quad (2.23)$$

This formula required only the mode shape of the unmodified structure plus changes in the frequency of the modes. So a crack which caused a local stiffness change could then be detected, located and quantified. Similar equations could be obtained for mass and damping changes. Cracks were located by observing the change of stiffness or damping or mass.

The method is good theoretically, but not of practical use in real situations.

The frequency changes are quite small in real structure. So the functions are not sufficiently sensitive to cracks.

There are also many other variations to this method, viz., (i) flexibility monitoring method presented by Rubin et al. (1983) which used changes in the deflection shapes to detect damages; and (ii) method presented by Park et al. (1988), and He and Ewins (1986), which used modal shape and natural frequency to find the difference between element stiffness matrices for undamaged and damaged structures.

Another sensitivity method, known as the Local Modal Crack Sensitivity (LMCS) method, was developed to find the location of a crack (Meneghetti and Maggiore, 1994). The sensitivity function given by these workers combined natural frequencies with mode shapes.

At the crack location x^* , the following relationship was obtained:

$$\frac{d\omega_r}{\omega_r} = \frac{1}{2k_r} \left(\frac{d^2\phi_r}{dx^2} \right)_{x^*}^2 \delta B \quad (2.24)$$

where, $\delta B = \delta D dx$, $D = EI$. The Local Modal Crack Sensitivity (LMCS) for a beam in bending was defined as

$$S_r = \frac{1}{2k_r} \left(\frac{d^2\phi_r}{dx^2} \right)_{x^*}^2 \quad (2.25)$$

where ϕ_r was the r th mode shape, ω_r and k_r the natural frequency and stiffness of r th mode.

Considering only the flexural vibration, in a given plane, at abscissa x^* , where the crack was localized,

$$\delta B = \frac{\delta\omega_j/\omega_j}{S_j(x^*)} = \frac{\delta\omega_l/\omega_l}{S_l(x^*)} \quad (2.26)$$

where ω_j and ω_l are frequencies at modes j and l .

Considering

$$W_j(x) = \frac{\delta\omega_j/\omega_j}{S_j(x)}, \quad W_l(x) = \frac{\delta\omega_l/\omega_l}{S_l(x)}$$

and plotting the two functions $W_j(x)$ and $W_i(x)$, one would obtain the crack location at the intersection of W_j and W_i .

In many cases the crack sizes could not be determined by this method. Moreover, there were other shortcomings for this method. Because of the symmetry of the curves obtained in the plotted figures, one could not judge from the intersections whether there existed one or two cracks; or in the case of one crack, one would not know whether the crack was at $x/L = 0.25$ or 0.75 .

Ko et al. (1994) detected damage in steel framed structures with the combination of MAC, COMAC and sensitivity analysis. The results showed that particular mode pairs could indicate damage, but when all mode pairs were used, the indication of damage was masked by modes that were not sensitive to the damage.

Strain Energy Method: Dong et al. (1994) presented a method using fracture mechanics theory and finite element computation that could be used to detect cracks in a reliable manner. They developed a special cracked element and used a general dynamic analysis procedure to compute the eigenparameters; thereafter, experimental modal analysis was carried out in the time domain using strain gauges. The stiffness matrix of the cracked element was obtained by considering the changes in strain energy produced by the crack.

The strain energy of an element without a crack could be expressed by

$$W^0 = \frac{1}{2EI} (M_{i+1}^2 L + M_{i+1} P_{i+1} L^2 + \frac{1}{3} P_{i+1}^2 L^3) \quad (2.27)$$

where E was the modulus of elasticity, I the moment of inertia of the cross section, M_i the moment at the i th cross section and P_i the shear force at the i th cross section.

The change in strain energy produced by the crack was

$$W' = \frac{1-\nu}{E} b \int_0^a [(K_{IM_{i+1}} + K_{IP_{i+1}})^2 + K_{IIP_{i+1}}^2] da \quad (2.28)$$

where ν was the Poisson's ratio, a the depth of the crack, and b the width of the cross section. $K_{IM_{i+1}}$, $K_{IP_{i+1}}$ and $K_{IIP_{i+1}}$ were the I and II types of stress intensity factors caused by M_{i+1} and P_{i+1} , respectively.

The flexibility matrix of such a cracked element (with the right end fixed) could be obtained according to Charles' theorem (Dong et al. 1994),

$$C_{jk} = \frac{\partial^2 W^0}{\partial P_j \partial P_k} + \frac{\partial^2 W'}{\partial P_j \partial P_k} \quad (j, k = 1, 2) \quad (2.29)$$

where, $P_1 = P_{i+1}$, $P_2 = M_{i+1}$

The stiffness matrix of cracked element can be obtained from

$$[K]_c = [T][C][T]^T \quad (2.30)$$

where

$$[T] = \begin{bmatrix} -1 & -L & 1 & 0 \\ 0 & -1 & 0 & 1 \end{bmatrix}^T \quad (2.31)$$

$$(P_i, M_i, P_{i+1}, M_{i+1})^T = [T](P_{i+1}, M_{i+1})^T \quad (2.32)$$

Therefore, the eigen equation of the cracked beam was

$$([K'] - \lambda_i[M])\{\phi\}_i^j = 0 \quad (2.33)$$

where $[K']$ was the global stiffness matrix of cracked beam, λ_i the eigenvalue of the i th mode, and ϕ_i^j the mass orthonormalized displacement eigenvector of the beam with j^{th} crack depth for i th mode. Experimental verification was carried out for the equivalent beam specimen with a crack at the center. Numerical and experimental results showed that the natural frequencies could reflect both the crack location and crack size; but changes that occurred in natural frequencies were very small and not easy to measure.

Generally, the first mode shape was observed to be most sensitive to damage occurring in the beam, because it had no node. When a crack occurred at the node, the corresponding natural frequency did not experience any change.

Stubbs et al. (1995) presented a method based on the fractional modal strain energies for a Bernoulli-Euler beam. The technique did not require computation of sensitivity matrices from a prior model. However, it required the structure to be well-suited for representation by beam elements.

Curvature Mode Shape Method: Pandey et al. (1991) developed the curvature mode shape method in time domain. The curvature change that occurred in the structure was found to be local. The method did not require extensive computation. Damages were found by comparing curvature mode shapes and the natural frequencies. The problem was analyzed using the finite element method. Curvature at a point in a beam was given by

$$v'' = M/(EI) \quad (2.34)$$

where v'' was the curvature at a section, M the bending moment at a section, E the modulus of elasticity and I the second moment of the cross-sectional area. From the displacement mode shapes, curvature mode shapes were obtained, using a central difference approximation,

$$v_i'' = (v_{i+1} - 2v_i + v_{i-1})/h^2 \quad (2.35)$$

where h was the length of the element.

Two cases were investigated in the paper, viz., a cantilever beam, and a simply supported beam. The absolute changes in displacement mode shapes and the curvature mode shapes between the uncracked and cracked beam were plotted over the length of the beam.

For the cantilever beam model, the absolute changes in displacement mode shapes

were not localized in crack region; but for each curvature mode shape, the maximum absolute difference between damaged and undamaged beams occurred in the damaged region. The damage was detected by the absolute maximum difference for damaged/undamaged curvature shapes. When severity of the crack increased, the difference also increased in the cracked zone. Since curvature was proportional to the bending strain, curvature mode shapes could be obtained directly by measuring strains instead of displacements or accelerations.

Applying Pandey et al.'s idea (1991), Perchard (1993) & Salawu and Williams (1994) did experiments on cantilever and simply supported steel beams. Salawu and Williams (1994) detected damage by two methods, viz., curvature mode shape and mode shape relative difference methods. The definition of curvature mode shape was the same as in Eqn. (2.35); while the mode shape relative difference was defined as

$$\{RD\}_r = \frac{\{\phi_o\}_r - \{\phi_D\}_r}{\{\phi_o\}_r} \quad (2.36)$$

where $\{\phi_o\}_r$ was the r th mode shape of the undamaged structure and $\{\phi_D\}_r$ the r th mode shape of the damaged structure. From their experiments and analyses, they concluded that neither the curvature mode shape method nor the mode shape relative difference method were satisfactory for locating damage.

It must be noted, however, that there were three deficiencies in their experiments and analyses: (i) they did not simulate the damage properly for detection, since the size of the damage they examined was too large; (ii) more accelerometers should have been used (which meant that a larger number of experimental elements would have been considered) so as to make the resultant curves more realistic of the mode shapes; and (iii) a curve fitting procedure should have been used in order to see the trends in modal shapes clearly.

Chance et al. (1994) found that the numerical calculation of curvature from

mode shapes resulted in unacceptable errors. However, the results could be improved dramatically when measured strains were used instead of directly measured curvature.

Zhang and Aktan (1995) stated that changes in curvature of the uniform load surface were sensitive indicators of local damage. The uniform load surface was the deformed shape of the structure when subjected to a uniform load.

2.2.3.3 Nonlinear Method

Actis et al. (1989) developed a finite element model for a beam with an opening and closing crack. Crack presence was determined by observing the sign of the bending moment at the crack location. Their results showed that higher harmonics were generated due to opening and closing of the crack.

Shen et al. (1992) developed a closed-form solution for the vibration of a beam with an opening and closing crack subjected to low-frequency harmonic excitation. They modeled the cracked location of the beam as a bilinear oscillator, and indicated the possibility of identifying damage based on the frequency and magnitude of harmonic vibration.

Prime et al. (1996) found by experiments that "harmonic mode shapes" were more sensitive to crack depth, and they located cracks better than conventional mode shapes. They examined the nonlinear response of a cantilever beam containing an opening and closing crack using the Wigner-Ville distribution techniques. The Wigner-Ville Distribution (WVD) determines the energy density of a signal as a function of time and frequency. When a number of frequencies appear as possible sum and difference of all natural frequencies due to the opening and closing of crack, the energy gets distributed into these side frequencies, as may be shown by the WVD.

Shumin et al. (1995) presented a crack model with the stiffness of the solid mate-

rial in the plane of the crack changing gradually due to the opening and closing of the crack. The dynamic responses of a beam were investigated for this model. The nonlinear behavior of a cantilever beam changing with crack severities was examined. It was seen that the natural frequency of a specimen containing a continuously opening and closing crack was between that of the specimen with a completely closed crack and one with a completely open crack. Use of a completely open crack model, to predict a fatigue crack influence, would underestimate the crack severity and could lead to catastrophic failure. It was also seen that when the crack was small, the nonlinearity for displacement response was negligible.

2.2.3.4 Neural Network-Based Methods

Neural network-based methods have only been developed during recent years. They aim at locating and sizing the damage in complex structures. The most popular method used is the multilayer perception concept (MLP) trained by back propagation.

Neural networks are computational models inspired by the neuron architecture and operation of the human brain. They were developed to mimic the pattern recognition capabilities of the human brain. The strength of neural network solutions lies in their pattern recognition capabilities. When statistical curving fitting, or other equation solving methods fail because of rank deficiency or other related numerical problems, neural networks often give very usable results. A neural network is an assembly (network) of a large number of highly connected processing units, the so-called nodes or neurons. The neural networks are capable of self-organization and knowledge acquisition, i.e learning. Neural networks "learn" from examples and exhibit some structural capability for generalization. Training consists of providing a set of known input-output pairs, patterns, to the network. The network iteratively

adjusts the weights of each of the nodes so as to obtain the desired outputs (for each input set) within a requested level of accuracy. Error is defined as a measure of the difference between the computed pattern and the expected output pattern.

Kudva et al. (1991) used a back propagation neural network to identify damage in a stiffened panel consisting of 4×4 array bays. Damage was modeled by cutting holes of various diameters in the plate at the center of the bays. The authors found that a neural network was able to predict the location of the damaged bay without an error, but there were errors of 50% or more on the prediction of hole size.

Leath and Zimmerman (1993) used an MLP neural network, based on a training algorithm, to identify damage in a four element cantilevered beam. The damage in the beam was modeled by reducing Young's modulus up to 95%. The algorithm was able to identify damage with a maximum error of 35 %.

Ceravolo and Stefano (1995) used a back propagation neural network to identify damage in a truss structure modeled using a finite element method. Damage was modeled by removing elements of the truss. The network located the damage well. The authors did not discuss how noisy measurements or multiple damage would affect the results.

While neural network methods have been used by others in an attempt to detect and locate structural defects or damage, they have not been used in this thesis.

2.3 Conclusions

From the literature survey carried out above, it is found that the dynamical methods for defect/crack detection have advantages over conventional methods presently used for monitoring cracks and damage in off-shore structures. Conventional methods are quite difficult to use for deep sea inspection due to: (i) prohibitive costs of equip-

ment and operation; (ii) some procedures cannot be used on complex structures; (iii) most off-shore structures need cleaning of joints; (iv) these methods cannot monitor the structural deterioration continuously; and (v) the need for diver-assistance. Hence modern dynamical methods present an attractive alternative to the conventional methods such as radiography or magnetic particle inspection.

Of the four methods of vibrational crack detection outlined in the literature review given above, viz., (i) frequency-based methods; (ii) modal analysis methods; (iii) nonlinear methods; and (iv) neural network based methods, a modal analysis method has been selected for detailed investigation of the problem outlined in this thesis. The strain modal analysis method which uses the outputs from the strain gauge sensors to identify cracks, will be utilized in the subsequent studies to identify the crack damage in tubular T-joints. In addition to strain mode approaches, displacement/acceleration based approaches will also be used to interpret the results obtained from accelerometers. Nonlinear approaches necessitated by the nonlinear crack opening and closing experienced by the tubular T-joints, under dynamic excitation loads, will also be used to interpret some of the characteristic experimental results obtained in this study.

Chapter 3

Theoretical Background for Analysis and Experiment

3.1 Introduction

For the investigation considered in this thesis, modal testing was carried out on four fatiguing tubular T-joints to determine the characteristic behavior of progressively-deteriorating structures. The experimental procedure used fatigue and modal testing techniques, along with ink staining and beach marking procedures to mark the crack profile. In the modal testing and analysis procedure, the structural component was vibrated using a known excitation; outputs from accelerometer and strain gauge sensors, located at preselected critical locations, were acquired and analyzed with a parameter identification algorithm to identify critical modal parameters. The test was carried out under closely controlled laboratory conditions to obtain accurate and detailed information on dynamic or vibratory behavior.

The experimental results, consisting of static and dynamic response data (stresses, natural frequencies and strain frequency response functions) were correlated with results obtained from numerical analysis carried out using an experimentally validated dynamic finite element analysis procedure. The finite element model used eight noded and six noded shell elements for the structure and six noded line spring elements for

the crack.

3.2 Modal Analysis and Vibration Theory

3.2.1 Modal Analysis

Based on vibration theory described in section 3.2.2 to section 3.2.5, vibration testing and measurement for modeling purposes are also referred as modal testing, modal analysis, or experimental modal analysis. Experimental modal analysis is the determination of natural frequencies, mode shapes, and damping ratios from experimental vibration measurements. Modal analysis procedure includes instrumentation, signal processing or modal data acquisition, modal parameter estimation and modal data presentation.

A vibration measurement generally requires several hardware components. The basic hardware elements required consist of a source of excitation, called an exciter, for providing a known or controlled input force to the structure, a transducer to convert the mechanical motion of the structure into an electrical signal, a signal conditioning amplifier to match the characteristics of the transducer to the input electronics of the digital data acquisition system, and an analysis system (or analyzer) in which signal processing and modal analysis computer programs reside.

The two most commonly used exciters in modal testing are the shaker and the impulse hammer. The preferred device is often the electromagnetic exciter and this is used in this research. The details of the exciter used are given in section 4.6.2. The most popular and widely used transducers, such as accelerometers, are made from piezoelectric crystals. Strain gauges can also be used to pick up vibration

responses. Among many available strain gauges such as electrical-resistance strain gauges, metal-foil strain gauges and semiconductor strain gauges, electrical-resistance strain gauges are the most common choice of the great majority of experimentalists and were selected for this research. This choice is based on the fact that the electrical-resistance strain gauges are usually the cost-effective method of measurement because the gauges exhibit most of the optimum characteristics commonly used to judge the adequacy of a strain-gauge system.

Once the response signal has been properly conditioned, it is routed to an analyzer for signal processing. The type of the analyzer used in this research is a digital Fourier analyzer, also called the fast Fourier transform (often abbreviated FFT) analyzer. The analyzer's task is to convert analog time domain signals into digital frequency domain information compatible with digital computing and then to perform the required computations with these signals. Also, all of the commercially available analyzers are marketed as turn-key devices. The theory of the digital signal processing built in the analyzer in this investigation is described in section 4.10.

Once the frequency response function is calculated by the analyzer, many methods could be used to extract modal parameters such as natural frequencies, damping ratios and modal amplitudes associated with each resonant peaks. The most common methods used for the extraction are polynomial curve fit and circle-fit methods. In this study, the first method was adopted for modal parameter extraction which is described in section 4.11. A single curve was fitted first, and multi-curve fits were performed after the single curve fitting.

Modal data presentation is simply the numerical tabulation of the frequency, damping, and modal vectors along with the associated geometry of the measured degrees of freedom (Ewins 1995, Inman 1994).

3.2.2 Vibration Theory General Description

Our world is attractive because it is filled with many varieties of structures. Unfortunately, it is almost impossible to establish the equations of motion for most of the continuous systems we see around us. The structures are usually considered as sub-units and modeled as simpler representations using discrete modeling before any analysis is carried out. The most basic discrete system is the single degree-of-freedom system (SDOF). Very few structures can be fully represented by this single-degree-of-freedom system; but the dominant behavior of many structures can be modeled by a single-degree-of-freedom system. Generally, a structure is modeled as a multi-degree-of-freedom (MDOF) system; the MDOF system can be considered to be made up of the summation of responses from a number of related SDOF systems.

A number of independent coordinates are required to describe the motion of a system; these are called the degrees-of-freedom of the system. In a MDOF formulation, a structural or mechanical system subjected to dynamic excitation requires the specification of displacements at a number of locations in the structure and along more than one coordinate direction. The system properties are expressed by mass $[M]$, stiffness $[K]$ and damping matrices $[C]$.

In a theoretical analysis, three consecutive models should be considered, i.e., a spatial model, a modal model and a response model, whereas in an experimental study it is done in the reverse manner. In a spatial model, mass, stiffness and damping matrices are used to describe the physical structural characteristics; the terms within these matrices are dependent on the geometric characteristics of the location selected for the degrees of freedom of the system. The analysis of the spatial model gives the modal model wherein a description of the structural behavior in terms

of the eigenvalues and eigenvectors of the structure are obtained, i.e., a set of natural frequencies with corresponding vibration mode shapes and modal damping ratios. The modes are called natural modes since they are obtained without any external excitation. When a structure is set to vibrate under a given excitation, the system is described as a response model. The response model consists of a set of frequency response functions (FRFs), which describes the characteristic modal behavior of the structure to a given external excitation. The FRF for a system under harmonic or sinusoidal input gives a well-posed mathematical problem and its solution gives the distinct system properties of a frequency response function. For a system under periodic or transient excitation, the force can be represented by a series of sinusoidal functions and hence the corresponding FRF derived. For a system subjected to random vibration, FRF is derived using the results of spectral analysis.

3.2.3 Governing Equations of Motion

Normally, a structural system has hysteretic damping properties which leads to a nonlinear behavior of the system. In a weakly damped system, the system is treated as a linear system; consequently system nonlinearity is neglected. Hence, in this study only viscous damping behavior is considered for the structural characterization.

For a multi-degree-of-freedom damped vibration system, the matrix equation of motion is given by

$$[M]\{\ddot{u}\} + [C]\{\dot{u}\} + K\{u\} = \{f\} \quad (3.1)$$

In the analysis, it is easier and more meaningful to specify modal damping ratios than to construct a damping matrix since damping resistance is difficult to relate to any measurable physical characteristics. As a general case, the viscous damping matrix can be selected to be a linear combination of the mass and stiffness matrices.

Proportional viscous damping is defined as

$$[C] = \alpha[M] + \beta[K]$$

where $[C]$ is the damping matrix, and α and β are real scalars.

For a system with proportional viscous damping, it is well known that the mode shapes or eigenvectors are equal to the ones of the undamped system; similarly the eigenvalues are the same as the undamped ones.

The typical variation of ζ_r (representing α or β with ω_r) is shown Figure 3.1; this can be specialized to either mass-proportional ($\beta=0$) or stiffness-proportional ($\alpha = 0$) damping (Petyt, 1990). Substitution of

$$\{u\} = [M]^{-\frac{1}{2}}\{q\} \quad (3.2)$$

into Eqn. (3.1) and pre-multiplying by $[M]^{-\frac{1}{2}}$, and neglecting $\{f\}$, gives (Inman, 1995)

$$\{\ddot{q}\} + (\alpha[I] + \beta[\bar{K}])\{\dot{q}\} + [\bar{K}]\{q\} = 0 \quad (3.3)$$

where $[\bar{K}] = [M]^{-\frac{1}{2}}[K][M]^{-\frac{1}{2}}$.

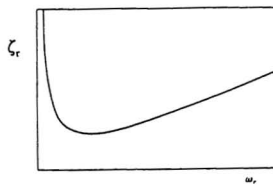
Substitution of $\{q\} = [\psi]\{r\}$ and premultiplying by $[\psi]^T$ which are eigenvectors of $[\bar{K}]$, gives

$$[I]\{\ddot{r}\} + (\alpha[I] + \beta[\Lambda])\{\dot{r}\} + [\Lambda]\{r\} = 0 \quad (3.4)$$

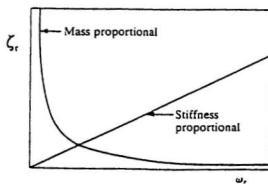
or the decoupled equation can be written as

$$\ddot{r}_r + 2\zeta_r\omega_r\dot{r}_r + \omega_r^2 r_r = 0 \quad (3.5)$$

where, $\zeta_r = \alpha/2\omega_r + \beta\omega_r/2$.



(a)



(b)

Figure 3.1: (a) Rayleigh damping; (b) Mass- and stiffness- proportional damping

$$[\Lambda] = [\psi]^T [\bar{K}] [\psi] = [\omega^2] \quad (3.6)$$

The response is

$$r_r = A_r e^{-\zeta_r \omega_r t} \sin(\omega_r' t + \phi_r) \quad (3.7)$$

and

$$\{u\} = [S] \{r\} \quad (3.8)$$

where $[S] = [M]^{-\frac{1}{2}} [\psi]$, A_r and ϕ_r are constants and determined by initial conditions.

The eigenvalues and eigenvectors for the above equation are

$$s_{1,2} = -\omega_r \zeta_r \pm i \omega_r \sqrt{1 - \zeta_r^2} \quad (3.9)$$

$$\omega_r' = \omega_r \sqrt{1 - \zeta_r^2} \quad (3.10)$$

$$[\psi]_{\text{damped}} = [\psi]_{\text{undamped}} \quad (3.11)$$

When the applied forces are harmonic, then the force vector can be expressed as

$$\begin{aligned} \{f\} &= \{F e^{i\omega t}\} \\ &= [M]^{-\frac{1}{2}} [\psi] \{\bar{F} e^{i\omega t}\} \end{aligned} \quad (3.12)$$

Equation (3.1) now becomes

$$\{\ddot{r}\} + [\bar{C}]\{\dot{r}\} + [\Lambda]\{r\} = \{Q e^{i\omega t}\} \quad (3.13)$$

where,

$$\begin{aligned}\{\bar{C}\} &= [2\zeta_r\omega_r I] \\ \{Q\} &= [M]^{-\frac{1}{2}}[\psi]\{\bar{F}\}\end{aligned}\quad (3.14)$$

The steady state response is obtained by assuming that response is harmonic with frequency ω . This gives

$$r = \bar{r}e^{i\omega t} \quad (3.15)$$

which leads to

$$[\Lambda - \bar{\omega}^2 I + i\bar{\omega}\bar{C}]\{\bar{r}\} = \{Q\} \quad (3.16)$$

Hence

$$\{\bar{r}\} = [\Lambda - \bar{\omega}^2 I + 2i\zeta_r\bar{\omega}\omega_r I]^{-1}\{Q\} \quad (3.17)$$

Substitution of Eqns. (3.17) and (3.15) into (3.2) gives

$$\begin{aligned}\{u\} &= [M]^{-\frac{1}{2}}[\psi]^T[\Lambda - \bar{\omega}^2 I + 2i\zeta_r\bar{\omega}\omega_r I]^{-1}[\psi][M]^{-\frac{1}{2}}\{F\}e^{i\omega t} \\ &= [H(\bar{\omega})]\{F\}e^{i\omega t}\end{aligned}\quad (3.18)$$

where

$$[H(\bar{\omega})] = [M]^{-\frac{1}{2}}[\psi]^T[\Lambda - \bar{\omega}^2 I + 2i\zeta_r\bar{\omega}\omega_r I]^{-1}[\psi][M]^{-\frac{1}{2}} \quad (3.19)$$

is the matrix of receptances. $H_{jk}(\omega)$ is a transfer function of receptance (displacement response) which is the response in degree of freedom j due to a harmonic force of

unit magnitude and frequency ω applied in degree of freedom k ; $H_{jk}(\omega)$ is called a point receptance. From Eqn. (3.19), it can be seen that (Petyt 1990, Ewins 1995)

$$H_{jk}(\bar{\omega}) = \sum_{r=1}^N \frac{M_r^{-\frac{1}{2}} \psi_{jr} \psi_{kr} M_r^{-\frac{1}{2}}}{\omega_r^2 - \bar{\omega}^2 + 2i\bar{\omega}\omega_r\zeta_r} \quad (3.20)$$

3.2.4 Random Vibration

Section 3.2.3 gives the analytical formulation for the vibration characteristics of MDOF systems and their frequency response functions under the harmonic vibratory force of $F e^{i\omega t}$. In the experimental modal analysis, the structure is subjected to a swept sine excitation and the relevant theory is obtained by assuming the forcing function to be a random one. For random vibration analysis, which has no regular response pattern at any time t , statistical methods are used to obtain the FRF characteristics. In addition (since responses are governed by the varying environmental and contact conditions at the site of excitation/measurement) performing a number of identical tests and averaging the results gives more accurate solutions.

For random vibration, the excitation force f at a certain time is only known in a statistical sense. The frequency response function $H(\omega)$ is given by the estimation of the relevant spectral densities and can be expressed as (Inman 1994, Ewins 1995)

$$H(\omega) = S_{uu}(\omega)/S_{uf}(\omega) \quad (3.21)$$

or

$$H(\omega) = S_{fu}(\omega)/S_{ff}(\omega) \quad (3.22)$$

where $S_{uu}(\omega)$ and $S_{ff}(\omega)$ are power spectral densities which are the Fourier transforms of autocorrelation functions $R_{uu}(\tau)$ and $R_{ff}(\tau)$, respectively; these can be expressed as

$$S_{uu}(\omega) = \frac{1}{2\pi} \int_{-\infty}^{\infty} R_{uu}(\tau) e^{-i\omega\tau} d\tau \quad (3.23)$$

$$S_{ff}(\omega) = \frac{1}{2\pi} \int_{-\infty}^{\infty} R_{ff}(\tau) e^{-i\omega\tau} d\tau \quad (3.24)$$

$$R_{uu}(\tau) = \lim_{T \rightarrow \infty} \frac{1}{T} \int_0^T u(t)u(t+\tau) dt \quad (3.25)$$

$$R_{ff}(\tau) = \lim_{T \rightarrow \infty} \frac{1}{T} \int_0^T f(t)f(t+\tau) dt \quad (3.26)$$

where T is period of the signal.

$S_{uf}(\omega)$ and $S_{fu}(\omega)$ are cross-spectral densities which are the Fourier transform of the cross correlation functions $R_{uf}(\tau)$ and $R_{fu}(\tau)$, respectively. They can be expressed as

$$S_{uf}(\omega) = \frac{1}{2\pi} \int_{-\infty}^{\infty} R_{uf}(\tau) e^{-i\omega\tau} d\tau \quad (3.27)$$

$$R_{uf}(\tau) = \lim_{T \rightarrow \infty} \frac{1}{T} \int_0^T u(t)f(t+\tau) dt \quad (3.28)$$

$$S_{uf}(\omega) = S_{fu}^*(\omega) \quad (3.29)$$

where $S_{fu}^*(\omega)$ is the complex conjugate of $S_{uf}(\omega)$.

The coherence function is used to check the noise in the signal. It is defined as

$$\gamma^2 = \frac{|S_{uf}(\omega)|^2}{S_{uu}(\omega)S_{ff}(\omega)} \quad (3.30)$$

γ^2 lies between 0 and 1. $\gamma^2 = 1$ means a pure signal and $\gamma^2 = 0$ means pure noise.

Normally, near the structural resonant frequency, γ^2 should be equal to 1.

3.2.5 Strain Frequency Response Functions

Strain gauges were used in the present experimental measurements to get the strain frequency response functions; accelerometers were also used to obtain the acceleration frequency response functions. The strain gauge technique for modal testing has been developed only during the past decade. The formulation of the strain frequency response function was developed by Ewins (1987) and Li et al. (1989) which is summarized below. The strain frequency response function is defined as the strain per unit force, expressed in the frequency domain.

For a proportionally damped system under harmonic excitation, the equation of motion is expressed as

$$[M]\{\ddot{u}\} + [C]\{\dot{u}\} + K\{u\} = \{f\} \quad (3.31)$$

where $\{f\} = \{F\}e^{i\omega t}$.

For three dimensional problems, the displacement has three components U, V and W in the directions x, y and z , respectively. Similarly the exciting force has three components. They can be expressed as

$$\{u\} = \begin{Bmatrix} U \\ V \\ W \end{Bmatrix} \quad (3.32)$$

$$\{F\} = \begin{Bmatrix} F_x \\ F_y \\ F_z \end{Bmatrix} \quad (3.33)$$

Assuming $\{u\} = \{\tilde{U}\}e^{i\omega t}$, where $\{\tilde{U}\}$ can be expressed in terms of eigenvectors

$$\{\tilde{U}\} = [\phi]\{q\} \quad (3.34)$$

Substitution of above equation into Eqn. 3.31 yields

$$\begin{aligned}
\{\bar{U}\} &= [\phi](-\bar{\omega}^2[M_r] + [K_r] + i\bar{\omega}[C_r])^{-1}[\phi]^T\{F\} \\
&= [\phi][\lambda]^{-1}[\phi]^T\{F\}
\end{aligned} \tag{3.35}$$

where $[\lambda]^{-1} = (-\bar{\omega}^2[M_r] + [K_r] + i\bar{\omega}[C_r])^{-1}$.

According to the theory of elasticity, the relationships between displacements $\{u\}$ and strains $\{\epsilon\}$ are given by

$$\epsilon_x = \frac{\partial U}{\partial x}, \quad \epsilon_y = \frac{\partial V}{\partial y}, \quad \epsilon_z = \frac{\partial W}{\partial z} \tag{3.36}$$

$$\gamma_{xy} = \frac{\partial U}{\partial y} + \frac{\partial V}{\partial x}, \quad \gamma_{yz} = \frac{\partial V}{\partial z} + \frac{\partial W}{\partial y}, \quad \gamma_{zx} = \frac{\partial W}{\partial x} + \frac{\partial U}{\partial z} \tag{3.37}$$

Hence

$$\{\epsilon\} = \begin{Bmatrix} \epsilon_x \\ \epsilon_y \\ \epsilon_z \\ \gamma_{xy} \\ \gamma_{yz} \\ \gamma_{zx} \end{Bmatrix} \tag{3.38}$$

$$= [H^\epsilon]\{F\}e^{i\bar{\omega}t} \tag{3.39}$$

where $H^\epsilon = [\phi^\epsilon][\lambda]^{-1}[\phi]^T$ is strain frequency response function, $[\phi^\epsilon]$ is strain mode shape and $[\phi]$ is displacement mode shape. Its elements are expressed by

$$H_{jk}^\epsilon = \sum_{r=1}^N \frac{(\phi_{jr}^\epsilon)(\phi_{kr})}{(\omega_r^2 - \bar{\omega}^2 + 2i\zeta_r\omega_r\bar{\omega})} \tag{3.40}$$

3.3 Finite Element Method

It is almost impossible to get an exact mathematical solution for the dynamical properties of a complex structure. Hence, approximate numerical results are obtained using the finite element method. When the finite element method is used in analysis, a geometrically complex domain of the structure is divided into a number of geometrically simple sub-domains called elements; and the elements are connected together by nodes. Interpolation functions are normally assumed for the elements. When solving a problem using the finite element method, an energy method of solution utilizing a variational procedure is made use of. In solving a problem, the following procedures are used: (i) element geometry is defined first; (ii) displacement fields are assumed; (iii) strain-displacement matrix, stress-strain matrix, element stiffness and mass matrices are derived, based on elastic or plastic behavior. The general equations of elasticity, as used in the FEM analysis, may be found in Appendix A for reference.

3.3.1 Shell Element

Figure 3.2 shows the eight noded quadrilateral and six noded triangular elements which are used in this study. These elements are known as degenerate thin shell elements in which the transverse shear stiffness acts as a penalty function to impose the Kirchhoff constraints. Unlike the elements based on thin shell theory, these elements could be applied to any general shell with a complex loading and complex boundary conditions (ABAQUS Manual 1994, Hinton and Owen 1984, Bull 1990, Ashwell et al. 1976). The details may be found in Appendix A for reference.

3.3.2 Solution Procedure

The general purpose finite element computer program ABAQUS was used for solving the assembled matrix equations of motions. In ABAQUS the dynamic response

studies were performed by using the eigenmodes of the system as a basis for calculating the response. Eigenvalue techniques were used to extract the frequencies and mode shapes of the system. The subspace iteration technique was used and a suitable number of basis vectors were chosen to start the iterative procedure. In addition to computing the natural frequencies and mode shapes, ABAQUS would automatically compute the generalized mass of the system also.

After carrying out the eigenmode extraction procedure, the modal response was obtained by using the steady-state harmonic response analysis procedure available in ABAQUS. The harmonic response at any given frequency was obtained as a frequency sweep by applying the harmonic loading at a series of different frequencies and recording the response. The steady-state harmonic response was calculated from the eigenvectors and eigenmodes of the system.

3.3.3 Line Spring Element

Line spring elements are designed to model part-through cracks in plate or shell-type structures. Line spring elements work because the only key parameters of interest that characterize the crack at any location are J and K , and we know that these parameters can be estimated without detailed knowledge of the local solution around the crack front. The basic concept is that these elements introduce the local solution, dominated by the singularity at the crack tip, into a plate or shell model of the uncracked geometry.

The degrees of freedom will be decreased dramatically for finite element analysis when line spring elements are introduced to replace a crack. Line spring elements provide inexpensive evaluation of part-through cracks in shell or plate members. The concept is based on replacing the part-through crack with equivalent distributed springs which match the compliance characteristics introduced into the structure by

the crack. Line spring elements provide great savings and the possibility of carrying out a linear structural analysis. However, the results obtained from a line spring element will not be accurate when the crack front has large curvature; also the local stresses around the crack front will not be very accurate. This method does not provide useful results when crack depths are less than 2% or greater than 95% (ABAQUS, 1996). Moreover the opening and closing of the crack, occurring due to the cyclic loading of a structure, is not modeled by the line spring elements. A line spring element is shown in Figure 3.2.

The stiffnesses of a line spring element are obtained by matching the local compliance of the crack with that of a single edge notch specimen shown in Figure 3.3. In the figure, the specimen is under remote tension N_I and moment M_I , where the subscript I indicates loading that will lead to mode I (opening) cracking. Δu_I and $\Delta \phi_I$ are the additional displacement and rotation due to the introduction of a crack.

Since the stress intensity varies linearly with load, the stress intensity K_I can be written as (ABAQUS, 1994).

$$K_I = k_1 N_I + k_2 M_I = k_i Q_i \quad i = 1, 2 \quad (3.41)$$

where k_i is stress intensity factor for a single edge notch specimen under unit remote tension or bending. k_i is a function of both crack depth a and specimen thickness t . Q_i is a generalized force.

The complementary energy Ω_c of the cracked single edge specimen can be expressed as

$$\Omega_c = \frac{1}{2} Q_i C_{ij} Q_j \quad (3.42)$$

where C_{ij} is the compliance of the cracked specimen. Also

$$q_i = C_{ij}Q_j$$

where q_i is conjugate generalized displacements with $q_1 = \Delta u_I$ and $q_2 = \Delta \phi_I$.

The stress intensity factor is related to the energy release rate per crack tip advance according to

$$\frac{K_I^2}{E'} = G = \frac{\partial \Omega_c}{\partial a} \Big|_Q \quad (3.43)$$

where G is energy release rate, $E' = E$ for plane stress, and $E' = E/(1 - \nu^2)$ for plane strain. E is Young's modulus and ν is Poisson's ratio.

Then

$$\frac{K_I^2}{E'} = \frac{1}{2} Q_i \frac{\partial C_{ij}}{\partial a} Q_j \quad (3.44)$$

For any Q_i and Q_j , K_I^2 is defined as

$$K_I^2 = Q_i k_i k_j Q_j \quad (3.45)$$

Therefore, the compliance is defined by

$$\frac{\partial C_{ij}}{\partial a} = \frac{2}{E'} k_i k_j \quad (3.46)$$

which gives

$$C_{ij} = \frac{2}{E'} \int_0^a k_i(s) k_j(s) ds \quad (3.47)$$

The stiffness is obtained by

$$[K_{ij}] = [C_{ij}]^{-1} \quad (3.48)$$

The insertion of line spring elements in the shell elements is shown in Figure 3.4.

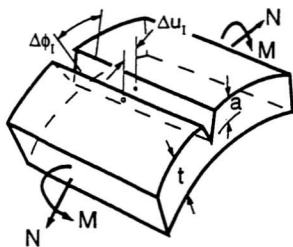


Figure 3.2: Line spring element .

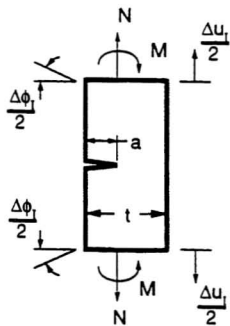


Figure 3.3: Single edge notch specimen

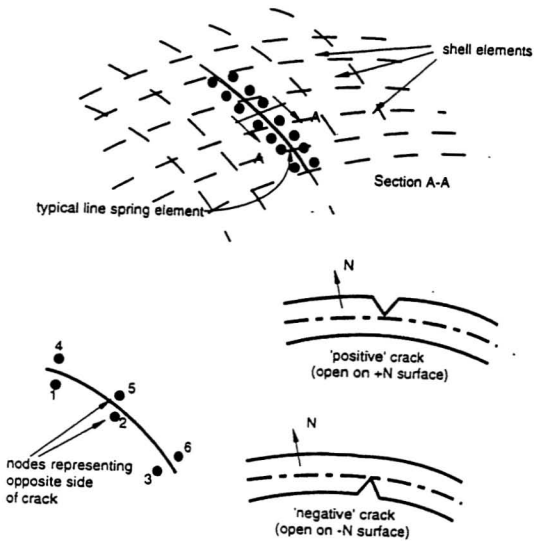


Figure 3.4: Line spring elements used with shell elements

3.4 Fatigue and Fracture Mechanics

Damage accumulated in materials under repeated loading, viz. fatigue, often causes crack initiation and propagation in structural members. Under small scale-yielding conditions, the stress distribution near the crack-tip can be described by linear elastic fracture mechanics (LEFM), which states that the stress at a distance, r , away from the crack-tip, is inversely proportional to the square root of this distance, i.e., $\sigma \propto r^{-\frac{1}{2}}$. The proportional constant, in LEFM terms, is called the stress intensity factor, K , which can be generally expressed as

$$K = Y\sigma\sqrt{\pi a} \quad (3.49)$$

where σ is the nominal stress in absence of the crack, a is the crack length, and Y is a shape factor taking into account the effect of the geometrical configuration of the crack.

Using this LEFM parameter, Paris (1961) found that fatigue crack growth rates in specimens of different geometry under different loads can be empirically consolidated into one equation:

$$da/dN = C\Delta K^n \quad (3.50)$$

where ΔK is the cyclic stress intensity range which is equal to the stress intensity factor at the maximum load minus that at the minimum load. N is the number of fatigue cycles and C , n are constants.

Wu et al. (Wu, Koul and Krausz, 1994) obtained the same equation based on the mechanism of restricted slip reversal (RSR), and showed that the theoretical exponent value of crack growth in pure mechanical fatigue is 3. The validity of the Equation (3.50) and the theoretical model is assumed for cracks that keep fully open during

the fatigue loading processes, presumably at positive stress ratios. However, in a real fatigue crack situation, due to the elastic constraint of the surrounding material on the plastic enclave in the wake of the crack, premature contact of the two mating surfaces may happen before the load drops to the minimum (or zero). This phenomenon is often referred to as crack closure (Elber, 1970) and a schematic is shown in Figure 3.5. The surface roughness and debris of corrosion, which inevitably exist due to microstructural inhomogeneity and environmental effects, may also enhance the crack closure (Ritchie, 1982).

The mechanical characteristics of crack closure were first identified by Elber as deflection in the load versus displacement curve, which implies a change in the stiffness of the specimen as the crack closes. Extensive experimental exploration has demonstrated that continuous change in the specimen's stiffness, below a certain load point, can occur especially during load shedding tests or after the application of an overload (Bäcklund, 1981). The scenario is shown schematically in Figure 3.6.

Figure 3.6a illustrates the local strain or displacement response of a loaded structure containing a crack. The lower portion (below P_3) of the curve, which has a constant slope (stiffness), is assumed to correspond to the fully closed state of the crack. As the load increases above P_3 , the crack begins to open and the structure enters a period of non-linear response where stiffness changes progressively. Finally, when the crack is fully open (at P_1), another period of linear response is encountered, when the stiffness remains constant, but with a lower value than the initial value. Upon unloading, the reverse behavior is observed. P_1 is often defined as P_{op} , the crack opening load. Figure 3.6b shows the non-linear portion of the curve for a specimen with cracks of different length ($a=15.9$ mm to $a=17.9$ mm). The point on each curve where the crack is fully open during loading is identified as P_{op} - the crack opening load. This also corresponds to the point of first contact between asperities

on the fracture surface during unloading. The non-linear stiffness characteristics of a cracked structure, observed in the transition region of Figure 3.6, will be taken into account in chapter 7, when models will be developed to predict the dynamic response of a specimen containing an opening and closing crack.

Intuitively, one can image that crack closure should shield a certain portion of the magnitude of the applied fatigue load and hence reduce the effective stress intensity at the crack tip. Recently, the mechanics of crack closure have been treated by Wu (Wu, 1995) using Irwin's energy method. Further discussion on the effective stress intensity range is beyond the scope of this thesis.

3.5 Summary

Basic theories of vibration and the finite element method have been provided in this chapter. Equations of motion, and the solution procedure for eigensolutions and frequency response functions have been summarized for a general multi-degree-of-freedom system. Theories for strain frequency response function and random vibration have been provided so as to provide a basis for understanding the methodology used for computing the analytical and experimental frequency response functions. Theories required for thin shell elements and line spring elements have also been summarized, along with a brief review of relevant information on fatigue and fracture mechanics.

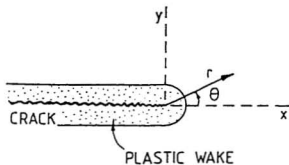
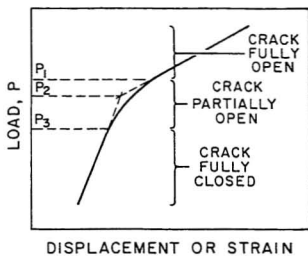
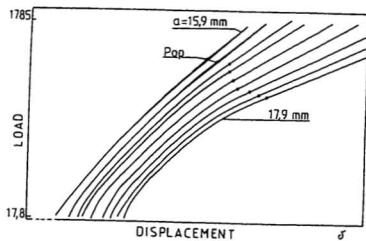


Figure 3.5: Schematic of crack closure



(a)



(b)

Figure 3.6: Schematic load-displacement curve (Bäcklund, 1981, Newman, 1988)

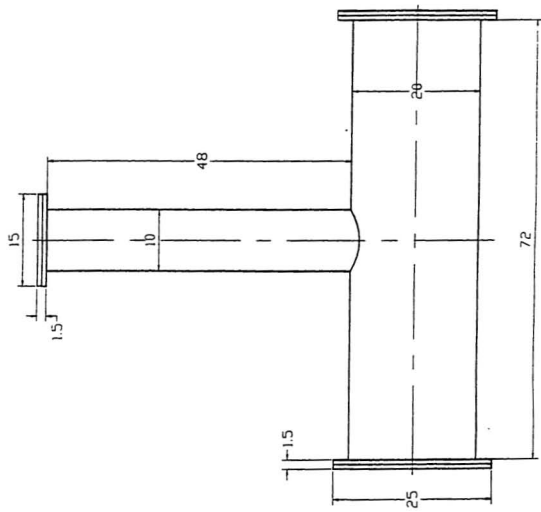
Chapter 4

Tubular Joint Fabrication, Experimental Setup, Instrumentation, Calibration, and Measurement of Responses

4.1 Introduction

In this investigation, procedures for non-destructive detection of cracks are examined using experimental and theoretical studies. Modal testing and analysis are used to identify cracks and to determine the dynamic behavior of the tubular T-joint. The tubular T-joint has a chord of length 72 inches and a brace of length 48 inches as shown in Figure 4.1. The structural details are given in Appendix B.

As summarized in the earlier literature review and discussed in the theoretical background development, any crack present in the structure will change the physical characteristics of the spatial model, viz., mass, stiffness and damping properties. The change of stiffness or damping will change the eigenvalues and eigenvectors of the modal model. These changes will consequently change the frequency response functions of the response model including displacement, velocity, acceleration, and strain frequency response functions etc. Since the crack influence on the mass is neg-



All dimensions in inches

Figure 4.1: Tubular T-joint under test

ligible, researchers normally focus their attention on the change of stiffness to detect a crack. Damping is quite sensitive to environmental conditions such as temperature and moisture, and as such it is almost impossible to use damping as a reliable crack indicator. In the present set of experiments, no definite trend in damping ratio was found when a crack was initiated and propagated under cyclic fatigue loading.

Among the variety of methods available for crack detection, using vibration procedures, strain frequency functions were used in this study. Strain gauges were used as the main transducers to measure frequency response functions of the tubular T-joints. In addition, accelerometers were used to determine the response and to verify the reliability of the results obtained using strain gauges.

This chapter deals with experimental setup, instrumentation, calibration and measurement of structural responses. These are the most important preliminary requirements to ensure the accuracy and reliability of data. Data processing and analysis will be meaningful only when proper data acquisition has been made using the correct experimental parameters.

Four specimens were tested in this study. Unfortunately, testing of the second specimen was discontinued after the crack was initiated on one side since unreasonable frequency shifts were observed; the bolts which connected the chord end plates to the chord had gradually become very loose. These results could not be presented in the thesis since the computer in which the data were stored, was also lost during a subsequent break-in and theft from the laboratory.

The tested specimens will be discussed later, and for convenience will be identified as 1, 2, and 3 instead of 1, 3, and 4.

Strain and acceleration frequency response functions of the tubular T-joints were obtained and utilized to locate and size the cracks. Static strains/stresses, natural frequencies and damping ratios were also measured and assessed as crack indicators.

Forty strain gauge channels and seven accelerometers were located at salient points of the structure to monitor the response.

4.2 The Fabrication of Tubular T-Joints

The tubulars were ordered from Welded Tube of Canada Limited, Concord, Ontario. The material was CSA G40.21-92 50W CLS. C. ERW steel piling of 20" OD, 0.26" wall thickness and 54.81 lbs per foot length for the chord; it was 10" OD, 0.26" wall thickness, for the brace. This material had an ultimate tensile strength of 80,576 psi and a yield strength of 58,770 psi at 2 % offset and 24 % total elongation, as per the company data sheets.

Before starting the fabrication of the tubular T-joint, a load frame shown in Figure 4.2 was set up. The actuator mounted to the overhead frame (used for dynamic testing) was lined up to be truly vertical. The verticality of the brace and the horizontality of the chord were established with reference to the actuator and the load frame. Spot welding was done to connect the chord and brace; for detailed welding the partially welded joint was removed from the load frame and welded on the shop floor. Since it was not possible to exactly line up the chord and the brace, a slight eccentricity was introduced during the welding of the chord and brace. This eccentricity would lead to assembly stresses when the test specimens were mounted in the loading frame.

Welding was carried out by shielded metal arc welding; in this arc welding process an arc is struck between a covered metal electrode and the components to be joined. This causes heating and melting of the component material, and hence joining as the liquid metal resolidifies. The details of the welding process are given in Appendix C.

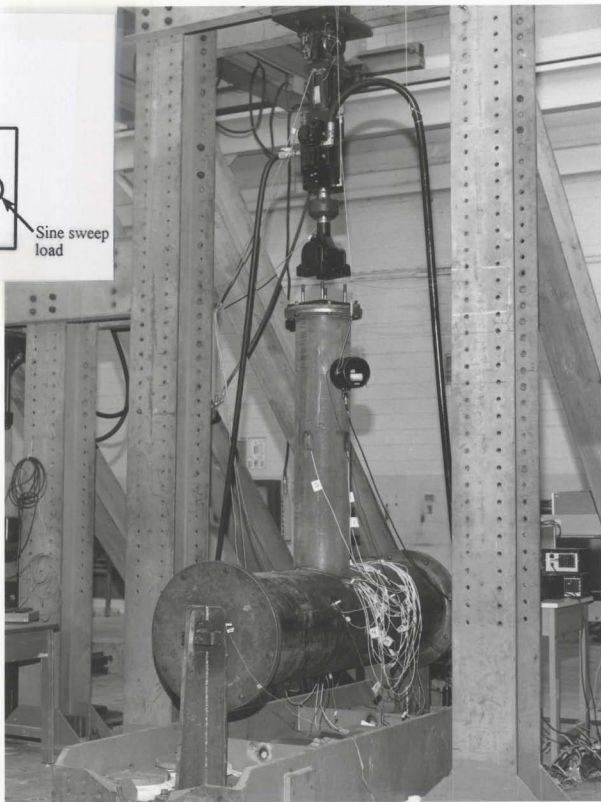
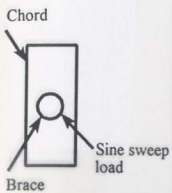


Figure 4.2: Tubular T-joint under modal test

4.3 Characteristic Stresses Developed in Tubular T-joints

The stresses that are developed around these welded joints are quite complex. Large stress concentrations and consequent plastic deformations occur in these weld-toe regions and may lead to cracking. Most of the failures that occur in platforms having these types of complex joints are due to the growth of small cracks, that exist around the weld-toe regions. Crack growth will finally lead to a catastrophic loss of strength and failure. The basic configuration of these tubular joints is shown in Fig. 4.3.

Generally, stresses that develop at a joint could be considered to be made up of three components, viz., nominal stresses, deformation stresses and geometric stresses. Nominal stresses are the average stresses that develop at a joined region, due to axial or bending loads acting on the brace (mainly). They do not take into account any discontinuities in the structure. Global analysis of the structure is required to compute these stresses. The deformation stresses occur as a consequence of the chord and brace trying to maintain the joint compatibility during the process of structural deformation. Geometric stresses are caused by the discontinuity around the welded joints and will dominate the stresses that are generated around these joints. These geometric stresses create stress and strain concentrations and exert the major effect on tubular T-joint.

The large stress concentrations that occur at the intersections of the chord and brace may lead to cracking along the intersection. Under a brace axial load (for the present series of tests), the maximum geometric stresses occur at the saddle points. Generally for all specimens under test, one saddle point will have a larger geometric stress than the other due to errors in alignment during manufacture. During fatigue testing, the crack tends to develop on this side. Hence, in the present study, the

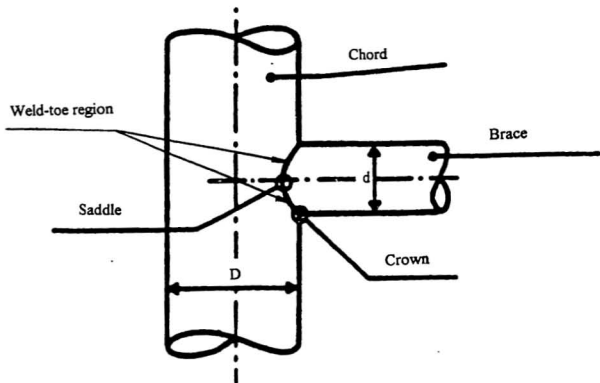


Figure 4.3: Tubular T-joints

weld-toe region containing the other saddle point was ground smooth to prevent any crack development on that side. In spite of this precaution, it will be seen later that cracks developed around both the saddle regions in specimen 2.

4.4 Geometric Properties of Tubular T-Joints

The tubular T-joints under test and their dimensions as given by the fabricator are shown as Table 4.1. However, due to manufacturing errors, the real dimensions will not be the same as those given in the fabricator's data sheet. The dimensions for the tested specimens were measured and listed in Table 4.1. The detailed structural manufacturing drawings are shown in Appendix B.

4.5 Experimental Setup

Figure 4.2 shows the experimental setup for the tubular T-joints under modal testing; The exciter was hung freely from the load frame. The exciting force was applied at the side of the brace. Figure 4.4 shows the experimental setup for the tubular T-joints under fatigue testing. The actuator was fixed vertically on the load frame to apply an axial load along the brace. The tubular T-joint was fixed to a heavy steel test bed, measuring 9'8" \times 4'3" (2763 mm \times 1250 mm) (Figure 4.5). The test bed was fixed to the 3.0 feet (914 mm) thick concrete test floor; another 450 kg (4410 N) weights were added to the test bed to increase the mass of the test bed. A rigid steel support was designed and fabricated to support the tubular T-joints, providing simply supported boundary conditions (Figure 4.7). Rotation around the chord axis was prevented by a pin, inserted during modal testing. Free rotation was allowed around the chord axis, when the tubular T-joint was fatigue tested under axial loading of the brace.

In order to connect the actuator to the tubular joint during fatigue testing, an

Table 4.1: T-joint Geometry

Geometry	Fabrication data sheet	Experimental specimen measurements (Variations cover all three tubular T-joints)	Manufacturing tolerance allowed	
Chord diameter	20 inch	20-20.08 inch	19.8-20.2 inch	±1%
	(508 mm)	(508-510 mm)	(502.92-513.08 mm)	
Chord length	72 inch	71.81-71.89 inch	—	—
	(1828.8 mm)	(1824-1826 mm)		
Brace diameter	10 inch	10.74-10.83 inch	9.9-10.1 inch	±1%
	(254 mm)	(273-275 mm)	(251.46-256.54 mm)	
Brace height	48 inch	48.19-48.43 inch	—	—
	(1219.2 mm)	(1224-1230 mm)		
Chord wall thickness	0.25 inch	0.24 - 0.29 in	0.22-0.28 in	±12½%
	(6.35 mm)	(6.23-7.366 mm)	5.56-7.14 mm	
Brace wall thickness	0.25 inch	0.248-0.29 inch	0.22-0.28 in	±12½%
	(6.35 mm)	(6.3-7.366 mm)	(5.56-7.14 mm)	
End plate diameter	25 inch	25.08-25.16 inch	—	—
	(635 mm)	(637-639 mm)		
End plate thickness	0.75 inch	0.76-0.77 inch	—	—
	(19.05 mm)	(19.4-19.6 mm)		
Top plate diameter	15 inch	15.08 inch	—	—
	(381 mm)	(383 mm)		
Top plate thickness	0.75 inch	0.752-0.768 inch	—	—
	(19.05 mm)	(19.1-19.5 mm)		

1 inch = 25.4 mm

extra square plate of 10 inch sides and 1 inch thickness was welded on the top of the plate connecting the brace to the actuator (Figure 4.6). To prevent the buckling of the end plates of the chord of the tubular T-joint, a heavy stiffening framework was welded on to the end plate, as shown in Figures 4.8 and 4.9. The shaker was suspended freely from the supporting frame for modal testing, as shown in Figure 4.2, to allow for inertial force loading on the T-joint. The shaker was at an angle of about 45° to the chord axis and excited the brace of the tubular in a horizontal direction, generating in-plane and out-of-plane bending motions.

4.6 Instrumentation

In this investigation, the method of single-point excitation and multiple-point data acquisition was adopted. The instrument setup is shown in Figure 4.10 with the flow chart for system operation given in Figure 4.11. Fatigue loads were applied by the hydraulic actuator (MTS 244) to generate fatigue cracks; an MTS 407 controller was used to control the hydraulic actuator. During modal analysis, the hydraulic actuator was removed, and a B & K 4809 PM vibration exciter was connected to the T-joint through a stinger for carrying out modal excitation; a Kistler model 912 load cell was attached to the stinger and connected to the tubular joint excitation point. Basically, an exciter, transducers and a signal analyzer were required to set the system up. Swept sine signals having different frequency ranges were generated from an HP 3314A function generator. The signal was passed through a B & K 2706 power amplifier to the vibration exciter which excited the specimen. The excitation force was measured by the Kistler load cell, model 912. The strain-gauge signals from the strain gauges were passed through a Keithley 706 scanner and through a Vishay 2120 strain gauge conditioner to a KH 3323 filter and finally to the first

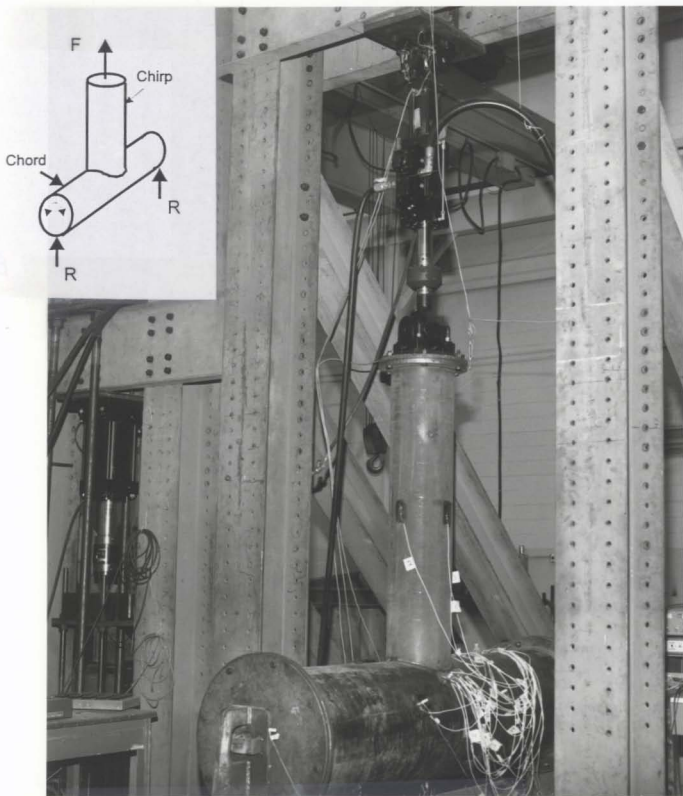


Figure 4.4: Tubular T-joint under fatigue test

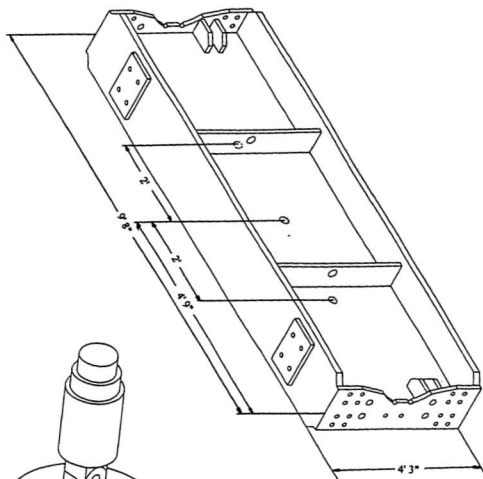


Figure 4.5: Test bed

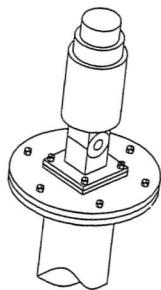


Figure 4.6: The connection between the specimen and actuator

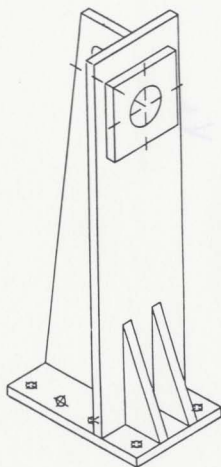
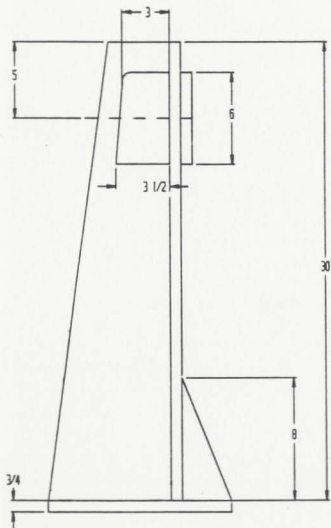
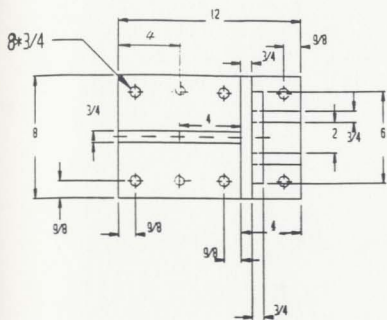


Figure 4.7: Test specimen support

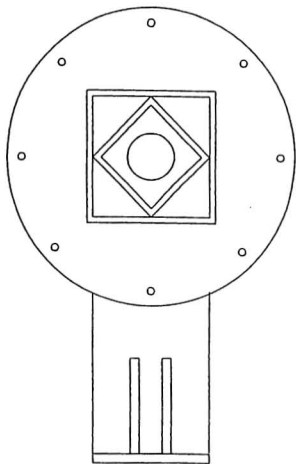


Figure 4.8: The stiffening ring on the end plate

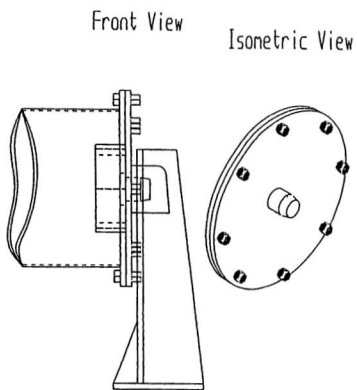


Figure 4.9: The connection between the specimen and support

channel of the B & K dual channel 2034 signal analyzer. The force signal from the load cell was passed through a 2626 B & K conditioning amplifier to the second channel of the same signal analyzer. Also, the acceleration signals from STRUCTCEL accelerometers were passed to the signal analyzer, to obtain acceleration FRFs. The STAR program was used to acquire the data from the analyzer for further analysis. The division of the strain-gauge/accelerometer signals by the force signal, carried out by the software available in the signal analyzer, gave the strain/acceleration FRF for the strain-gauge/accelerometer location.

4.6.1 Command Signals and the Function Generator

Many signals can be used to excite the structure for modal testing such as swept sine, random, transient and sine chirp. Swept sine signals were used in the present investigations. A swept sine input consists of a harmonic force of constant magnitude f_i with frequencies ranging from a small value to the specified maximum value. A sample of a swept sine signal is shown in Figure 4.12.

The swept sine signal was generated by a HP 3314A function generator. The HP 3314A was a multi-mode, HP-IB programmable function generator featuring sine, square and triangular functions ranges from 0.001 Hz to 19.99 MHz. It had a sophisticated implementation of the operating modes plus precision control of the trigger signal.

4.6.2 Exciter

The exciter provides the driving force for the modal analysis. The two most commonly used exciters are the electromagnetic shaker and the impulse hammer. The electromagnetic shaker has the advantage of providing large enough input to give easily measurable and controlled response. The input electrical signal from the function

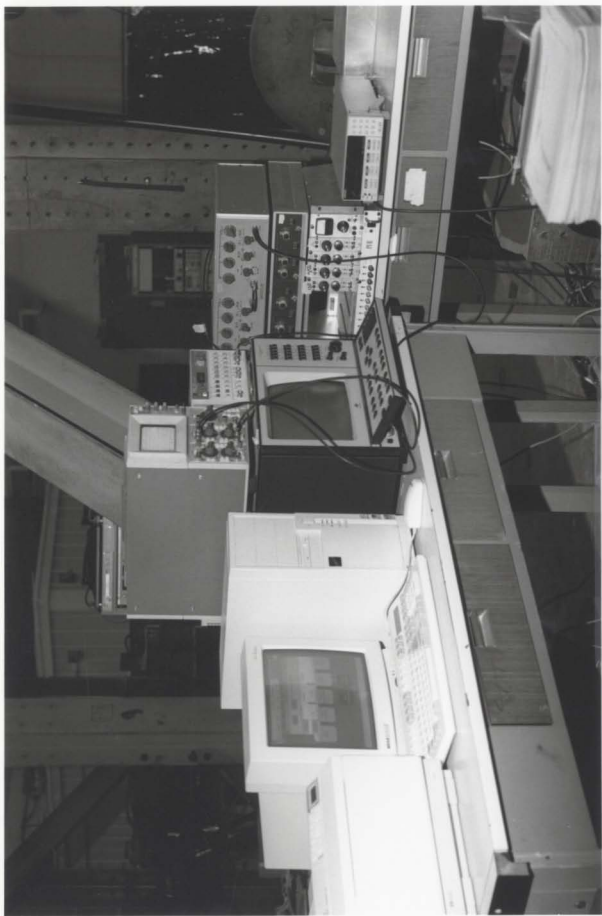


Figure 4.10: Instrument set up

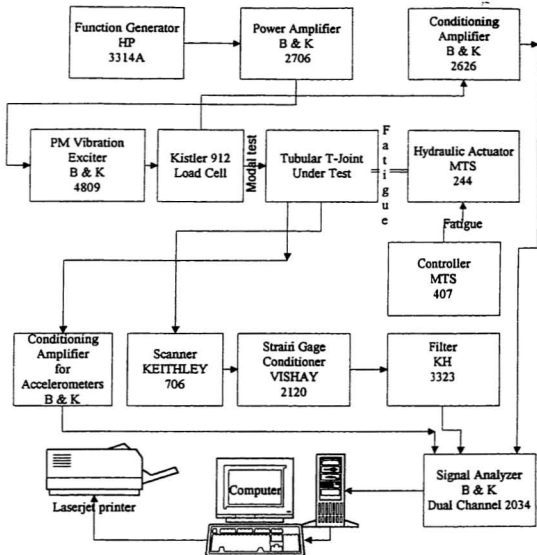


Figure 4.11: Instrument flow chart

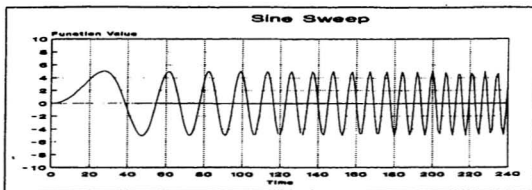


Figure 4.12: Sine sweep signal

generator to the shaker is a voltage that causes a proportional force to be applied to the test structure.

A PM vibration exciter type 4809 was used in the present experiments to provide modal excitation. The maximum force rating was 44.5 N (10 lbf) for vibrating specimens at frequencies ranging from 10 Hz up to 20 kHz. The moving coil of the exciter had a nominal impedance of 2 Ω with a maximum current rating of 5 A RMS. With assisted air cooling the maximum current and force rating may be extended up to 7 A RMS and 60 N (13.5 lbf), respectively.

4.6.3 Transducers

Strain gauges and accelerometers were used to measure the responses which were later used to obtain strain and acceleration frequency response functions, respectively. Three types strain gauges were used in the present set of experiments. They were EA-06 240 LZ-120 uniaxial gauges, EA-06-125 RA-120 rosette gauges, and EA-13-125 BZ-350 rosette gauges. The gauges were made by Micro-Measurements Division of Measurements Group Inc., USA. The gauge property data at 24°C are listed in Table 4.2.

Table 4.2: Strain Gauge Properties

Gauge	Resistance	Gauge Factor	Transverse Sensitivity
EA-06-240LZ-120	120.0 \pm 0.3%	2.070 \pm 0.5%	(+0.5 \pm 0.2)%
EA-06-125RA-120	120.0 \pm 0.2%	2.030 \pm 1.0%	(+0.9 \pm 0.2)%
EA-13-125BZ-350	350.0 \pm 0.15%	2.145 \pm 0.5%	(+0.3 \pm 0.2)%

STRUCTCEL accelerometers (Model No. 330A) were used for measuring the

accelerations during the test. These accelerometers provided a low cost, low mass acceleration measuring device with a 3-pin transistor header configuration encased in a plastic cap. The specifications of these accelerometers are listed in Table 4.3.

Table 4.3: Accelerometer Features

Sensitivity (mV/g)	200
Range ($\pm 10V$)(g)	10
Resolution (g)	0.001
Frequency range ($\pm 5\%$ sens. dev.) (Hz)	1 - 1000
Resonant frequency (Hz)	3000
Excitation (\pm VDC)	15
Temperature range ($^{\circ}$ F)	0 - 130
Shock (max) (g)	5000
Weight (gm)	2
Connector (pin)	3

4.6.4 Load Cell

A Kistler model 912 S/N 2010 quartz dynamic load cell was attached to the exciter, through a stinger, to measure forces and transmit the force signal to the tubular T-joint. The load cell was screwed directly onto the brace of the tubular T-joint and the stinger from the exciter was attached to the other end of the load cell. The model 912 quartz load cell, was rigid and had a very high sensitivity, near infinite resolution and fast response; it measured compression forces from less than one lb. to 5000 lbs and tension forces from zero to 100 lbs.

4.6.5 Analyzer

A B & K 2034 dual channel signal analyzer was used for data acquisition. The dual channel signal analyzer was a flexible, easy-to-use, and fully self-contained two-channel FFT analysis system with 801 lines of resolution. It had a built-in digital zoom to 25.6 kHz. It can measure frequency response, coherence, auto- and cross-spectra, auto- and cross-correlation, impulse response, signal-to-noise ratio, sound intensity, orbits, and probability density/distribution functions. The operator is required to select the total frequency range under study. However, the analyzer itself was internally programmed to automatically select the sampling interval and to ensure appropriate definition of the recorded singles. The coherence function was used to confirm the validity of the FRF.

4.6.6 Actuator

Hydraulic actuator (MTS series 244) was used for applying fatigue loads to the test specimen. It was a double-acting, double-ended, heavy-duty actuator that operated under precision servovalve control in the MTS closed-loop servohydraulic system. Its typical applications included static testing or cyclic tension-compression fatigue testing. The actuator could also be used in systems requiring precision force generation or accurate control of piston rod displacement.

4.6.7 Controller

A model 407 controller controlled the hydraulic actuator. The MTS model 407 was a single channel, digitally-supervised, proportional, integral, derivative, feed-forward servo controller that provided a complete control of one servohydraulic channel/station in a MTS testing system. The controller included ac and dc transducer conditioning, basic function generation (with the capability to accept externally gen-

erated command signals), servovalve drive signal generation, and hydraulic pressure control. Multiple 407 controllers could be interconnected to accommodate multiple-channel testing, and can be quickly configured to accommodate a variety of tests.

4.6.8 STAR Software

Structural Testing, Analysis and Reporting (STAR) software was used for testing and analyzing the dynamics of the structural system. After the data was transferred from the analyzer via a GPIB bus to the computer, STAR could carry out curve fitting to extract modal parameters such as natural frequencies, damping, amplitudes, and phases.

4.7 Calibration of Transducers

To provide for accuracy of the measured experimental data, the transducers used in the experiments were carefully calibrated. The calibration chart given by the instrument designer guaranteed the linearity of the instruments over the specified frequency range.

4.7.1 Calibration of the Load Cell in Exciter for Modal Analysis

The load cell used was a Kistler Model 912 S/N 2010. Since no standard equipment for the calibration of load cells was available in the laboratory, calibration was done by a hand-held calibrator (PCB model 394B05) and oscilloscope. The logic diagram for the calibration is shown in Figure 4.13.

According to the menu for load cell Model 912, the nominal sensitivity was 50 pico-Coulombs/lbf. Hence a value of 50 pC/V was assumed and set first on the charge amplifier (conditioning amplifier type 2626); then a 2.0 gram weight was placed on

the load cell. The weight of the load cell was determined as 16.8 gram. Considering the transducer in the load cell to be mounted at the middle of the cell, the force applied on the load cell was calculated as half the weight of the load cell plus the weights applied. The exciter inside the hand held calibrator was driven by a stabilized oscillator at a level of $1.0 \text{ gram} \times 9.81 \text{ m/s}^2$. The force on the load cell could then be calculated as

$$F = \left(\frac{1}{2} \text{ load cell weight} + \text{weights}\right) \times 9.81 \times 0.2248 \text{ (lbf)} \quad (4.1)$$

where $1 \text{ N} = 0.2248 \text{ lbf}$.

The sensitivity was calculated as

$$S = \frac{V}{F} \quad (4.2)$$

where S was sensitivity and V the voltage.

When the 2.0 gram weight was applied, the force applied on the load cell was calculated as

$$F = 10.4 \times 10^{-3} \times 9.81 \times 0.2248 \approx 0.023 \text{ (lbf)} \quad (4.3)$$

The voltage output was measured as 26 mv; hence, the sensitivity was

$$\frac{0.026 \text{ V}}{0.023 \text{ lbf}} \times 50 \text{ pC/V} = 56.74 \text{ pC/lbf} \quad (4.4)$$

With the calibration factor of 56.7 pC/lbf, different weights were added to verify the accuracy of the calibration. The results are shown in Table 4.4.

According to the manufactures specifications for the load cell, the voltage output should be linear over the rated range of the device. In this work, because of the limited availability of equipment, it was only possible to calibrate over the low end of

Table 4.4: Calibration of Load Cell

Weight (gm)	Force (lbf)	Voltage Output (V)	Sensitivity (V/lbf)	Error (%)
1.0	0.0207	0.0202	0.976	2.40
2.0	0.0229	0.0230	1.004	0.40
3.0	0.0251	0.0250	0.996	0.40

the range, and the linearity observed has been assumed to exist over the full range. While this may not be absolutely true, any errors arising are not considered to be serious because only relative differences are required rather than absolute values.

4.7.2 Calibration of Accelerometer

The calibration of accelerometers was done using the hand-held calibrator (PCB model 394B05) and oscilloscope. The flow chart for calibration is shown in Figure 4.14.

The calibration factors for accelerometers are listed in Table 4.5.

Table 4.5: Calibration Factors for Accelerometers

No.	1	2	3	4	5	6	7
Series No. (S/N)	19907	20403	19912	19944	19579	20397	19612
Calibration factor (V/g)	1.5	1.7	1.6	1.65	1.6	1.7	1.2

4.7.3 Calibration Factors for Other Transducers

Calibration factors obtained for other transducers are listed in Table 4.6.

Table 4.6: Calibration Factors for Other Transducers

Actuator for load cell	120 Ω strain gauge	350 Ω strain gauge
2000 lbf/v	7.85 mv/unit ($\mu\epsilon$)	7.85 mv/unit ($\mu\epsilon$)

4.8 Location of Strain Gauges and Accelerometers

4.8.1 Strain Gauge Arrangement

Because of the difficulty experienced in exactly lining up the center of the brace and chord, it was difficult to obtain equal strain readings on both saddle regions of the brace; moreover the weld profile and tubular brace profile were also not identical on both sides of the chord axis. In order to develop the crack on one side only during fatigue testing, the saddle region with the larger level of strain was determined. The other side, with the smaller strain readings, was ground neatly to avoid the development of a crack. Therefore, for monitoring the weld toe crack growth, the strain gauges were mainly applied to the side with larger strains. In spite of these precautions, it will be seen from the results of specimen 2, that cracks developed on both sides.

The strain gauge arrangements for specimen 1 are shown in Figures 4.15 to 4.18. Gauges 1 to 12 were rosette gauges while 13 to 16 were uniaxial gauges. Gauges 1 - 3 were arranged near the hot spot of the weld toe of the chord on the 0° , $+15^\circ$ and

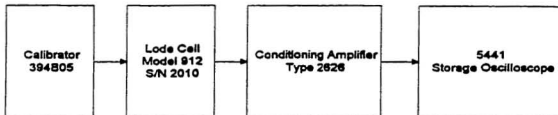


Figure 4.13: Calibration flow chart for load cell

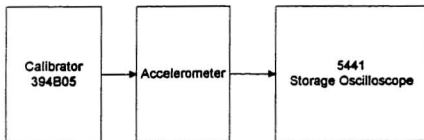


Figure 4.14: Calibration flow chart for accelerometers

-15° lines, respectively, to investigate how the strain FRF was influenced by a crack in the vicinity of the gauges. Gauge 4 was placed so that an angle of 5° was included between the weld toe and the gauge 4. Gauges 5 and 6 were placed on the +15° and -15° lines, respectively. Locations of gauges 5 and 6 were linearly interpolated between 0° and 90° lines. Gauges 4 to 6 were used to examine how the strain FRFs were affected by a crack occurring a little distance away from the gauge locations. The positions of gauges, 1 and 4, from the weld intersection were according to the traditional gauge practice for fatigue testing, and are shown in Figure 4.19 (Wardenier et al. 1991). The locations of gauges 1 and 4 at A_1 and A_2 , in Figure 4.19, were calculated as

$$a = 0.2\sqrt{rt} = 0.22 \text{ (inch)} \approx 5.6 \text{ (mm)} \quad (4.5)$$

$$b_{90} = R \frac{\pi\theta}{180} = 0.87 \text{ (inch)} \approx 22.1 \text{ (mm)} \quad (4.6)$$

where R was the outer diameter of the chord, r was the outer diameter of the brace, t was the thickness of the brace of the tubular T-joint, and b_{90} was the distance between the saddle and A_2 .

The gauges 2, 3, 5 and 6 were on the 15° and -15° lines of the chord. Their distances to the weld toe were calculated by linearly interpolating between A_1 & A_3 and A_2 & A_4 .

$$b_{90} = 0.4\sqrt{rtRT} = 0.53 \text{ (inch)} \approx 13 \text{ (mm)} \quad (4.7)$$

where T was the wall thickness of the chord.

$$b_{15} = (b_{90} - a) - \frac{15}{90}(b_{90} - b_{90}) = 0.59 \text{ inch} \approx 15 \text{ (mm)} \quad (4.8)$$

The center line row of gauges (gauges 7-9) was used to see whether far field strains would be influenced by cracks. Gauges 8 and 9 were located at $+45^{\circ}$ and -45° , respectively.

$$b_{45^{\circ}} = (b_{0^{\circ}} - a) - \frac{45}{90}(b_{0^{\circ}} - b_{90^{\circ}}) = 0.48 \text{ inch} \approx 12(\text{mm}) \quad (4.9)$$

The bottom gauge 12 was used to see whether the farthest gauges were influenced by cracks. Gauges 10 and 11 were located on the noncracking side of the tubular T-joint. Gauge 10 was at a similar location to gauge 1 but mirrored; gauge 11 was mirrored from gauge 4. At the same time, four unidirectional gauges 13 to 16 were placed on the brace to monitor the strains in the brace.

Figures 4.20 to 4.22 give channel numbers for the data acquisition channels on specimen 1. Each unidirectional strain gauge had one channel and each rosette strain gauge had three channels. The strain gauges used on this specimen were all 120Ω gauges.

The arrangements for specimens 2 and 3 were the same. However, there were some differences between this arrangement and the arrangement for specimen 1. Figures 4.23 to 4.26 show the strain gauge arrangement on specimen 2 and 3. In these two specimens, five 350Ω rosette strain gauges were used for gauge numbers 7 to 9, 12 and 15 because these locations were the farthest from the crack and signals were relatively weak (Figures 4.24 & 4.25). 350Ω strain gauges were used to see how more sensitive gauges enhanced the signal levels. In these two specimens, one uniaxial gauge on the brace was removed as seen in Figure 4.26 due to the limited channels available in the scanner. Hence, three gauges were used on the brace. Two 120Ω rosette gauges (gauges 13 and 14) were added along the perpendicular line on the chord drawn from the crown, to see how distant gauges were influenced by the cracks (Figure 4.25).

Gauge 11 was used to decide on the applied fatigue load level and was disconnected from the scanner after the fatigue load had been decided; only 40 channels were available in the scanner and the unnecessary channels were disconnected.

Figures 4.27 to 4.29 show the channel distribution for specimens 2 and 3. These channel lines show the directions of bonding the gauges. The cable connections that joined the strain gauges and scanners are shown in Figures 4.30 and 4.31.

4.8.2 Marking of the Strain Gauge Location

The marking of the gauge locations on the specimens was not so easily accomplished, especially for the gauges on the 15° and 45° lines, since the lines on the tubular T-joints were curved; and the specimens were huge. In this case, horizontal and vertical grids were drawn first, and the 15° and 45° lines were drawn by connecting the intersection points of these grids.

4.8.3 Accelerometer Arrangement

Seven accelerometers were placed on each tubular T-joint to compare their performances with those of strain gauges. One was located near the hot spot of the weld toe. Three were located around the location of gauges 7, 8 and 9, and the fifth one was placed on the bottom beside strain gauge 15 (specimens 2 and 3), or gauge 12 for specimen 1. The sixth and the seventh accelerometers were placed on the support to see whether the bolts were becoming loose or not. However, the accelerometers could not be placed at the exact desired locations because of the bonded strain gauges and the connecting cables, as shown in Figure 4.30.

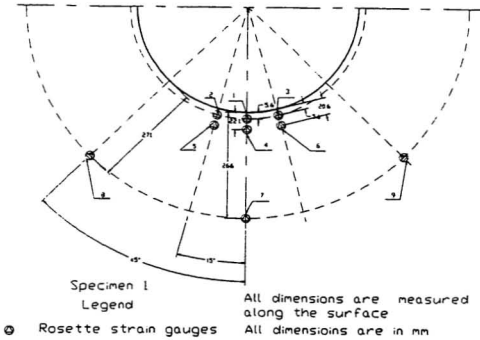


Figure 4.15: Strain gauges on the chord (cracking side) for specimen I

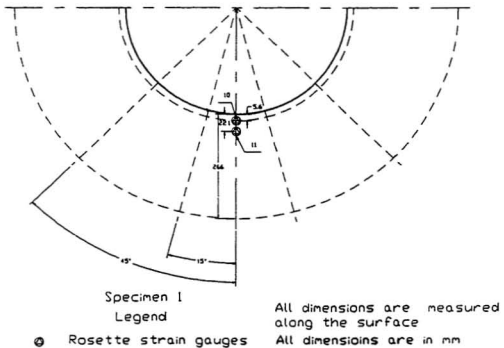
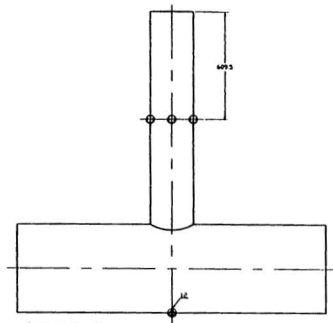


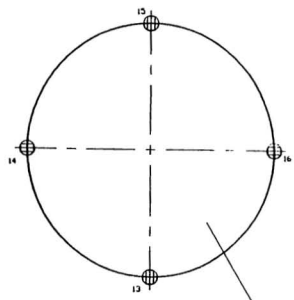
Figure 4.16: Strain gauges on the chord (noncracking side) for specimen I



Specimen 1
Legend

All dimensions are measured along the surface
All dimensions are in mm

● 120 ohm rosette strain gauges



Specimen 1
Legend

○ Unidirectional gauges

brace

Figure 4.17: Strain gauges on the brace (front view) for specimen 1

Figure 4.18: Strain gauges on the brace (top view) for specimen 1

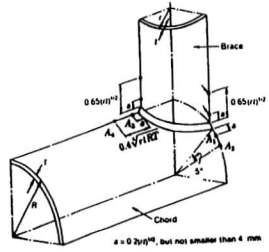
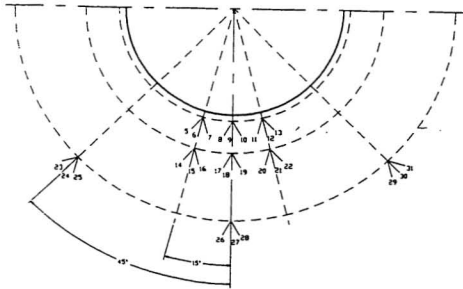
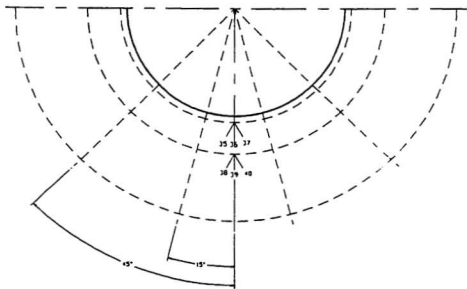


Figure 4.19: Traditional strain gauge locations (Wardenier et al 1991)



Specimen 1

Figure 4.20: Strain gauge channels on the chord (cracking side) for specimen 1



Specimen 1

Figure 4.21: Strain gauge channels on the chord (noncracking side) for specimen 1

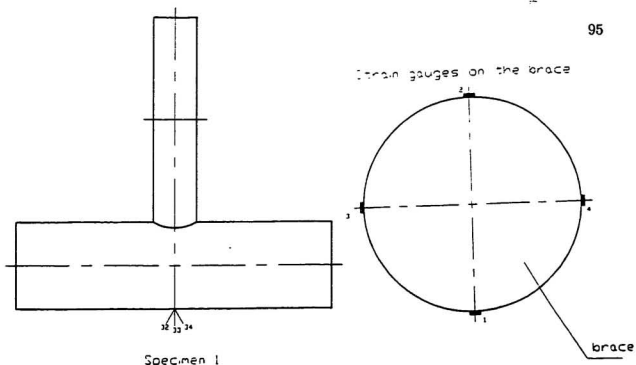


Figure 4.22: Strain gauge channels on the brace for specimen 1

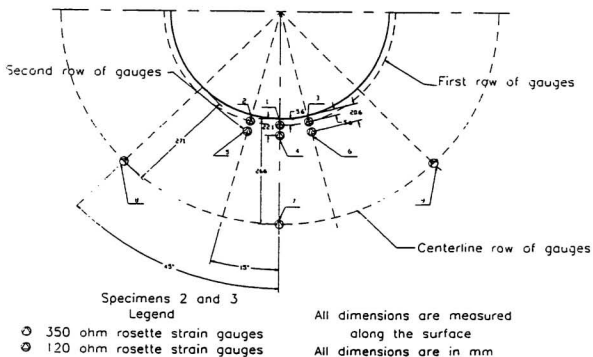
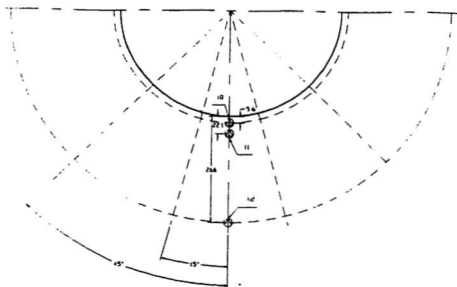


Figure 4.23: Strain gauges on the chord (cracking side) for specimens 2 and 3



Specimens 2 and 3

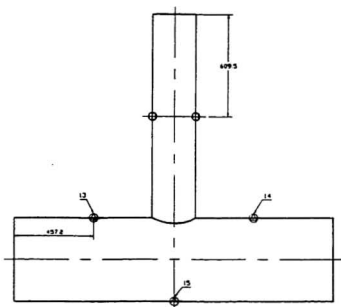
Legend

- ⊙ 350 ohm rosette strain gauges
- ⊙ 120 ohm rosette strain gauges

All dimensions are measured
along the surface

All dimensions are in mm

Figure 4.24: Strain gauges on the chord (noncracking side) for specimens 2 and 3



Specimens 2 and 3

Legend

- ⊙ 350 ohm rosette strain gauges
- ⊙ 120 ohm rosette strain gauges

All dimensions are measured
along the surface

All dimensions are in mm

Figure 4.25: Strain gauges on the brace (front view) for specimens 2 and 3

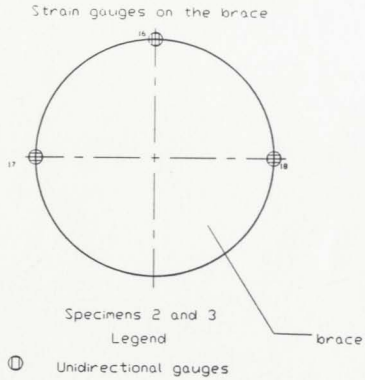


Figure 4.26: Strain gauges on the brace (top view) for specimens 2 and 3

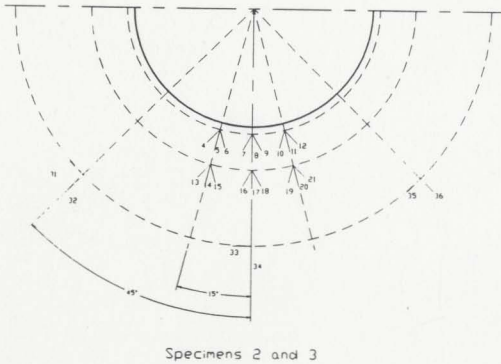
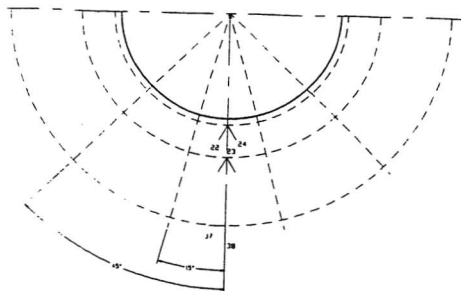
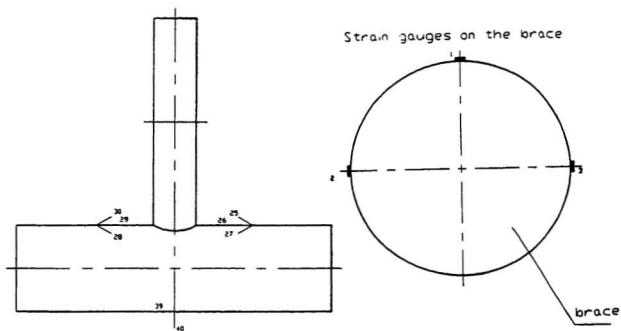


Figure 4.27: Strain gauge channels on the chord (cracking side) for specimens 2 and 3



Specimens 2 and 3

Figure 4.28: Strain gauge channels on the chord (noncracking side) for specimens 2 and 3



Specimens 2 and 3

Figure 4.29: Strain gauge channels on the brace for specimens 2 and 3

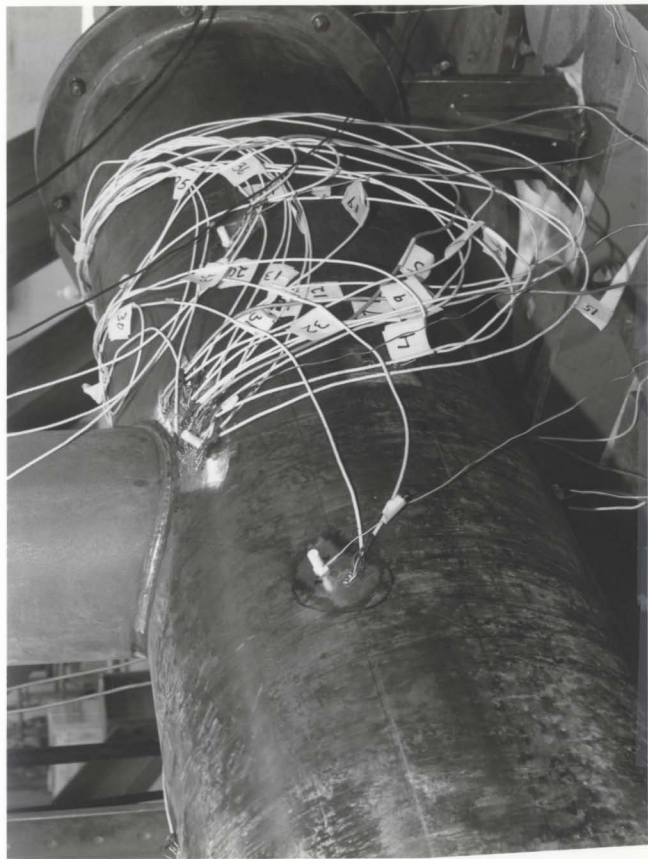


Figure 4.30: Cable connections on the chord (cracking side) for specimen 3

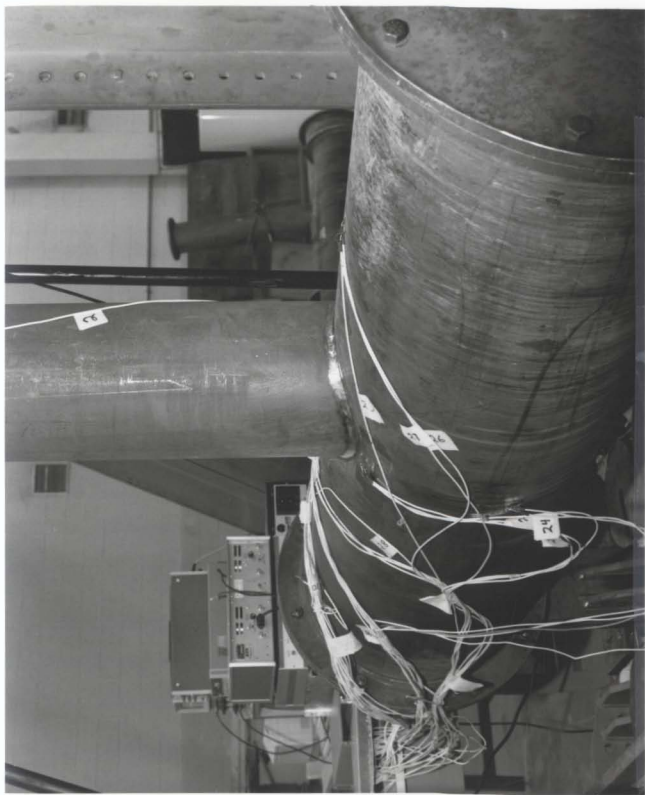


Figure 4.31: Cable connections on the chord (noncracking side) for specimen 3

4.9 Determination of Fatigue Load on the Tubular T-Joint

The applied fatigue load was governed by the stresses developed at the hot spot of the weld toe. To measure these applied stresses, two rosette gauges were installed on each side of the chord of the tubular T-joint, namely, gauges 1 & 4 on the side with the larger stresses, and gauges 10 & 11 on the other side. The procedure used for determining the fatigue load is given below:

1. Determine the approximate fatigue load.

According to a previous study for a similar structure (Paranavitane, 1996), a nominal stress of 250MPa (36260 psi) at the weld toe would be sufficiently close to yield so as to cause fatigue cracking in less than 10^6 cycles. Also, a stress of 7.23 MPa (1049 psi) applied to the top of the brace would generate this stress of 250 MPa at the weld toe. Hence, the approximate fatigue load was computed by the following equation:

$$\begin{aligned}
 P_1 &= \sigma_a \frac{\pi(D^2 - d^2)}{4} = 7.23 \times 10^6 \times \frac{\pi \times (254^2 - 241.3^2)}{4} \times 10^{-6} \\
 &\approx 35719 \text{ N} \approx 8030 \text{ lb}
 \end{aligned}
 \tag{4.10}$$

The initial loading was only half of P_1 and the hot spot strains and hence stresses were determined. Load was then increased until the stress in the hot spot region reached the desired value of 250 MPa.

2. Four strain gauges located along the weld toe were selected (e.g gauges 1, 4 and 10, 11 for specimen 1) and the gauge outputs were recorded. These data were used to determine which saddle point was the most highly stressed, and hence

the most likely to crack. The output was also used to determine the nominal stress in the chord at the weld toe, and this was done by extrapolation.

3. The maximum principal stress was computed.

The strains from the three branches $\epsilon_{\alpha_1}, \epsilon_{\alpha_2}, \epsilon_{\alpha_3}$ of a rosette strain gauge could be obtained by readings. Using the following equations:

$$\begin{aligned}\epsilon_{\alpha_1} &= \frac{\epsilon_x + \epsilon_y}{2} + \frac{\epsilon_x - \epsilon_y}{2} \cos 2\alpha_1 - \frac{\gamma_{xy}}{2} \sin 2\alpha_1 \\ \epsilon_{\alpha_2} &= \frac{\epsilon_x + \epsilon_y}{2} + \frac{\epsilon_x - \epsilon_y}{2} \cos 2\alpha_2 - \frac{\gamma_{xy}}{2} \sin 2\alpha_2 \\ \epsilon_{\alpha_3} &= \frac{\epsilon_x + \epsilon_y}{2} + \frac{\epsilon_x - \epsilon_y}{2} \cos 2\alpha_3 - \frac{\gamma_{xy}}{2} \sin 2\alpha_3\end{aligned}\quad (4.11)$$

the strains were computed. For a right angled rosette gauge, ϵ_x, ϵ_y and γ_{xy} could be derived as follows:

$$\begin{aligned}\epsilon_x &= \epsilon_{90} \\ \epsilon_y &= \epsilon_{90} \\ \gamma_{xy} &= \epsilon_{90} + \epsilon_{90} - 2\epsilon_{45}\end{aligned}\quad (4.12)$$

Hence the equations for principal strains were given by

$$\begin{aligned}\epsilon_1 &= \frac{\epsilon_{90} + \epsilon_{90}}{2} + \frac{\sqrt{2}}{2} \sqrt{(\epsilon_{90} - \epsilon_{45})^2 + (\epsilon_{45} - \epsilon_{90})^2} \\ \epsilon_2 &= \frac{\epsilon_{90} + \epsilon_{90}}{2} - \frac{\sqrt{2}}{2} \sqrt{(\epsilon_{90} - \epsilon_{45})^2 + (\epsilon_{45} - \epsilon_{90})^2}\end{aligned}\quad (4.13)$$

Thereafter, the equations for the principal stresses were computed as:

$$\begin{aligned}\sigma_1 &= \frac{E(\epsilon_{0^\circ} + \epsilon_{90^\circ})}{2(1 - \mu)} + \frac{\sqrt{2}E}{2(1 + \mu)} \sqrt{(\epsilon_{0^\circ} - \epsilon_{45^\circ})^2 + (\epsilon_{45^\circ} - \epsilon_{90^\circ})^2} \\ \sigma_2 &= \frac{E(\epsilon_{0^\circ} + \epsilon_{90^\circ})}{2(1 - \mu)} - \frac{\sqrt{2}E}{2(1 + \mu)} \sqrt{(\epsilon_{0^\circ} - \epsilon_{45^\circ})^2 + (\epsilon_{45^\circ} - \epsilon_{90^\circ})^2}\end{aligned}\quad (4.14)$$

The direction of the principal stresses and strains was derived as

$$\tan 2\alpha_0 = \frac{2\epsilon_{45^\circ} - \epsilon_{0^\circ} - \epsilon_{90^\circ}}{\epsilon_{0^\circ} - \epsilon_{90^\circ}}\quad (4.15)$$

4. Using results of gauges 1 & 4 and 10 & 11, the stresses were linearly extrapolated to the weld toe. The strain gauge stresses, that would give 250 MPa at the hot spot, were computed. Since the distance of the first gauge to the weld toe was 0.22 inch (5.588 mm), and the distance of the second gauge to the weld toe was 0.87 inch (22.1 mm), the maximum stresses at the weld toe could be obtained from the principal stresses at the gauge 1 and gauge 4 locations. The equation for this linear distribution could be expressed as

$$\frac{\Delta\sigma_w}{\Delta\sigma_1} = \frac{22.1}{16.51}\quad (4.16)$$

where $\Delta\sigma_w$ was the stress difference between the maximum principal stress of gauge 4 and the weld toe, and $\Delta\sigma_1$ was the stress difference between the maximum principal stresses of gauges 1 and 4. Hence the maximum stress at the hot spot of the weld toe under force P_1 can be expressed as

$$\sigma_w = \sigma_4 + \Delta\sigma_w = 1.338\sigma_1 - 0.338\sigma_4\quad (4.17)$$

where σ_1 and σ_4 are the maximum principal stresses at gauge locations 1 and 4.

5. The force P_2 which would apply a weld toe principal stress of 250 MPa at the hot spot was determined. The equation for this purpose may be expressed as:

$$P_2 = \frac{250 \times 10^6}{\sigma_w} \times P_1(\text{lb}) \quad (4.18)$$

where P_1 was the applied force for the present iteration.

6. Apply $P_3 = 90\%P_2$ on the tubular joint specimen to compute the stresses from the four gauges at the weld toe.
7. Extrapolate the stresses to determine the stresses at the weld toe.
8. Repeat steps 2 - 5 and 7 at load P_3 until a stress level of 250MPa was obtained at the hot spot of the weld toe.
9. Cycle the tubular T-joint 2 - 3 times at 5 Hz and load P_2 to release the residual stresses occurring at the weld toe.

The fatigue load which was to be applied on the top of the brace is determined by a number of iterations. The results of this trial procedure are shown in Table 4.7. The details of the final applied fatigue load which takes the static load P_2 as its range are shown in Table 4.8.

4.10 Signal Processing

The signals generated by the transducers, i.e., strain gauges, accelerometers, and load cells are analog in nature. The analog time-domain signals are converted into digital frequency-domain signals by the analyzer. First, the analog signal $x(t)$ is sampled at a sample rate of $\Delta t = 1/f_s$ where f_s is the sampling rate. From this digitization, a number of strain/acceleration values at time 0, Δt , $2\Delta t$, \dots , $k\Delta t \dots$ are obtained as

Table 4.7: Computation of Fatigue Load

Specimen	Load trials	Load (lb)	σ_1 (MPa)	σ_4 (MPa)	σ_{w2} (MPa)	σ_w (MPa)	P_2 (lb)	$P_3(90\%P_2)$ (lb)
1	1	4015	106.5188	53.0632	137.9809	153.3121	8056.6324	7250.9692
	2	7250	208.2177	103.7419	219.1774	243.5305	7443.6255	6699.2630
2	1	4015	108.0562	54.9334	126.0117	140.0130	7965.5298	7168.9768
	2	7168	191.8914	97.5262	223.7868	248.6250	8008.7114	7207.8403
	3	7208	193.2694	97.9245	225.4960	250.5011	7991.2734	7192.1461
	4	7991	214.0350	108.8289	224.6352	249.5947	8004.2511	7203.8260
3	1	4015	114.3801	57.1864	133.7116	148.5684	7506.8298	6756.1468
	2	6756	193.7293	97.2205	226.3493	251.4992	7461.9192	6715.7273
	3	7461	212.7926	106.9151	223.7186	248.5792	7504.5693	6754.1124
	4	7504	213.2901	107.6748	224.0830	248.9811	7535.0691	6781.5622
	5	7535	213.3957	107.4667	224.2364	249.1515	7560.7921	6804.6562

Table 4.8: Characteristics of Fatigue Loads

Specimen	Load Ratio	P_{max} (lb)	P_{min} (lb)	P_{mean} (lb)
1	0.2	9305	1861	5583
2	0.2	10005	2001	6003
3	0	7561	0	3781

$\{x(t_k)\}$, ($k = 1, 2, \dots, N$). t_k is a discrete value of the time. The Nyquist frequency is defined as $f_{Nyq} = f_s/2$.

Aliasing will occur when the sample interval is too large since the Nyquist frequency falls below the signal frequency. Hence the sampling frequency should be at least twice the highest signal frequency and this was selected automatically by the analyzer. The results shown later, will illustrate that even though the frequency shifts were small, they were readily detected, and this confirms that the automatic selection feature of the analyzer was performing satisfactorily. An example of aliasing is shown in Figure 4.32.

Another problem that occurs in the digital analysis of signals is leakage; the problem arises because the total length of the signal may not be an integral multiple of its period. An example of leakage is shown in Figure 4.33. Leakage can be corrected by the use of window functions. A Hanning window was selected in the analyzer for these studies to reduce the leakage [Figure 4.34].

Digital Fourier Transform equations can be expressed as

$$x_k = x(t_k) = \frac{a_0}{2} + \sum_{i=1}^{N/2} \left(a_i \cos \frac{2\pi i t_k}{T} + b_i \sin \frac{2\pi i t_k}{T} \right) \quad (4.19)$$

where T is period, $k = 1, 2, \dots, N$, a_i and b_i are digital spectral coefficients which are given by

$$a_0 = \frac{1}{N} \sum_{k=1}^N x_k$$

$$a_i = \frac{1}{N} \sum_{k=1}^N x_k \cos \frac{2\pi i k}{N}$$

$$b_i = \frac{1}{N} \sum_{k=1}^N x_k \sin \frac{2\pi i k}{N}$$

Linear overlap averaging was selected in these studies to remove spurious random noise and to increase the signal reliability. It is necessary to perform an averag-

The RFLS method available in the STAR System was a polynomial curve fitting algorithm which identified modal frequency, damping and residue simultaneously, for each mode of vibration. It could be used in either an SDOF or a multiple-degrees-of-freedom (MDOF) form, depending on the degree of modal coupling in the FRF measurements. For cases of light coupling, the following SDOF curve fitting model was used on data in the vicinity of a modal resonance peak.

The polynomial equation 4.21 was curve-fitted in a least-squares-error sense to the measurement data. As a result of the curve fitting, estimates of the modal frequency (ω_k), modal damping (σ_k) and complex residue ($r_k = r_{1,k} + jr_{2,k}$) could be obtained.

The three residual function constraints (A_0, A_1, A_2) were also identified during the curve fitting process. These additional terms were used to compensate for the effects of out-of-band modes in the measurement data band. Without the use of the residual terms, the modal parameter estimates would contain large errors.

The mode shapes were constructed in the STAR System by a residue sorting process from elements of the residue matrix which were determined during curve fitting.

In general, the ij^{th} element of the residue matrix for mode k could be written as the product of the i^{th} and j^{th} elements of the k^{th} mode shape vector.

$$r_{ij}(k) = u_i(k)u_j(k) \quad (4.22)$$

where $r_{ij}(k)$ was ij^{th} element of the residue matrix for the k^{th} mode, $u_i(k)$ was i^{th} element of the mode for the k^{th} mode and $u_j(k)$ was j^{th} element of the mode shape for the k^{th} mode.

4.12 Procedure for Testing

1. Four strain gauges 1, 4, 10 and 11 (specimen 1) were initially fixed to the tubular T-joint.
2. Static loads were applied at certain levels to determine the saddle side that contained the maximum stress.
3. The fatigue load was computed according to the procedure given in Section 4.9.
4. The remaining strain gauges were fixed to the tubular T-joint.
5. The uncracked tubular T-joint was tested modally to obtain the initial modal parameters, using frequency domain analysis. Frequency response functions were also obtained.
6. Fatigue testing was carried out at the prescribed stress level and load ratio, according to the procedure given earlier in Section 4.9. Fatigue testing was conducted at the frequency of 5 Hz and the loading conditions determined in Section 4.9.
7. Fatigue testing was stopped at pre-specified cycles to acquire crack signatures from the tubular T-joint. Ink staining was used when the weld toe crack first became visible to the eye. Beach-marking was performed during subsequently specified load cycles by applying loads at half the previous values and twice the previous frequency; the beach-marking load cycles were decided by a trial and error process so that there would be measurable crack growth.
8. Modal testing was carried out prior to every beach-marking cycle.

9. Steps 6 to 8 were repeated at specified fatigue cycle levels until the specimen failed.

4.13 Conclusions

Non-destructive assessment of cracks in tubular T-joints, using vibration procedures, is an involved process which requires a knowledge of vibration, modal analysis, fatigue testing, fracture mechanics, electronic instrumentation, signal processing and system identification using a dedicated software. Proper experimental setup and calibration, validation, instrument selection, careful test parameter identification, and intelligent and precise experimental measurement are required for the accuracy and reliability of the experimental results.

These procedures have been meticulously followed in this study to obtain proper and well-conditioned data for use in subsequent analysis.

Chapter 5

Experimental Studies and Salient Findings

5.1 Introduction

The fatigue and modal tests of tubular T-joints carried out in this study were the first successful dynamical and statical combined tests on tubular T-joints to detect growing fatigue cracks. Initially four specimens were tested but one failed prematurely as described in Chapter 4. Therefore, in this chapter, the data from the three successful specimens, labeled 1, 2, and 3, were compiled and analyzed. Static strains were measured at different stages of crack growth using a precise digital volt-meter. Principal stresses were then calculated for the weld toe rosette gauges. The purpose of the static test and analysis was to evaluate the static response of the structure to fatigue cracking. The magnitudes of the static loads were so chosen as to be comparable with the maximum fatigue design loads, at which cracking was projected to occur. Therefore, the static strains and stresses measured under monotonic loading could represent the maximum strains and stresses that are likely to occur in an off-shore structure.

Modal testing was conducted over different frequency ranges, i.e. 0 - 50 Hz, 50 - 150 Hz, 150 - 250 Hz, 250 - 350 Hz, 350 - 550 Hz, etc. All the recorded frequency

ranges were joined together and the frequency response behavior was examined to find the dominant characteristics of crack growth. Modal parameters such as natural frequencies and damping were extracted from the frequency response functions through curve fitting.

In addition, postmortem fractographic examinations of the crack surfaces were carried out to determine the cracking mode and the crack profiles. These fractographic observations provided supporting evidence for the observations made using static and vibration methods.

Static strains and stresses obtained from gauges, located around the weld toe, were analyzed to determine the influence of cracks. The identified natural frequencies and modal damping ratios were utilized to determine how these global parameters were related to the profile of a crack. A characteristic equation was derived for relating the static strains to fatigue cycles of all the three specimens.

Reliability of the measured data was verified by comparing the successive data obtained for a point, on a common plot. Coherence functions were frequently checked in the experiment to ensure the correctness of the data. In practice, coherence is plotted versus frequency and is taken as an indication of how accurate the measurement process was over a given range of frequencies. Generally, for good data, the values of $\gamma^2 = 1$ should occur at frequencies near the structure's resonant frequencies where the signals are large.

Three indicators which could be used for practical crack detection, at various crack growth levels, were obtained through the analysis of the frequency response functions. In addition, clear evidence was obtained to confirm the opening and closing of the crack during modal testing, and this evidence was correlated with the output from strain gauges.

5.2 Crack Profile Determination

The fatigue crack profiles were determined from the inking and beach marking traces left on the crack surfaces, after cutting open the cracked sections of the weld toe. The inking was done when a visible crack was present. The existence of the cracks became evident with the aid of the "pumping in and out" of isopropyl alcohol used around possible crack locations. The inking medium was a slow drying red ink made from finger nail polish diluted with 100% pure isopropyl alcohol. This red ink stain stayed permanently and marked clearly the initial crack profile. Beach marking was performed by doubling the cyclic frequency and halving the fatigue load range. Digitized photos of the crack profiles, taken for the three specimens, are shown in Figures 5.1 to 5.6. It was noticed that in specimens 1 and 3, a single large crack developed only on one side (side 1, which had experienced a slightly larger strain at the weld toe than the other side during the initial measurements made on the tubular joint) of the chord, while in specimen 2, multiple thumb-nail cracks developed on both sides of the chord. The crack profiles were then traced and shown in Figures 5.7 to 5.9 for specimens 1, 2, 3, respectively. The cracked section of specimen 1 was rusted heavily when it was cut open since the alcohol used for the crack observation was partially mixed with water; consequently the crack profile was traced according to the record of the observed surface lengths kept for the specimen. The crack profiles of the second and third specimens were traced by the digitizer. The crack profile for specimen 3 was the clearest among all of them.

The distinguishing feature of fracture in specimen 2, compared with specimens 1 and 3, is that the main crack was formed by the coalescence of several small size thumb-nail cracks, while in the other two specimens, a single semi-elliptical crack had formed by the time of inking. This could happen by either the growth of a

single thumb-nail crack or the successive coalescence of several such cracks that had occurred earlier. The latter process was most likely to be the case because the scanning electron microscopy (given later in section 5.3) revealed that a nonuniform distribution of welding defects (crack initiation sites) existed along the weld toe and there were small thumb-nail cracks on either side of the main cracks. These thumb-nail cracks would eventually coalesce to form a dominant fatigue crack. As indicated by the trace of beach marking, in all specimens, these semi-elliptical cracks broke through the thickness of the chord after a certain number of fatigue cycles and became a large through-the-thickness crack.

The measured crack width and depth are shown in Table 5.1 to 5.3 for specimens 1, 2 and 3, respectively.

At the time of inking, when the crack could be clearly seen with a naked eye (by the "pumping in and out" of isopropyl alcohol), the crack size in specimen 3 was about 72 mm long and about 3.2 mm deep. By definition (section 2.2.1), the normalized crack size was 0.074, whereas the published results show that this parameter in other studies was above 0.125 (Gomes, 1990). This statement will be confirmed by the results of the analyses in the later sections.



Figure 5.1: Photo of crack profile for specimen 1, side 1



Figure 5.2: Photo of crack profile for specimen 2, side 1



Figure 5.3: Photo of crack profile for specimen 2, side 2

Table 5.1: Fatigue Cycles and Measured Crack Parameters

Specimen 1		
Cycles	Crack Width	Crack Depth
620,000	109mm	2.5 mm
(inking)	4.29 inch	0.10 inch
732,500	120 mm	4 mm
	4.72 inch	0.16 inch
887,500	136 mm	5.5 mm
	5.35 inch	0.22 inch
1117,500	165 mm	7 mm
	6.5 inch	0.27 inch
1282,500	185 mm	7 mm
(failure)	7.28 inch	0.28 inch

5.3 Fracture Surface Analysis

Fracture surface analysis was carried on two specimens using an Hitachi S-570 scanning electron microscope (SEM). The specimens were chosen to include one that had been fatigue tested at a load ratio R (ratio of minimum to maximum load) of zero and the other a load ratio of $R = 0.2$. The specimens were specimens 3 and 2, respectively. These studies, reported below, provided information on the crack initiation sites, on the early stages of fatigue crack growth and on whether crack opening and closing were also occurring during modal testing, as well as during the fatigue crack growth process itself.

Figure 5.10 represents a series of photographs showing part of the 231 mm long



Figure 5.4: Photo of crack profile for specimen 3, side 1



Figure 5.5: Photo of crack profile for specimen 3, detail left



Figure 5.6: Photo of crack profile for specimen 3, detail right

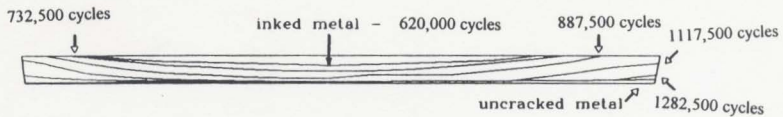


Figure 5.7: Traced crack profile for specimen 1, side 1

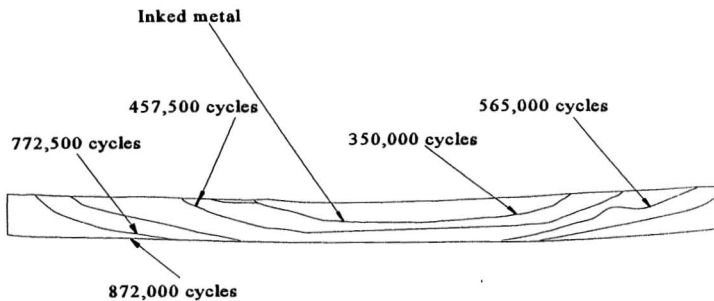


Figure 5.9: Traced crack profiles for specimen 3, side 1

Table 5.2: Fatigue Cycles and Measured Crack Parameters

Specimen 2				
	Side 1		Side 2	
Cycles	Crack Width	Crack Depth	Crack Width	Crack Depth
650,000	109 mm	5.4 mm	53 mm	1.4 mm
(inking)	4.29 inch	0.21 inch	2.09 inch	0.06 inch
812,500	166 mm	5.4 mm	182 mm	2.0 mm
	6.54 inch	0.21 inch	7.17 inch	0.08 inch
970,000	198 mm	6.8 mm	205 mm	3.4 mm
	7.80 inch	0.26 inch	8.07 inch	0.13 inch
1126,250	228 mm	6.8 mm	217 mm	6.8 mm
	8.98 inch	0.26 inch	8.54 inch	0.26 inch
1426,250	231 mm	6.8 mm	220 mm	6.8 mm
(failure)	9.09 inch	0.27 inch	8.66 inch	0.27 inch

main fatigue crack from specimen 2. It includes the areas that were present after 650,000 cycles when the ink staining was carried out, and these ink stained regions are clearly visible in the pictures. Figure 5.10a and 5.10b show that at least two cracks had been present on ink staining at 650,000 cycles. However, Figure 5.10c, which shows the fracture surface to the right of Figure 5.10b, shows that three other small cracks, appearing as small thumb-nail regions, had also been present at the time of the ink staining operation. These thumb-nail cracks are indicated by arrows in Figure 5.10c.

These photographs show that the fatigue fracture process occurs by the formation of multiple, isolated, and closely spaced, semi-elliptical or thumb-nail shaped cracks located around the weld toe of the brace-to-chord T-joint. The cracks increase in surface length and depth until they overlap, or coalesce, to form longer cracks. It is impossible to determine whether the two ink stained cracks shown in Figure 5.10a and 5.10b started life as individual thumb-nail cracks, or whether they were each formed by the nucleation and growth of a series of smaller thumb-nail cracks of the type shown in Figure 5.10c. It will be appreciated that the three small thumb-nail cracks shown in Figure 5.10c were surrounded by and separated by ligaments of uncracked metal, and therefore any opening and closing of these cracks either during fatigue or modal testing would be restricted by the presence of these ligaments. However, as the cracks grow and coalesce, as in Figure 5.10 a and 5.10b, the structure becomes more compliant and crack opening and closing occurs more readily.

Figure 5.11 shows the same three thumb-nail cracks as observed in figure 5.10c, but at a higher magnification of 10 times. The sequence of photographs shown in moving from Figure 5.11a to Figure 5.11c simply shows the three cracks in Figure 5.10c from right to left. The solid arrows in these photographs indicate the points of intersection of the crack faces with the external surface of the T-joint, and hence

the distance between the solid arrows is the surface crack length. The crack depths are between about $1/8$ th and $1/4$ of the tube wall thickness. In contrast, the two larger cracks, shown in Figure 5.10a and 5.10b, had depths of about $1/2$ and $3/4$ of the wall thickness at the time of ink staining, and therefore they were close to becoming through cracks at this point. Further fatigue testing, beyond the stage of ink staining, caused the cracks to become through cracks, and in fact the entire area of fracture, shown in Figure 5.10, is due to fatigue cracking.

Examination of the fracture surface regions of Figure 5.11 reveals the presence of many steps and ledges and some secondary cracks running approximately perpendicular to the direction of fatigue crack growth, and lying in the plane of the tube wall. The steps and ledges appear to be related to the crystallographic structure of the steel tube material. Most of the fracture surface in these regions has a dull grey appearance, but there were some areas, and especially towards the edges of the specimen and the regions of the saw cuts where the fracture surface had a bright and shining metallic appearance. These are most likely areas that were damaged by shearing and smearing of the fracture surfaces as the specimens were cut from the T-joint specimens for SEM examination. Great care was taken to avoid these damaged areas during subsequent SEM examination so that only fracture surface features produced by fatigue or modal testing were examined. The SEM examinations concentrated on the dull grey areas of the fracture surface.

The fracture surface was very rough and irregular, typically consisting of deep troughs or valleys and raised or elevated regions. Figure 5.12a shows the fracture surface topography typical of the protected areas in the troughs or valleys. It had a fibrous appearance, which may possibly be related to the microstructural features of the underlying steel. However, the microstructures were not examined in detail. The raised or elevated regions sometimes had the appearance of mountain ranges or ridges,

and these possibly correspond to grain boundaries. However, more often than not these raised regions had a plateau-like appearance, as shown in Figure 5.12b, which suggested that the peaks had been beaten or pounded flat by contacting between the crack faces during the closing portion of the fatigue cycle or the corresponding stage of any opening and closing cycle caused by modal testing. This point is discussed in more detail later.

Features similar to those observed in specimen 2 were also observed in specimen 3. Clear evidence was found in this specimen that fatigue crack initiation had occurred at weld defects at the weld toe. Figure 5.13 shows a fatigue crack initiation site in specimen 3. The left hand side of the figure is the external surface of the T-joint in the region of the weld toe while the lower right region of the figure is the fatigue fracture surface and the open arrow indicates the local direction of fatigue crack growth. The region marked 'P' in this figure is an area of shrinkage porosity in a resolidified region of the once liquid pool of the weld metal. It contains a number of isolated small grains or particles of resolidified weld metal or non-equilibrium second phase particles.

Figure 5.14 shows a region of secondary cracking observed in specimen 3. The cracks lie in the plane of the tube wall plate and perpendicular to the direction of fatigue crack propagation which is from the left to the right hand side of the photograph in Figure 5.14, as indicated by the arrow.

The plastic deformation and tearing of metal at the tip of a growing fatigue crack often leaves behind a pattern of surface markings in the form of parallel lines or striations on the fracture surfaces. They are usually clearly visible on fracture surfaces produced in ductile materials, such as aluminum. They are usually less well formed and more difficult to find in more brittle materials, and particularly so in materials that deform by planar slip on a very limited number of crystallographic planes, as

in steel. However, striations were found in specimen 3, as shown in Figures 5.15a and 5.15b. Striations appear on the fracture surface as ripples on a pond, radiating outward from the point of crack initiation and lying approximately perpendicular to the direction of fatigue crack growth. The arrows in Figure 5.15a and 5.15b indicate the directions of fatigue crack growth.

Fatigue striations, such as those shown in Figure 5.15, were found primarily in the depressed regions of the fracture surface; that is in the troughs and valleys that were protected from damage caused by the beating or pounding of the fracture surfaces during crack closure. As observed for specimen 2, the elevated regions of the fracture surface of specimen 3 were flattened, so as to produce a multitude of plateau-like regions on the fracture surface. Typical examples are indicated by white circles in Figure 5.16. It should be noted that there is no evidence of surface smearing or shearing on these flat plateaus, such as would have been the case had these plateaus been caused by a shearing action during specimen preparation. The evidence suggests, therefore, that these plateaus had been caused by direct normal contact between the fracture surfaces during crack closure.

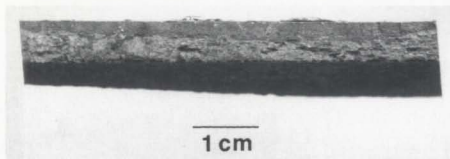
Evidence of crack closure has been presented for two specimens. In the case of specimen 3, where indeed the evidence was abundant, the closure damage may have been produced during the closing period of each fatigue cycle. In this case, at a load ratio of zero, the crack faces should be fully closed at the minimum load, and the crack faces should be in intimate contact. Closure induced damage is fully expected as a result of fatigue. This is further elucidated in a model for contact of crack surfaces (Sehitoglu and Garcia, 1997). In the case of specimen 2, fatigue tested at $R = 0.2$, the crack faces should never be fully closed during fatigue and therefore the opportunity for closure damage during fatigue is minimal. Normally, during ΔK -increasing fatigue crack growth at a positive load ratio, the closure force is minimal

and the impacting and flattening of crack surfaces is not evident (Wu et al. 1995). These observations strongly suggest that the cracks in the present case have not only experienced fatigue loads but also excitation forces during modal testing that have been sufficient to cause crack closure and fracture surface pounding. The inertia forces generated at frequencies near resonance would add to the nominal compressive load to produce a large closure force that would be sufficient to deform the micro-fracture features of the local high areas and produce plastically flattened plateaus. This provides evidence of severe beating of the crack surfaces during vibration.

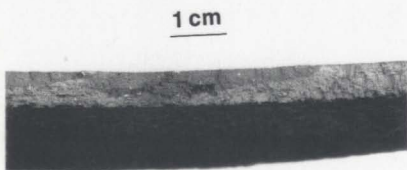
In summary of the above fractographic observations, it can be concluded that small fatigue cracks, initially in thumb-nail form, were first generated at multiple sites along the weld toe during fatigue. These cracks grew and coalesced to form a single large crack which then continued to grow to become a through-the-thickness crack. Crack opening and closing during fatigue and modal testing were evidenced by the presence of both fatigue striations and the deformed plateaus on the crack surfaces. Even under fatigue loading at a positive load ratio of 0.2, which would not normally cause significant crack closure, clear evidence was found of deformed areas on the crack surface, which are believed to be caused by the repeated pounding (opening and closing) of the two mating surfaces driven by the inertia forces caused by resonance during modal testing.

5.4 Description of Crack Growth

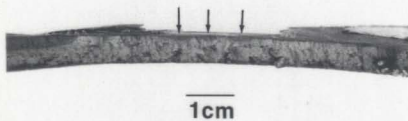
The values of crack width/depth in specimen 3 were measured by inking or beach marking, as a function of cycle numbers. The data are plotted in Figure 5.17 and 5.18 respectively. From Figure 5.17 and referring to the crack profiles shown in Figure 5.9, it appears that crack growth can be divided into two stages, i) the growth of



(a)

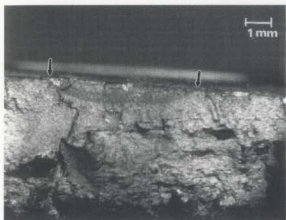


(b)

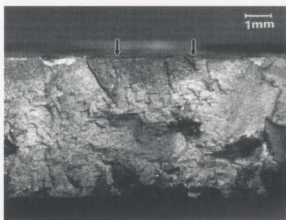


(c)

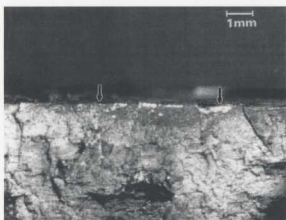
Figure 5.10: The presence of thumb-nail or elliptical cracks, as indicated by ink staining, along the weld toe of specimen 2 from left to right: (a) a single surface crack in half elliptical shape; (b) joining of two elliptical cracks; (c) three smaller thumb-nail cracks in the left of the coalesced crack



(a)

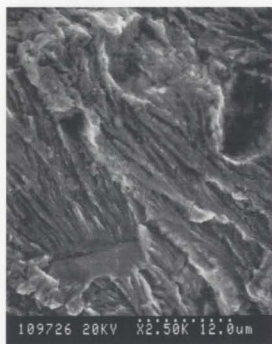


(b)



(c)

5.11: A closer look of the three individual thumb-nail cracks: (a) the one in the left; (b) the one in the middle; (3) the one in the right, as shown in Figure 5.10 (c)



(a)



(b)

Figure 5.12: Fracture surface features of (a) the trough area showing the texture and (b) the elevated area which has been pounded flat



Figure 5.13: A crack initiation site near the surface of the weld toe

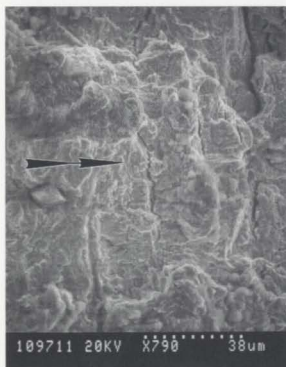
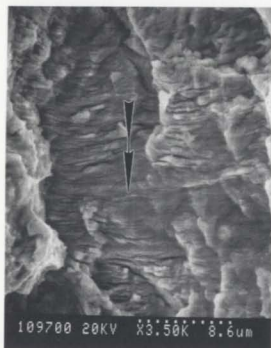


Figure 5.14: Secondary cracking perpendicular to the direction of crack growth through the thickness

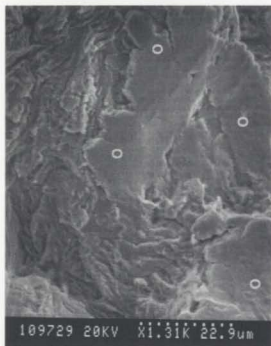


(a)

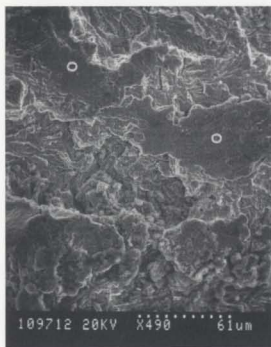


(b)

Figure 5.15: Fatigue striations in some trough areas, (a) and (b), in specimen 3



(a)



(b)

Figure 5.16: Flattened areas showing the evidence of crack closure (a) in specimen 2 and (b) in specimen 3

thumb-nail cracks and ii) the growth of a through-the-thickness crack. Each stage of the crack growth curve can be fitted with a Paris type equation of the form

$$da/dN = Ba^m \quad (5.1)$$

where a is the crack width and N is the number of fatigue cycles. Equation 5.1 is a variant form of Equation 3.50. The coefficient B , depending upon the direction of crack growth, will depend on the load magnitude, load ratio and crack characteristics. The value of the fitting constants B and m are given in Table 5.4.

Table 5.4: Fitting Constants for Crack Growth Curves

Cycles (N)	B	m
$< 5.65 \times 10^5$	2.273×10^{-7}	1.55
$> 5.65 \times 10^5$	2.273×10^{-7}	1.6

It should be noted that in Figure 5.17 the back-extrapolation of Equation 5.1 at $N = 0$ only assumes that an initial crack of size 37 mm would have existed had the crack growth process started from a single crack. However, in reality as shown in the fractographic pictures, the fatigue crack is formed by the coalescence of a number of thumb-nail cracks. Unfortunately, the detailed nucleation, growth and coalescence processes were not recorded in the study. Thus, a quantitative interpretation of crack initiation and growth before 3×10^5 cycles is missing.

From Figure 5.18 it appeared that crack growth in the thickness direction had followed a linear behavior at a constant growth rate $da/dN = 1.6 \times 10^{-5}$. The line intercepts the $b=0$ line with a finite number of cycles 1.4×10^5 , which would be termed as the initiation life in a "popular" sense; but it should be remembered that

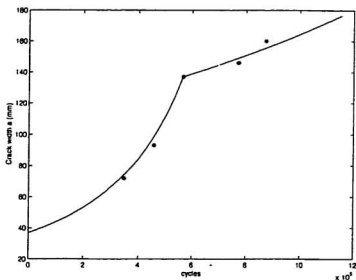


Figure 5.17: Experimental observations (*) of crack width as a function of the number of cycles in fatigue for specimen 3. The line represents the interpolation of LFM

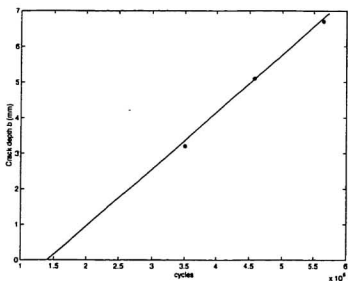


Figure 5.18: Experimental observations (*) of crack depth as a function of the number of cycles in fatigue for specimen 3. The line represents the observed behavior. $N = 1.4 \times 10^5 + 6.25 \times 10^4 b$

the crack growth behavior at small crack depths would be nonlinear and have flatter slopes. Also the linear crack growth behavior shown by the cracking of a tubular T-joint will not be the same for other types of welded joints; hence the two equations given in these pages are not universal.

5.5 Static Response During Fatigue Crack Growth

5.5.1 Static Strains

During fatigue testing, static strains were continuously monitored from 120 Ω rosette gauges at two locations on each side of the chord. The exact locations of these gauges are shown in Figures 4.15-4.29 for specimen 1 as gauge number 1 (8, 9, 10), 4 (17, 18, 19), 10 (35, 36, 37) and 11 (38, 39, 40); for specimen 2 and 3 as gauge number 1 (7, 8, 9), 4 (16, 17, 18), 10 (22, 23, 24) and 11 (26, 27, 28), the numbers in the brackets being the channel numbers. The static strains measured at these locations for the maximum loads (given in Table 4.8) are given in Tables 5.5 - 5.10 for the three specimens.

Plotting the relative strain ϵ/ϵ_0 (the ratio of the fatigue strain ϵ to the initial static strain ϵ_0) against the logarithm number of fatigue cycles N , a general trend of decreasing ϵ/ϵ_0 with $\log N$ is observed for all the three specimens, as shown in Figures 5.19 to 5.21. By this normalization, the static strain data taken at different gauge points fall close to a curve (which will be discussed later in detail) for each specimen. The relative strain remained fairly constant for a certain number of fatigue cycles, then it fell steeply as $\log N$ increases. The turning point in the ϵ/ϵ_0 vs $\log N$ relation was observed to be approximately 10^4 for specimen 1 and 3, where the cracking process appeared to start by the formation of a single thumb-nail crack which then grew to form a single major fatigue crack as shown in Figures 5.1 to 5.9,

but the turning point was about $0.6 - 0.8 \times 10^6$ for specimen 2 where the cracking process consisted of the successive nucleation, growth and coalescence of a number of small thumbnail cracks as shown in Figures 5.8, 5.10 and 5.11. It appears most likely that the fracture process was the same in all three specimens and occurred as described above for specimen 2. These observations indicate that the change in static strain is sensitive to the formation of large cracks, which grow either as a single crack or by coalescence of a number of thumb-nail cracks, but rather insensitive to the initiation of small thumb-nail cracks. This scenario was not totally unexpected because the formation of individual thumb-nail cracks causes only a minimal loss of load-bearing area. Only when these small cracks have joined to form a large crack, did the loss of load bearing area began to influence the strain at the gauge points. The static strain data measured at the noncracking side of the chord, as shown in Figure 5.21, also agrees with the above observation. Only some abnormality was observed in specimen 2 and 3 where the relative strain increased above 1.0 before it dropped along with crack growth. This was, perhaps, due to the effect of asymmetrical cracking and stress redistribution in the specimen, which will be explained in more detail in section 5.5.2. Indeed, although the specimens were identical in geometrical design and under similar fatigue loads, due to variations in the defect distribution along the weld toe, the fatigue cracking process in each specimen was different, as described by the three curves in Figure 5.19 and 5.20.

To describe the general trend of the variations of the static strain during fatigue crack growth in tubular T-joint, an equation is proposed of the form

$$\log_{10} N = A(\Delta\epsilon/\epsilon_0)^n \quad (5.2)$$

where $\Delta\epsilon = \epsilon - \epsilon_0$ is the change in the static strain caused by cracking; A can be

defined as the fatigue life index at 100 % strain range, i.e.,

$$A = \log_{10} N |_{\Delta\epsilon/\epsilon_0=1}; \quad (5.3)$$

and n is defined as the strain sensitivity index.

All static strain data can be monitored using Equation 5.2. Table 5.11 lists the values of A and n for each specimen. It is noticed that, for all the three specimens fatigued under similar loads, the life index A (≈ 6) is approximately a constant, but n varies between 0.005 to 0.08. Therefore, it may be concluded that A depends largely on the amplitude of the fatigue load whereas n is sensitive to the crack profile and configuration. The fitting of Equation 5.2, at all ϵ/ϵ_0 values is within a factor of 2. Therefore, Equation 5.2 can be used to monitor the fatigue crack growth process in tubular T-joints. More significantly, it would allow early detection/assessment of fatigue cracks in the structure, and thus allow one to avoid the danger of catastrophic failure.

Other types of formulations based on the actual curve fitting of the experimental data, in a least-squared sense and piecewise cubic spline approach are given in Appendix D, E and F.

5.5.2 Static Principal Stresses

The static principal stresses were derived from the strain measurements of the rosette gauges according to Eqns. 4.11 to 4.15. They are given in Tables 5.12 to 5.17. In the calculation, Young's modulus of the steel was taken as $E = 206.8 \text{ GPa} = 30.0 \times 10^6 \text{ lb/in}^2$, and Poisson's ratio as $\mu = 0.3$. The maximum principal stress at the hot spot, when the specimens were not cracked, was approximately 250 MPa along the transverse symmetric axis located at gauges 1 and 4. The principal stresses at the hot spots decreased as cracks developed in all the three specimens. The relative stress

Table 5.6: Static Strains for Specimen 1

Cycles	Strains ($\mu\epsilon$)					
	Gauge 10			Gauge 11		
	35	36	37	38	39	-40
0 *	443.0817	823.9122	539.5971	287.3230	383.0537	265.3520
70,000	399.2357	734.5223	485.7325	256.6879	340.1274	236.0510
620,000 *	395.1592	733.6306	484.7134	248.7898	337.0701	233.8854
680,000	395.6688	730.8280	487.8981	255.2866	333.8854	231.7197
720,000 *	389.2994	719.7452	480.5096	251.8471	329.1720	228.4076
722,500	391.3376	724.3312	485.8599	252.6115	330.0637	227.8981
725,000	390.9554	722.9299	484.0764	252.6115	328.9172	227.5159
727,500	391.9745	725.8599	485.0955	252.9936	330.7006	228.7898
732,500	389.8089	724.8408	485.3503	254.2675	328.6624	229.1720
812,500	387.7707	720.1274	486.7516	251.9745	325.6051	227.5159
852,500	387.1338	718.9809	487.2611	251.5924	325.4777	226.2420
872,500 *	407.5159	754.1401	515.0318	266.4968	348.5350	242.8025
880,000	407.5159	758.5987	513.7580	268.1529	347.3885	242.9299
887,500	406.1146	760.1274	513.5032	267.3885	349.0446	241.7834
977,500	398.5987	746.2420	506.7516	264.5860	341.2739	238.3439
1087,500 *	385.7325	723.6943	494.0127	258.3439	330.7006	231.5924
1095,000	377.0701	709.4268	484.4586	253.2484	325.0955	228.2803
1102,500	373.8854	707.1338	483.9490	253.6306	325.2229	228.1529
1110,000	364.2038	691.2102	474.9045	250.7006	321.2739	225.2229
1117,500	354.1401	670.3185	463.9490	246.3694	311.8471	198.9809
1282,500 *	337.9618	647.0064	450.5732	241.2739	302.2930	215.1592
* Modal testing performed at these intervals						

Table 5.9: Static Strains for Specimen 3

Cycles	Strains ($\mu\epsilon$)					
	Gauge 1			Gauge 4		
	7	8	9	16	17	18
0 *	548.8788	887.3582	520.7574	292.7182	419.2691	309.9746
350,000 *	281.6561	449.8089	348.5350	191.9745	235.2866	224.7134
450,000 *	117.3248	133.6306	231.8471	112.9936	60.1274	150.4459
457,500	105.8599	107.1338	226.3694	108.9172	58.9809	150.5732
557,500 *	71.2102	-44.2038	217.8344	67.0064	-96.8153	108.1529
565,000	70.1911	-51.2102	216.1783	64.8408	-108.6624	106.2420
765,000 *	-61.2739	-121.2739	257.3248	-41.1465	-258.5987	37.7070
772,500	-31.0828	-115.7962	232.4841	-35.0318	-250.4459	27.5159
872,500 *	-36.9427	-104.7134	212.7389	-55.2866	-248.4076	11.3376
* Modal testing performed at these intervals						

Table 5.10: Static Strains for Specimen 3

Cycles	Strains ($\mu\epsilon$)		
	Gauge 10		
	22	23	24
0 *	559.7452	856.8153	500.5096
350,000 *	556.4331	879.8726	541.4013
450,000 *	532.1019	890.9554	595.4140
457,500	530.5732	902.9299	609.5541
557,500 *	375.1592	755.1592	591.7197
565,000	366.7516	748.5350	588.5350
765,000 *	106.8790	384.5860	458.4713
772,500	108.5350	388.1529	459.7452
872,500 *	56.6879	213.5032	380.7643

* Modal testing performed at these intervals

Table 5.11: Equation Constants

Gauge	Specimen	A	n
1	1	6.1	0.05
	2	6.1	0.005
	3	5.8	0.08
2	1	6.1	0.05
	2	5.9	0.008
	3	5.9	0.08
10	1, 2 and 3	6.0	0.005

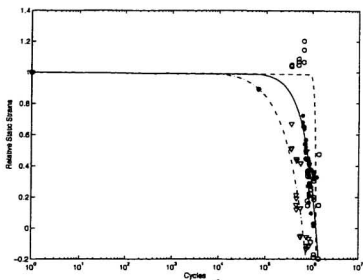


Figure 5.19: The observation of static strain (at gauge 1) as a function of the number of cycles in fatigue ("*" specimen 1; "o" specimen 2, "Δ" specimen 3). The lines are obtained from Equation , with the parameter values in Table ("-" specimen 1; "-." specimen 2, "-.-" specimen 3).

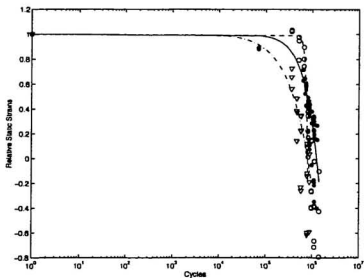


Figure 5.20: The observation of static strain (at gauge 4) as a function of the number of cycles in fatigue. ("*" specimen 1; "o" specimen 2, "Δ" specimen 3). The lines are obtained from Equation , with the parameter values in Table ("-" specimen 1; "-." specimen 2, "-.-" specimen 3).

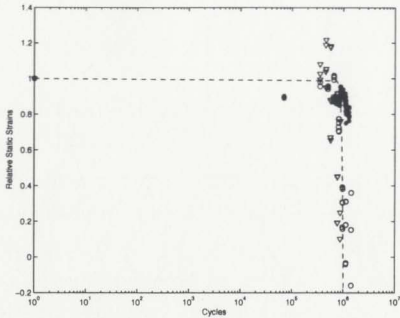


Figure 5.21: The observation of static strain (at gauge 10) as a function of the number of cycles in fatigue. ("*" specimen 1; "o" specimen 2, "△" specimen 3). The lines are obtained from Equation , with the parameter values in Table ("-" specimens 1, 2 and 3).

as a function of the number of fatigue cycles are shown in Figures 5.22 to 5.24. Only few data were recorded before visible crack formation because no obvious changes in strain readings were observed during this period. This general behavior is similar to that of the static strain as expected.

The maximum principal stress σ_1 and the minimum stress σ_2 remained essentially constant during the early stages of fatigue up until the cycle value of $10^4 - 10^5$ (the same as the static strains). Beyond this, the plots exhibit a marked change towards low and even the negative values of the stress. The drastic decrease in stress is believed to correspond to the onset of fatigue cracking, because the tractions would be lost on the crack surfaces.

In specimen 2, however, the relative principal stress had undergone a period of gradual increase (> 1) before it dropped to low values as shown in Figure 5.22. This seemingly abnormal behavior can be explained in relation to the specific fatigue crack growth process in specimen 2. As evidenced by the crack profile pictures (Figure 5.2 and 5.8), the main crack on side 1 of this specimen was formed by the coalescence of two elliptical surface cracks. The figures show the trace of the coalescence at 650,000 cycles. But it can be imagined that these two cracks were initially separated. At the time of their nucleation, being small in size, they did not influence the stresses transmitted across the section. As they grew larger, the fronts of these two cracks approached each other and therefore the ligament in between becomes thinner and thinner. As a result, the local stress in the ligament would increase, which also caused an increase in strain. Once these two cracks were joined, the load bearing area was totally lost, and the entire crack surface became stress free. Since the strain gauges were in close alignment with this joining point, the change in stress and strain at the weld toe would certainly be reflected in the strain gauge readings. In specimen 1 and 3, only one dominant crack grew during fatigue. Therefore, the stresses at

locations (the gauges) near the crack decreased as the crack (traction free) surface area increased.

The change of the stress with cracking should show the same trend as that of the strain because stress values are simply computed from the measured strains within the elastic region. We have discussed in detail the static strain behavior as a function of fatigue cycles in the previous section. In that we have observed that the change in strain was not sensitive to multiple site nucleation of thumb-nail cracks. In this section, we understand that the nucleation of thumb-nail cracks would only cause a minimal lose of load bearing area and thus did not disturb the stress distribution at a macroscopic level, as seen by the strain gauges. The description for the behavior of the stress can be omitted because the stress is proportional to the strain by the Young's modulus.

In order to appreciate the validity of the computed stresses, Table 5.18 gives a tabulation of the principal stresses σ_1 and σ_2 and the angles contained between the principal stress axes and the first gauge (viz., channels 7, 16 and 22 of specimen 2) of the rosette gauges 1, 4 and 10. It is seen that except for gauge 10, the stresses and the angles are almost the same; the variation in stress at the gauge 10 location of specimen 1 may be due to local thickness variation.

Table 5.12: Static Principal Stresses for Specimen 1

Cycles	Gauge 1		Gauge 4	
	σ_1 MPa(MN/m ²)	σ_2 MPa(MN/m ²)	σ_1 MPa(MN/m ²)	σ_2 MPa(MN/m ²)
0 *	213.7786	107.0436	106.5125	74.2035
70,000	190.5456	95.5497	94.1584	66.8031
620,000 *	142.8886	81.7501	70.6526	58.3952
680,000	123.1676	83.7077	61.1550	55.3229
720,000 *	98.1548	58.5917	54.4901	51.2620
722,500	101.2429	65.5896	54.9699	51.8736
725,000	101.2714	69.0987	54.4731	51.5425
727,500	101.6276	69.3446	52.5062	51.3642
732,500	102.0185	72.0397	54.9994	51.8818
812,500	69.0140	62.4423	52.2077	34.1628
852,500	66.2758	59.1967	50.5709	28.0470
872,500 *	59.3062	46.7847	47.1814	20.4473
880,000	62.2140	54.8660	48.7913	23.7675
887,500	63.7956	56.3328	48.5737	24.7753
977,500	66.0202	36.4954	49.4040	10.3215
1087,500 *	—	—	50.6967	0.4858
1095,000	—	—	50.4708	0.2225
1102,500	—	—	50.7568	-1.1173
1110,000	—	—	51.6295	-7.4093
1117,500	—	—	53.0953	-13.3912
1282,500 *	—	—	54.7575	-17.3867
* Modal testing performed at these intervals				

Table 5.13: Static Principal Stresses for Specimen 1

Cycles	Gauge 10		Gauge 11	
	σ_1 MPa(MN/m ²)	σ_2 MPa(MN/m ²)	σ_1 MPa(MN/m ²)	σ_2 MPa(MN/m ²)
0 *	186.8607	86.8825	92.0312	60.9804
70,000	177.6856	83.7592	87.7893	57.7798
620,000 *	177.2296	82.7099	86.5729	56.0231
680,000	177.0773	83.9536	86.4372	57.4384
720,000 *	174.3719	82.5945	85.2276	56.6534
722,500	175.6456	83.5036	85.3992	56.5570
725,000	175.2577	83.2517	85.1965	56.6469
727,500	175.8588	83.2528	85.5819	56.7506
732,500	175.5977	82.9493	85.3848	57.4371
812,500	174.8604	83.4984	84.6238	57.0314
852,500	174.6878	83.6334	84.4996	56.6663
872,500 *	183.6401	88.9069	90.2842	60.1774
880,000	183.6401	88.9069	90.2421	60.7464
887,500	184.3720	87.3094	90.3755	60.0484
977,500	181.2186	86.2478	88.7281	59.8517
1087,500 *	175.9145	83.9874	86.1736	58.5675
1095,000	172.4043	82.1159	84.6900	57.5673
1102,500	171.8297	81.5991	84.7336	57.5990
1110,000	168.0504	79.8462	83.5075	57.0939
1117,500	163.3139	78.3730	80.4272	51.0291
1282,500 *	157.6685	75.2873	79.3872	55.4562

* Modal testing performed at these intervals

Table 5.14: Static Principal Stresses for Specimen 2

Cycles	Gauge 1		Gauge 4	
	σ_1 MPa(MN/m ²)	σ_2 MPa(MN/m ²)	σ_1 MPa(MN/m ²)	σ_2 MPa(MN/m ²)
0 *	214.0350	102.5816	108.8289	72.4551
350,000 *	222.7843	108.2463	111.4270	75.1634
500,000 *	226.6771	114.9663	101.2898	59.4836
650,000 *	236.6339	135.6061	88.7083	59.9844
800,000 *	63.2616	51.4475	39.1922	15.4150
812,500	61.4645	45.0027	36.0398	10.8901
962,500 *	70.4680	4.4994	20.9188	-30.6285
970,000	69.6444	4.6456	20.8858	-31.1976
1120,000 *	85.3659	-5.9201	21.2370	-57.1024
1126,250	86.0096	-8.9347	17.2838	-54.0901
1426,250 *	104.0559	-6.9972	17.1878	-64.8327
* Modal testing performed at these intervals				

Table 5.15: Static Principal Stresses for Specimen 2

Cycles	Gauge 10		Gauge 11	
	σ_1 MPa(MN/m ²)	σ_2 MPa(MN/m ²)	σ_1 MPa(MN/m ²)	σ_2 MPa(MN/m ²)
0 *	212.8957	105.8661	92.1511	64.0685
350,000 *	207.7620	100.8009	89.0656	62.4121
500,000 *	202.1529	100.3885	—	—
650,000 *	212.7815	109.7813	—	—
800,000 *	154.0806	85.4988	—	—
812,500	154.0701	89.0469	—	—
962,500 *	62.6557	48.4405	—	—
970,000	62.0968	46.7789	—	—
1120,000 *	66.0278	11.1599	—	—
1126,250	64.7579	12.8815	—	—
1426,250 *	84.7741	-4.3874	—	—
* Modal testing performed at these intervals				

Table 5.16: Static Principal Stresses for Specimen 3

Cycles	Gauge 1		Gauge 4	
	σ_1 MPa(MN/m ²)	σ_2 MPa(MN/m ²)	σ_1 MPa(MN/m ²)	σ_2 MPa(MN/m ²)
0 *	214.1037	101.8643	107.8233	70.2108
350,000 *	115.1684	71.0081	66.5658	56.5358
450,000 *	62.7767	40.3786	50.6856	27.1419
457,500	62.4879	35.6621	49.9393	26.5710
557,500 *	74.9036	10.4885	55.3885	-3.6415
565,000	75.3328	9.2689	56.3397	-5.7970
765,000 *	72.0774	-14.1584	40.8340	-41.8501
772,500	70.0682	-10.5685	38.4462	-40.6667
872,500 *	62.4807	-10.5454	29.9161	-42.8999
* Modal testing performed at these intervals				

Table 5.17: Static Principal Stresses for Specimen 3

Cycles	Gauge 10	
	σ_1 MPa(MN/m ²)	σ_2 MPa(MN/m ²)
0 *	208.7964	104.4331
350,000 *	214.8268	109.5049
450,000 *	218.8428	114.2576
457,500	221.7358	115.0904
557,500 *	189.3518	96.2918
565,000	187.6729	94.5460
765,000 *	115.8347	51.1859
772,500	116.4103	51.4759
872,500 *	90.4079	38.8280
* Modal testing performed at these intervals		

Table 5.18: Static Principal Stresses for Intact Specimens

Specimen	Gauge 1					
	σ_1			σ_2		
	MPa(MN/m ²)	psi(lb/in ²)	Degree	MPa(MN/m ²)	psi(lb/in ²)	Degree
1	213.7786	31006	46.5029	107.0436	15526	-43.4971
2	214.0350	31044	45.9325	102.5816	14878	-44.0675
3	214.1037	31056	43.8580	101.8643	14774	-16.1420
Specimen	Gauge 4					
	σ_1			σ_2		
	MPa(MN/m ²)	psi(lb/in ²)	Degree	MPa(MN/m ²)	psi(lb/in ²)	Degree
1	106.5125	15449	49.3520	74.2035	10762	-40.6480
2	108.8289	15785	46.9007	72.4551	10509	-43.0993
3	107.8233	15639	47.0925	70.2108	10183	-42.9075
Specimen	Gauge 10					
	σ_1			σ_2		
	MPa(MN/m ²)	psi(lb/in ²)	Degree	MPa(MN/m ²)	psi(lb/in ²)	Degree
1	186.8607	27102	48.9134	86.8825	12602	-41.0866
2	212.8957	30878	43.1002	105.8661	15355	-46.8998
3	208.7964	30284	42.4098	104.4331	15147	-47.5902
Specimen	Gauge 11					
	σ_1			σ_2		
	MPa(MN/m ²)	psi(lb/in ²)	Degree	MPa(MN/m ²)	psi(lb/in ²)	Degree
1	92.0312	13348	41.6137	60.9804	8845	-48.3863
2	92.1511	13366	45.9718	64.0685	9293	-44.0282

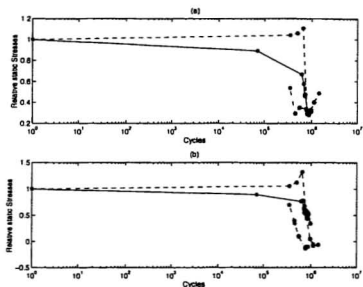


Figure 5.22: (a) Maximum static principal stress σ_1 at gauge 1, specimen 1 (—), specimen 2 (- -), & specimen 3 (-.); (b) Minimum static principal stress σ_2 gauge 1, specimen 1 (—), specimen 2 (- -), & specimen 3 (-).

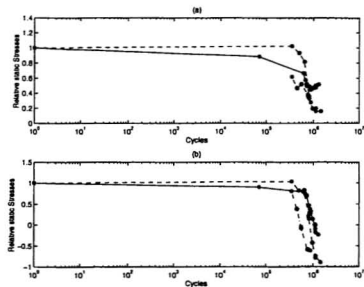


Figure 5.23: (a) Maximum static principal stress σ_1 at gauge 4, specimen 1 (—), specimen 2 (- -), & specimen 3 (-.); (b) Minimum static principal stress σ_2 at gauge 4, specimen 1 (—), specimen 2 (- -), & specimen 3 (-).

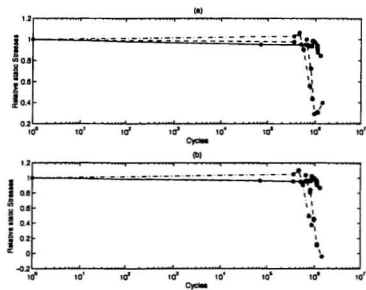


Figure 5.24: (a) Maximum static principal stress σ_1 at gauge 10, specimen 1 (—), specimen 2 (- -), & specimen 3 (-.); (b) Minimum static principal stress σ_2 at gauge 10, specimen 1 (—), specimen 2 (- -), & specimen 3 (-.).

5.6 Natural Frequencies and Damping

5.6.1 Natural Frequency Variations

The changes of natural frequencies with fatigue cycles are listed in Tables 5.19 to 5.29. The curves which show the non-dimensional natural frequencies as a function of fatigue cycles are shown in Figures 5.25 to 5.28.

From Figs. 5.25 to 5.28, it can be seen that for cycles less than about $10^5 - 10^6$, the non-dimensional frequency remains essentially constant, while beyond about $10^5 - 10^6$ the overall trend is for non-dimensional frequency ratio to fall. In this regard the overall form of these plots is very similar to the plots of non-dimensional static strain/stress (Figs. 5.19-5.24).

These plots support the previous observation that significant changes were occurring in the structures around $10^5 - 10^6$ cycles, and as suggested previously this was most likely associated with the first formation of large cracks, greater than about 50 mm in width/surface-crack-length, through the coalescence of multiple thumbnail cracks. The fatigue cycle of the specimen could be predicted by knowing the non-dimensional frequency ratio f^* . For specimen 2, there was a 16.5 % decrease in the frequency (for mode 1) between the crack free structure and the structure at failure - defined as the point when the crack extended beyond 50% of the total joint length (approximately distributed 25 % - i.e. one quarter - at each saddle point); this decrease was 3.68 % for mode 3 and 4.08 % for mode 6. These changes were much larger in specimen 2, than in specimens 1 and 3, since cracking occurred on both saddle hot spots of the tubular T-joint; consequently the total crack length at failure was greater than 50 % of the total weld toe length. When the cracking occurred on one side only as in the case of specimens 1 and 3, the maximum change in frequencies, were 8.5 % (for specimen 1) and 12.5 % (for specimen 3), respectively. In these cases the total

length of cracking was only about 25% of the total weld line. Comparing these values (for mode 1) with those given by Rytter(1993) for a box beam ($80 \times 80 \times 2$ thick) (since no results were available for a tubular T-joint, for comparison purpose) the percentage reduction in frequencies for a tubular T-joint was much less than that for a beam (which was 25 to 30 % for 55 to 60 % through the depth cracking). It was also much less than that obtained for a plated T-joint (Chen, 1996) (which was 13 - 14 % at 53 % through-the-thickness cracking from the top).

For the frequency response function measurements, the load level was that which was applied during modal tests. In one of the tests the maximum load amplitude (in the load cell) was observed to be 4 to 5 lbs. This would be analogous to the non-destructive assessment situation of an offshore structure wherein the structure would be excited by a modal exciter under quiescent environmental conditions, and the dynamic response measured to assess the condition of the structure.

The amplitude changes and frequency shifts were very small and hence could not be properly used for non-destructive assessment of the tubular joint. Also the FRF amplitude changes and frequency shifts were obvious only when the crack had gone through the thickness of the chord and extended around the weld toe when the normalized crack size was more than 0.31. During this part of crack growth, the major changes were observed in the quasi-static responses and anti-resonant frequencies along with the static strains; the other dominant feature was the sudden appearance of "apparent" noisy behavior in between the resonant frequencies. This was due to the nonlinear resonant behavior resulting in the generation of subharmonic and superharmonic responses generated from the opening and closing of the crack. These are discussed in the subsequent analysis of the data. Since results from the modal tests on each tubular joint were large [5 frequency ranges \times 11 to 21 crack stages \times (40 strain gauge + 7 accelerometer) channels] and they had to be superposed channel

by channel and connected together to form a single FRF (0 to 550 Hz) to observe the dominant changes, only the salient results in the low frequency domain (up to 50 Hz) have been presented in this thesis; otherwise no meaningful interpretation and presentation could have been made.

5.6.2 Damping Ratio Variations

The damping ratio variations with fatigue cycles are shown in Tables 5.30 to 5.40. The changes in non-dimensional data are shown in Figures 5.29 to 5.32 to relate the damping ratio variations with crack growth.

The damping ratio generally increased as the crack formed, perhaps to the point where the crack break-through occurred; beyond that the non-dimensional damping ratio decreased. The maximum increase in damping was nearly 2 times that obtained for the uncracked specimen. These values were much smaller than those reported by Hearn and Testa (1991) and Rytter (1993) for beams, who reported damping increases of 70 times that of uncracked ones; they also stated that damping increases occurred even for small cracks. Such changes were not observed in our experiments. Chen (1996) also reported only small increases during the modal tests on fatigued plated T-joints.

No consistent changes were observed in the damping ratios when plotted against relative fatigue cycles. For example, the value for mode 4 for specimen 2 increased with imposed fatigue cycles (Figure 5.30), while for specimens 1 and 3 this value decreased. For mode 1, the changes were less pronounced and the data remained essentially constant up to a relative cycle value of 0.4; beyond this point the overall trend was for the data to increase. The general conclusion reached from these observations was that non-dimensional damping ratio was not a particularly good parameter to use as an indicator of structural integrity.

Table 5.19: Natural Frequencies for Specimen 1 (mode 1 - 4)

Cycles	Modes							
	1		2		3		4	
	strain	acc	strain	acc	strain	acc	strain	acc
0	11.22	11.26	30.64	30.61	46.50	46.53	47.66	47.83
620,000	11.04	10.95	30.68	30.71	46.27	46.26	47.78	47.79
720,000	11.57	11.57	30.88	30.85	46.78	46.78	48.44	48.45
872,500	10.76	10.77	30.66	30.65	46.06	46.06	47.65	47.60
1087,500	10.51	10.51	30.57	30.56	45.81	45.83	47.45	47.46
1282,500	10.23	—	30.44	—	45.42	—	47.39	—

Table 5.20: Natural Frequencies for Specimen 1 (mode 5 – 8)

Cycles	Modes							
	5		6		7		8	
	strain	acc	strain	acc	strain	acc	strain	acc
0	167.89	167.89	287.43	287.36	299.31	299.29	303.01	302.96
620,000	167.85	167.83	287.07	287.11	299.34	299.41	303.03	303.14
720,000	167.72	167.69	286.39	286.31	299.36	299.35	302.98	303.01
872,500	167.37	167.35	285.68	285.64	299.49	299.31	302.94	302.88
1087,500	166.92	166.92	284.43	284.37	299.32	—	302.82	—
1282,500	166.27	—	282.31	—	299.09	—	302.51	—

Table 5.21: Natural Frequencies for Specimen 1 (mode 9 – 12)

Cycles	Modes							
	9		10		11		12	
	strain	acc	strain	acc	strain	acc	strain	acc
0	330.66	330.58	340.22	340.14	359.67	357.47	366.38	366.45
620,000	330.56	330.51	340.21	340.29	—	—	363.34	363.51
720,000	330.43	330.15	340.20	340.18	—	—	363.15	363.28
872,500	330.31	330.27	340.18	340.13	—	—	363.39	363.39
1087,500	330.07	330.09	340.06	—	—	353.02	363.22	363.20
1282,500	329.51	—	340.05	—	—	—	363.03	—

Table 5.22: Natural Frequencies for Specimen 1 (mode 13 – 16)

Cycles	Modes							
	13		14		15		16	
	strain	acc	strain	acc	strain	acc	strain	acc
0	395.52	395.43	426.25	426.25	438.44	438.45	444.44	444.38
620,000	393.78	394.10	426.26	426.20	438.74	438.76	444.63	444.62
720,000	—	—	426.33	426.32	438.56	438.67	444.39	444.43
872,500	—	393.56	426.08	426.02	438.54	438.61	444.39	444.27
1087,500	392.99	392.98	426.06	426.02	438.39	438.42	—	444.01
1282,500	393.46	—	426.03	—	438.19	—	444.42	—

Table 5.23: Natural Frequencies for Specimen 1 (mode 17 – 20)

Cycles	Modes							
	17		18		19		20	
	strain	acc	strain	acc	strain	acc	strain	acc
0	460.50	460.50	484.62	484.40	501.52	501.56	533.94	533.88
620,000	460.71	—	484.90	484.38	501.31	501.51	533.84	533.88
720,000	460.45	—	484.99	484.25	502.05	502.05	533.76	533.80
872,500	460.45	—	485.31	484.75	500.96	500.88	533.56	533.58
1087,500	—	—	485.70	484.22	500.71	500.63	533.51	533.56
1282,500	—	—	484.68	—	500.32	—	533.28	—

Table 5.25: Natural Frequencies for Specimen 2 (mode 5 – 8)

Cycles	Modes							
	5		6		7		8	
	strain	acc	strain	acc	strain	acc	strain	acc
0	165.70	165.73	279.38	279.28	293.66	293.62	298.02	297.98
350,000	165.64	165.58	279.39	279.22	293.74	293.68	298.10	298.05
500,000	165.62	165.55	279.15	279.10	293.62	293.65	297.99	297.99
650,000	165.45	165.43	278.70	278.68	293.64	293.65	297.89	297.89
800,000	164.70	164.67	276.37	276.37	293.69	293.67	297.74	297.72
962,500	163.70	163.71	273.03	273.11	293.56	293.54	297.38	297.33
1120,000	163.07	163.04	270.93	271.00	293.32	293.30	297.12	297.06
1426,250	162.18	162.18	267.96	267.91	292.94	292.94	296.88	296.87

Table 5.28: Natural Frequencies for Specimen 3 (mode 5 – 8)

Cycles	Modes							
	5		6		7		8	
	strain	acc	strain	acc	strain	acc	strain	acc
0	162.33	162.33	272.02	271.97	296.32	296.30	301.29	301.29
350,000	162.23	162.18	271.12	271.07	296.40	296.37	301.37	301.36
450,000	161.84	161.86	269.88	269.90	296.39	296.38	301.25	301.26
557,500	161.42	161.46	268.42	268.42	296.39	296.37	301.13	301.12
765,000	160.50	160.51	264.56	264.56	296.17	296.15	300.85	300.86
872,500	160.02	160.00	262.87	262.72	296.04	296.04	300.84	300.84

Table 5.29: Natural Frequencies for Specimen 3 (mode 9 – 12)

Cycles	Modes							
	9		10		11		12	
	strain	acc	strain	acc	strain	acc	strain	acc
0	320.26	320.25	354.09	354.07	416.24	416.57	422.75	422.99
350,000	320.39	320.37	354.41	354.35	416.43	416.70	422.82	422.99
450,000	320.30	320.26	354.30	354.28	416.43	416.74	422.76	422.94
557,500	320.14	320.12	354.21	354.18	416.14	416.43	422.41	422.80
765,000	318.93	318.95	353.15	353.13	415.53	417.00	422.99	422.59
872,500	318.00	318.03	352.22	352.22	415.20	416.56	—	422.39

Table 5.30: Damping (%) for Specimen 1 (mode 1 – 4)

Cycles	Modes							
	1		2		3		4	
	strain	acc	strain	acc	strain	acc	strain	acc
0	1.28	1.14	0.5967	0.5560	0.6854	0.5624	0.8552	1.18
620,000	1.10	1.42	0.3021	0.3593	0.5321	0.4360	0.5758	0.5465
720,000	0.6754	0.8945	0.3500	0.3519	0.4451	0.5153	0.6852	1.03
872,500	1.41	1.51	0.3867	0.3770	0.5001	0.4460	0.6045	0.5706
1087,500	1.76	1.68	0.5934	0.4800	0.4970	0.4515	0.6213	0.5564
1282,500	2.12	—	0.1954	—	0.5107	—	0.6016	—

Table 5.31: Damping (%) for Specimen 1 (mode 5 – 8)

Cycles	Modes							
	5		6		7		8	
	strain	acc	strain	acc	strain	acc	strain	acc
0	0.1598	0.1594	0.1378	0.1296	0.0418	0.0433	0.0596	0.0562
620,000	0.1139	0.1271	0.1377	0.1372	0.0457	0.0480	0.0541	0.0578
720,000	0.1416	0.1360	0.1409	0.1502	0.0423	0.0452	0.0504	0.0536
872,500	0.1277	0.1338	0.1349	0.1390	0.0062	0.0349	0.0529	0.0507
1087,500	0.1433	0.1375	0.1538	0.1561	0.0343	0.0445	0.0479	0.0529
1282,500	0.1494	—	0.1392	—	0.0426	—	0.0653	—

Table 5.32: Damping (%) for Specimen 1 (mode 9 – 12)

Cycles	Modes							
	9		10		11		12	
	strain	acc	strain	acc	strain	acc	strain	acc
0	0.0867	0.0859	0.1207	0.0777	0.2109	0.2030	0.2653	0.2704
620,000	0.0787	0.0463	0.0718	0.0657	—	—	0.0897	0.1065
720,000	0.1797	0.1745	0.1146	0.0790	0.1672	0.1848	0.097	0.3408
872,500	0.0865	0.0896	0.0811	0.0820	—	—	0.0999	0.1060
1087,500	0.0940	0.0958	0.0885	—	—	0.4278	0.0994	0.0861
1282,500	0.0502	—	0.0784	—	—	—	0.0927	—

Table 5.33: Damping (%) for Specimen 1 (mode 13 – 16)

Cycles	Modes							
	13		14		15		16	
	strain	acc	strain	acc	strain	acc	strain	acc
0	0.3495	0.2507	0.1807	0.1879	0.0996	0.1031	0.0693	0.0615
620,000	0.2364	0.2982	0.2304	0.2001	0.0935	0.1133	0.0771	0.0756
720,000	0.2124	0.2785	0.1780	0.1722	0.0749	0.0900	0.0642	0.0605
872,500	—	0.3075	0.1773	0.1890	0.0970	0.1068	0.0943	0.0724
1087,500	0.2635	0.2931	0.1746	0.1800	0.1265	0.1310	—	0.0736
1282,500	0.2762	—	0.1808	—	0.0857	—	0.0553	—

Table 5.34: Damping (%) for Specimen 1 (mode 16 – 20)

Cycles	Modes							
	17		18		19		20	
	strain	acc	strain	acc	strain	acc	strain	acc
0	0.1405	—	0.2957	0.2522	0.1269	0.1290	0.0773	0.0820
620,000	0.1344	—	0.3961	0.5201	0.1441	0.1524	0.0750	0.0771
720,000	0.1564	—	0.2972	0.3630	0.1275	0.1250	0.0672	0.0679
872,500	0.1932	—	0.2687	0.6525	0.1519	0.1568	0.0715	0.0707
1087,500	—	—	0.3973	0.8675	0.1611	0.1571	0.0691	0.0731
1282,500	—	—	0.3101	—	0.1581	—	0.0667	—

Table 5.35: Damping (%) for Specimen 2 (mode 1 - 4)

Cycles	Modes							
	1		2		3		4	
	strain	acc	strain	acc	strain	acc	strain	acc
0	0.5369	0.5214	0.1642	0.1652	0.2672	0.2645	0.2965	0.2946
350,000	0.6857	0.5856	0.1971	0.1706	0.2641	0.2584	0.3275	0.3202
500,000	0.6418	0.4908	0.1650	0.1671	0.2367	0.2753	0.3182	0.3141
650,000	0.5413	0.6397	0.1690	0.1763	0.2549	0.2747	0.3146	0.3460
800,000	0.6020	0.5195	0.1731	0.1686	0.2435	0.2830	0.3356	0.3176
962,500	1.03	1.03	0.1864	0.1914	0.3728	0.3687	0.3795	0.1758
1120,000	0.8847	0.8537	0.1776	0.1976	0.3748	0.3673	0.4425	0.4431
1426,250	0.4139	0.3467	0.2287	0.2268	0.3100	0.2927	0.3972	0.3699

Table 5.36: Damping (%) for Specimen 2 (mode 5 – 8)

Cycles	Modes							
	5		6		7		8	
	strain	acc	strain	acc	strain	acc	strain	acc
0	0.1809	0.1951	0.1537	0.1544	0.0369	0.0357	0.0604	0.0587
350,000	0.2276	0.2413	0.2104	0.1962	0.0373	0.0378	0.0688	0.0658
500,000	0.1687	0.1819	0.1825	0.1768	0.0702	0.0614	0.1159	0.1021
650,000	0.1862	0.1913	0.1814	0.1862	0.0657	0.0590	0.1042	0.1033
800,000	0.1956	0.1898	0.1811	0.1970	0.0378	0.0577	0.1091	0.1047
962,500	0.1984	0.1909	0.2060	0.2023	0.0699	0.0623	0.1165	0.1112
1120,000	0.2048	0.1995	0.1837	0.1838	0.0584	0.0601	0.1206	0.1079
1426,250	0.1829	0.1865	0.1709	0.1980	0.0672	0.0605	0.3271	0.1086

Table 5.37: Damping (%) for Specimen 2 (mode 9 - 12)

Cycles	Modes							
	9		10		11		12	
	strain	acc	strain	acc	strain	acc	strain	acc
0	0.0834	0.0834	0.0879	0.0994	0.0485	0.0475	0.1531	0.1559
350,000	0.1172	0.1112	0.1153	0.1185	0.0663	0.0565	—	0.1733
500,000	0.1118	0.1109	0.0337	0.1254	0.0644	0.0644	0.1533	0.1900
650,000	0.1217	0.1132	0.0370	0.1321	0.0769	0.0660	0.1505	0.1991
800,000	0.3487	—	0.1149	0.2275	0.0712	0.0639	0.1523	0.2093
962,500	0.1134	0.1112	—	0.1210	0.0843	0.0745	—	218.61e-3
1120,000	0.1067	0.1073	—	0.1301	0.0726	0.0681	—	0.4250
1426,250	0.1194	0.1182	—	0.1209	0.0911	0.0704	—	—

Table 5.38: Damping (%) for Specimen 3 (mode 1 - 4)

Cycles	Modes							
	1		2		3		4	
	strain	acc	strain	acc	strain	acc	strain	acc
0	0.5726	1.03	0.2049	0.2102	0.4128	0.4111	0.5858	0.5956
350,000	0.5187	0.6238	0.1889	0.2013	0.3164	0.3200	0.5751	0.3062
450,000	0.5923	0.6090	0.1738	0.1779	0.2811	0.2956	0.5161	0.5643
557,500	0.6967	0.1900	0.1829	0.2187	0.3914	0.3827	0.6391	0.6724
765,000	0.7562	0.7768	0.1912	0.2164	0.2991	0.2989	0.5416	0.4844
872,500	0.4710	0.3381	0.2490	0.2366	0.2993	0.3074	0.4828	0.5664

Table 5.39: Damping (%) for Specimen 3 (mode 5 – 8)

Cycles	Modes							
	5		6		7		8	
	strain	acc	strain	acc	strain	acc	strain	acc
0	0.2046	0.1944	0.1931	0.2103	0.0586	0.0609	0.0756	0.0723
350,000	0.02116	0.0205	0.2054	0.2013	0.0645	0.0608	0.0883	0.0863
450,000	0.2241	0.2256	0.2086	0.2050	0.0630	0.0653	0.0875	0.0969
557,500	0.2588	0.2389	0.1988	0.1932	0.0604	0.0597	0.0923	0.0929
765,000	0.2347	0.2334	0.2064	0.1987	0.0710	0.0623	0.1104	0.1375
872,500	0.1957	0.2081	0.2190	0.2153	0.0675	0.0650	0.0622	0.0958

Table 5.40: Damping (%) for Specimen 3 (mode 9 – 12)

Cycles	Modes							
	9		10		11		12	
	strain	acc	strain	acc	strain	acc	strain	acc
0	0.1162	0.1202	0.0872	0.0704	0.1357	0.0986	0.2709	0.1948
350,000	0.1407	0.1371	0.0696	0.0760	0.1360	0.1240	0.2155	0.1836
450,000	0.1436	0.1422	0.0857	0.0780	0.1230	0.1347	0.1880	0.2104
557,500	0.1453	0.1391	0.0787	0.0762	0.1946	0.0809	0.2050	0.1882
765,000	0.1593	0.1375	0.0838	0.0758	0.1714	0.1071	0.1836	0.2091
872,500	0.1506	0.1415	0.0786	0.0745	0.1781	—	0.2470	—

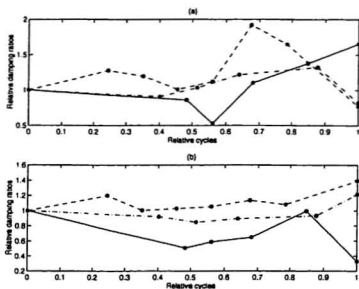


Figure 5.29: (a) Damping changes with cycles for mode 1, specimen 1 (—), specimen 2 (- -), & specimen 3 (- · -); (b) Damping changes with cycles for mode 2, specimen 1 (—), specimen 2 (- -), & specimen 3 (- · -).

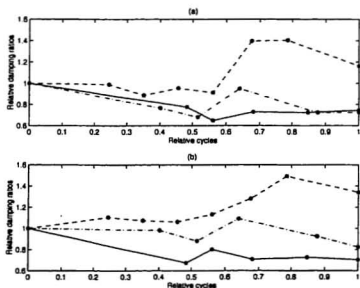


Figure 5.30: (a) Damping changes with cycles for mode 3, specimen 1 (—), specimen 2 (- -), & specimen 3 (- · -); (b) Damping changes with cycles for mode 4, specimen 1 (—), specimen 2 (- -), & specimen 3 (- · -).

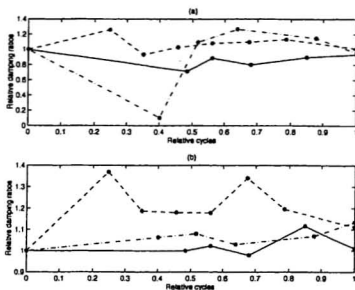


Figure 5.31: (a) Damping changes with cycles for mode 5, specimen 1 (—), specimen 2 (- -), & specimen 3 (-.); (b) Damping changes with cycles for mode 6, specimen 1 (—), specimen 2 (- -), & specimen 3 (-.)

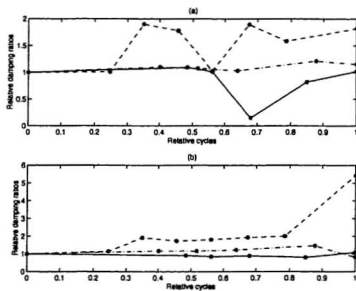


Figure 5.32: (a) Damping changes with cycles for mode 7, specimen 1 (—), specimen 2 (- -), & specimen 3 (-.); (b) Damping changes with cycles for mode 8, specimen 1 (—), specimen 2 (- -), & specimen 3 (-.)

5.7 Salient Features of Dynamic Response

5.7.1 Introduction

The dynamic responses measured from the three tubular joints, using strain gauges and accelerometers, were analyzed and salient findings from the analyses are presented and discussed in this section. First of all, clear signals were obtained from both the strain gauges and accelerometers in all frequency regions. In spite of this, the FRFs in the high frequency region were rather insensitive to the crack size where the normalized crack size was small to medium. Therefore all discussions would be concentrated on the low frequency region ($< 50\text{Hz}$). In this region the strain gauges showed more distinguishable responses than the accelerometers, as shown in Figures 5.33 and 5.34. Frequency shifts were observed in both the resonant and anti-resonant frequency regions, but the anti-resonant frequency shift appeared to be more sensitive to the presence of cracks. This was even more evident in the signals obtained from strain gauges than from accelerometers. Therefore, the anti-resonant shift in strain FRF was chosen as a crack indicator. The FRF curves numbered from 1 to 7 (Figure 5.33) represent the measurements taken over a time period, typically, of four months. During this period, frequent checks were made to see whether the readings were consistent and reliable. The reliability of FRF data were assured as the resonant natural frequency (for example, mode 1) shifted consistently towards the lower values.

Earlier studies on the modal characterization of cracking in structures mostly focused on resonant amplitude reduction, frequency changes and damping changes. The modal assurance criterion (MAC) and coordinate modal assurance criterion (COMAC) were utilized to identify the maximum values of modal coordinates at the resonance. These values had appreciable changes only when the crack occurring in

the structure was very large (when the crack extended over 50 % of the total load-bearing area). By this time, most likely a significant portion of the fatigue life had been consumed in generating the crack. Even in Figures 5.33 and 5.34, frequency shifts became noticeable only when more than 60 % of the fatigue life had been spent in generating the crack; amplitude changes were also not appreciable even during the entire life of cracking. The insensitivity of these vibration measurements have hindered the application of vibration methods for NDE. Therefore, in this study, attention was focused on other crack indicators that would reveal the presence of cracks in the early stage of fatigue.

Three salient observations were made from a detailed examination of the experimental results. They were based on (i) the presence of quasi-static components ($f < 5$ Hz) in the frequency response functions; (ii) response in the anti-resonant region; and (iii) nonlinearities observed in the frequency response functions as indicated, for example, in Figure 5.46. As discussed in the following sections, these features are indicative of the presence of cracking in the specimen.

5.7.2 Quasi-Static Components in Frequency Response Functions

Quasi-static components refer to the strain/acceleration components near zero frequency. Examination of Figures 5.33 and 5.34 will show that both cracked and uncracked specimens produced some quasi-static response. Clearly a significant contributor to this response was quite independent of the presence or absence of cracks. The low frequency components presented in the response of intact (or uncracked) specimens were due to the low frequency vibrations of the massive floor, the massive steel supporting base, etc.

The FRF signals at the locations closer to the driving force were stronger than

those far away. However, closer examination of the quasi-static response, as illustrated in Figures 5.35 to 5.39, strongly suggested that there was an additional component of the FRFs that was very sensitive to the presence of cracks. As may be seen in all of these figures, the FRF magnitude for the uncracked specimens (zero cycles) consistently fell below the magnitude for the cracked specimens. It should be noted that this type of behavior was obtained from gauges placed quite far from the crack locations (e.g gauge 12) as well as from gauges close to the cracks; this observation was valid for both strain gauge and accelerometer data. The nature of changes observed in the FRF amplitude presented here therefore suggests that this change was due to a parameter contributing to a global behavior of the structure.

At resonance, inertia forces arising from the mass of the structure, contributed substantially to the overall loading on the structure and gave rise to displacements at the crack locations that were much larger than would be expected to occur simply as a result of the excitation force.

Due to crack opening and closing, the modal stiffness of the structure went through small sequential changes which led to a series of changes in the natural frequency of the structure during one load cycle. Any two consecutive frequencies would generate a low frequency $((\omega_{n_2} - \omega_{n_1})/2)$ and a high $((\omega_{n_2} + \omega_{n_1})/2)$ frequency response of similar magnitudes. Here, ω_{n_1} and ω_{n_2} were the two close incremental frequencies corresponding to the stiffness change before and after a step of crack opening and closing. The superposition of these two frequency components would result in a beating phenomena leading to the increase of quasi-static components observed near the zero frequency region. Since the lower beating frequency, $(\omega_{n_2} - \omega_{n_1})/2$, is nearly zero, the beating effect was more pronounced in the quasi-static region. This was observed at all points of strain gauges and accelerometers as shown in Figures 5.33 to 5.53. This beating phenomenon could not be produced with either an "always open"

or an "always closed" crack because no change of the stiffness was involved.

The quasi-static component of the beating due to crack opening and closing would superpose itself on the strain/acceleration FRF magnitudes of the pristine (uncracked) structure in the near zero frequency region. The magnitude of beating was of the same order as or even larger than the FRF magnitude of the pristine specimen in the near zero frequency region. Therefore the overall quasi-static response of the structure containing a beating crack became larger than that of the pristine structure, as could be seen from Figures 5.33 and 5.34. This change in the quasi-static phenomenon cannot be explained by (a) the static strain change in response due to cracking; or (b) the loosening of the bolts tying the tubular T-joint support to the massive steel frame and the test floor, for the following reasons. The presence of a crack would normally reduce the static strain near the weld toe as shown in Figures 5.19 to 5.21. The near zero strain frequency FRF would rather have been reduced than increased if beating had not occurred. Generally loosening of bolts could only influence the response of the accelerometers but not the strain FRF, because it only introduces rigid body movements. Apparently, this did not happen during the tests because otherwise the acceleration magnitude in FRF would have increased dramatically at resonant frequencies which was not noticed in Figure 5.34 or any other accelerometer measurements.

The low frequency response, generated due to the successive beating in association with crack opening and closing, adds to the strain or acceleration FRF of the pristine specimen at near zero frequencies. This distinct behavior was observed for all crack sizes, even as small as 72mm wide (note that this size may be rather "large" by other definitions, but in terms of the ratio of detectable normalized crack size to the entire load bearing section, it is regarded as small since the value is only 0.07).

Figure 5.35 shows the weld toe strain FRF at the location of gauge 1, channel

8, for specimen 2. Even before the crack had developed to become a through-crack, small but significant differences could be observed in the frequency response functions below about 4 Hz. Figure 5.36 shows the changes that occurred in the strain FRF at gauge 5, channel 13, of specimen 2. Figure 5.37 shows the strain FRF change that occurred at gauge 12, channel 33, of specimen 1; this gauge was the farthest one from the weld toe. Even there the changes in the quasi-static region were quite significant. This observation further confirms that the beating component was significant (it had the same order of magnitude as the FRF resonant magnitude of the pristine structure) and this low frequency quasi-static response could be observed at any location in the structure. Therefore it can be chosen as a crack indicator.

Figure 5.38 shows the acceleration FRF change that occurred for the accelerometer #5 located at the bottom of the chord; once again there is small but significant difference in the quasi-static response between the cracked and uncracked specimen. Figure 5.39 shows the change in acceleration FRF for accelerometer #2, located on the chord surface along the longitudinal axis, \perp to the hot spot weld toe line (close to strain gauge # 7).

The presence of these quasi-static responses has been indicated in other studies carried out earlier, but no one has identified them carefully to give a logical explanation. In the experimental studies, reported by Prime (1996) and the analytical studies reported by Barltop and Adams (1991), the quasi-static response was present due to crack opening and closing; but the authors did not explain the origin of the response, nor did they comment on its presence. Also no specific theoretical model was proposed for the behavior. It has been stated earlier that the opening and closing of a crack causes additional subharmonic and superharmonic peaks in the auto-spectral density function of the response (Friswell and Penny, 1992).

The results presented above show that the presence of cracking in a structure

could be confirmed by the increases in FRF amplitude observed in the low frequency region.

5.7.3 Response in the Anti-Resonant Region

It may be seen in Figure 5.33 and Figure 5.34 that only small frequency shifts and changes of peak magnitude were observed for the first resonant mode, although of the two sets of data, the strain data showed greater changes in peak magnitudes than the acceleration data. The reason is that strain shows the deformation state of the material better than accelerometers. Displacement and acceleration, however, also include rigid body movements which are not sensitive to the presence of cracks. However, the changes in the anti-resonant regions were observed to be very distinct.

From Figures 5.40 to 5.45, showing the FRF data obtained from strain gauges and accelerometers, it could be seen that the changes in the anti-resonant regions with cracking were very distinct. Figure 5.40 shows strain FRFs at the location of gauge 6, channel 20, of specimen 2. First, a shift in anti-resonance frequency from 34 to 32.5 Hz, between the second and third of resonance peaks, occurred when the specimen was cycled from the no crack condition to 650,000 cycles with a crack of 109 mm. This change (5 %) in the anti-resonant frequency was about 7 times the natural frequency shift (0.6 %, Table 5.24) at the first mode resonance. Furthermore, a second anti-resonant frequency was formed at 29 Hz after 800,000 cycles when the crack had grown to 166 mm. At this time the anti-resonant frequency shift increased to 17 %. Similar behavior was also observed at gauge 3, channel 10, of specimen 2, as shown in Figure 5.41. At this location, the anti-resonance frequency shift (11.9 %) was nearly 19 times the shift that occurred at the first mode resonance (0.62 % - Table 5.24). At gauge 1 (channel 9) and gauge 8 (channel 31) of specimen 2, however, the anti-resonance occurred between the first and second resonance mode, and the

shifts went towards higher frequencies as could be seen from Figures 5.42 and 5.43. Although the anti-resonant frequency shifting phenomenon was not as pronounced as that at gauges 3 and 6, the changes were also easily detectable.

Anti-resonance phenomena were also obtained from accelerometers #1 and #5. The data are presented in Figures 5.44 and 5.45. These acceleration FRFs did not exhibit anti-resonant frequency shifts as large as the strain FRFs; but they were much larger than the shifts that occurred around resonant frequencies.

5.7.4 Nonlinearity in Frequency Response Functions

It has been realized from earlier studies on the vibration of cracked beams that the presence of a crack may lead to non-linear changes in the stiffness of the beam which has been modeled by piecewise linear springs for cracks. Nonlinearity in piecewise linear spring models would cause subharmonic and superharmonic peaks in the autospectral density functions (defined as the square of the FRF magnitude times autospectral density of the driving force) of the response of the structure (Rytter, 1993); hence in the FRF also.

From all the experimentally recorded and digitally analyzed frequency response functions, nonlinear responses (as subharmonic and superharmonic response peaks) could be observed, but only in the cracked specimens. They were never observed in the crack-free specimens. Furthermore the magnitude of these nonlinearities increased as crack length increased, as illustrated for example in Figures 5.46 and 5.47. The nonlinearities became particularly severe when cracks had grown to become through-cracks, at least at one location. A consistent trend of increasing magnitude of subharmonic or super-harmonic peaks with increasing number of cycles (or increasing crack length) could be observed, comparing Figures 5.42 and 5.46. This does not appear to be a random noise, generated due to the low level of signals.

From Figures 5.46 to 5.53, it can be seen that nonlinear responses are present between 5 to 8 Hz, 17 to 23 Hz and 37 to 43 Hz, when the fatigue cycles increased beyond 60% of the total fatigue life of the tubular T-joint. It is surmised that at this stage, the crack had almost penetrated across the wall thickness at the hot spot region of the weld toe and that the fluctuating in-plane and the bending surface strains tend to be larger than that permissible in a small-displacement formulation. This leads to nonlinear responses in the frequency domain.

It will be noted that the FRF signals were generally weaker from the cracked specimens than from the uncracked specimens, and therefore one might simply conclude that the non-linearities were merely due to increased levels of noise relative to the actual signals. However, this was not always the case, and for example Figure 5.50 provides an example where the signal strengths for cracked and uncracked specimens were of the same order of magnitude, and yet only the cracked specimen produced indications of non-linearity.

Comparison of the strain FRFs from gauge 10 and from gauges 1 and 4 (Figures 5.50, 5.46 and 5.47) indicate that the strength of the signals depends on the degree of shielding of the gauge by the main crack. The signals were generally strong where the gauge was located far away from the crack, and not affected much by the strain release due to it; whereas signals were weak when the gauge was located close to the center of the crack, and therefore the strain level was rather low.

This nonlinearity seems to be visibly present in the strain FRFs, whereas in the acceleration FRFs, it is less evident. Since the in-plane and bending deformations tend to change suddenly due to the crack break-through (of the chord wall), the strain gauges tend to show this nonlinear effect. The "crack opening and closing" did not produce any conspicuous change in the displacement behavior of the chord plate material and hence the nearby accelerometer did not sense significant changes.

By comparing Figures 5.46 to 5.49, it would be seen that the closer the gauge to the growing crack, the stronger were the non-linearities in the FRFs. For example, in Figures 5.46 and 5.47, where the gauges were close to the cracks, the nonlinearities were strong. In Figure 5.48, where the gauge was on the center-line row, and quite far from the crack the nonlinearities were barely visible. In Figure 5.49, where the gauge was far removed from the crack, at the bottom of the chord, any small nonlinearities were lost in the general noise, these observations provide a basis for the approximate location of the cracks with reference to the sensed strain gauge.

The presence of these nonlinear regions in the strain FRFs gives an indication that a crack (or cracks) has (have) grown to a considerable size somewhere in the structure. Once the presence of this nonlinearity is noticed, a detailed survey of the structure should be carried out to locate the cracked region(s) and repair it (or them).

5.8 Conclusions

Fatigue and modal testing of tubular T-joints were conducted carefully producing reliable results. The fractured surfaces of the two representative specimens were examined using optical and electron microscopes. From the fractographic study, the process of crack initiation and growth along the weld toe in this tubular T-joints were identified. Particularly, evidence of crack opening and closing were found. In analyzing the static strain behavior as a function of fatigue cycles, an empirical equation was proposed to describe the general trend of the static strain changes. It was shown that the equation was valid for all gauge locations, but the parameters depended on the crack profiles and configurations under a constant amplitude of fatigue loading. The crack growth behavior was also described by a Paris type equation which could be used to predict (by back extrapolation) the fatigue life to crack initiation. These

equations would allow early detection of fatigue cracks in the tubular T-joints.

In addition, natural frequencies and damping ratios were also identified for the three tubular T-joints. Experimental frequency response functions were analyzed and three salient indicators (features of FRFs) for crack detection were identified: (i) the presence of quasi-static components in strain/acceleration FRFs; (ii) the frequency shift in the anti-resonance (of strain FRFs); and (iii) nonlinear responses of the strain FRFs of cracked specimens. These FRF features could all clearly indicate the presence of cracks in tubular T-joints.

From the experimental study, it has been concluded that both strain gauges and accelerometers were sensitive to the presence of cracks in structures; but strain gauges was more sensitive than accelerometers. Moreover the cost of strain gauges was much less than accelerometers. It was observed that natural frequency changes were very small as cracks initiated and grew. However, the changes in quasi-static components of the frequency response functions, response in the anti-resonant region, and non-linear response could be used to good advantage to detect the presence of cracking in structures.

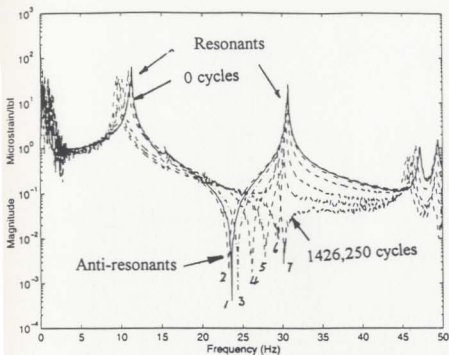
Based on the observations as described in this chapter, the effects of fatigue cracks on the static and dynamic response of the tubular T-joint structures can be summarized as below.

During the period of initiation and growth of small thumb-nail cracks, i.e. $10^4 - 10^5$ cycles, the static as well as the dynamic response at strain gauge locations some distance away from the crack(s) did not change appreciably. After the coalescence of some thumb-nail cracks to form a larger fatigue crack, typically with a surface crack length greater than 70 mm, the static strain began to drop dramatically with the increasing number of fatigue cycles and the changes in the dynamic response, viz., the increase in the magnitude of FRFs in the quasi-static region, and anti-resonant

shifts began to be noticeable. These FRF characteristics increased with increasing size of cracks or number of fatigue cycles.

When the fatigue crack grew into a large through-the-thickness crack, typically after 970,000 cycles, nonlinearity in FRF, in terms of subharmonic or superharmonic peaks became prominent. The occurrence of this non-linear feature appeared to be the warning sign of the presence of dangerously large cracks.

Through the entire crack growth process, however, the changes in resonant frequency remained rather small and those in damping ratio non-systematic.



Stage	Approximate crack size	
	Width (mm)	Depth (mm)
1	0	0
4	166	5.4
6	228	6.7
7	231	6.8

Figure 5.33: Strain frequency response functions at gauge 2, channel 6, for specimen 2 at 0, 350,000, 500,000, 800,000, 962,500,000, 1,120,000 and 1,426,250 fatigue cycles

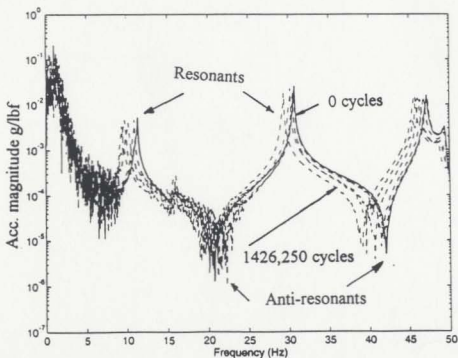


Figure 5.34: Acceleration frequency response functions at accelerometer 2 for specimen 2 at 0, 350,000, 500,000, 800,000, 962,500,000, 1,120,000 and 1,426,250 fatigue cycles

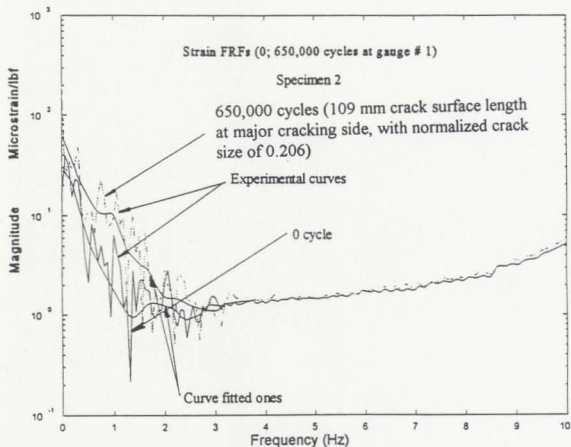


Figure 5.35: Strain FRF at gauge 1, channel 8, of specimen 2

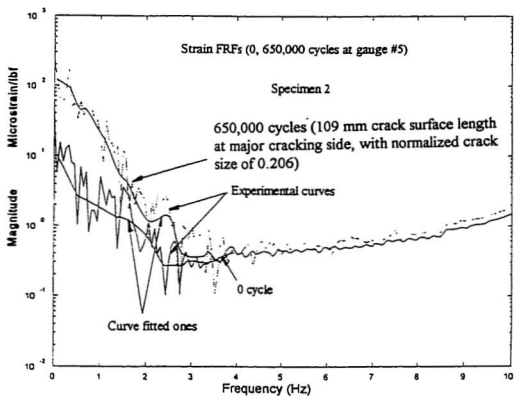
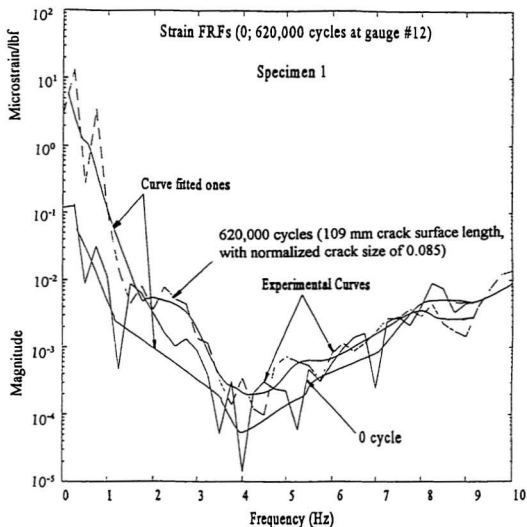


Figure 5.36: Strain FRF at gauge 5, channel 13, of specimen 2



Strain gauge located at a point farthest away from the two saddle points

Figure 5.37: Strain FRF at gauge 12, channel 33, of specimen 1

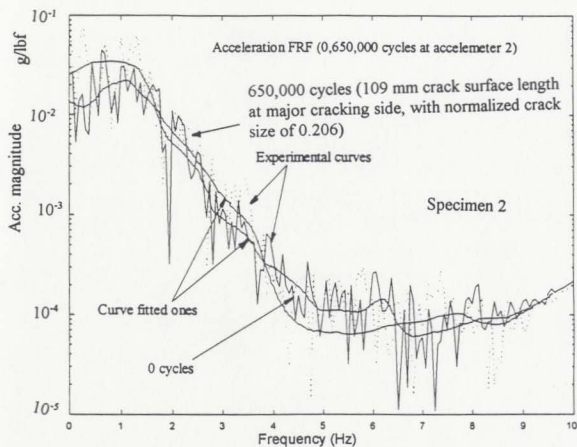


Figure 5.39: Acceleration frequency response functions at accelerometer #2 for specimen 2

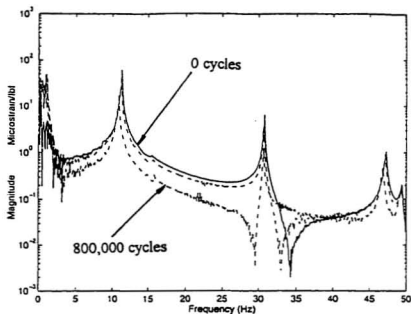


Figure 5.40: Strain FRF at gauge 6, channel 20, of specimen 2 at 0, 650,000, 800,000 cycles

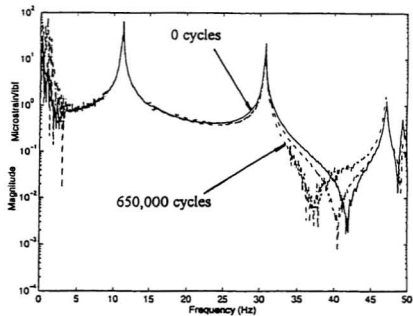


Figure 5.41: Strain FRF at gauge 3, channel 10, of specimen 2 at 0, 500,000, 650,000 cycles

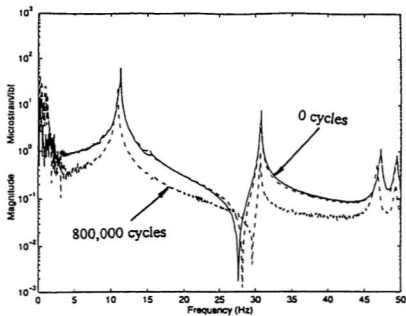


Figure 5.42: Strain FRF at gauge 1, channel 9, of specimen 2 at 0, 500,000, 800,000 cycles

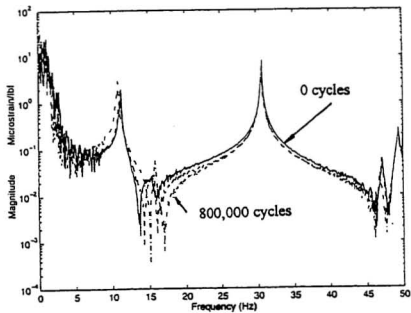


Figure 5.43: Strain FRF at gauge 8, channel 31, of specimen 2 at 0, 650,000, 800,000 cycles

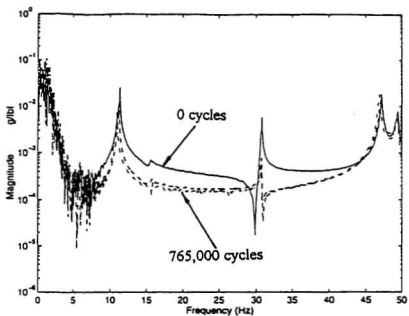


Figure 5.44: Acceleration frequency response functions at accelerometer #1, of specimen 3 at 0, 557,000, 765,000 cycles

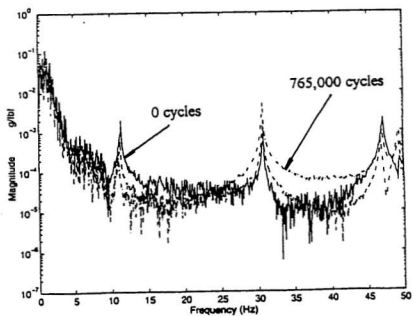


Figure 5.45: Acceleration frequency response functions at accelerometer #5, of specimen 3 at 0, 557,000, 765,000 cycles

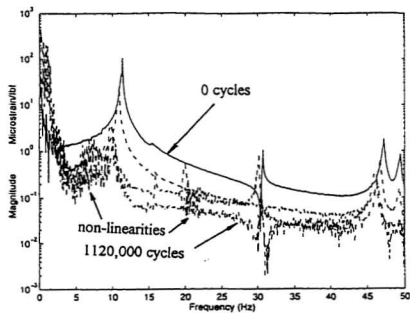


Figure 5.46: Strain FRF at gauge 1, channel 8, of specimen 2 at 0, 800,000, 962,000, 1120,000 cycles

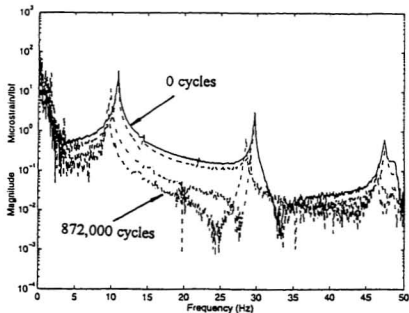


Figure 5.47: Strain FRF at gauge 4, channel 16, of specimen 3 at 0, 350,000, 765,000, 872,000 cycles

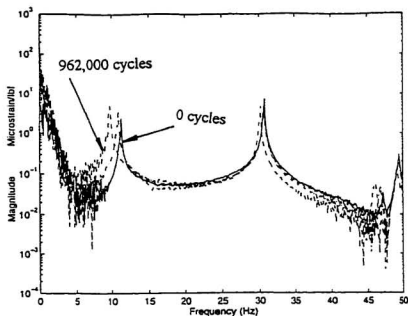


Figure 5.48: Strain FRF at gauge 9, channel 35, of specimen 2 at 0, 500,00, 800,000, 962,000 cycles

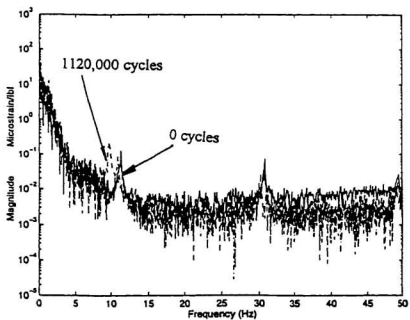


Figure 5.49: Strain FRF at gauge 15, channel 40, of specimen 2 at 0, 500,00, 800,000, 1120,000 cycles

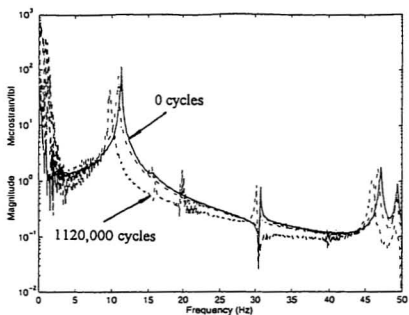


Figure 5.50: Strain FRF at gauge 10, channel 23, of specimen 2 at 0, 500,00, 800,000, 1120,000 cycles

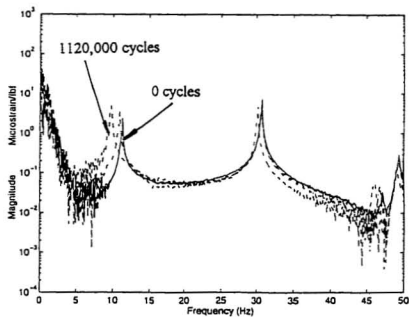


Figure 5.51: Strain FRF at gauge 16, channel 1, of specimen 2 at 0, 500,00, 800,000, 1120,000 cycles

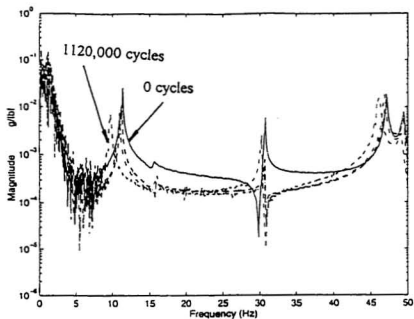


Figure 5.52: Acceleration frequency response functions at accelerometer #1, of specimen 2 at 0, 650,000, 800,000, 1120,000 cycles

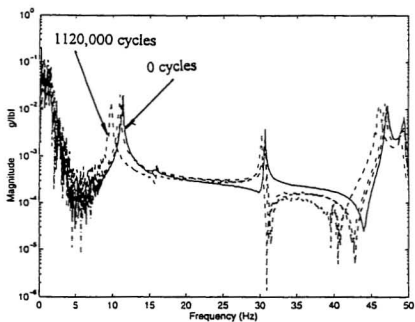


Figure 5.53: Acceleration frequency response functions at accelerometer #4, of specimen 2 at 0, 650,000, 800,000, 1120,000 cycles

Chapter 6

Results of Finite Element Analyses

6.1 Introduction

The displacement-based finite element method was used to model the structure and to carry out analyses for structural response. Correlation and comparison of the statical and dynamical finite element analysis results with those from experiments were made, using an iterative approach to update the finite element analysis results. The updated finite element model was utilized to provide supplemental modal properties, which were eventually used in the development of the reduced structural models in chapter 7.

The updated finite element model was also used for the prediction of cracked structural response and the estimation of the crack profile.

Since the test specimens were large and their dynamic behavior similar to asymmetrical shell structures, hundreds of strain gauges and/or accelerometers would be needed for the estimation of mode shapes from experiments. Therefore the updated finite element model results were used to obtain the correct mode shapes.

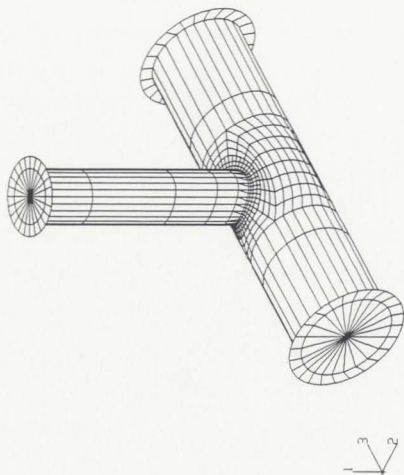


Figure 6.1: Finite element model of the tubular T-joint

6.2 Finite Element Model

6.2.1 Element Selection

According to the procedures given in section 3.3, a finite element model was assembled using S8R5 and STRI65 elements for the tubular T-joints as shown in Figure 6.1. S8R5 is an eight-noded doubly curved thin shallow shell element with reduced integration (Figure 3.2); each node of the S8R5 element has five degrees of freedom. STRI65 is a six-noded triangular thin shell element with the same number of degrees-of-freedom per node. S8R5 has four integration points while STRI65 has 3; reduced integration was used to form the elemental stiffness matrix. The mass matrix and distributed loading were integrated exactly. Reduced integration provided more accurate results and significantly reduced running time (ABAQUS, 1996).

The tubular T-joint was modeled mainly with S8R5 elements while the STRI65 elements were used during transition from one domain to the other; the accuracy of S8R5 element was reduced significantly when it was degenerated to a triangular element.

Line spring elements were used to simulate the part-through crack present on the shell surface, as shown in Figure 6.2. The line spring elements were located between the first and second rows of finite elements located on the chord; the first row represented the weld-plate region of the chord. The part-through crack was assumed to be semi-elliptical with different crack depths to generate various crack profiles. The crack depths were calculated with a separate FORTRAN program and incorporated into ABAQUS. The use of line spring elements for crack representation provided inexpensive calculations. Otherwise thousands of three dimensional crack tip elements had to be used around the crack front to model the sharp stress variation occurring around the weld toe region. The theory of line spring elements has been

described in the earlier Section 3.3.3. The procedure for computing the length of the line spring element is given in Section 6.3.

6.2.2 Simplifications

In the actual experimental tubular T-joint, salient dimensions such as thickness/diameter of the chord and brace were varying; this was inevitable because of the available manufacturing accuracy, tolerance, roundness, etc. It was not possible to make the theoretical model exactly the same as the experimental one. Moreover each test specimen was slightly different. Hence some simplifications became essential for the theoretical model.

The simplifications made for the finite element model could be summarized as:

- The material was assumed to be uniform and homogeneous;
- The thickness of the tubular T-joint (chord and brace) was assumed to be uniform;
- The diameters of the analytical models of the chord and brace were assumed to be constant, whereas the diameters for the actual experimental T-joint were varying slightly, depending on the manufacturing tolerance;
- The tubular T-joint was assumed to be symmetric;
- The stiffeners welded to the end plates of the chord were assumed to provide an end plate of variable thickness;
- The bolts which connected the end plates and the chord were not considered in the analysis; thus the end plates and the chord were assumed to be rigidly connected; and

- The cracks were assumed to be semi-elliptical in configuration.

It may also be noticed, from Figures 4.2 and 4.4, that the boundary conditions of the experimental specimens were quite complex and not simply supported as assumed in the theoretical model.

The simplifications given above reduced the size of the matrix so that it could be handled by the finite element procedure; it also ensured that the results obtained at the points of interest did not vary greatly from those obtained from a detailed analytical, finite element model.

6.2.3 Mesh Generation and Simulation of Boundary Conditions

In finite element analysis, element size and computation time are two of the most important factors. A small element size will directly result in more accurate results; however, this will also lead to a large number of degrees of freedom which may exceed the effective capacity of the computer. The computation time increases approximately as the square of the number of degrees-of-freedom. Hence, the mesh size cannot be too small.

In order to obtain a reasonable mesh size distribution that would give results with sufficient accuracy, the mesh had to be carefully sized and distributed especially for dynamic analysis. The dynamic analysis consisted of a large number of time steps and iterations and hence needed a much larger computer capacity than that needed for a static analysis.

In this investigation, the smaller mesh sizes were used for elements located around the weld toe where the hot spot was located and the crack development would also occur. The mesh sizes at other locations were relatively coarse, especially for locations where there were no stress concentrations or variations. Since the tubular T-joint was

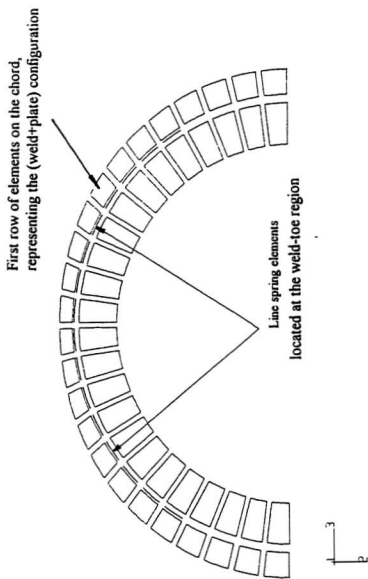


Figure 6.2 Line spring elements and the connected elements

a spatial structure, the inclusion angle of neighboring elements normally should not exceed 20° to prevent the element distortion. The mesh was developed first in a plane, with the intersection line between the chord and the brace mapped on the plane; a mapping procedure was then used to transform the whole plane mesh to the spatial configuration. In order to guarantee the symmetric configuration of the structure, half the model was generated first, and then mirrored to obtain the whole model. The finite element model had 944 elements, 3684 nodes and 21114 degrees of freedom plus Lagrangian multipliers; this resulted in a matrix size that had almost reached the limit of the available computer work station.

The supporting boundary conditions were applied to the central nodes of the two end plates that connected the chord to the base support. Due to the complexity of supporting boundaries including the base, the end support, connecting bolts, supporting steel base, etc., the boundary conditions were simplified and simulated in numerical analysis. The boundary conditions were basically taken to represent a simple support and additional modifications were made by providing stiff horizontal spring elements to simulate the z direction (axis of the chord) movement of the end support; no vertical movement was allowed at the end support.

The weld zone, present at the weld toe, was simulated by providing extra thickness to the intersecting row of chord elements present along the intersection line between chord and brace. The stiffener, welded to the end plate connecting the chord to the supporting base, was simulated by increasing the thickness of the end plate. The bolts connecting the end plate to the chord were all neglected and the connection modelled as an integral one. The top plate (Figure 4.2) which connected the actuator and the brace was simulated by increasing the thickness of the top plate that was connected to the brace.

6.2.4 Length of Line Spring Elements

The length of each line spring element was determined according to the three dimensional intersection length present at the weld toe.

The parametric equation of the intersection line was derived as follows:

$$\begin{aligned}x &= R \cos\phi = R \cos[\arcsin(\frac{r}{R} \sin\alpha)] = \psi_x(\alpha) \\y &= r \sin\alpha = R \sin\phi = \psi_y(\alpha) \\z &= r \cos\alpha = \psi_z(\alpha)\end{aligned}\quad (6.1)$$

where ϕ was the angle between the radius and the x axis of the cord (along the weld toe intersection line) and α the angle between the radius and z axis on the brace. The small curved length between the angles α_i and α_{i+1} could be expressed as

$$ds = \sqrt{(dx)^2 + (dy)^2 + (dz)^2} = \sqrt{\psi_x'^2(\alpha) + \psi_y'^2(\alpha) + \psi_z'^2(\alpha)} d\alpha$$

where $\psi_x'(\alpha)$, $\psi_y'(\alpha)$, $\psi_z'(\alpha)$ were the derivatives with respect to α .

$$\begin{aligned}\psi_x'(\alpha) &= -\frac{r^2 \sin(\alpha)\cos(\alpha)}{R\sqrt{(1 - \frac{r^2 \sin^2(\alpha)}{R^2})}} \\ \psi_y'(\alpha) &= r \cos(\alpha) \\ \psi_z'(\alpha) &= -r \sin(\alpha)\end{aligned}\quad (6.2)$$

The length of the intersection line or line spring length between angles α_i to α_{i+1} could be obtained as

$$s = \int_{\alpha_i}^{\alpha_{i+1}} \sqrt{\psi_x'^2(\alpha) + \psi_y'^2(\alpha) + \psi_z'^2(\alpha)} d\alpha \quad (6.3)$$

$$\begin{aligned}
&= \int_{\alpha_i}^{\alpha_{i+1}} \sqrt{\frac{r^4 \sin^2(\alpha) \cos^2(\alpha)}{R^2(1 - \frac{r^2 \sin^2(\alpha)}{R^2})} + r^2 \cos^2(\alpha) + r^2 \sin^2(\alpha)} d\alpha \\
&= \int_{\alpha_i}^{\alpha_{i+1}} \sqrt{\frac{r^2(R^2 - r^2 + 2r^2 \cos^2(\alpha) - r^2 \cos^4(\alpha))}{R^2 - r^2 + r^2 \cos^2(\alpha)}} d\alpha \\
&= \int_{\alpha_i}^{\alpha_{i+1}} f(\alpha) d\alpha
\end{aligned}$$

The integral was computed using numerical trapezoidal integration rule. The integration equation was

$$s = \frac{\alpha_{i+1} - \alpha_i}{2n} [f(\alpha_{i,0}) + 2f(\alpha_{i,1}) + \dots + 2f(\alpha_{i,n-1}) + f(\alpha_{i,n})] \quad (6.4)$$

The interval $[\alpha_i, \alpha_{i+1}]$ was divided into n equal sections, i.e., $(j=0, \dots, n)$. $\alpha_{i,j}$ represented the integration points of the numerical procedure with $\alpha_{i,0} = \alpha_i$, and $\alpha_{i,n} = \alpha_{i+1}$. $f(\alpha_{i,j})$ was the integrand.

6.3 Matching of Finite Element Results to Experimental Results

The matching of the results of the finite element model with the experimental model was carried out for static principal stresses, natural frequencies and strain response functions. The procedure involved adjusting features such as the thickness of the elements used to describe the chord and brace in the finite element model so that the outputs from the model describing the static and dynamic response of the crack-free T-joint, were almost the same as the observed experimental response. This guaranteed an exact numerical description of the crack-free specimen, and assured that any changes predicted following the insertion of the crack could only be due to the crack. The matchings were done for the crack-free specimen (# 3) and on the cracked specimen at crack stage one (350,000 cycles), stage two (457,500 cycles)

and stage three (565,000 cycles). Since the line spring element formation was based on the theory of part through cracks, no reasonable results would be obtained when the crack was already through. Moreover the line spring element would not provide useful results for crack depths less than 2 % or greater than 95 % of the wall thickness (ABAQUS, 1994). Hence no numerical modelling was done beyond these fatigue cycles, since the crack had broken through the thickness at the next stage of fatigue cycling (772,500).

The results of the static hot spot principal stresses, at gauge locations 1 and 4 (from the finite element model), were compared with the experimental results of specimen 3 and listed in Table 6.1. Generally in all cases the experimental results and the finite element results were within 5%. Since the line spring elements would not give accurate results when the crack depth approached the wall thickness, the error tended to increase. However, a good match between theoretical and experimental results could be observed from Table 6.1.

The matching of natural frequencies between experimental results for crack-free specimens and the finite element model is given in Table 6.2 – 6.4. Good match was obtained for all three specimens for this global parameter. Very good matching was obtained for the first mode. The maximum error of 6.77 % was observed for the third frequency, which was very close to the fourth. Among the frequencies, the finite element model frequencies 5, 7 – 11, 15 and 17 were not sensed or excited in the experimental model. The generalized masses of the frequencies 7 – 11 were very small, being 10^{-3} times smaller than the others. The frequencies obtained for the cracked finite element model are listed in Tables 6.5 – 6.7; while the experimental values obtained for the cracked tubular joints are given in Tables 5.19 to 5.29. The computed frequency change for the 1st mode, between the crack-free and the cracked specimens (at 565,000 cycles) was only 2 %. For comparison, the frequency change observed

Table 6.1: Static Principal Stresses for Finite Element Model and Experimental Specimen 3

Cycles		Gauge 1		Gauge 4	
		σ_1 (psi)	σ_2 (psi)	σ_1 (psi)	σ_2 (psi)
0	Expt.	31056	14774	15639	10183
	FEM	31341	14175	16404	9924
	Error	0.91%	-4.23%	4.66%	-2.61%
350,000	Expt.	16704	10299	9655	8200
	FEM	16050	11094	10054	7846
	Error	-4.07%	7.17%	3.97%	-4.51%
457,500	Expt.	9063	5172	7243	5854
	FEM	10337	4869	7210	3714
	Error	12.32%	-6.22%	-0.46%	-3.77%
565,000	Expt.	10926	1344	8172	-841
	FEM	14777	1383	9760	-847.8
	Error	26%	2.82%	16.28%	0.92%

experimentally for this mode after 565,500 cycles was 5 %. Clearly, the agreement between theory and experiment was extremely good. The natural frequency drop ratio may not be exactly the same since: (a) the finite element mesh could not exactly model the real physical model of the tubular T-joint and supporting conditions; and (b) crack opening and closing were involved in the experimental model and only the open crack could be modeled in the finite element model, using the available provisions of the ABAQUS program.

The matched frequency response functions at the locations of weld toe gauges 1 and 4 and center line gauge 7, for specimen 3, were plotted for the following states: (i) no crack; (ii) first monitored crack; (iii) second monitored crack; and (iv) third monitored crack in Figures 6.3 – 6.14. Good match was obtained between the experimental and theoretical results as may be seen from these figures.

Even though the experimental data indicated the presence of a natural frequency around 29.45 Hz (along with the computed eigenvalues), the analytically computed frequency response function showed no such resonance (Figure 6.3 to 6.14) at that frequency. This was due to the fact that the gauge was located along the axis of symmetry (y -axis) while the bending deformation for mode 2 took place along the z -axis. Whereas the experimental model indicated the presence of the crack even from the "no crack" due to the inherent asymmetry of the physical model in the xz plane. Even during the cracking stages, the analytically computed frequency response functions did not indicate the presence of a second frequency due to the symmetric nature of the crack configuration about the global y -axis and the location of the sensed gauge along the axis of symmetry passing through the xy -plane.

It is seen that the experimental frequencies 3 and 4 are closely spaced while the analytical frequencies are separated (with third having +ve error and the fourth a -ve error). Once again this could be explained in terms of the asymmetric configu-

Table 6.2: Natural Frequencies of Experimental Specimens and Finite Element Model

Natural Frequencies							
Specimen	Method	1st	2nd	3rd	4th	5th	6th
	FEM	11.09	29.45	44.05	50.56	110.03	169.38
3	Expt.	10.91	29.72	47.25	48.69	—	162.33
	Error	-1.65%	0.91%	6.77%	-3.48%	—	-4.34%
2	Expt.	11.35	30.74	47.25	49.38	—	165.70
	Error	2.29%	4.2%	6.77%	-2.39%	—	-2.22%
1	Expt.	11.22	30.64	46.50	47.66	—	167.89
	Error	1.16%	3.88%	5.27%	6.08%	—	-0.89%

Table 6.3: Natural Frequencies of Experimental Specimens and Finite Element Model

Natural Frequencies							
Specimen	Method	7th	8th	9th	10th	11th	12th
	FEM	192.69	192.69	195.82	195.82	214.87	283.53
3	Expt.	—	—	—	—	—	272.02
	Error	—	—	—	—	—	-4.23%
2	Expt.	—	—	—	—	—	279.38
	Error	—	—	—	—	—	-1.49%
1	Expt.	—	—	—	—	—	287.43
	Error	—	—	—	—	—	1.36%

Table 6.4: Natural Frequencies of Experimental Specimens and Finite Element Model

Natural Frequencies							
Specimen		13th	14th	15th	16th	17th	18th
	FEM	289.88	305.54	310.35	313.37	340.89	348.84
3	Expt.	296.32	301.29	—	320.25	—	354.09
	Error	2.17%	-1.41%	—	2.15%	—	1.48%
2	Expt.	293.66	298.02	—	323.79	335.84	356.03
	Error	1.29%	-2.52%	—	3.22%	-1.5%	2.02%
1	Expt.	299.31	303.01	—	—	330.66	340.22
	Error	3.15%	-0.83%	—	—	-3.09%	-2.47%

Table 6.5: Natural Frequencies Obtained from Finite Element Model

Natural Frequencies							
Crack stage	Corresponding experimental cycles	1st	2nd	3rd	4th	5th	6th
0	0	11.09	29.45	44.05	50.56	110.03	169.38
1	350,000	11.07	29.45	43.51	50.53	109.50	169.04
2	457,500	11.04	29.44	42.70	50.47	108.74	168.54
3	565,000	10.96	29.41	40.84	50.18	107.02	167.51

Table 6.6: Natural Frequencies Obtained from Finite Element Model

Natural Frequencies							
Crack stage	Corresponding experimental cycles	7th	8th	9th	10th	11th	12th
0	0	192.69	192.69	195.82	195.82	214.87	283.53
1	350,000	192.69	192.69	195.82	195.82	214.29	283.07
2	457,500	192.69	192.69	195.82	195.82	213.45	282.37
3	565,000	192.69	192.69	195.82	195.82	211.62	280.65

Table 6.7: Natural Frequencies Obtained from Finite Element Model

Natural Frequencies							
Crack stage	Corresponding experimental cycles	13th	14th	15th	16th	17th	18th
0	0	289.88	305.54	310.35	313.37	340.89	348.84
1	350,000	289.86	304.90	310.34	313.28	340.86	348.84
2	457,500	289.84	304.00	310.33	313.18	340.81	348.83
3	565,000	289.83	302.22	310.26	313.08	340.49	348.80

ration of the tubular T-joint associated with fabrication errors and elasticity of the supporting bracket. While the amplitudes for crack-free specimens matched closely, the frequencies of the analytical and experimental models were well separated; unless the asymmetric configuration built into the experimental model can also be modeled by the analytical model, it would be difficult to match these frequencies. Nevertheless the errors were small and hence a closer matching of these frequencies was not attempted.

While the match between the experimentally observed and computed values of the frequency and the amplitude of the first resonance was very good, the differences were larger for higher order resonances. The greatest difference was in the frequency value, which for the third resonant was about 7 %. The match in the resonant free region (15 to 40 Hz) was extremely good (see Figures 6.3, 6.7 and 6.11 for examples). Since the order of difference between the amplitudes of first and higher frequencies was nearly of an order of 10^2 , the matching of higher frequencies would require a much larger number of smaller-sized finite elements that would match exactly the positions of the strain gauges; this was found to be impossible due to the available computer disk space.

The near-zero frequency amplitudes of the frequency response function of the crack-free specimens, shown in Figures 6.3, 6.7 and 6.11, are believed to be due to the foundation compliance which would produce resonance at very low frequencies. It could be observed that as the crack grew, the near-zero amplitudes also increased (or decreased at gauge 7, since the direction of strains were reversed at that point) due to the interaction between "opening and closing" frequencies, setting up lower frequencies due to energy exchange between the two close frequencies, producing a phenomenon similar to "beating". Clear evidence of this has been presented in Chapter 5, section 5.5.1.

The comparison of the predicted crack profiles of the finite element model (obtained from the matching of static strain and used in the analytical modeling for FRF response) and experimental specimen 3, at the three crack stages, are listed in Table 6.8. The predicted crack profiles of the finite element model are shown in Figure 6.15.

It would be desirable to use the results of modal testing to predict crack geometry; that is to be able to predict crack surface length and crack depth. With this in mind it was decided to model the dynamic and static response of the cracked structures using a finite element model in which an assumed crack had been inserted. The assumed cracks were defined in terms of the experimentally measured lengths of the cracks, as observed on the specimen's free surface, and the crack depths, as revealed by ink staining and beach marking of the fracture surfaces. Essentially, these measurements defined the aspect ratios of the observed semi-elliptical cracks.

Figure 6.15 provides a comparison of the experimentally observed crack profiles, and the assumed semi-elliptical crack geometries that were built into the finite element model. The upper figure in Figure 6.15, shows the experimentally observed crack profiles as a function of the fatigue cycles applied, and the lower figure shows the correct crack geometries assumed for the finite element model. A very good correlation exists between the computed and measured values.

In carrying out the matching procedure, finite element calculations were first carried out to compute the static and dynamic responses of the cracked structure and the results were compared with the experimentally observed response. Further refinements of the model, in terms of the assumed crack geometries (by changing the depth and width of the assumed semi-elliptical crack), were made until a close agreement was obtained between calculated and observed response. Table 6.8 compares the experimentally observed crack geometries with the geometries assumed in the final

version of the FEM model, after several stages of iteration. The table also shows the apparent errors, or differences between the observed and assumed crack shapes; the maximum error obtained was +5.47 % in crack width at the second crack stage.

6.4 Mode Shapes

Mode shapes were obtained from the finite model since it was not possible to obtain them from the experimental specimens; this would have required a large number of strain gauges located all over the tubular T-joint. The mode shapes are shown in Figures 6.16 – 6.21.

It may be seen from Figures 6.16 to 6.21 that the predicted modal shapes for these tubular joints were as follows.

1. The first mode was the cantilever bending mode of the brace rotating about axis z (Figure 6.16 (a));
2. The second mode was the cantilever bending of the brace rotating about axis y with a shortening of the chord (Figure 6.16 (b));
3. The third mode was a combination mode of the brace bending (along the y -axis) and local bending of the chord (Figure 6.17 (a));
4. The fourth mode was once again, the brace cantilever bending mode (along the z -axis) with some z -directional shortening of chord (Figure 6.17 (b));
5. Mode 5 was the first bending mode of the chord (Figure 6.18 (a));
6. The sixth mode was mainly the chord bulging mode (Figure 6.18 (b));
7. The seventh, eighth, ninth and tenth modes were two pairs of double modes which were similar to one another with motion at two different opposite loca-

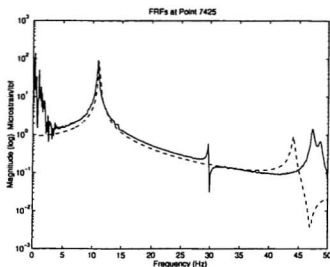


Figure 6.3: Strain FRFs obtained from FE model (- -) and crack free experimental model (-): Gauge 1 of specimen 3

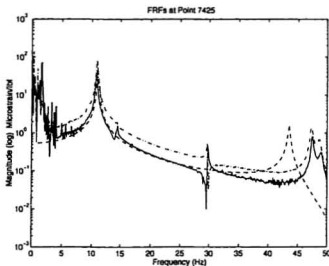


Figure 6.4: Strain FRFs obtained from the FE model (- -) and the experimental model (-) at the first crack stage: Gauge 1 of specimen 3. The experimental data for the crack-free specimen are indicated by (- .)

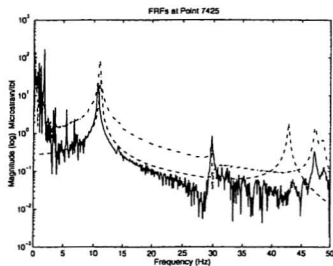


Figure 6.5: Strain FRFs obtained from the FE model (- -) and the experimental model (-) at second crack stage: Gauge 1 of specimen 3. The experimental data for the crack-free specimen are indicated by (-.)

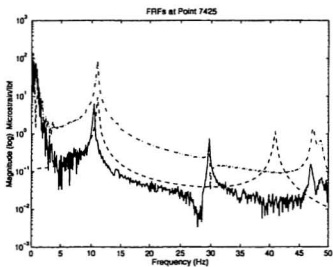


Figure 6.6: Strain FRFs obtained from the FE model (- -) and the experimental model (-) at third crack stage: Gauge 1 of specimen 3. The experimental data for the crack-free specimen are indicated by (-.)

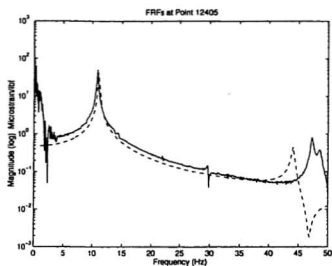


Figure 6.7: Strain FRFs obtained from FE model (- -) and crack-free experimental model (-): Gauge 4 of specimen 3

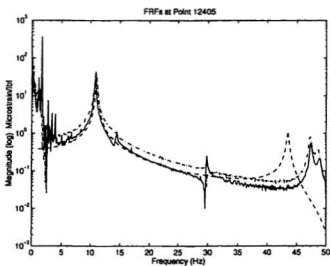


Figure 6.8: Strain FRFs obtained from FE model (- -) and the experimental model (-) at first crack stage: Gauge 4 of specimen 3. The experimental data for the crack-free specimen are indicated by (-).

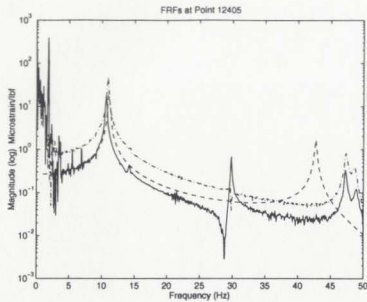


Figure 6.9: Strain FRFs obtained from FE model (- -) and the experimental model (-) at second crack stage: Gauge 4 of specimen 3. The experimental data for the crack-free specimen are indicated by (-.)

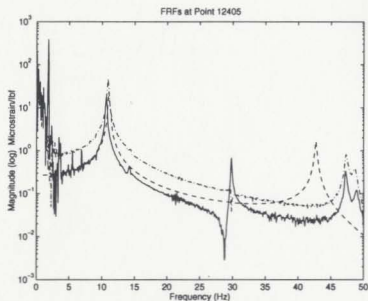


Figure 6.10: Strain FRFs obtained from FE model (- -), experimental model (-) at third crack stage: Gauge 4 of specimen 3. The experimental data for the crack-free specimen are indicated by (-.)

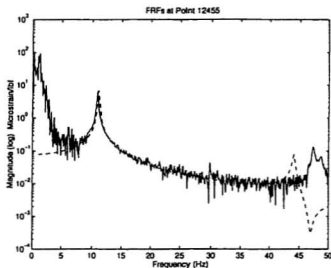


Figure 6.11: Strain FRFs obtained from FE model (- -) and crack-free experimental model (-): Gauge 7 of specimen 3

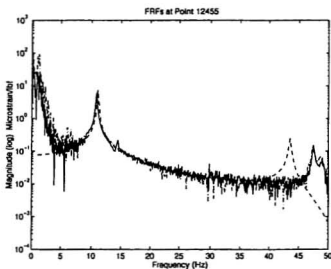


Figure 6.12: Strain FRFs obtained from FE model (- -), experimental model (-) at first crack stage: Gauge 7 of specimen 3. The experimental data for the crack-free specimen are indicated by (-.)

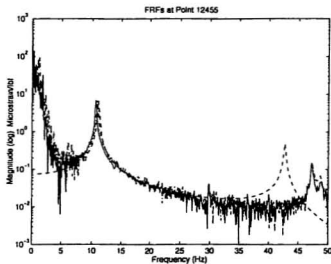


Figure 6.13: Strain FRFs obtained from FE model (- -), experimental model (-) at second crack stage: Gauge 7 for specimen 3. The experimental data for the crack-free specimen are indicated by (-.)

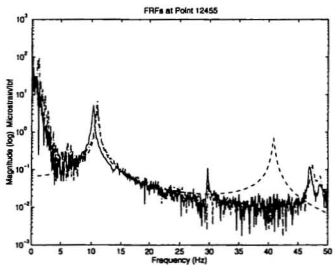


Figure 6.14: Strain FRFs obtained from FE model (- -), experimental model (-) at third crack stage: Gauge 7 of specimen 3. The experimental data for the crack-free specimen are indicated by (-.)

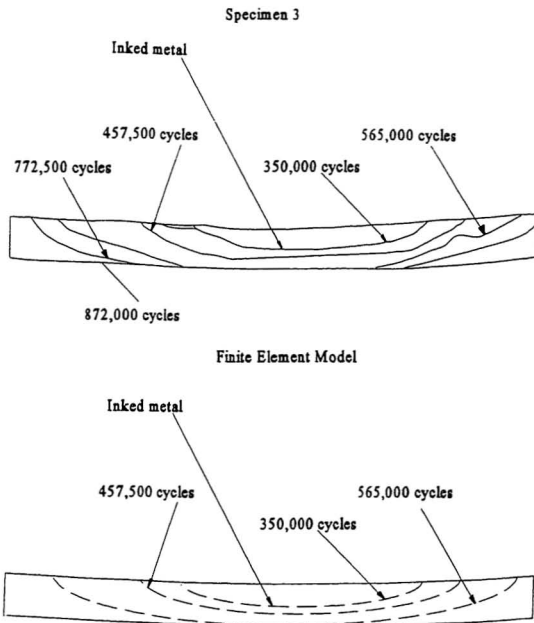


Figure 6.15: Crack profiles from finite element model compared to specimen 3

- tions. Both the double modes had very small generalized masses and unchanged natural frequencies during cracking (Figure 6.19 (a), (b), (c) and (d));
8. Mode eleven was a local mode that produced a bulging of the chord (Figure 6.20 (a));
 9. Modes 12 and 13 were similar producing primarily an upward or sideward bending of the chord (Figure 6.20 (b) and (c));
 10. Mode fourteen was an overall bulging mode of the chord (Figure 6.20 (c));
 11. Modes 15 and 16 were brace local modes (Figure 6.21 (a) and (b));
 12. Modes seventeen and eighteen were higher order bending modes of chord; while mode seventeen could not be properly sensed due its weak response, mode eighteen was sensed well by its strong response (Figure 6.21 (c) and (d)).

6.5 Conclusions

In this chapter, finite element modeling was carried out to correlate the analytical and experimental results. The finite element model was generated using eight and six noded doubly curved, thin, shallow shell elements for the structure and six noded line spring elements for crack. Some simplifications were applied to the finite element model to make the matrix size smaller and amenable to computation.

A good match was obtained between the finite element predictions and experimental data: (1) the static principal stresses at the hot spot locations and the near hot spot were matched; (2) the natural frequencies were also matched with a maximum error of 6.77% for the third mode of the uncracked tubular T-joint; (3) frequency response functions were matched at salient points. The matching validated both the experimental method and the experimental results, and particularly so for the

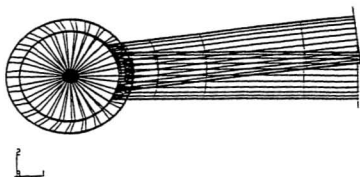
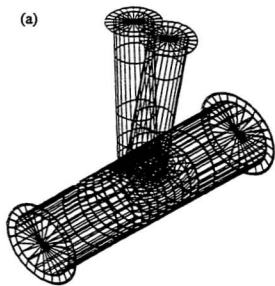
uncracked specimens. It also provides some degree of assurance that modal testing results from the cracked specimens were valid. Frequency shifts were observed in the resonant peaks of the cracked specimens, and these were within 2 to 6 % of the theoretically predicted shifts.

Parameters such as mode shapes which couldn't be obtained from experiments were obtained from the analysis results. The dynamic behavior of the tubular T-joint became more explicit by observing these mode shapes. Crack profiles (width, depth and locations) were determined experimentally and built into the finite element model. The FE model for the cracked structure was then used to predict the static and dynamic responses of the cracked structure and excellent agreement was obtained with the experimentally measured static and dynamic responses.

Table 6.8: Crack Profiles Predicted by Finite Element Model

Crack Stage	Experimental Cycles	Means	Crack Width	Crack Depth
1	350,000	Expt.	72 mm	3.2 mm
		FEM	70.18 mm	3.2 mm
		Error	2.53 %	0
2	457,500	Expt.	93 mm	5.1 mm
		FEM	87.91 mm	5.3 mm
		Error	5.47 %	-3.92 %
3	565,000	Expt.	137 mm	6.7 mm
		FEM	141.67 mm	6.6 mm
		Error	-3.41 %	-1.54 %

(a)



Isometric view of mode 2

Front view of mode 2

(b)

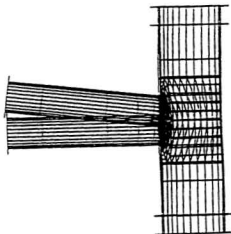
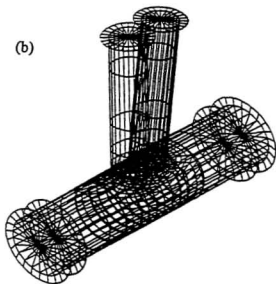
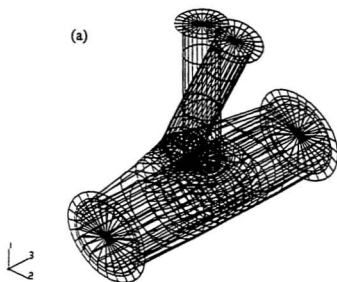
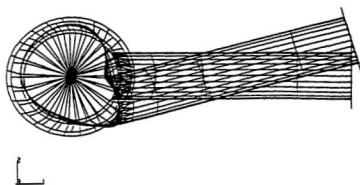


Figure 6.16: (a) Mode shapes 1 and (b) 2 of the tubular T-joint

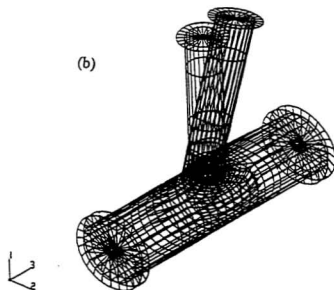
Isometric view of mode 3



Side view of mode 3



Isometric view of mode 4



Front view of mode 4

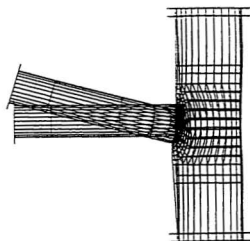
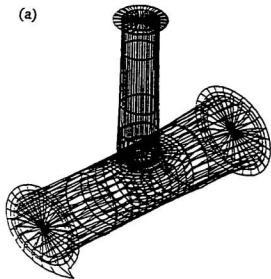


Figure 6.17: (a) Mode shapes 3 and (b) 4 of the tubular T-joint

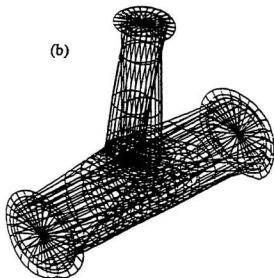
Mode 7

(a)



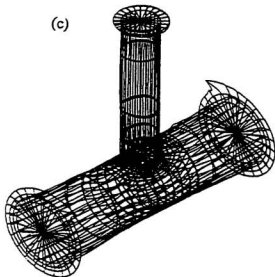
Mode 8

(b)



Mode 9

(c)



Mode 10

(d)

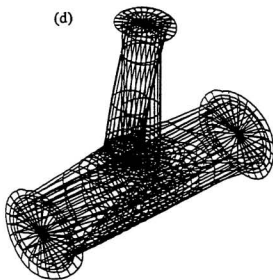


Figure 6.19: (a) Mode shapes 7, (b) 8, (c) 9 and (d) 10 of the tubular T-joint

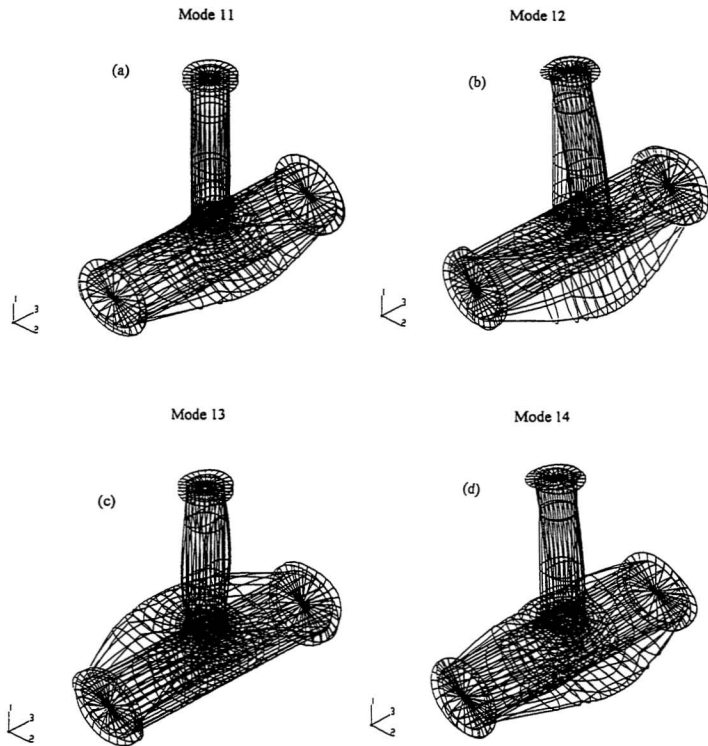
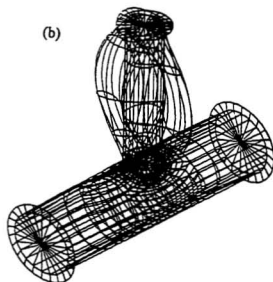
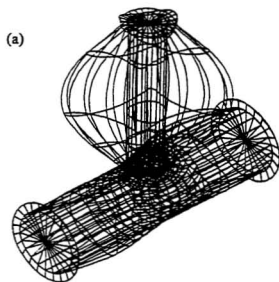
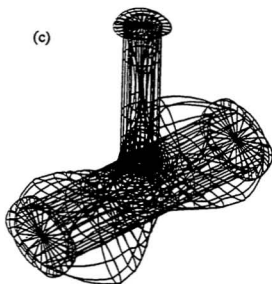


Figure 6.20: (a) Mode shapes 11, (b) 12, (c) 13 and (d) 14 of the tubular T-joint



Mode 17



Mode 18

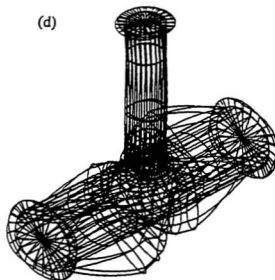


Figure 6.21: (a) Mode shapes 15, (b) 16, (c) 17 and (d) 18 of the tubular T-joint

Chapter 7

Response of a Structure With an Opening and Closing Crack

7.1 Introduction

As illustrated in Chapter 5 thumb-nail cracks initiate in these tubular T-joints as a result of the fatigue cycling. Their early stages of growth involve their progressive advance through the thickness of the tubular joint, while the cracks exist as discrete and independent discontinuities, separated from each other by ligaments of crack-free material. Eventually these cracks coalesce to form single cracks of significant length. The process of crack initiation and growth involves reversed plastic straining of the metal at regions of macroscopic stress concentration and also at microstructural discontinuities such as inclusions, shrinkage induced micro-voids and grain boundaries, in the fusion zone and heat affected zone of the T-joint welds. This reversed plastic straining occurs as a result of the opening and closing of the crack, or cracks, during the load increasing and load decreasing portions of the fatigue cycle.

Just as cracks open and close during fatigue cycling, they also open and close during vibration testing. Here the main driving force for crack opening and closing is not the applied force from the exciter, but it is the inertia forces that are excited by the tubular T-joints during resonance. This leads to a non-linear dynamic response

due to the continuously varying stiffness at the crack location.

A mathematical model for this structure with continuously changing stiffness was developed in this study. The model is equally applicable to the fatigue and vibration cases. This mathematical model was then applied to a two-degrees-of-freedom system, extracted from the combination of experimental (for specimen 3) and finite element results of the tubular T-joint. The results of this study are presented in this chapter.

7.2 Response of a Structure Containing an Opening and Closing Crack

As mentioned in the section "Fatigue and Fracture Mechanics", observations of the phenomena of fatigue-crack opening and closing have been well documented. Without losing generality, a typical load-displacement curve is shown in Figure 3.6a. To understand the influence of crack opening and closing on the vibration response of a structure containing a fatigue crack (e.g., during modal testing in the present case), this non-linear load-displacement behavior deserves some further discussion.

First of all, it should be understood that under small scale conditions (which means that the entire structure behaves predominantly as an elastic body except that at the crack tip a small size plastic zone exists) the nonlinear behavior shown in Figure 3.6b is not caused by change in the material's property such as modulus, but rather change in the flexibility (or stiffness) of the structure as the crack opens and closes during fatigue loading. The resulting non-linearity in the load-displacement relation can be easily explained using LEFM.

It is assumed that at the maximum load the crack is fully open, which must be true because otherwise fatigue crack growth would be dormant. The linear portion above P_{op} (crack opening load) has a constant slope which represents the stiffness of the structure or specimen containing a visible fatigue crack of length a . As the load

drops below P_{op} , partial crack closure occurs by premature contact of either plasticity humps, roughness asperities or corrosion debris along the crack wake. Then, pressure will be transmitted through the contacting points such that the structure or specimen behaves as if it contained a smaller crack (we notice that the stiffness,

$$k = dP/du$$

increases as the load decreases). The closed crack is by no means as intact as the pristine material. But, as far as its mechanical behavior is concerned, a one-to-one correspondence can be established between the instantaneous elastic compliance (or inversely, stiffness) and the instantaneous crack size as

$$k(t) = k[a(t)].$$

Indeed, such relationships are widely used in fatigue crack growth experiments to monitor crack growth and to evaluate the effect of crack closure on crack propagation (Saxena and Hudak, 1978). Generally described as the non-linear load-displacement behavior, it can be imagined that a fatigue crack opens and closes periodically during fatigue loading, or any repeated loading for that matter, which causes a periodical change in the stiffness of the structure or specimen as a function of time, i.e.,

$$k = k(t)$$

At this point, it should be noted that it is not appropriate to express the stiffness as a function of displacement,

$$k = dP/du = k(u)$$

Although such a relationship could be drawn mathematically from the plot, Figure 3.6a, as it might seem plausible, it does not truly reflect the physics of crack closure,

but rather suggests some kind of non-linear constitutive behavior of the material, which is obviously contrary to LEFM.

In summary of the above, the non-linear behavior in Figure 3.6a should reflect the change in the stiffness of the specimen as the crack opens and closes during fatigue loading. Having realized that, we shall concentrate on deriving the profile of the variation of k as a function of time.

For a theoretical crack which has perfectly flat surfaces, the specimen has two limiting values: the upper limit corresponds to the fully-closed state and the lower limit corresponds to the fully-open state of the crack. Then, ideally, the variation of the stiffness has a square wave form. However, for a real fatigue crack as represented by the load-displacement curve in Figure 7.1, the variation of $k(t)$ can have quite complex wave forms, depending on the amplitude of the exciting force and the load ratio. Figure 7.1 shows some possible wave forms of $k(t)$, all presumably have the same frequency as that of the exciting force, $F = F_0 e^{i\omega t}$. Taking crack closure into consideration, a sine or cosine wave form of $k(t)$ can be assumed for the real structure containing a fatigue crack in a modal test. This profile is a more realistic representation than the square wave and yet is mathematically manageable. It can be affirmed that the approximation of the peak/valley values for a fully closed/open crack will not make a noticeable difference in a lumped mass model because the overall stiffness of the structure and its mass are not significantly affected by the presence of a fatigue crack well below its fracture-limit, as evidenced by the insignificant shift in the resonance frequency of the structure(s) reported in this study and in the literature. The use of the lumped mass model, as illustrated later in the chapter, is to simulate the non-linear or beating response of a fatigue crack by introducing a time-variant stiffness into the Mathieu-Hill equation form. Hence in the further analysis carried out in this chapter, the stiffness of the structure is modelled to vary continuously

with time in a cosine form, superposed over a constant value.

7.3 Continuously Opening and Closing Crack Model

When a cracked structure is subjected to a cyclic load, the crack opens gradually during one half of the load cycle and then closes gradually during the other half of the cycle. A similar, periodical opening and closing of the crack, occurs during the vibration of a single degree of freedom system, and may be modeled by a stiffness change as

$$k(t) = k_0 + k_{\Delta c}(1 + \cos \omega_1 t) = k_1 + k_2(t) \quad (7.1)$$

where ω_1 is the crack breathing frequency (excitation frequency), $k_1 = k_0$ is the stiffness of the structure when the crack is fully open, $k_{\Delta c} = \frac{1}{2}(k_c - k_0)$, and k_c is the stiffness when the crack is closed. Also

$$k_2(t) = k_{\Delta c}(1 + \cos \omega_1 t) \quad (7.2)$$

It may be seen from Eqn. 7.2, that when $\omega_1 t = 2l\pi$ ($l = 1, \dots, m$, is any integer number), then $k_2(2l\pi/\omega_1) = k_c - k_0$. At this time the crack is completely closed. When $\omega_1 t = (2l-1)\pi$ ($l = 1, \dots, m$, is any integer number), then $k_2((2l-1)\pi/\omega_1) = 0$ and the crack is completely open. Otherwise the crack is in the transitional stage.

This model treats the structural stiffness due to crack opening and closing as a continuous function, i.e., the structure is gradually changing its local stiffness properties during the crack opening and closing at a rate of ω_1 . The coefficients k_0 and k_c are determined from the stiffness properties of the structure when the crack is completely open and completely closed, respectively. When the crack is completely closed, the structure acts as one without a crack, and the stiffness k_c is determined. When the crack is completely open the stiffness k_0 is determined using the principles

of fracture mechanics.

The equation of motion for the forced vibration of undamped and damped single-degree-of-freedom systems can be expressed respectively, as:

$$m\ddot{u} + [k_0 + k_{\Delta c}(1 + \cos \omega_1 t)]u = f \quad (7.3)$$

$$m\ddot{u} + c\dot{u} + [k_0 + k_{\Delta c}(1 + \cos \omega_1 t)]u = f \quad (7.4)$$

where f is the exciting force.

Equations (7.3) and (7.4) are of the Mathieu-Hill form. Moreover the application of the above "opening and closing" crack procedure to multi-degree-of-freedom systems raises up other issues (such as phase coherence between input and output, application of model analysis procedure, etc.) besides stability. The modal decoupling procedure has to be applied judiciously to the stable solution regions.

7.4 Establishment of a Two-Degrees-of-Freedom Model of a Tubular T-Joint with "Opening and Closing" Crack

Without losing generality, assume the system to have proportional damping. The equation of motion of a multi-degree of freedom can be expressed as;

$$[M]\{\ddot{u}\} + [C]\{\dot{u}\} + [K]\{u\} = \{f\} \quad (7.5)$$

Let

$$\{u\} = [\psi]\{q\} \quad (7.6)$$

where $[\psi]$ are the eigenvectors and $\{q\}$ the modal coordinates.

Substitution of Equation 7.6 into Equation 7.5, yields;

$$[M][\psi]\{\ddot{q}\} + [C][\psi]\{\dot{q}\} + [K][\psi]\{q\} = \{f\} \quad (7.7)$$

Multiplying the left hand side by $[\psi]^T$ yields;

$$[\psi]^T[M][\psi]\{\ddot{q}\} + [\psi]^T[C][\psi]\{\dot{q}\} + [\psi]^T[K][\psi]\{q\} = [\psi]^T\{f\} \quad (7.8)$$

According to the orthogonality of eigenvectors;

$$[\psi]^T[M][\psi] = [M_r]$$

$$[\psi]^T[K][\psi] = [K_r]$$

$$[\psi]^T[C][\psi] = [C_r]$$

where $[M_r]$, $[K_r]$ and $[C_r]$ are diagonal modal mass, stiffness, and damping matrix, respectively.

Let

$$\{q\} = [M_r]^{-\frac{1}{2}}\{r\}$$

where r is the mass normalized modal coordinate; substituting the above into Eqn. 7.8, one obtains;

$$[\psi]^T[M][\psi][M_r]^{-\frac{1}{2}}\{\ddot{r}\} + [\psi]^T[C][\psi][M_r]^{-\frac{1}{2}}\{\dot{r}\} + [\psi]^T[K][\psi][M_r]^{-\frac{1}{2}}\{r\} = [\psi]^T\{f\} \quad (7.9)$$

Multiplying the left hand side by $[M_r]^{-\frac{1}{2}}$, yields;

$$\begin{aligned} & [M_r]^{-\frac{1}{2}}[\psi]^T[M][\psi][M_r]^{-\frac{1}{2}}\{\ddot{r}\} + [M_r]^{-\frac{1}{2}}[\psi]^T[C][\psi][M_r]^{-\frac{1}{2}}\{\dot{r}\} \quad (7.10) \\ & + [M_r]^{-\frac{1}{2}}[\psi]^T[K][\psi][M_r]^{-\frac{1}{2}}\{r\} = [M_r]^{-\frac{1}{2}}[\psi]^T\{f\} \end{aligned}$$

Normalizing of the eigenvector $[\psi]$, yields;

$$[\phi] = [\psi][M_r]^{-\frac{1}{2}}$$

Hence

$$[\phi]^T = [M_r]^{-\frac{1}{2}}[\psi]^T$$

Substituting the above equations into Equation 7.10, gives;

$$\{\ddot{r}\} + [\phi]^T[C][\phi]\{\dot{r}\} + [\phi]^T[K][\phi]\{r\} = [\phi]^T\{f\} \quad (7.11)$$

Hence the mass normalized stiffness and damping matrices for the two-degrees-of-freedom system are given by;

$$[\omega^2] = [\phi]^T[K][\phi] = [K_{m,r}] \quad (7.12)$$

where $k_{m,1} = \omega_1^2$ and $k_{m,2} = \omega_2^2$.

$$[2\zeta_r\omega_r] = [\phi]^T[C][\phi] = [C_{m,r}] \quad (7.13)$$

where $C_{m,1} = 2\zeta_1\omega_1$ and $C_{m,2} = 2\zeta_2\omega_2$.

Hence the mass, stiffness and damping matrices are obtained as follows:

$$[M] = [\psi]^{-T}[M_r][\psi]^{-1} \quad (7.14)$$

$$[K] = [\phi]^{-T}[K_{m,r}][\phi]^{-1} \quad (7.15)$$

$$[C] = [\phi]^{-T}[C_{m,r}][\phi]^{-1} \quad (7.16)$$

Equation 7.11 corresponds to two decoupled modal equations for the two-degrees-of-freedom system, viz.,

$$\ddot{r}_i + C_{m,i}\dot{r}_i + K_{m,i}r_i = f_i \quad (r = 1, 2) \quad (7.17)$$

Using the theory given above, the two-degrees-of-freedom model for the tubular T-joint can be extracted from the finite element model combined with the experimental data. The top center node, located on the brace, was used to obtain the mode shapes. According to the first two mode shapes obtained in the FE model of the tubular T-joint, the first mode is the cantilever bending along the y direction. This mode is responsible for crack opening and closing. The second is the cantilever bending along z direction. This mode is the least influenced by crack opening and closing, since the crack is located along the neutral axis of bending of the cantilever.

Since the finite element model can only deal with the open crack, the results of a two-degrees-of-freedom model with an open crack were obtained first. For illustrative purposes, the crack stage was taken as that corresponding to 565,000 cycles, as applied to specimen 3.

For an opening and closing crack, with changing stiffness, the equation of motion for mode one may be expressed by;

$$\ddot{r}_1 + C_{m,1}\dot{r}_1 + [(K_{m,1})_o + (K_{m,1})_{\Delta c}(1 + \cos\omega_1 t)]r_1 = f_1 \quad (7.18)$$

Similarly, the equation of motion for mode two may be written as;

$$\ddot{r}_2 + C_{m,2}\dot{r}_2 + (K_{m,2})_o r_2 = f_2 \quad (7.19)$$

Hence, the modal stiffness for the opening and closing crack may be expressed as;

$$[K]_{m,oc} = \begin{bmatrix} (k_{m,1})_o + (k_{m,1})_{\Delta c}(1 + \cos\omega_1 t) & 0 \\ 0 & (k_{m,2})_o \end{bmatrix} \quad (7.20)$$

Since nonlinearity was small, modal analysis was assumed to be still applicable.

The generalized mass for the tubular T-joint was obtained from the FE model as;

$$[M_r] = \begin{bmatrix} 0.331 & 0 \\ 0 & 0.766 \end{bmatrix} \quad (7.21)$$

where M_r was expressed in terms of $\text{lbs} \cdot \text{sec}^2 / \text{in}^4$.

Using lumped mass concepts, the mode shapes for the cracked tubular T-joint were;

$$[\psi] = \begin{bmatrix} 1 & -5.614E-6 \\ 5.977E-7 & 1 \end{bmatrix} \quad (7.22)$$

According to Equations 7.14 - 7.16 the mass matrix could be derived as;

$$[M] = \begin{bmatrix} 0.331 & 0 \\ 0 & 0.767 \end{bmatrix} \quad (7.23)$$

The mass normalized mode shapes were expressed as;

$$[\phi] = \begin{bmatrix} 1.739 & 0 \\ 0 & 1.142 \end{bmatrix} \quad (7.24)$$

and hence;

$$[\phi]^{-T} = [\phi]^{-1} = \begin{bmatrix} 0.575 & 0 \\ 0 & 0.876 \end{bmatrix} \quad (7.25)$$

The mass normalized stiffness matrix for the uncracked system was;

$$[K_{m,r}] = \begin{bmatrix} 4856 & 0 \\ 0 & 34235 \end{bmatrix} \quad (7.26)$$

The mass normalized stiffness for the open cracked system was;

$$[K_{m,r}] = \begin{bmatrix} 4744 & 0 \\ 0 & 34142 \end{bmatrix} \quad (7.27)$$

Hence, $(k_{m,1})_o$ was obtained as;

$$(K_{m,1})_o = 4744$$

$$(K_{m,1})_{\Delta c} = 56$$

Substituting $(K_{m,1})_o$, $(K_{m,1})_{\Delta c}$ and Eqn. (7.27) into equation (7.20)

$$[K_{m,r}]_{oc} = \begin{bmatrix} 4744 + 56(1 + \cos\omega_1 t) & 0 \\ 0 & 34142 \end{bmatrix} \quad (7.28)$$

Substitution of equations (7.25) and (7.28) into equation (7.15) yielded;

$$[K]_{oc} = \begin{bmatrix} 1569 + 19(1 + \cos\omega_1 t) & 0 \\ 0 & 26168 \end{bmatrix} \quad (7.29)$$

Similarly the mass normalized modal damping matrix could be derived from FE model and experimental results;

$$[C_{m,r}] = \begin{bmatrix} 0.9567 & 0 \\ 0 & 0.6759 \end{bmatrix} \quad (7.30)$$

Substitution of Eqn. (7.30) into Eqn. (7.16) yielded;

$$[C] = \begin{bmatrix} 0.3173 & 0 \\ 0 & 0.5180 \end{bmatrix} \quad (7.31)$$

Hence, the two degrees of freedom system for the tubular T-joint was obtained as;

$$\begin{cases} 0.311\ddot{u}_1 + 0.3173\dot{u}_1 + [1569 + 19(1 + \cos \omega_1 t)]u_1 = F_1(t) \\ 0.767\ddot{u}_2 + 0.5180\dot{u}_2 + 26168u_2 = F_2(t) \end{cases} \quad (7.32)$$

When a sine sweep function was applied to the system, to simulate the experimental situation, the sine sweep function could be expressed as;

$$F_1(t) = F_2(t) = F(t) = a \sin 2\pi[\omega_0 + (\omega_f - \omega_0)\frac{n}{N}]n\Delta t \quad (7.33)$$

where a is the force amplitude, ω_0 is the starting frequency and ω_f is the stopping frequency. Assuming the frequency range of observation to be 0 – 50 Hz, the sampling interval Δt was given by;

$$\Delta t = \frac{1}{2f_{max}} = 1/100 = 0.01\text{sec} \quad (7.34)$$

According to the B&K analyzer, the sampling period was $T = 16$ secs. for this frequency range. The sampling frequency became;

$$\Delta f = \frac{1}{T} = 1/16(\text{Hz}) \quad (7.35)$$

The total number of sampling points in the sampling period was expressed as

$$N = \frac{T}{\Delta t} = \frac{16}{0.01} = 1600 \quad (7.36)$$

Adding zeros to the buffer to increase N to $2^{11} = 2048$, yielded;

$$\Delta f = \frac{1}{N\Delta t} = 1/20.48 = 0.0488(\text{Hz}) \quad (7.37)$$

Using the starting frequency $\omega_0 = 4\pi$ radians, the swept sine forcing function could be expressed as:

$$F = a \sin 2\pi \left[2 + \frac{50-2}{2048} n \right] n \Delta t, \quad n = 1, 2, \dots, N \quad (7.38)$$

Substitution of Eqn. 7.38 into Eqn. 7.32, for $n\Delta t < 16.0$ sec, gave,

$$\begin{cases} 0.311\ddot{u}_1 + 0.3173\dot{u}_1 + [1569 + 19(1 + \cos \omega_1 t)]u_1 = \sin[2\pi(2 + \frac{48}{2048}n)]n\Delta t \\ 0.767\ddot{u}_2 + 0.5180\dot{u}_2 + 26168u_2 = \sin[2\pi(2 + \frac{48}{2048}n)]n\Delta t \end{cases} \quad (7.39)$$

where the crack breathing frequency was assumed to be the same as the forcing frequency, giving;

$$\omega_1 = 2\pi(2 + \frac{48}{2048}n) \quad (7.40)$$

7.5 Results and Discussions

Equations 7.39 were solved using the numerical integration procedure available in MATLAB program. The routine ODE45, which used the 4th/5th order Runge-Kutta-Fehlberg method for numerical integration, was used in the solution procedure. The system of nonlinear differential equations was expressed as a set of first order differential equations

$$\begin{aligned} \frac{du}{dt} &= f(u, t) + F(t) \\ y &= g(u, t) \end{aligned} \quad (7.41)$$

where $F(t)$ was the forcing function, u was an intermediate state vector, y was a vector, t was time and f was a function that returned the state derivatives as a function of u and t . The desired accuracy for the solution was kept as 10^{-6} .

While solving the differential equation in a numerical manner, the automatic step size Range-Kutta algorithm took larger steps where the solution was changing more

slowly. This fact must be accounted for in the subsequent Fourier transform operations carried out for interpreting the results. The unequal time steps were converted to equal time steps by an interpolating subroutine; spline curve fitting was used to get the proper time values for equal time step intervals. The number of values used in the Fourier transform had to be of an order of 2^n ; otherwise aliasing into lower frequency domain took place and gave erroneous results. While solving the governing equations of motion, initial conditions had to be compatible with the stiffness properties of the structure. An improper specification would lead to erroneous results. In order to obtain measurable and meaningful responses, $F_2(t)$ was multiplied by 100. This led to the increased deformation seen for $u_2(t)$ in Figure 7.3.

Figure 7.2 shows the swept sine function utilized for the forcing function. The function was generated using Eqn. 7.38. The frequency of the function progressively changed from 2.0 Hz to 50.0 Hz; it could be seen from Figure 7.2, that as the time parameter increased, the width of the individual sine curve decreased considerably. Hence the Δt used for the digitization interval should be decreased to give a better and smoother sinusoidal curve in the higher frequency ranges.

The response functions $u_1(t)$ and $u_2(t)$ obtained by solving Equations 7.39 are shown in Figure 7.3 where it can be seen that they are non-linear time decay functions rather than a simple sinusoidal function. As expected the response curves peaked at their natural frequencies. The responses increased progressively as the natural frequencies were approached (by the forcing function frequencies), and then decreased as the forcing frequencies moved away from natural frequencies. The same would be repeated after every 16.0 secs, which was the sampling period T set in Equations 7.35 and 7.36.

Figures 7.4 give the Fourier transforms of $u_1(t)$ and $u_2(t)$ given in Figure 7.3. Since the actual curves were obtained by interpolation of time steps and spline curve

fitting of response values, the Fourier transforms of functions $u_1(t)$ and $u_2(t)$ were not smooth as they should be; also the peaks around resonance points were not sharp. This might be improved by refining $\Delta t = (0.01 \text{ sec})$ used in the digitization. Anyhow it could be seen from the top curve of Fig. 7.4, that the curve seems to have nonlinear trends around 15 to 18 Hz and 23 to 27 Hz, respectively. Results similar to these were observed earlier from Figures 5.46 to 5.53 and discussed in Section 5.5.3. The quasi-static responses were also not dominant in Figure 7.4; but the tendency could be seen by closely observing and comparing the two curves of Figure 7.4. As observed earlier in Section 5.5.3, the presence of cracking would have been shown dominantly by the strain frequency response function rather than the displacement frequency response function; however, strain frequency response function equations could not be obtained using lumped mass concepts.

It was observed from an earlier study on beams [Cheng, 1995] that the crack "opening and closing" effect produced a much larger crack than an "open" crack model, for the same change in frequencies. Hence the use of an "open crack" model to numerically predict the fatigue crack influence would seriously underestimate the severity of the actual crack.

7.6 Conclusions

An "opening and closing" crack model was developed for the tubular T-joint, using lumped mass modeling concepts. The response of the model to a sine sweep function was determined using a numerical integration procedure; the Runge-Kutta-Fehlberg algorithm available in the MATLAB program was used to solve the nonlinear differential equation. A typical case of "crack opening and closing" was solved when the crack size around the saddle point was at a fatigue cycle of 565,000 cycles (specimen

3). It was observed that the crack "opening and closing" introduced quasi-static and both sub- and super- harmonic responses.

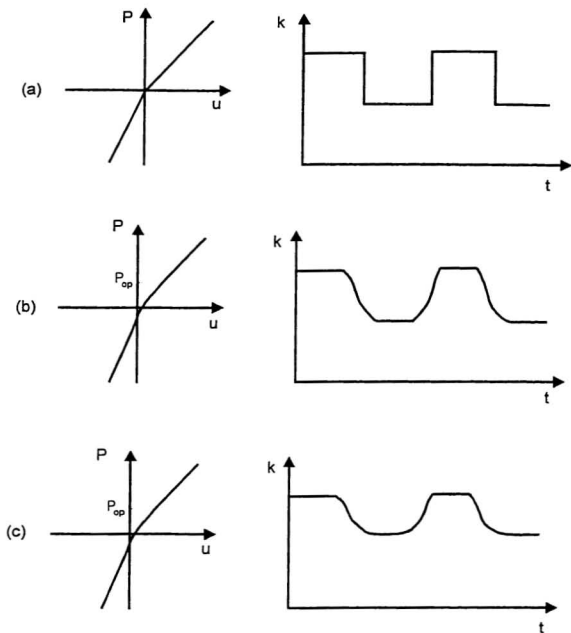


Figure 7.1 Load (P)-displacement (u) relations and the derived stiffness (k) for a crack under cyclic loading: a) an ideal crack, b) a fatigue crack under vibrational load, $F_0 > P_{op}$, with $F_0 > P_{op}$ and c) a fatigue crack under vibrational load with $F_0 < P_{op}$.

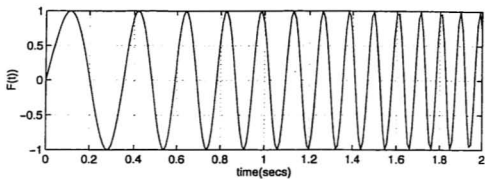


Figure 7.2: Sine sweep forcing function

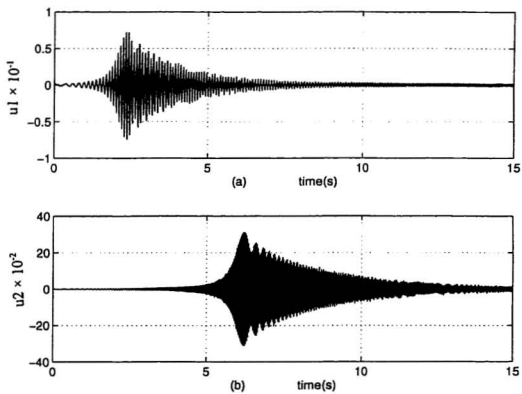


Figure 7.3: Response time history

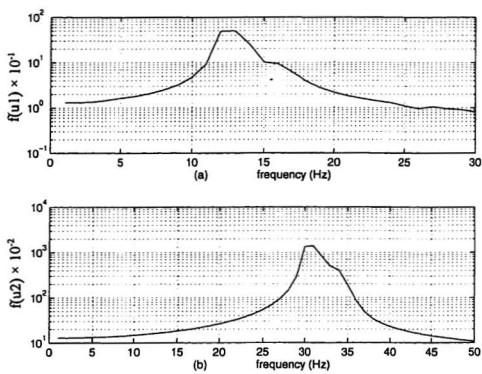


Figure 7.4: Fourier transform

Chapter 8

Conclusions, Contributions and Recommendations for Further Investigation

8.1 Review of Original Objectives

This investigation was aimed primarily at developing procedures that would accurately detect and predict the initiation and propagation of fatigue cracks in tubular T-joints. It was hoped that these procedures could also be applied to other similar structures. In addition, numerical procedures were to be developed to characterize the properties of uncracked and cracked tubular T-joints. Towards this end the following tasks were to be completed:

1. Experimental studies were to be performed of the fatigue crack initiation and growth process in three tubular T-joints.
2. Experimental studies were to be performed of the vibration response of the crack-free and cracked structures so as to identify parameters that could be used for crack detection.
3. Finite element analyses were to be carried out to correlate and interpret the experimental results.

4. Phenomenological and mathematical models were to be developed to explain the initiation and growth of fatigue cracks in these tubular T-joint structures, and to explain their response to dynamic excitation.

8.2 Major Observations and Contributions

1. Cyclic loading of these tubular T-joints, under the conditions employed in this study, has been shown to give rise to fatigue cracking, which occurs by the formation of small, surface connected thumb-nail cracks, at the weld toe.
2. The thumb-nail cracks initiate at multiple sites, either simultaneously or in close succession, and their growth eventually leads to interlinking and the resulting formation of cracks of high aspect ratio (surface length to depth) and even through-the-thickness cracks. A Paris type equation has been used to describe fatigue crack growth before and after the break through the thickness.
3. Strain gauge data was found to be more reliable and more sensitive in detecting fatigue induced damage. Little or no change was observed in the strain gauge output during the initiation and the early stages of growth of the thumb-nail cracks, but sharp drops were observed in the strain gauge output as the thumb-nail cracks coalesced to form single cracks of significant level. The change in the static strain, associated with above crack growth process, has been successfully correlated with the number of fatigue cycles by an equation of the form

$$\log_{10} N = A(\Delta\epsilon/\epsilon_0)^n$$

which is valid for all strain gauge locations. Thus the ground-work has been laid for the development of a method for detecting the presence of cracks before they reach critical dimensions.

4. The initiation and growth of fatigue cracks in the tubular T-joints were accompanied by modal analysis, and a number of parameters were evaluated in terms of their ability to detect and locate these fracture processes. Both strain and accelerometer frequency response functions were used, to extract meaningful indicators of cracking, namely; 1) quasi-static components, 2) anti-resonance shifts, and 3) nonlinearity in frequency response functions.
5. To the best of this researcher's knowledge, this is the first successful attempt to detect growing fatigue cracks in simulated off-shore structural T-joints. Furthermore, it has been shown that the cracks may be detected remotely by a non-destructive method, at a relatively small crack size and long before the cracks have reached critical dimensions.
6. The normalized crack size (crack area/loading bearing area) has been improved to 0.0714 compared to the traditional 0.125. The lower this value, the more sensitive is the method of crack detection.
7. The frequency response functions have been examined in detail and three specific features have been identified that are consistent with the presence of coalesced cracks. They include, in the first instance, amplitude shifts in the quasi-static region which provide for differentiation between cracked and "crack-free" structures. This method is unlikely to be successful in detecting the presence of thumb-nail or micro-cracks, but it does appear to be capable of detecting coalesced cracks of high aspect ratio. The second feature is the progressive displacement of the antiresonance frequencies to lower or higher values as cracks initiate and grow. Once again this method is very sensitive to the presence of coalesced cracks, but its ability to detect the presence of isolated microcracks remains to be determined. Finally, non-linear response in the frequency response

functions, provides an additional indication of the presence of cracking.

8. All the techniques described in 7 above have been shown to provide reliable and reproducible indications of cracking, and indications that are clearly visible well before the cracks have penetrated across the entire wall thickness, and hence well before they have reached critical proportions. Further work remains to be done to establish their limits of sensitivity, and their ability to detect the presence of microcracks.
9. The initiation and growth of fatigue cracks has been explained in terms of the reversed plastic flow that occurs in regions of stress concentration in the structure. During crack growth, the reversed plastic flow occurs in the plastic zone at the crack tip, and this occurs due to the repeated loading and unloading of the crack, and the repeated opening and closing of the crack. The compliance, and hence local stiffness of the structure varies in a cyclic manner as a result of this crack opening and closing.
10. Cracks present in a structure during modal testing also open and close as a result of forces generated during resonance. The nonlinear stiffness changes associated with crack opening and closing during vibration have been shown to give rise to the changes in dynamic response observed during modal testing.
11. Crack opening and closing during modal testing produces a beating or breathing action between the crack faces, and leads to the flattening of asperities on the fracture surfaces. Flattened faces, devoid of normal fatigue fracture surface features, are predominant characteristics of the vibration tested specimens. This includes the specimens that were fatigue tested at positive load ratios where complete crack closure and fracture surface beating during fatigue would be

unlikely to occur.

12. A lumped mass model has been developed of the crack opening and closing process, which incorporates a time dependent stiffness response.
13. A finite element model was also developed and correlated with experimental results. The finite element model was found to agree with the experimental data very well, and it provided a solid theoretical basis for the explanation of a) variations in principal static stresses, b) natural frequencies and c) frequency response functions.
14. A particularly valuable achievement of this study was the demonstrated ability to predict crack size and shape, as a function of the number of fatigue cycles applied, using finite element methods.

8.3 Recommendations for Further Research

The following areas could be investigated further to advance the state-of-art of crack prediction

1. Using substructure approach, the above study could be extended to a plane frame fabricated of tubular T-, Y-, and K- joints to consider the possibility of developing crack prediction equations that would relate the presence of cracks at different joints of a real structure;
2. Further work should be performed to determine the sensitivities of these methods of crack detection. In particular, it would be useful to follow the very early stages of crack formation when the surface crack lengths are in the range 0 to about 50 mm, and to correlate their appearance with changes in static and dynamic response. Methods such as dye penetrant inspection, acoustic

Reference

- ABAQUS Manual*, (1996). Hibbitt, Karlsson & Sorensen, Inc.
- ABAQUS Manual*, (1994). Hibbitt, Karlsson & Sorensen, Inc.
- Actis, R. L., and Dimarogonas, A. D., (1989). "Non-Linear Effects due to Closing Cracks in Vibrating Beams," *ASME Design Engineering Division Publication DE - Structural Vibration and Acoustics*, Vol. 18, no. 2, pp. 99-104.
- Adams, R. D., Cawley, P., Pye, C. J., and Stone, B. J., (1978). "A Vibration Technique for Non-Destructively Assessing the Integrity of Structures", *Journal of Mechanical Engineering Science*, Vol. 20, No. 2, pp. 93-100.
- Afolabi, D., (1987). "An Anti-Resonance Technique for Detecting Structural Damage," *Proceedings of 5th International Modal Analysis Conference*, Vol. 1, pp. 491-495.
- Allemang, R. J., and Brown, D. L., (1982). "A Correlation Coefficient for Modal Vector Analysis", *Proceedings of the 1st International Modal Analysis Conference*, pp. 110-116.
- Ashwell, D. G., and Gallagher, R. H., (1976). *Finite Elements for Thin Shells and Curved Members*, John Wiley & Sons, London, New York, Sydney, Toronto, 268p.
- Bäcklund, J., Blom, A. F. and Beevers, C. J. (1981). *Fatigue Thresholds*, EMAS, U.K., pp. 1123, 1174p.
- Barnasconi, O., and Ewins, D.J., (1989). "Modal Strain/Stress Fields," *Journal of Modal Analysis*, April, pp. 68-76.
- Barnasconi, O., and Ewins, D. J., (1989). "Application of Strain Modal Testing to Real Structures," *Proceedings of the 7th International Modal Analysis Conference*, Vol. 2, pp. 1453-1464.
- Bayliss, M., Short, D., and Bax, M., (1988). *Underwater Inspection*, London, E. & F. N. Spon Ltd, London.
- Beckwith, T. G., Marangoni R. D., and Lienhard, V. J. H., (1993). *Mechanical Measurements*, Fifth edition, Addison-Wesley Publishing Company, Reading, Massachusetts, 876p.
- Bray, D. E., and McBride, D., (1992). *Nondestructive Testing Techniques*, John Wiley & Sons, Inc.
- Berens, A. P., and Hovey, P. W., (1981). "Statistical Methods for Estimating Crack Detection Probabilities," *Probabilistic Fracture mechanics and Fatigue Methods*, ASTM STP 798, pp.79-94.

- Bishop, C. M., (1994). "Neural Networks and Their Applications", *Review of Scientific Instrumentation*, Vol. 65, No. 6, pp. 1803-1832.
- Brown, D., (1992). *Advanced Modal Parameter Estimation Concepts*, Prepared for the Tenth International Modal Analysis Conference.
- Bull, J. W., (1990). *Finite Element Applications to Thin-Walled Structures*, Elsevier Applied Science, London and New York, 307 p.
- Cawley, P., and Adams R. D., (1979). "The Location of Defects in Structures from Measurements of Natural Frequencies," *Journal of Strain Analysis*, Vol. 14, No. 2, pp. 49-57.
- Ceravolo, R., and Stefano, A. D., (1995). "Damage Location in Structures Through a Connectivistic Use of FEM Modal Analyses," *Modal Analysis: The International Journal of Analytical and Experimental Modal Analysis*, Vol. 10, no 3, pp. 176.
- Chance, J., Tomlinson, G. R., and Worden, K., (1994). "A Simplified Approach to the Numerical and Experimental Modeling of the Dynamics of a Cracked Beam," *Proceedings of the 12th International Modal Analysis Conference*, Vol. I, pp. 778-785.
- Chen, Y., and Swamidias, A. S. J., (1993). "Change of Modal Parameters due to Crack Growth in a Tripod Tower Platform," *Canadian Journal of Civil Engineering*, October, Vol. 20, No. 5, pp. 801-813.
- Chen, Y. (1996). Crack Detection in Plated T-joints Through Vibration Techniques, *Ph.D. thesis*, Memorial University of Newfoundland, St.John's, Newfoundland, Canada, 160 p.
- Cheng, S. M., and Swamidias, A. S. J., (1995). "Nonlinear Dynamic Response of a Beam due to the Opening and Closing of a Fatigue crack," *International Conference on Structural Dynamics, Vibration, Noise and Control*, Vol. 1, pp. 610-615.
- Chu, Y.C., and Shen, M.H.H., (1992). "Analysis of Forced Bilinear Oscillators and the Application to Cracked Beam Dynamics," *AIAA Journal*, Vol. 30, No. 10, pp 2512-2519.
- Collins, K. R., Plaut, R. H., and Wauer, J., (1992). "Free and Forced Longitudinal Vibrations of a Cantilevered Bar with a Crack," *Journal of Vibration and Acoustics*, Vol. 114, pp. 171-177.
- Crespo, C., Ruotolo, R., and Surace, C., (1996). "Non-linear Modelling of a Cracked Beam", *Proceedings of the 14th International Modal Analysis Conference*, Vol. II, pp 1017-1022.
- Desvaux, G.J., (1985). The Line Spring Model for Surface Flaw, An Extension to Mode II and Mode III, *M. Sc. thesis in Mechanical Engineering*, Massachusetts Institute of Technology, Cambridge, Boston, Massachusetts, U.S.A., 92 p.
- Dimarogonas, A.D., and Chondros, T. G., (1980). "Identification of Cracks in Welded Joints of Complex Structures," *Journal of Sound and Vibration*, Vol. 69, No. 4, pp.

531-538.

Doebling, S. W., Farrar, C. R., Prime, M. B., and Shevitz, D. W., (1996). *Damage Identification and Health Monitoring of Structural and Mechanical Systems from Changes in Their Vibration Characteristics: A Literature Review*, Los Alamos National Laboratory, 127 p.

Doebling, S. W., (1995). Measurement of Static Flexibility Matrices for Experiments with Incomplete Reciprocity, *Ph.D. Dissertation*, University of Colorado, Boulder, CO, Department of Aerospace Engineering Sciences, CU-CAS-95-10.

Dong, C. Zhang, P. Q., Feng, W. Q., and Huang, T. C., (1994). "The Sensitivity Study of the Modal Parameters of a Cracked Beam", *Proceedings of the 12th International Modal Analysis Conference*, Vol. 1, pp. 98-104.

Emmons, P.H., (1993). *Concrete Repair and Maintenance Illustrated*, R.S. Means Company Inc., Kingston, Massachusetts, U.S.A., pp. 88.

Erwins, D.J., (1995). *Modal Testing: Theory and Practice*, Research Studies Press Ltd., Taunton, Somerset, England, 313p.

Elber, W., (1970). "Fatigue Crack Closure Under Cyclic Tension", *Engineering Fracture Mechanics* 2, pp. 37-45.

Feldman, M., and Braun, S., (1995). "Identification of Nonlinear System Parameters via the Instantaneous Frequency: Application of the Hilbert Transform and Wigner-Ville Techniques," *Proceedings of 13th International Modal Analysis Conference*, Vol. I, pp 637-642.

Friswell, M. I. and Penny, J. E. T., (1992). "A Simple Nonlinear Model of a Cracked Beam." *Proceedings of the 10th International Modal Analysis Conference*, Vol. 1, pp. 516-521.

Fox, C. H. J., (1992). "The Location of Defects in Structures: a Comparison of the Use of Natural Frequency and Mode Shape Data," *Proceedings of the 10th International Modal Analysis Conference*, Vol. 1, pp. 522-528.

Gomes, A. J. M. A., and Silva, J. M. M. E., (1990). "On the Use of Modal Analysis for Crack Identification," *Proceedings of the 8th International Modal Analysis Conference*, Vol. 2, pp. 1108-1115.

Gomes, A. J. M. A., and Silva, J. M. M. E., (1991). "Theoretical and Experimental Data on Crack Depth Effects in the Dynamic Behavior of Free-Free Beams." *Proceedings of the 9th International Modal Analysis Conference*, Vol. 1, pp. 274-283.

Gu, S. N., Zhang, J. L., Jiang, J. S., and He, C. A., (1989). "A Vibration Diagnosis Approach to Structural Fault," *Journal of Vibration, Acoustics, Stress, and Reliability in Design*, ASME, January, Vol. 111, pp. 88-93.

Haisty, B. S., and Springer, W. T., (1985). "The Longitudinal Vibration Characteristics of a Uniform Beam Containing Two Symmetric Discontinuities", *Proceedings of*

the Society for Experimental Mechanics Spring Conference, pp. 389-393.

Haisty, B. S., and Springer, W. T., (1988). "A General Beam Element for Use in Damage Assessment of Complex Structures," *Journal of Vibration, Acoustics, Stress, and Reliability in Design*, Vol. 110, pp. 389-394.

He, J., and Ewins, D. J., (1986). "Analytical Stiffness Matrix Correction Using Measured Vibration Modes," *International Journal of Analytical and Experimental Modal Analysis*, Vol. 1, No. 3, pp. 1-9.

Hearn, G., and Testa, R. B., (1991). "Modal Analysis for Damage Detection in Structures," *Journal of Structural Engineering*, Vol. 117, no. 10, pp. 3042-3063.

Hemez, F. M., (1993). Theoretical and Experimental Correlation Between Finite Element Models and Modal Tests in the Context of Large Flexible Space Structures, Ph.D. Dissertation, Department of Aerospace Engineering Science, University of Colorado, Boulder, Colorado.

Hinton, E., and Owen, D. R. J., (1984). *Finite Element Software for Plates and Shells*, Pineridge Press, Swansea, U.K., 403 p.

Huang, F., and Gu, S., (1993). "Application of Higher Order Cumulants to Structure Fault Diagnosis," *Proceedings of 11th International modal Analysis Conference*, Vol II, pp. 1237-1240.

Hughes, T.J.R., Cohen, M., and Haroun, M., (1978). "Reduced and Selective Integration Techniques," *Journal of Nuclear Engineering and Design*, Vol. 46, pp. 203-222.

Ibrahim, A., Ismail, F., and Martin, H. R., (1987). "Modeling of Dynamics of Continuous Beam Including Nonlinear Fatigue Crack," *International Journal of Analytical and Experimental Modal Analysis*, Vol. 2, No. 2, pp. 76-82.

Ismail, F., Ibrahim, A., and Martin, H. R., (1990). "Identification of Fatigue Cracks from Vibration Testing," *Journal of Sound and Vibration*, Vol. 140, No. 2, pp. 305-317.

Inman, D.J., (1994). *Engineering Vibration*, Prentice Hall, Englewood Cliff, New Jersey, 560 p.

Kaouk, M., (1993). Finite Element Model Adjustment and Damage Detection Using Measured Test Data, Ph.D. Dissertation, Department of Aerospace Engineering Mechanics and Engineering Science, University of Florida, Gainesville, Florida.

Kirkegaard, P. H., and Rytter, A., (1994). "Use of Neural Networks for Damage Assessment in a Steel Mast," *Proceedings of the 12th International Modal Analysis Conference*, pp. 1128-1134.

Ko, J. M. Wong, C. W., and Lam, H. F., (1994). "Damage Detection in Steel Framed Structures by Vibration Measurement Approach," *Proceedings of the 12th International Modal Analysis Conference*, pp. 280-286.

- Kobayashi, A. S., (1993). *Handbook on Experimental Mechanics*, VCH Publishers, Inc.
- Krawczuk, M., and Ostachowicz, W. M., (1992). "Parametric Vibrations of a Beam with Crack," *Archive of Applied Mechanics*, Vol. 62, pp. 463-473.
- Kudva, J., Munir, N., and Tan, P., (1991). "Damage Detection in Smart Structures Using Neural Networks and Finite Element Analysis," *Proceeding of ADPA/AIAA/ASME /SPIE Conference on Active Materials and Adaptive Structures*, pp 559-562.
- Law, S. S., Waldron, P., and Taylor, C., (1992). "Damage Detection of a Reinforced Concrete Bridge Deck Using the Frequency Response Function," *Proceedings of the 10th International Modal Analysis Conference*, pp. 772-778.
- Leath, W. J., and Zimmerman, D. C., (1993). "Analysis of Neural Network Supervised Training with Application to Structural damage Detection," *Damage and Control of Large Structures-Proceedings of the 9th VPI&SU Symposium*, pp. 583-594.
- Li, D. B., Zhuge H. C., and Wang, B., (1989). "The Principles and Techniques of Experimental Strain Modal Analysis," *Proceedings of the 7th International Modal Analysis Conference*, Vol. 2, pp. 1285-1289.
- Li, D. B., Zheng, Z. C., He, K., and Wang, B., (1992). "Damage Detection in Offshore Structures by the FRF Method," *Proceedings of the 11th International Conference on Offshore Mechanics and Arctic Engineering*, Vol. 1, part B, pp. 601-604.
- Lieven, N. A. J., and Ewins, D. J., (1988). "Spatial Correlation of Mode Shapes, the Coordinate Modal Assurance Criteria (COMAC)," *6th International Modal Analysis Conference*, Vol. 1, pp. 690-695.
- Lin, R. M., and Ewins, D. J., (1990). "On the Location of Structural Nonlinearity from Modal Testing - A Feasibility Study," *Proceedings of the 8th International Modal Analysis Conference*, Vol. 1, pp. 358a-364.
- Mannan, M. A., and Richardson, M. H., (1990). "Detection and Location of Structural Cracks using FRF Measurements," *Proceedings of the 8th International Modal Analysis Conference*, Vol. 1, pp. 652-657.
- Manson, G., Worden, K., and Tomlison, G.R., (1993). "Pseudo-Fault Induction in Engineering Structures," *ASME Adaptive Structures and Materials System*, AD35, pp. 449-455.
- Mayes, R. L., (1995). "An Experimental Algorithm for Detecting Damage Applied to the 1 - 40 Bridge over the Rio Grande," *Proceedings of the 13th International Modal Analysis Conference*, pp. 219-225.
- Meneghetti, U., and Maggiore, A., (1994). "Crack Detection by Sensitivity Analysis", *Proceedings of the 12th International Modal Analysis Conference*, Vol. 2, pp. 1292-1298.

- Mottershead, J. E., and Friswell, M. I., (1993). "Model Updating in Structural Dynamics: A Survey," *Journal of Sound and Vibration*, Vol. 167, No. 2, pp. 347-375.
- Newman, J. C., Jr. and Wilber, W., (1988). *Mechanics of Fatigue Crack Closure*, ASTM, Philadelphia, PA, pp. 172, 668 p.
- Pandey, A. K., Biswas, M., and Samman, M. M., (1991) "Damage Detection from Changes in Curvature Mode Shapes," *Journal of Sound and Vibration*, Vol. 145, No. 2, pp. 321-332.
- Pandey, A. K., and Biswas, M., (1994). "Damage Detection in Structures Using Changes in Flexibility," *Journal of Sound and Vibration*, Vol. 169, no. 1, pp. 3-17.
- Paris, P. C., Gomez, M. P. and Anderson, W. E. (1961). *The trend in Engineering*, Univ. of Washington, Seattel, WA, Vol. 13, pp. 9-14.
- Park, Y. S., Park, H. S., and Lee, S. S., (1988). "Weighted Error - Matrix (WEM) Application to Detect Stiffness Damage by Dynamic Characteristic Measurement", *The International Journal of Analytical and Experimental Modal Analysis*, Vol. 3, No. 3, pp. 101-107.
- Papadopoulos, C. A., and Dimarogonas, A. D. (1987). "Coupled Longitudinal and Bending Vibrations of a Rotating Shaft with an Open Crack," *Journal of Sound and Vibration*, Vol. 117, No. 1, pp. 81-93.
- Papadopoulos, C. A., and Dimarogonas, A. D., (1988). "Coupled Longitudinal and Bending Vibrations of a Cracked Shaft," *Journal of Vibration, Acoustics, Stress, and Reliability in Design*, Vol. 110, pp. 1-8.
- Paranavitana, S., (1996). *Symmetric and Asymmetric Crack Development in Tubular T-Joints*, *M.Eng. thesis*, Memorial University of Newfoundland, St. John's, Newfoundland, Canada, 101 p.
- Perchard, D.R., (1993). *Crack Detection in Slender Cantilever plates Using Modal Analysis*, *M.Eng. thesis*, Memorial University of Newfoundland, Canada, 236 p.
- Petyt, M., (1990). "Introduction to Finite Element Vibration Analysis," Cambridge University Press", Cambridge, ISBN 0 521 26607 6, pp. 1-48, 386-391.
- Prime, M. B., and Shevitz, D. W., (1996). "Linear and Nonlinear Methods for Detecting Cracks in Beams," *Proceedings of the 14th International Modal Analysis Conference*, pp. 1437-1443.
- Qian, G. L., Gu S. N., and Jiang, J. S., (1990). "The Dynamic Behavior and Crack Detection of a Beam with a Crack," *Journal of Sound and Vibration*, , Vol. 138, No. 2, pp. 233-243.
- Ritchie, R.O., (1982). "Environmental Effects on Near-Threshold Fatigue Crack Propagation in Steels: A Re-Assessment", *Fatigue Thresholds* vol. 1, Engineering Materials Advisory Services, pp.503.

- Richardson, M. H., and Mannan, M. A., (1991). "Determination of Modal Sensitivity Functions for Location of Structural Faults," *Proceedings of the 9th International Modal Analysis Conference*, Vol. 1, pp. 670-676.
- Richardson, M.H., (1980). "Detection of Damage in Structures from Changes in Their Dynamic (Modal) Properties - A Survey," NUREG/CR-1431, U.S. Nuclear Regulatory Commission, Washington, D.C.
- Rubin, S., and Coppolino, R. N., (1983). "Flexibility Monitoring of Offshore Jacket Platform," *Proceedings of the 15th Annual Offshore Technology Conference*, Houston, Texas, Vol. 2, OTC 4535, pp. 201-208.
- Rytter, A., (1993). *Vibrational Based Inspection of Civil Engineering Structures*, Ph. D. thesis, paper No. 44, Department of Building Technology and Structural Engineering, The University of Aalborg, Sohngaardsholmsvej 57, DK 9000, ISSN 0902 - 7513 R9314, May.
- Reddy, J. N., (1993). *An Introduction to Finite Element Method*, McGraw Hill Inc, New York, pp. 404-454.
- Salawu, O. S., and Williams, C., (1994). "Damage Location Using Vibration Mode Shapes", *Proceedings of the 12th International Modal Analysis Conference*, Vol. 1, pp. 933-939.
- Salawu, O. S., (1995). "Nondestructive Assessment of Structures Using the Integrity index Method Applied to a Concrete Highway Bridge," *Insight*, Vol. 37, no 11, pp. 875-878.
- Salawu, O. S., and Williams, C., (1995). "Bridge Assessment Using Forced - Vibration Testing," *Journal of Structural Engineering*, Vol. 121, no. 2, pp. 161-173.
- Saxena, A. and S.J. Hudak, (1978). " Review and extension of compliance information for common crack growth specimens", *International Journal of Fracture* 14, pp. 453.
- Schwarz, H.R., (1988). *Finite Element Methods*, Academic Press, London, U.K., ISBN 0-12-633010, pp. 67-101.
- Sehitoglu, H. and Garcia, A. M. (1997). "Contact of Crack Surfaces during Fatigue: Part 2. Simulations", *Metallurgical and Materials Transactions*, Vol. 28A, pp. 2277-2289.
- Sekhar, A. S., and Prabhu, B. S., (1992). "Crack Detection and Vibration Characteristics of Cracked Shafts", *Journal of Sound and Vibration*, Vol. 157, No.2, pp. 375-381.
- Shen, M. H. H., and Pierre, C., (1990). "Natural Modes of Bernoulli-Euler Beams with Symmetric Cracks", *Journal of Sound and Vibration*, Vol. 138, No. 1, pp. 115-134.
- Shen, M. H. H., and Chu, Y. C., (1992). "Vibrations of Beams with a Fatigue Crack," *Computers & Structures*, Vol. 45, no. 1, pp. 79-93.

- Silk, M. G., (1988). "Introductory Review on Reliability," *Reliability in Non-Destructive Testing*, NDT - 88, Pergamon Press, pp. 21-35.
- Skjaerbaek, P. S., Nielsen, S. R. K., and Cakmak, A. S., (1996). "Assessment of Damage in Seismically Excited RC-Structures from a Single Measured Response," *Proceedings of the 14th International Modal Analysis Conference*, pp. 133-139.
- Springer, W. T., Lawrence, K. L., and Lawley, T. J., (1987). "The Effect of a Symmetric Discontinuity on Adjacent Material in a Longitudinally Vibrating Uniform Beam", *Experimental Mechanics*, Vol. 27, pp. 168-171.
- Srinivasan, M. G., and Kot, C. A., (1992). "Effects of Damage on the Modal Parameters of a Cylindrical Shell," *Proceedings of the 10th International Modal Analysis Conference*, pp. 529-535.
- Stubbs, N., Broome, T. H., and Osegueda, R., (1990). "Nondestructive Construction Error Detection in Large Space Structures," *AIAA Journal*, Vol. 28, no. 1, pp. 146-152.
- Stubbs, N., Kim, J. T., and Farrar, C. R., (1995). "Field Verification of a Nondestructive Damage Localization and Severity Estimation Algorithm," *Proceedings of 13th International Modal Analysis Conference*, pp. 210-218.
- Swamidas, A.S.J., and Chen, Y., (1992). "Damage Detection in a Tripod Tower Platform (TTP) Using Modal Analysis," *Proceedings of ASME Conference on Offshore Mechanics and Arctic Engineering*, Vol I-B, pp 577-583.
- Thomson, W. T., and Madison, W., (1949). "Vibration of Slender Bars With Discontinuities in Stiffness", *Journal of Applied Mechanics*, , Vol. 17, pp. 203-207.
- Tsang, W. F., (1990). "Use of Dynamic Strain Measurements for the Modeling of Structures", *Proceedings of the 8th International Modal Analysis Conference, USA*, Vol. 2, pp. 1246-1251.
- Wang, W., (1987). "Sensitivity Analysis in Fault Vibration Diagnosis of Structures," *Proceedings of the 5th International Modal Analysis Conference*, Vol. 1, pp. 496-501.
- Wardenier J. and Shahi, E. P., (1991). "Tubular Structures," *Proceedings of 4th International Symposium*, Delft University Press, Delft.
- West, W. M., (1984). "Illustration of the Use of Modal Assurance Criterion to Detect Structural Changes in an Orbiter Test Specimen," *Proceedings of Air Force Conference on Aircraft Structural Integrity*, pp. 1-6.
- Wu, X. J., A. K. Koul and A.S. Kraus, (1994). "A Transgranular Fatigue Crack Growth Rate Model Based on the Restricted Slip Reversibility," *Metallurgical Transactions A*, 24A, pp.1373-1384.
- Wu, X. J., Wallace, W. and Koul, A. K., (1995). "A New Approach to Fatigue Threshold," *Fatigue and Fracture of Engineering Materials and Structures*, 18, pp.

833-845.

Wu, X.J., (1995). "An energy approach to crack closure," *International Journal of Fracture*, pp. 263-272.

Yuen, M. M. F., (1985). "A Numerical Study of the Eigenparameters of a Damaged Cantilever", *Journal of Sound and Vibration*, Vol. 103, No. 3, pp. 301-310.

Zhang, Z., and Aktan, A. E., (1995). "The Damage Indices for Constructed Facilities," *Proceedings of the 13th International Modal Analysis Conference*, pp. 1520-1529.

Appendix A

Finite Element Analysis Basic Theory

A.1 General Equations of Elasticity

The tensor form of the equations of elasticity could be expressed as [Schwarz 1988, Petyt 1990, Hughes 1978]:

- Equilibrium equations in terms of stresses:

$$\sigma_{ij,j} + \bar{f}_i = 0 \quad \text{in } V \quad (\text{A.1})$$

where σ_{ij} is stress in the element, \bar{f}_i the sum of body forces, inertial forces and dissipative forces, along x, y or z ($i, j = 1, 2, 3$) direction, respectively, and V the volume of the whole body.

- Strain-displacement relations:

$$\epsilon_{ij} = \frac{1}{2}(u_{i,j} + u_{j,i}) \quad \text{in } V \quad (\text{A.2})$$

where ϵ_{ij} is the strain, and u is displacement.

- Stress-strain (or constitutive) relations:

$$\sigma_{ij} = D_{ijkl}\epsilon_{kl} \quad \text{in } V \quad (\text{A.3})$$

where σ_{ij} is the stress, D_{ijkl} is the elasticity matrix and ϵ_{kl} is the strain. It has 2 independent constants for a homogeneous material, E and ν .

- Force boundary condition:

$$T_i = \bar{T}_i \quad \text{on force boundary} \quad (\text{A.4})$$

where $T_i = \sigma_{ij}n_j$, n_j is the directional cosine of the normal to the force boundary, and \bar{T}_i is the known area force.

- Displacement boundary condition:

$$u_i = \bar{u}_i \quad \text{on displaced boundary} \quad (\text{A.5})$$

where u_i is the displacement, \bar{u}_i is the known displacement on the displaced boundary.

- Strain energy

$$U(\epsilon_{mn}) = \frac{1}{2} D_{ijkl} \epsilon_{ij} \epsilon_{kl} \quad (\text{A.6})$$

where $\epsilon = u_{i,j}$ is the strain.

- Kinetic energy

$$T(\dot{u}) = \frac{1}{2} m_{ij} \dot{u}_i \dot{u}_j \quad (\text{A.7})$$

- Nonconservative work done

$$W_{nc} = f_i u_i - c_{ij} \dot{u}_i^T u_j \quad (\text{A.8})$$

- Total work integral (Hamilton's form)

$$I = \int_{t_0}^{t_1} (T - U - W_{nc}) dt \quad (\text{A.9})$$

- Variational (weak) formulation gives

$$\delta I = 0 \quad (\text{A.10})$$

A.2 Shape Functions for Six-Noded Triangular and Eight-Noded Rectangular Elements

A.2.1 Six-Noded Triangular Elements

For a triangular element, a complete quadratic approximation in two variables,

$$u(x, y) = c_1 + c_2 x + c_3 y + c_4 x^2 + c_5 xy + c_6 y^2 \quad (\text{A.11})$$

contains six coefficients and is uniquely determined by the values of u at six node points (Schwarz, 1988). As node points we take the three corners and the three mid-points of the sides of the triangle, which are numbered as in Fig. A.1. On each side of the triangle the approximating function reduces to a complete quadratic function of the length. This property once more guarantees the continuity of the approximating functions across the common side between two adjoining elements.

Substitution for x and y in Eqn. A.1 using the linear relation relation A.2 (given below) produces a quadratic function for u in the variable ξ and η :

$$x = b_1 + b_2\xi + b_3\eta \quad (\text{A.12})$$

$$y = b_4 + b_5\xi + b_6\eta$$

$$u(\xi, \eta) = \alpha_1 + \alpha_2\xi + \alpha_3\eta + \alpha_4\xi^2 + \alpha_5\xi\eta + \alpha_6\eta^2 \quad (\text{A.13})$$

The displacement function given by Eqn. A.3 is related to the nodal displacement values $\{u_c\}$ as

$$\{\alpha\} = [A]\{u_c\} \quad (\text{A.14})$$

where

$$A = \begin{bmatrix} 1 & 0 & 0 & 0 & 0 & 0 \\ -3 & -1 & 0 & 4 & 0 & 0 \\ -3 & 0 & -1 & 0 & 0 & 4 \\ 2 & 2 & 0 & -4 & 0 & 0 \\ 4 & 0 & 0 & -4 & 4 & -4 \\ 2 & 0 & 2 & 0 & 0 & -4 \end{bmatrix}$$

$$\alpha^T = [\alpha_1, \alpha_2, \alpha_3, \alpha_4, \alpha_5, \alpha_6]$$

$$u_c^T = [u_1, u_2, u_3, u_4, u_5, u_6]$$

From Eqn. A.3 and A.4, the shape functions for the six-noded triangle are obtained as

$$N_1(\xi, \eta) = 1 - 3\xi - 3\xi + 2\xi^2 + 4\xi\eta + 2\eta^2 \quad (\text{A.15})$$

$$\begin{aligned}
 &= (1 - \xi - \eta)(1 - 2\xi - 2\eta) \\
 N_2(\xi, \eta) &= -\xi + 2\xi^2 = \xi(2\xi - 1) \\
 N_3(\xi, \eta) &= -\eta + 2\eta^2 = \eta(2\eta - 1) \\
 N_4(\xi, \eta) &= 4\xi - 4\xi^2 - 4\xi\eta = 4\xi(1 - \xi - \eta) \\
 N_5(\xi, \eta) &= 4\xi\eta \\
 N_6(\xi, \eta) &= 4\eta - 4\xi\eta - 4\eta^2 = 4\eta(1 - \xi - \eta)
 \end{aligned}$$

A.2.2 Eight-Noded Rectangular Elements

The eight-noded rectangular element, shown in Fig. A.2, is described by an incomplete third-degree polynomial with eight independent coefficients having the form,

$$u(x, y) = c_1 + c_2x + c_3y + c_4x^2 + c_5xy + c_6y^2 + c_7x^2y + c_8xy^2 \quad (\text{A.16})$$

The function can be expressed in terms of nodal variable as

$$u(x, y) = \sum_{i=1}^8 u_i^e \psi_i(x, y) \quad (\text{A.17})$$

These types of elements with eight nodes are called the serendipity elements and the shape functions of these elements cannot be obtained using the tensor products of one-dimensional interpolation functions, similar to the ones given in Eqn. A.2. Instead, an alternative procedure that employs the interpolation function properties use (Reddy, 1993),

$$\begin{aligned}
 \sum_{i=1}^8 \psi_i^{(e)} &= 1 \\
 \sum_{i=1}^8 \frac{\partial \psi_i^{(e)}}{\partial x} &= 0 \\
 \sum_{i=1}^8 \frac{\partial \psi_i^{(e)}}{\partial y} &= 1
 \end{aligned} \quad (\text{A.18})$$

Using the isoparametric variables and the second form of Fig. A.2, the displacement polynomial can be written as

$$u(\xi, \eta) = \alpha_1 + \alpha_2\xi + \alpha_3\eta + \alpha_4\xi^2 + \alpha_5\xi\eta + \alpha_6\eta^2 + \alpha_7\xi^2\eta + \alpha_8\xi\eta^2 \quad (\text{A.19})$$

where $-1 < \xi < +1$ and $-1 < \eta < +1$. Eqn. A.20 is related to the nodal variables as

$$\{\alpha\} = [A]\{u_e\} \quad (\text{A.20})$$

where

$$A = \begin{bmatrix} 1 & 0 & 0 & 0 & 0 & 0 & 0 & 0 \\ -3 & -1 & 0 & 0 & 4 & 0 & 0 & 0 \\ -3 & 0 & 0 & -1 & 0 & 0 & 0 & 4 \\ 2 & 2 & 0 & 0 & -4 & 0 & 0 & 0 \\ 5 & -1 & -3 & -1 & -4 & 4 & 4 & 4 \\ 2 & 0 & 0 & 2 & 0 & 0 & 0 & -4 \\ -2 & -2 & 2 & 2 & 4 & 0 & -4 & 0 \\ -2 & 2 & 2 & -2 & 0 & -4 & 0 & 4 \end{bmatrix}$$

From the matrix A, given by Eqn. A.20, the shape functions for this element are obtained as

$$N_1(\xi, \eta) = (1 - \xi)(1 - \eta)(1 - 2\xi - 2\eta) \quad (\text{A.21})$$

$$N_2(\xi, \eta) = -\xi(1 - \eta)(1 - 2\xi - 2\eta)$$

$$N_3(\xi, \eta) = -\xi\eta(3 - 2\xi - 2\eta)$$

$$N_4(\xi, \eta) = -\eta(1 - \xi)(1 + 2\xi - 2\eta)$$

$$N_5(\xi, \eta) = 4\xi(1 - \xi)(1 - \eta)$$

$$N_6(\xi, \eta) = 4\xi\eta(1 - \eta)$$

$$\begin{aligned}
 N_7(\xi, \eta) &= 4\xi\eta(1 - \xi) \\
 N_8(\xi, \eta) &= 4\eta(1 - \xi)(1 - \eta)
 \end{aligned}$$

Two typical functions, $N_1(\xi, \eta)$ and $N_5(\xi, \eta)$, are shown in Fig. A.3.

A.3 Shell Element

A.3.1 Element Geometry

In the formulation of degenerate curved shell elements, four different coordinate systems are used: (1) Global coordinate (x, y, z) (Figure A.4) is a Cartesian coordinate system, freely chosen, in relation to which the geometry of the structure is defined in space; (2) A nodal coordinate system (x_i, y_i, z_i) is defined at each nodal point with origin at the reference surface; (3) A curvilinear orthogonal coordinate set (ξ, η, ζ) . ξ, η are two curvilinear coordinates in the middle plane of the shell element and ζ is a rectilinear coordinate in the thickness direction. It is assumed that ξ, η and ζ vary between -1 and +1 on the respective faces of the element; and (4) Local coordinate set (x'_i, y'_i, z'_i) is a Cartesian coordinate system defined at the sampling points wherein stresses and strains are to be calculated. The direction z' is taken perpendicular to the surface $\zeta = \text{constant}$. The direction x' can be taken tangent to the ξ -direction at the sampling point.

The global coordinates of pairs of points on the top and bottom surface at each node (Figure A.4) are usually input to define the element geometry. Alternatively, the mid-surface nodal coordinates and the corresponding directional thickness can be furnished. The global coordinate at any point of the shell can be expressed as

$$\begin{Bmatrix} x \\ y \\ z \end{Bmatrix} = \sum_{i=1}^n N_i(\xi, \eta) \begin{Bmatrix} x_i \\ y_i \\ z_i \end{Bmatrix}_{middle} + \sum_{i=1}^n N_i(\xi, \eta) \frac{\zeta}{2} \mathbf{V}_{3i} \quad (\text{A.22})$$

where N_i is shape function,

$$\begin{Bmatrix} x_i \\ y_i \\ z_i \end{Bmatrix}_{middle} = \frac{1}{2} \left(\begin{Bmatrix} x_i \\ y_i \\ z_i \end{Bmatrix}_{top} + \begin{Bmatrix} x_i \\ y_i \\ z_i \end{Bmatrix}_{bottom} \right)$$

are the global coordinates of nodes on the middle surface.

\mathbf{V}_{3i} is the vector from the bottom of i th node to the top. It can be expressed as

$$\mathbf{V}_{3i} = \begin{Bmatrix} V_{3ix} \\ V_{3iy} \\ V_{3iz} \end{Bmatrix} = \left(\begin{Bmatrix} x_i \\ y_i \\ z_i \end{Bmatrix}_{top} - \begin{Bmatrix} x_i \\ y_i \\ z_i \end{Bmatrix}_{bottom} \right) = \begin{Bmatrix} \Delta x_i \\ \Delta y_i \\ \Delta z_i \end{Bmatrix}$$

When \mathbf{V}_{3i} is defined in the direction of the normal of the middle face, the thickness t_i of point i can be expressed as

$$t_i = |\mathbf{V}_{3i}| = \sqrt{\Delta x_i^2 + \Delta y_i^2 + \Delta z_i^2}$$

The directional cosines of unit vector \mathbf{v}_{3i} of \mathbf{V}_{3i} is l_{3i} , m_{3i} and n_{3i} which can be expressed as

$$\mathbf{v}_{3i} = \begin{Bmatrix} l_{3i} \\ m_{3i} \\ n_{3i} \end{Bmatrix} = \frac{1}{t_i} \begin{Bmatrix} \Delta x_i \\ \Delta y_i \\ \Delta z_i \end{Bmatrix}$$

A.3.2 Displacement Field

According to the Kirchhoff constraints, a normal to the surface remains practically straight during deformation. Hence, the displacement of any point can be expressed in terms of three translational components u, v, w and two out-of-plane rotations α_i and β_i (Figure A.6). In the unit coordinate system \mathbf{v}_{ki} ($k = 1, 2, 3$), the displacement of any point in the element can be expressed as

$$\begin{Bmatrix} u \\ v \\ w \end{Bmatrix} = \sum_{i=1}^n N_i(\xi, \eta) \begin{Bmatrix} u_i \\ v_i \\ w_i \end{Bmatrix}_{middle} + \sum_{i=1}^n N_i(\xi, \eta) \frac{t_i}{2} \begin{bmatrix} l_{1i} & -l_{2i} \\ m_{1i} & -m_{2i} \\ n_{1i} & -n_{2i} \end{bmatrix} \begin{Bmatrix} \alpha_i \\ \beta_i \end{Bmatrix} \quad (\text{A.23})$$

where l_{ki} , m_{ki} and n_{ki} ($k=1, 2$) are the direction cosines of \mathbf{v}_{ki} ($k=1, 2$), respectively, i.e.

$$\mathbf{v}_{1i} = \begin{Bmatrix} l_{1i} \\ m_{1i} \\ n_{1i} \end{Bmatrix}$$

$$\mathbf{v}_{2i} = \begin{Bmatrix} l_{2i} \\ m_{2i} \\ n_{2i} \end{Bmatrix}$$

When the vector \mathbf{v}_{3i} defines the direction of the normal at node i , vector \mathbf{v}_{1i} is unit vector perpendicular to \mathbf{v}_{3i} and parallel to the global xz -plane. And the vector \mathbf{v}_{2i} is unit vector which is perpendicular to the plane defined by \mathbf{v}_{1i} and \mathbf{v}_{3i} . Vectors \mathbf{v}_{1i} and \mathbf{v}_{2i} define the rotations (α_i and β_i respectively) of the corresponding normal.

Hence, all the equation can be transferred to the middle surface. The displacement is written as

$$\begin{Bmatrix} u \\ v \\ w \end{Bmatrix} = [\mathbf{N}_1 \mathbf{N}_2 \cdots \mathbf{N}_n] \begin{Bmatrix} \mathbf{a}_1 \\ \mathbf{a}_2 \\ \vdots \\ \mathbf{a}_n \end{Bmatrix} \quad (\text{A.24})$$

where

$$\mathbf{a}_i = [u_i \ v_i \ w_i \ \alpha_i \ \beta_i]^T \quad (i = 1, 2, \dots, n)$$

$$\mathbf{N}_i = \begin{bmatrix} N_i & 0 & 0 & N_i \zeta \frac{t_i}{2} l_{1i} & -N_i \zeta \frac{t_i}{2} l_{2i} \\ 0 & N_i & 0 & N_i \zeta \frac{t_i}{2} m_{1i} & -N_i \zeta \frac{t_i}{2} m_{2i} \\ 0 & 0 & N_i & N_i \zeta \frac{t_i}{2} n_{1i} & -N_i \zeta \frac{t_i}{2} n_{2i} \end{bmatrix}$$

The unit vectors \mathbf{v}_{1i} and \mathbf{v}_{2i} are expressed as

$$\mathbf{v}_{1i} = \frac{\mathbf{i} \times \mathbf{V}_{3i}}{|\mathbf{i} \times \mathbf{V}_{3i}|}$$

$$\mathbf{v}_{2i} = \frac{\mathbf{V}_{3i} \times \mathbf{v}_{1i}}{|\mathbf{V}_{3i} \times \mathbf{v}_{1i}|}$$

A.3.3 Definitions of Strains and Stresses

According to Kirchhoff constraints, the stress in the direction of the normal to the middle surface is zero. Hence, the local coordinate is defined as the z' in the direction of the normal to the middle surface. The strains and stresses are calculated in the local coordinate system. The relationship between the global coordinate system $x y z$ and local coordinate system x', y' and z' is expressed as

$$\mathbf{X} = \theta \mathbf{X}' \quad (\text{A.25})$$

where $X = [x \ y \ z]^T$, $X' = [x' \ y' \ z']^T$, and

$$\theta = [\mathbf{v}_1 \ \mathbf{v}_2 \ \mathbf{v}_3] = \begin{bmatrix} l_1 & l_2 & l_3 \\ m_1 & m_2 & m_3 \\ n_1 & n_2 & n_3 \end{bmatrix}$$

Assuming that u', v', w' are the displacements in the local coordinate system x', y', z' , we have $\sigma_{z'} = 0$, and the strain is derived as

$$\epsilon' = \begin{Bmatrix} \epsilon'_x \\ \epsilon'_y \\ \gamma'_{x'y'} \\ \gamma'_{y'z'} \\ \gamma'_{z'x'} \end{Bmatrix} = \begin{Bmatrix} \frac{\partial u'}{\partial x'} \\ \frac{\partial v'}{\partial y'} \\ \frac{\partial u'}{\partial y'} + \frac{\partial v'}{\partial x'} \\ \frac{\partial v'}{\partial z'} + \frac{\partial w'}{\partial y'} \\ \frac{\partial u'}{\partial z'} + \frac{\partial w'}{\partial x'} \end{Bmatrix} = [\mathbf{B}'_1 \ \mathbf{B}'_2 \ \cdots \ \mathbf{B}'_n] \begin{Bmatrix} \mathbf{a}_1 \\ \mathbf{a}_2 \\ \vdots \\ \mathbf{a}_n \end{Bmatrix} \quad (\text{A.26})$$

The stress could be expressed for an isotropic body as

$$\sigma' = [\sigma_{x'} \ \sigma_{y'} \ \tau_{x'y'} \ \tau_{y'z'} \ \tau_{z'x'}]^T = \mathbf{D}\epsilon' \quad (\text{A.27})$$

where

$$D = \frac{E}{1-\nu^2} \begin{bmatrix} 1 & \nu & 0 & 0 & 0 \\ & 1 & 0 & 0 & 0 \\ & & \frac{1-\nu}{2} & 0 & 0 \\ & & & \frac{1-\nu}{2p} & 0 \\ \text{Symmetric} & & & & \frac{1-\nu}{2p} \end{bmatrix}$$

where p is correction coefficient equal to 1.2. It is a correction factor necessitated due to the nonuniform distribution of shear force along the thickness. The element stiffness matrix can be expressed in curvilinear coordinate system as

$$K^e = \int_{-1}^1 \int_{-1}^1 \int_{-1}^1 B^T D B' |J| d\xi d\eta d\zeta \quad (\text{A.28})$$

where

$$J = \begin{bmatrix} \frac{\partial x}{\partial \xi} & \frac{\partial y}{\partial \xi} & \frac{\partial z}{\partial \xi} \\ \frac{\partial x}{\partial \eta} & \frac{\partial y}{\partial \eta} & \frac{\partial z}{\partial \eta} \\ \frac{\partial x}{\partial \zeta} & \frac{\partial y}{\partial \zeta} & \frac{\partial z}{\partial \zeta} \end{bmatrix}$$

In a similar manner, the mass and damping matrices are obtained as

$$M^e = \int_{-1}^1 \int_{-1}^1 \int_{-1}^1 \rho N^T N |J| d\xi d\eta d\zeta \quad (\text{A.29})$$

$$C^e = \int_{-1}^1 \int_{-1}^1 \int_{-1}^1 \mu N^T N |J| d\xi d\eta d\zeta \quad (\text{A.30})$$

The load vector is given by

$$Q^e = \int_{-1}^1 \int_{-1}^1 \int_{-1}^1 N^T f |J| d\xi d\eta d\zeta + \int_{-1}^1 \int_{-1}^1 N^T T |J_s| d\xi d\eta \quad (\text{A.31})$$

The isoparametric shape functions used for the eight-noded quadrilateral elements and six-noded triangular elements are given in Appendix A.2.

The integrals given in the above equations cannot be evaluated in a closed form; hence it has to be approximated by numerical integration. The details of this numerical integration procedure for element stiffness, mass and damping matrices are given in any standard finite element text (Schwarz 1988, Reddy 1993).

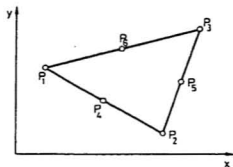


Figure A.1: Node points for quadratic approximation in triangular element

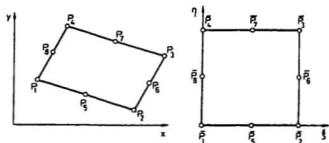


Figure A.2: Node points for quadratic approximation of serendipity class

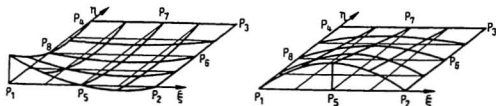


Figure A.3: Shape function, quadratic approximation of serendipity class

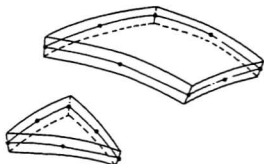


Figure A.4: 8 noded quadrilateral and 6 noded triangular elements

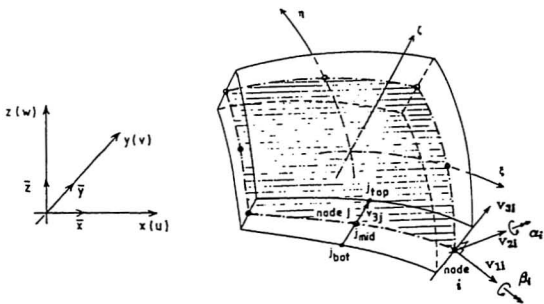


Figure A.5: (a) Global coordinate system and displacements (b) Nodal coordinate system at node i and curvilinear coordinates

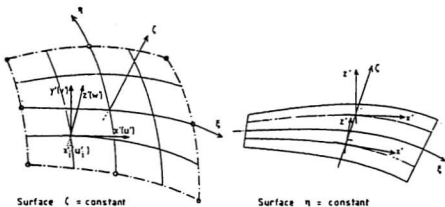
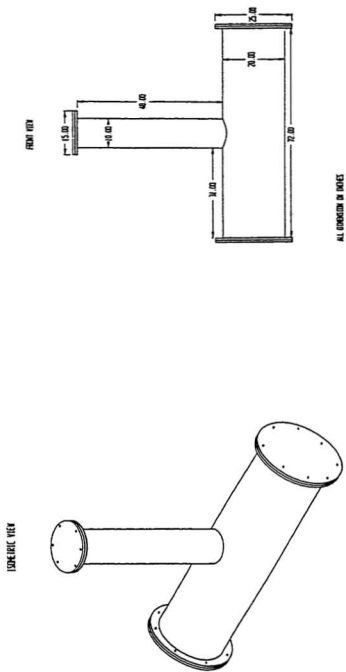


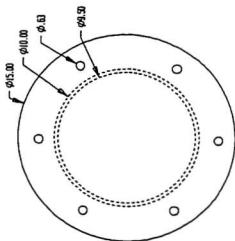
Figure A.6: Local coordinate system

Appendix B

Detailed Structural Drawings of Tubular T-Joint

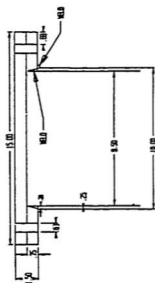


TOP VIEW OF THE TOP FLANGE

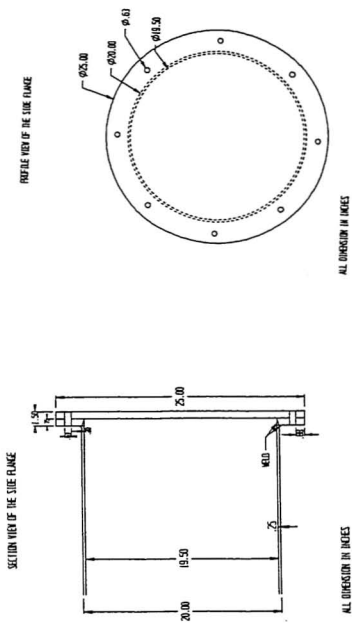


ALL DIMENSION IN INCHES

SECTION VIEW OF THE TOP FLANGE



ALL DIMENSION IN INCHES



Appendix C

Specifications for Welding Procedures

Welding Procedure Specification (WPS)

Welding Procedure Specification for the Welding of Tee Joints by the Manual Shielded Metal Arc Process in G40.21 Grade 350 WT Materials and Lloyds LT60

1. Scope

This specification covers welding and related operations for the fabrication of Tee type joints, and is generally in accordance with CSA Standard W59-1982 "Welded Steel Construction" (Metal Arc Welding).

2. Related Specifications

CSA W59-1982	Welded Steel Construction (Metal Arc Welding)
CSA W48.1-M1980	Mild Steel Covered Arc Welding Electrodes
CSA W47.1-1973	Certification of Companies for Fusion Welding of Steel Structures
UKOSRP	United Kingdom Offshore Steels Research Project - Guidelines
CSA G40.21	Structural Quality Steels

3. Welding

Welding will be performed by the Manual Shielded Metal Arc Process.

4. Base Metal

The base metal shall conform to the requirements of CSA G40.21 Grade 350 WT "Weldable Notch Tough Steel", or its equivalent.

5. Base Metal Thickness

This specification covers the welding the base metal in thicknesses up to 100mm.

6. Consumables

- a) Electrodes shall be based electrodes in accordance with the requirements of CSA Standard W48.1 and shall be of the E48018 classification.
- b) Storage and conditioning of electrodes shall be carried out in accordance with the requirements shown in Section 22 of this specification.

7. Weld Preparation

The welding preparation shall conform generally to the joint type M5-2 for the T-joints and M4-4 without backing for the pipe to plate joints.

8. Position of Welding

Welding shall be in the vertical up welding position (3G) for straight T joints. Welding will be in the horizontal welding position (2G) for pipe to plate joints.

9. Electrode Size and Weave

- a) The electrode diameters shall be as follows:
- | | |
|-------------|-----------------------------------|
| Root Run | 3.25mm diameter electrode |
| Fill to Cap | 3.25 or 4.0mm diameter electrodes |
- b) Maximum permissible weave allowed during Vertical Welding
- | | |
|---------|-------------------|
| 3-1/4mm | Max. Weave = 8mm |
| 4mm | Max. Weave = 10mm |

10. Preparation

Edges and surface of parts to be welded shall be prepared by flame-cutting. They shall be smooth, uniform and free from fins, tears, cracks and other defects which would adversely affect the quality or strength of the weld. Surfaces to be welded shall also be free, within two inches of any weld location, from loose or thick scale (except for tightly adhering small islands of scale), slag, rust, paint, grease, moisture and other foreign material that will prevent proper welding or produce objectionable fumes.

11. Run-Off Plates

Run-off plates used for the welding may be any of the steels or their equivalents as defined in CSA W59.

12. Preheat

- a) Prior to tacking or welding, the base metal shall be preheated and the heat maintained during welding at the minimum temperature shown in the following table.

Up to 15mm inc.	None*
Over 15mm to 38mm inc.	15°C
Over 38mm to 60mm inc.	70°C
Over 60mm	120°C

*When the base metal temperature is below 0°C, preheat the base metal to 15°C and maintain this temperature during welding.

- b) Preheating will be accomplished by means of flame torches.
- c) Preheating shall consist of heating a band of the base metal equal to the thickness of the base metal, but not less than 3 inches on either side of the joint to the desired temperature, and maintaining this temperature during welding.

13. Distortion Control

- a) In assembling and joining, the procedure and sequence shall be such as will minimize distortion and shrinkage.
- b) In so far as practicable, all welds shall be deposited in a sequence that will balance the applied heat of welding while the welding progresses.

14. Electrical Characteristics

The type of current, polarity and typical current value for any electrode class or size shall be substantially as shown in the attached Welding Data Sheets and may be altered to within 15% above or below the typical value.

15. Workmanship

All welding and its related operations shall be performed in accordance with good welding practice and within the recommendations and limitations outlined in CSA W59-1982.

16. Appearance of Welding Layers

The welding current and the manner of depositing the weld metal shall be such that undercutting on the side walls of the welding groove or the adjoining base material shall be limited to .25mm for areas subject to fatigue testing.

17. Cleaning

Cleaning of previously deposited layers shall be done by wire brushing or by mechanical means, if necessary, before the next layer is deposited.

18. Defects

Surface defects appearing on any weld bead shall be removed by grinding and rewelded, if necessary, before the next layer is deposited.

19. Treatment of Second Side of Welding Groove

The root of the joint shall be arc-gouged, when required by the WDS, to produce a groove contour substantially conforming to the prequalified single U-joint, and its depth shall be adequate to ensure complete penetration into the previously deposited weld metal.

20. Finished Joint Profile

The weld profile shall conform to a 45° reinforcing fillet as shown in the attached figure, and the capping runs shall be carried out by first depositing a buttering run, to give a good weld toe angle and then filling in the bulk of the capping runs. In all cases, the weld toe angle shall conform to the "dime" test as indicated in the figure. That is, a disc of radius $t/2$ (but the radius shall be a minimum of 8mm and a maximum of 25mm) shall be placed against the buttering weld run and the longitudinal plate, and a 1mm diameter wire shall not pass between the disc and the buttering run in the weld toe region. In all cases, the maximum amount of undercut at the weld toe shall not exceed 0.25mm. Weld leg lengths shall be as described by the Client.

21. Post Weld Heat Treatment

Post weld heat treatment is not required.

22. Storage and Conditioning of Electrodes

Basic Electrodes - All basic electrodes should be delivered in hermetically-sealed containers. All containers showing evidence of damage should not be accepted.

When a container is opened, all electrodes shall be stored in ovens held at a temperature of at least 120°C.

Basic electrodes of E480 classification that are not used within 4 hours after removal from ovens shall be discarded.

Appendix D

Equations for Static Strains and Stresses

D.1 Static Strains

Results from specimen 2 were used for relating cycles with static strains, stresses, natural frequencies and damping ratios since the cycles were monitored more carefully than specimen 1. Specimen 3 was used for relating crack profile with the static strains, static stress and dynamic measurements of frequency and damping since ink staining and beach markings were more clearly visible in specimen 3. The equations were developed by interpolating points with spline interpolation and curve fitting in a least-square sense. The equations would be applicable for all the specimens with small modifications since the difference in results between them was small.

The equations for strains and fatigue cycles were normalized as $\epsilon^* = \epsilon/\epsilon_0$ and $x = N/N_f$, where ϵ_0 was the strain at zero fatigue cycle and N_f was the final fatigue cycle. The equations were developed based on the results of specimen 2.

For channel 7:

$$\epsilon_f^* = 1.991315 \times 10^{13} x^{24} - 2.364114 \times 10^{14} x^{23} + 1.321213 \times 10^{15} x^{22} \quad (\text{D.1})$$

$$\begin{aligned}
& -4.621572 \times 10^{15} x^{21} + 1.134915 \times 10^{16} x^{20} - 2.080142 \times 10^{16} x^{19} \\
& + 2.953506 \times 10^{16} x^{18} - 3.328130 \times 10^{16} x^{17} + 3.024909 \times 10^{16} x^{16} \\
& - 2.241629 \times 10^{16} x^{15} + 1.363725 \times 10^{16} x^{14} - 6.836158 \times 10^{15} x^{13} \\
& + 2.826553 \times 10^{15} x^{12} - 9.625092 \times 10^{14} x^{11} + 2.688344 \times 10^{14} x^{10} \\
& - 6.116450 \times 10^{13} x^9 + 1.121990 \times 10^{13} x^8 - 1.635391 \times 10^{12} x^7 \\
& + 1.855631 \times 10^{11} x^6 - 1.591776 \times 10^{10} x^5 + 9.883527 \times 10^8 x^4 \\
& - 4.144858 \times 10^7 x^3 + 1.035855 \times 10^6 x^2 - 1.147139 \times 10^4 x^1 \\
& + 3.925651
\end{aligned}$$

For channel 8:

$$\begin{aligned}
\epsilon_8^* = & 3.421592 \times 10^{13} x^{24} - 4.108024 \times 10^{14} x^{23} + 2.322217 \times 10^{15} x^{22} \quad (\text{D.2}) \\
& - 8.218331 \times 10^{15} x^{21} + 2.042344 \times 10^{16} x^{20} - 3.789192 \times 10^{16} x^{19} \\
& 5.447584 \times 10^{16} x^{18} - 6.217420 \times 10^{16} x^{17} + 5.725347 \times 10^{16} x^{16} \\
& - 4.300018 \times 10^{16} x^{15} + 2.652079 \times 10^{16} x^{14} - 1.348199 \times 10^{16} x^{13} \\
& + 5.654564 \times 10^{15} x^{12} - 1.953648 \times 10^{15} x^{11} + 5.537323 \times 10^{14} x^{10} \\
& - 1.278580 \times 10^{14} x^9 + 2.380278 \times 10^{13} x^8 - 3.520593 \times 10^{12} x^7 \\
& + 4.052535 \times 10^{11} x^6 - 3.525147 \times 10^{10} x^5 + 2.218299 \times 10^9 x^4 \\
& - 9.421511 \times 10^7 x^3 + 2.382525 \times 10^6 x^2 - 2.665860 \times 10^4 x \\
& + 6.589210
\end{aligned}$$

For channel 9

$$\begin{aligned}
\epsilon_9^* = & 2.527562 \times 10^{13} x^{24} - 3.010564 \times 10^{14} x^{23} + 1.688145 \times 10^{15} x^{22} \quad (\text{D.3}) \\
& - 5.925533 \times 10^{15} x^{21} + 1.460321 \times 10^{16} x^{20} - 2.686426 \times 10^{16} x^{19} \\
& + 3.828863 \times 10^{16} x^{18} - 4.331501 \times 10^{16} x^{17} + 3.952890 \times 10^{16} x^{16}
\end{aligned}$$

$$\begin{aligned}
& -2.941644 \times 10^{16} x^{15} + 1.797370 \times 10^{16} x^{14} - 9.050353 \times 10^{15} x^{13} \\
& + 3.759322 \times 10^{15} x^{12} - 1.286196 \times 10^{15} x^{11} + 3.609776 \times 10^{14} x^{10} \\
& - 8.253160 \times 10^{13} x^9 + 1.521436 \times 10^{13} x^8 - 2.228592 \times 10^{12} x^7 \\
& + 2.541118 \times 10^{11} x^6 - 2.190259 \times 10^{10} x^5 + 1.366272 \times 10^9 x^4 \\
& - 5.755119 \times 10^7 x^3 + 1.444259 \times 10^6 x^2 - 1.605252 \times 10^4 x \\
& + 4.834323
\end{aligned}$$

For channel 16:

$$\begin{aligned}
\epsilon_{16}^* = & -1.007982 \times 10^{13} x^{24} + 1.236709 \times 10^{14} x^{23} - 7.146984 \times 10^{14} x^{22} \text{(D.4)} \\
& + 2.586837 \times 10^{15} x^{21} - 6.577501 \times 10^{15} x^{20} + 1.249117 \times 10^{16} x^{19} \\
& - 1.838889 \times 10^{16} x^{18} + 2.149877 \times 10^{16} x^{17} - 2.028592 \times 10^{16} x^{16} \\
& + 1.561583 \times 10^{16} x^{15} - 9.873311 \times 10^{15} x^{14} + 5.145794 \times 10^{15} x^{13} \\
& - 2.212655 \times 10^{15} x^{12} + 7.836419 \times 10^{14} x^{11} - 2.276184 \times 10^{14} x^{10} \\
& + 5.383736 \times 10^{13} x^9 - 1.026054 \times 10^{13} x^8 + 1.552400 \times 10^{12} x^7 \\
& - 1.826149 \times 10^{11} x^6 + 1.621446 \times 10^{10} x^5 - 1.040110 \times 10^9 x^4 \\
& + 4.496428 \times 10^7 x^3 - 1.155507 \times 10^6 x^2 + 1.311272 \times 10^4 x \\
& - 1.016011
\end{aligned}$$

For channel 17:

$$\begin{aligned}
\epsilon_{17}^* = & +2.748238 \times 10^{13} x^{24} - 3.319814 \times 10^{14} x^{23} + 1.887913 \times 10^{15} x^{22} \text{(D.5)} \\
& - 6.720626 \times 10^{15} x^{21} + 1.679792 \times 10^{16} x^{20} - 3.134241 \times 10^{16} x^{19} \\
& + 4.531189 \times 10^{16} x^{18} - 5.200058 \times 10^{16} x^{17} + 4.814601 \times 10^{16} x^{16} \\
& - 3.635488 \times 10^{16} x^{15} + 2.254173 \times 10^{16} x^{14} - 1.151960 \times 10^{16} x^{13}
\end{aligned}$$

$$\begin{aligned}
&+4.856658 \times 10^{15} x^{12} - 1.686585 \times 10^{15} x^{11} + 4.804491 \times 10^{14} x^{10} \\
&-1.114848 \times 10^{14} x^9 + 2.085449 \times 10^{13} x^8 - 3.098873 \times 10^{12} x^7 \\
&+3.583016 \times 10^{11} x^6 - 3.129946 \times 10^{10} x^5 + 1.977458 \times 10^9 x^4 \\
&-8.429736 \times 10^7 x^3 + 2.138969 \times 10^6 x^2 - 2.400325 \times 10^4 x \\
&+5.717370
\end{aligned}$$

For channel 18:

$$\begin{aligned}
\epsilon_{18}^* = & -3.593606 \times 10^{12} x^{24} + 4.539315 \times 10^{13} x^{23} - 2.697133 \times 10^{14} x^{22} \text{ (D.6)} \\
& +1.002440 \times 10^{15} x^{21} - 2.614252 \times 10^{15} x^{20} + 5.086286 \times 10^{15} x^{19} \\
& -7.663013 \times 10^{15} x^{18} + 9.159149 \times 10^{15} x^{17} - 8.826646 \times 10^{15} x^{16} \\
& +6.932565 \times 10^{15} x^{15} - 4.467775 \times 10^{15} x^{14} + 2.371113 \times 10^{15} x^{13} \\
& -1.037181 \times 10^{15} x^{12} + 3.733058 \times 10^{14} x^{11} - 1.100834 \times 10^{14} x^{10} \\
& +2.640717 \times 10^{13} x^9 - 5.098982 \times 10^{12} x^8 + 7.808013 \times 10^{11} x^7 \\
& -9.286331 \times 10^{10} x^6 + 8.327829 \times 10^9 x^5 - 5.389994 \times 10^8 x^4 \\
& +2.348708 \times 10^7 x^3 - 6.078053 \times 10^5 x^2 + 6.935438 \times 10^3 x \\
& +1.101579e - 1
\end{aligned}$$

For channel 22:

$$\begin{aligned}
\epsilon_{22}^* = & 6.730554 \times 10^{13} x^{24} - 8.163292 \times 10^{14} x^{23} + 4.662209 \times 10^{15} x^{22} \text{ (D.7)} \\
& -1.667177 \times 10^{16} x^{21} + 4.186912 \times 10^{16} x^{20} - 7.851257 \times 10^{16} x^{19} \\
& +1.141004 \times 10^{17} x^{18} - 1.316577 \times 10^{17} x^{17} + 1.225885 \times 10^{17} x^{16} \\
& -9.310719 \times 10^{16} x^{15} + 5.807750 \times 10^{16} x^{14} - 2.986168 \times 10^{16} x^{13} \\
& +1.266808 \times 10^{16} x^{12} - 4.426912 \times 10^{15} x^{11} + 1.269002 \times 10^{15} x^{10}
\end{aligned}$$

$$\begin{aligned}
& -2.963013 \times 10^{14} x^9 + 5.576707 \times 10^{13} x^8 - 8.336307 \times 10^{12} x^7 \\
& + 9.694286 \times 10^{11} x^6 - 8.514926 \times 10^{10} x^5 + 5.407343 \times 10^9 x^4 \\
& - 2.316105 \times 10^8 x^3 + 5.902429 \times 10^6 x^2 - 6.648238 \times 10^4 x \\
& + 1.306277 \times 10
\end{aligned}$$

For channel 23:

$$\begin{aligned}
\epsilon_{23}^* = & +6.525651 \times 10^{13} x^{24} - 7.913725 \times 10^{14} x^{23} + 4.519071 \times 10^{15} x^{22} \text{ (D.8)} \\
& - 1.615773 \times 10^{16} x^{21} + 4.057260 \times 10^{16} x^{20} - 7.607084 \times 10^{16} x^{19} \\
& + 1.105365 \times 10^{17} x^{18} - 1.275275 \times 10^{17} x^{17} + 1.187261 \times 10^{17} x^{16} \\
& - 9.016099 \times 10^{16} x^{15} + 5.623186 \times 10^{16} x^{14} - 2.890868 \times 10^{16} x^{13} \\
& + 1.226211 \times 10^{16} x^{12} - 4.284461 \times 10^{15} x^{11} + 1.228004 \times 10^{15} x^{10} \\
& - 2.866915 \times 10^{14} x^9 + 5.395165 \times 10^{13} x^8 - 8.063961 \times 10^{12} x^7 \\
& + 9.376505 \times 10^{11} x^6 - 8.234919 \times 10^{10} x^5 + 5.229004 \times 10^9 x^4 \\
& - 2.239512 \times 10^8 x^3 + 5.706759 \times 10^6 x^2 - 6.427352 \times 10^4 x \\
& + 1.268155 \times 10
\end{aligned}$$

For channel 24:

$$\begin{aligned}
\epsilon_{24}^* = & +9.251842 \times 10^{13} x^{24} - 1.120335 \times 10^{15} x^{23} + 6.388683 \times 10^{15} x^{22} \text{ (D.9)} \\
& - 2.281230 \times 10^{16} x^{21} + 5.721086 \times 10^{16} x^{20} - 1.071397 \times 10^{17} x^{19} \\
& + 1.555080 \times 10^{17} x^{18} - 1.792228 \times 10^{17} x^{17} + 1.666881 \times 10^{17} x^{16} \\
& - 1.264652 \times 10^{17} x^{15} + 7.880500 \times 10^{16} x^{14} - 4.048013 \times 10^{16} x^{13} \\
& + 1.715711 \times 10^{16} x^{12} - 5.990494 \times 10^{15} x^{11} + 1.715835 \times 10^{15} x^{10} \\
& - 4.003327 \times 10^{14} x^9 + 7.529430 \times 10^{13} x^8 - 1.124806 \times 10^{13} x^7
\end{aligned}$$

For channel 8:

$$\begin{aligned}
 \epsilon_8^* = & 1.920301 \times 10^{12} s^{24} - 2.249977 \times 10^{13} s^{23} + 1.237539 \times 10^{14} s^{22} \quad (D.11) \\
 & - 4.246713 \times 10^{14} s^{21} + 1.019233 \times 10^{15} s^{20} - 1.817795 \times 10^{15} s^{19} \\
 & + 2.498614 \times 10^{15} s^{18} - 2.709234 \times 10^{15} s^{17} + 2.352585 \times 10^{15} s^{16} \\
 & - 1.651617 \times 10^{15} s^{15} + 9.423309 \times 10^{14} s^{14} - 4.376764 \times 10^{14} s^{13} \\
 & + 1.652228 \times 10^{14} s^{12} - 5.044545 \times 10^{13} s^{11} + 1.234906 \times 10^{13} s^{10} \\
 & - 2.391347 \times 10^{12} s^9 + 3.589229 \times 10^{11} s^8 - 4.045580 \times 10^{10} s^7 \\
 & + 3.245634 \times 10^9 s^6 - 1.659112 \times 10^8 s^5 + 3.689974 \times 10^6 s^4 \\
 & + 9.657576 \times 10^4 s^3 - 7.589174 \times 10^3 s^2 + 1.070477 \times 10^2 s + 1.672134
 \end{aligned}$$

For channel 9

$$\begin{aligned}
 \epsilon_9^* = & 1.426011 \times 10^{12} s^{24} - 1.672821 \times 10^{13} s^{23} + 9.210587 \times 10^{13} s^{22} \quad (D.12) \\
 & - 3.163558 \times 10^{14} s^{21} + 7.598459 \times 10^{14} s^{20} - 1.355994 \times 10^{15} s^{19} \\
 & + 1.864665 \times 10^{15} s^{18} - 2.022364 \times 10^{15} s^{17} + 1.756246 \times 10^{15} s^{16} \\
 & - 1.232776 \times 10^{15} s^{15} + 7.030881 \times 10^{14} s^{14} - 3.263420 \times 10^{14} s^{13} \\
 & + 1.230739 \times 10^{14} s^{12} - 3.752566 \times 10^{13} s^{11} + 9.169467 \times 10^{12} s^{10} \\
 & - 1.771267 \times 10^{12} s^9 + 2.649620 \times 10^{11} s^8 - 2.972157 \times 10^{10} s^7 \\
 & + 2.366201 \times 10^9 s^6 - 1.190829 \times 10^8 s^5 + 2.483673 \times 10^6 s^4 \\
 & + 8.162616 \times 10^4 s^3 - 5.843574 \times 10^3 s^2 + 8.133170 \times 10 s \\
 & + 1.501920
 \end{aligned}$$

For channel 16

$$\epsilon_{16}^* = 1.594411 \times 10^{12} s^{24} - 1.863864 \times 10^{13} s^{23} + 1.023470 \times 10^{14} s^{22} \quad (D.13)$$

$$\begin{aligned}
& -3.508746 \times 10^{14} s^{21} + 8.419612 \times 10^{14} s^{20} - 1.502669 \times 10^{15} s^{19} \\
& + 2.068966 \times 10^{15} s^{18} - 2.249801 \times 10^{15} s^{17} + 1.961955 \times 10^{15} s^{16} \\
& - 1.385574 \times 10^{15} s^{15} + 7.969031 \times 10^{14} s^{14} - 3.740989 \times 10^{14} s^{13} \\
& + 1.432309 \times 10^{14} s^{12} - 4.456037 \times 10^{13} s^{11} + 1.118828 \times 10^{13} s^{10} \\
& - 2.243642 \times 10^{12} s^9 + 3.540164 \times 10^{11} s^8 - 4.303213 \times 10^{10} s^7 \\
& + 3.909447 \times 10^9 s^6 - 2.537574 \times 10^8 s^5 + 1.095294 \times 10^7 s^4 \\
& - 2.769970 \times 10^5 s^3 + 3.217298 \times 10^3 s^2 - 2.182397 \times 10^1 s \\
& + 1.563734
\end{aligned}$$

For channel 17:

$$\begin{aligned}
\epsilon_{17}^* &= 1.557560 \times 10^{12} s^{24} - 1.816033 \times 10^{13} s^{23} + 9.942583 \times 10^{13} s^{22} \quad (\text{D.14}) \\
& - 3.397094 \times 10^{14} s^{21} + 8.119971 \times 10^{14} s^{20} - 1.442625 \times 10^{15} s^{19} \\
& + 1.975697 \times 10^{15} s^{18} - 2.134723 \times 10^{15} s^{17} + 1.847314 \times 10^{15} s^{16} \\
& - 1.292350 \times 10^{15} s^{15} + 7.345910 \times 10^{14} s^{14} - 3.397359 \times 10^{14} s^{13} \\
& + 1.275811 \times 10^{14} s^{12} - 3.868387 \times 10^{13} s^{11} + 9.376717 \times 10^{12} s^{10} \\
& - 1.788481 \times 10^{12} s^9 + 2.618051 \times 10^{11} s^8 - 2.819692 \times 10^{10} s^7 \\
& + 2.054116 \times 10^9 s^6 - 7.877090 \times 10^7 s^5 - 9.502211 \times 10^5 s^4 \\
& + 2.672986 \times 10^5 s^3 - 1.153375 \times 10^4 s^2 + 1.539355 \times 10^2 s \\
& + 1.524615
\end{aligned}$$

For channel 18

$$\begin{aligned}
\epsilon_{18}^* &= 1.252158 \times 10^{12} s^{24} - 1.462235 \times 10^{13} s^{23} + 8.019477 \times 10^{13} s^{22} \quad (\text{D.15}) \\
& - 2.745363 \times 10^{14} s^{21} + 6.576680 \times 10^{14} s^{20} - 1.171413 \times 10^{15} s^{19}
\end{aligned}$$

$$\begin{aligned}
& +1.609032 \times 10^{15} s^{18} - 1.744656 \times 10^{15} s^{17} + 1.516148 \times 10^{15} s^{16} \\
& - 1.066162 \times 10^{15} s^{15} + 6.099355 \times 10^{14} s^{14} - 2.844062 \times 10^{14} s^{13} \\
& + 1.079509 \times 10^{14} s^{12} - 3.320452 \times 10^{13} s^{11} + 8.210372 \times 10^{12} s^{10} \\
& - 1.611877 \times 10^{12} s^9 + 2.466667 \times 10^{11} s^8 - 2.862258 \times 10^{10} s^7 \\
& + 2.410257 \times 10^9 s^6 - 1.360494 \times 10^8 s^5 + 4.248385 \times 10^6 s^4 \\
& - 1.673532 \times 10^4 s^3 - 2.945692 \times 10^3 s^2 + 4.827644 \times 10 s \\
& 1.433363
\end{aligned}$$

For channel 22

$$\begin{aligned}
\epsilon_{22}^* = & -3.616684 \times 10^{11} s^{24} + 4.256206 \times 10^{12} s^{23} - 2.338518 \times 10^{13} s^{22} \text{(D.16)} \\
& + 7.967029 \times 10^{13} s^{21} - 1.884737 \times 10^{14} s^{20} + 3.284493 \times 10^{14} s^{19} \\
& - 4.363177 \times 10^{14} s^{18} + 4.506832 \times 10^{14} s^{17} - 3.654741 \times 10^{14} s^{16} \\
& + 2.327275 \times 10^{14} s^{15} - 1.149853 \times 10^{14} s^{14} + 4.255739 \times 10^{13} s^{13} \\
& - 1.063590 \times 10^{13} s^{12} + 1.011995 \times 10^{12} s^{11} + 5.088427 \times 10^{11} s^{10} \\
& - 3.084470 \times 10^{11} s^9 + 9.380356 \times 10^{10} s^8 - 1.928915 \times 10^{10} s^7 \\
& + 2.836151 \times 10^9 s^6 - 2.985653 \times 10^8 s^5 + 2.187725 \times 10^7 s^4 \\
& - 1.050075 \times 10^6 s^3 + 2.925261 \times 10^4 s^2 - 3.494449 \times 10^2 s \\
& + 9.062033 \times 10^{-1}
\end{aligned}$$

For channel 23:

$$\begin{aligned}
\epsilon_{23}^* = & -4.550016 \times 10^{11} s^{24} + 5.288528 \times 10^{12} s^{23} - 2.870281 \times 10^{13} s^{22} \text{(D.17)} \\
& + 9.657631 \times 10^{13} s^{21} - 2.254998 \times 10^{14} s^{20} + 3.873912 \times 10^{14} s^{19} \\
& - 5.062093 \times 10^{14} s^{18} + 5.124377 \times 10^{14} s^{17} - 4.046462 \times 10^{14} s^{16}
\end{aligned}$$

$$\begin{aligned}
&+2.479334 \times 10^{14} s^{15} - 1.149692 \times 10^{14} s^{14} + 3.742665 \times 10^{13} s^{13} \\
&-6.179449 \times 10^{12} s^{12} - 1.380812 \times 10^{12} s^{11} + 1.445529 \times 10^{12} s^{10} \\
&-5.882957 \times 10^{11} s^9 + 1.584384 \times 10^{11} s^8 - 3.079910 \times 10^{10} s^7 \\
&+4.394801 \times 10^9 s^6 - 4.550445 \times 10^8 s^5 + 3.305276 \times 10^7 s^4 \\
&-1.580442 \times 10^6 s^3 + 4.400999 \times 10^4 s^2 - 5.274848 \times 10^2 s \\
&+9.013551 \times 10^{-1}
\end{aligned}$$

For channel 24:

$$\begin{aligned}
\epsilon_{24}^* &= -7.895349 \times 10^{11} s^{24} + 9.107066 \times 10^{12} s^{23} - 4.913818 \times 10^{13} s^{22} \text{(D.18)} \\
&+1.646884 \times 10^{14} s^{21} - 3.838950 \times 10^{14} s^{20} + 6.601953 \times 10^{14} s^{19} \\
&-8.666185 \times 10^{14} s^{18} + 8.855391 \times 10^{14} s^{17} - 7.109814 \times 10^{14} s^{16} \\
&+4.483559 \times 10^{14} s^{15} - 2.191634 \times 10^{14} s^{14} + 7.990691 \times 10^{13} s^{13} \\
&-1.932628 \times 10^{13} s^{12} + 1.451538 \times 10^{12} s^{11} + 1.154672 \times 10^{12} s^{10} \\
&-6.454155 \times 10^{11} s^9 + 1.932434 \times 10^{11} s^8 - 3.965095 \times 10^{10} s^7 \\
&+5.850702 \times 10^9 s^6 - 6.200979 \times 10^8 s^5 + 4.583615 \times 10^7 s^4 \\
&-2.221657 \times 10^6 s^3 + 6.251251 \times 10^4 s^2 - 7.538613 \times 10^2 s \\
&+8.217338 \times -1
\end{aligned}$$

It could be seen that the equations, developed above are valid only within a range of $0.15 < x < 0.80$; beyond this range the strains and life are not related by the developed equations. For these ranges ($0 < x < 0.15$ and $0.80 < x < 1.00$), higher order spline curve fitting or a piecewise equation that relates the variables within various ranges may be required. The crack initiation or early crack growth life could be reasonably obtained from this equation. A better relationship could be obtained by carrying out modification techniques that would match the average experimental

strains, stresses, crack depths and lengths to the theoretical strains, stresses, crack depths and lengths obtained from analysis.

D.2 Static Principal Stresses

The equations relating the non-dimensional static principal stresses $\sigma^* = \sigma_{crack}/\sigma_{uncracked}$ to corresponding non-dimensional fatigue cycles were derived using MATLAB (computer software) as:

Maximum principal stress σ_1 for gauge 1:

$$\begin{aligned} \sigma_{1,1}^* = & +3.649614 \times 10^{13} x^{24} - 4.365936 \times 10^{14} x^{23} + 2.459332 \times 10^{15} x^{22} \\ & - 8.673853 \times 10^{15} x^{21} + 2.148401 \times 10^{16} x^{20} - 3.973147 \times 10^{16} x^{19} \\ & + 5.694249 \times 10^{16} x^{18} - 6.479321 \times 10^{16} x^{17} + 5.949077 \times 10^{16} x^{16} \\ & - 4.455410 \times 10^{16} x^{15} + 2.740401 \times 10^{16} x^{14} - 1.389417 \times 10^{16} x^{13} \\ & + 5.812586 \times 10^{15} x^{12} - 2.003318 \times 10^{15} x^{11} + 5.664733 \times 10^{14} x^{10} \\ & - 1.305053 \times 10^{14} x^9 + 2.424350 \times 10^{13} x^8 - 3.578495 \times 10^{12} x^7 \\ & + 4.111311 \times 10^{11} x^6 - 3.569889 \times 10^{10} x^5 + 2.242735 \times 10^9 x^4 \\ & - 9.510756 \times 10^7 x^3 + 2.401733 \times 10^6 x^2 - 2.684149 \times 10^4 x \\ & + 6.797020 \end{aligned} \quad (D.19)$$

Minimum principal stress σ_2 for gauge 1:

$$\begin{aligned} \sigma_{1,2}^* = & -5.994807 \times 10^{12} x^{24} + 7.643564 \times 10^{13} x^{23} - 4.581750 \times 10^{14} x^{22} \\ & + 1.717122 \times 10^{15} x^{21} - 4.513521 \times 10^{15} x^{20} + 8.847580 \times 10^{15} x^{19} \\ & - 1.342525 \times 10^{16} x^{18} + 1.615592 \times 10^{16} x^{17} - 1.567071 \times 10^{16} x^{16} \\ & + 1.238431 \times 10^{16} x^{15} - 8.028371 \times 10^{15} x^{14} + 4.284724 \times 10^{15} x^{13} \end{aligned} \quad (D.20)$$

$$\begin{aligned}
& -1.884246 \times 10^{15} x^{12} + 6.816164 \times 10^{14} x^{11} - 2.019616 \times 10^{14} x^{10} \\
& + 4.866530 \times 10^{13} x^9 - 9.436463 \times 10^{12} x^8 + 1.450675 \times 10^{12} x^7 \\
& - 1.731610 \times 10^{11} x^6 + 1.558060 \times 10^{10} x^5 - 1.011472 \times 10^9 x^4 \\
& + 4.419498 \times 10^7 x^3 - 1.146437 \times 10^6 x^2 + 1.310793 \times 10^4 x \\
& - 5.871500 \times 10^{-1}
\end{aligned}$$

Maximum principal stress σ_1 for gauge 4:

$$\begin{aligned}
\sigma_{4,1}^* = & -6.228243 \times 10^{12} x^{24} + 7.740761 \times 10^{13} x^{23} - 4.527097 \times 10^{14} x^{22} \text{ (D.21)} \\
& + 1.656740 \times 10^{15} x^{21} - 4.255686 \times 10^{15} x^{20} + 8.158233 \times 10^{15} x^{19} \\
& - 1.211482 \times 10^{16} x^{18} + 1.427742 \times 10^{16} x^{17} - 1.357163 \times 10^{16} x^{16} \\
& + 1.051834 \times 10^{16} x^{15} - 6.691902 \times 10^{15} x^{14} + 3.507665 \times 10^{15} x^{13} \\
& - 1.516160 \times 10^{15} x^{12} + 5.395255 \times 10^{14} x^{11} - 1.573883 \times 10^{14} x^{10} \\
& + 3.737114 \times 10^{13} x^9 - 7.147201 \times 10^{12} x^8 + 1.084719 \times 10^{12} x^7 \\
& - 1.279505 \times 10^{11} x^6 + 1.138821 \times 10^{10} x^5 - 7.320616 \times 10^8 x^4 \\
& + 3.170547 \times 10^7 x^3 - 8.160703 \times 10^5 x^2 + 9.270480 \times 10^3 x \\
& - 3.548114 \times 10^{-1}
\end{aligned}$$

Minimum principal σ_2 for gauge 4:

$$\begin{aligned}
\sigma_{4,2}^* = & -2.994547 \times 10^{12} x^{24} + 3.700517 \times 10^{13} x^{23} - 2.160165 \times 10^{14} x^{22} \text{ (D.22)} \\
& + 7.918644 \times 10^{14} x^{21} - 2.044044 \times 10^{15} x^{20} + 3.948940 \times 10^{15} x^{19} \\
& - 5.924403 \times 10^{15} x^{18} + 7.068672 \times 10^{15} x^{17} - 6.814546 \times 10^{15} x^{16} \\
& + 5.363770 \times 10^{15} x^{15} - 3.469317 \times 10^{15} x^{14} + 1.850111 \times 10^{15} x^{13} \\
& - 8.139459 \times 10^{14} x^{12} + 2.948505 \times 10^{14} x^{11} - 8.755141 \times 10^{13} x^{10}
\end{aligned}$$

$$\begin{aligned}
&+2.115401 \times 10^{13} x^9 - 4.114670 \times 10^{12} x^8 + 6.346824 \times 10^{11} x^7 \\
&-7.602325 \times 10^{10} x^6 + 6.864136 \times 10^9 x^5 - 4.471031 \times 10^8 x^4 \\
&+1.959658 \times 10^7 x^3 - 5.097911 \times 10^5 x^2 + 5.847292 \times 10^3 x \\
&+3.106507 \times 10^{-1}
\end{aligned}$$

Maximum principal stress σ_1 for gauge 10:

$$\begin{aligned}
\sigma_{10,1}^* &= +6.467051 \times 10^{13} x^{24} - 7.837368 \times 10^{14} x^{23} + 4.472589 \times 10^{15} x^{22} \quad (D.23) \\
&-1.598173 \times 10^{16} x^{21} + 4.010718 \times 10^{16} x^{20} - 7.515628 \times 10^{16} x^{19} \\
&+1.091495 \times 10^{17} x^{18} - 1.258633 \times 10^{17} x^{17} + 1.171201 \times 10^{17} x^{16} \\
&-8.890022 \times 10^{16} x^{15} + 5.542107 \times 10^{16} x^{14} - 2.847985 \times 10^{16} x^{13} \\
&+1.207536 \times 10^{16} x^{12} - 4.217599 \times 10^{15} x^{11} + 1.208402 \times 10^{15} x^{10} \\
&-2.820183 \times 10^{14} x^9 + 5.305504 \times 10^{13} x^8 - 7.927545 \times 10^{12} x^7 \\
&+9.215284 \times 10^{11} x^6 - 8.091215 \times 10^{10} x^5 + 5.136526 \times 10^9 x^4 \\
&-2.199426 \times 10^8 x^3 + 5.603508 \times 10^6 x^2 - 6.310021 \times 10^4 x \\
&+1.251999 \times 10
\end{aligned}$$

Minimum principal stress σ_2 for gauge 10:

$$\begin{aligned}
\sigma_{10,2}^* &= 1.089927 \times 10^{14} x^{24} - 1.320624 \times 10^{15} x^{23} - 7.535238 \times 10^{15} x^{22} \quad (D.24) \\
&-2.692165 \times 10^{16} x^{21} - 6.755405 \times 10^{16} x^{20} - 1.265776 \times 10^{17} x^{19} \\
&1.838174 \times 10^{17} x^{18} - 2.119574 \times 10^{17} x^{17} - 1.972313 \times 10^{17} x^{16} \\
&-1.497107 \times 10^{17} x^{15} - 9.333410 \times 10^{16} x^{14} - 4.796538 \times 10^{16} x^{13} \\
&2.033873 \times 10^{16} x^{12} - 7.104445 \times 10^{15} x^{11} - 2.035751 \times 10^{15} x^{10} \\
&-4.751652 \times 10^{14} x^9 - 8.940317 \times 10^{13} x^8 - 1.336064 \times 10^{13} x^7
\end{aligned}$$

$$\begin{aligned}
& 1.553322 \times 10^{12} x^6 - 1.364053 \times 10^{11} x^5 - 8.660650 \times 10^9 x^4 \\
& - 3.708949 \times 10^8 x^3 - 9.450569 \times 10^6 x^2 - 1.064344 \times 10^5 x \\
& 2.040048 \times 10
\end{aligned}$$

The normalized principal stresses are related to the normalized crack area parameter s , as shown in Eqns. 5.7 and 5.8. Similar equations developed for other gauges are given in this part of the thesis.

Minimum principal stress σ_2 for gauge 1:

$$\begin{aligned}
\sigma_{1,2}^* = & -6.283647 \times 10^{13} s^{24} + 7.807475 \times 10^{14} s^{23} - 4.563051 \times 10^{15} s^{22} \quad (D.25) \\
& + 1.668123 \times 10^{16} s^{21} - 4.278699 \times 10^{16} s^{20} + 8.187227 \times 10^{16} s^{19} \\
& - 1.213070 \times 10^{17} s^{18} + 1.425854 \times 10^{17} s^{17} - 1.351264 \times 10^{17} s^{16} \\
& + 1.043669 \times 10^{17} s^{15} - 6.614470 \times 10^{16} s^{14} + 3.452331 \times 10^{16} s^{13} \\
& - 1.485264 \times 10^{16} s^{12} + 5.258312 \times 10^{15} s^{11} - 1.525419 \times 10^{15} s^{10} \\
& + 3.600290 \times 10^{14} s^9 - 6.841006 \times 10^{13} s^8 + 1.031055 \times 10^{13} s^7 \\
& - 1.207231 \times 10^{12} s^6 + 1.066125 \times 10^{11} s^5 - 6.797746 \times 10^9 s^4 \\
& + 2.919818 \times 10^8 s^3 - 7.454475 \times 10^6 s^2 + 8.398605 \times 10^4 s - 7.548668
\end{aligned}$$

Minimum principal stress σ_2 for gauge 4:

$$\begin{aligned}
\sigma_{4,2}^* = & -7.361247 \times 10^{13} s^{24} + 9.178486 \times 10^{14} s^{23} - 5.382036 \times 10^{15} s^{22} \quad (D.26) \\
& + 1.973647 \times 10^{16} s^{21} - 5.077271 \times 10^{16} s^{20} + 9.742409 \times 10^{16} s^{19} \\
& - 1.447323 \times 10^{17} s^{18} + 1.705486 \times 10^{17} s^{17} - 1.620145 \times 10^{17} s^{16} \\
& + 1.254201 \times 10^{17} s^{15} - 7.966026 \times 10^{16} s^{14} + 4.166343 \times 10^{16} s^{13} \\
& - 1.795960 \times 10^{16} s^{12} + 6.370082 \times 10^{15} s^{11} - 1.851183 \times 10^{15} s^{10}
\end{aligned}$$

$$\begin{aligned}
&+4.376378 \times 10^{14} s^9 - 8.328575 \times 10^{13} s^8 + 1.257078 \times 10^{13} s^7 \\
&-1.473860 \times 10^{12} s^6 + 1.303215 \times 10^{11} s^5 - 8.319004 \times 10^9 s^4 \\
&+3.576985 \times 10^8 s^3 - 9.140902 \times 10^6 s^2 + 1.030713 \times 10^5 s \\
&-9.380789
\end{aligned}$$

Maximum principal stress σ_1 for gauge 10:

$$\begin{aligned}
\sigma_{10,1}^* = & 1.905417 \times 10^{13} s^{24} - 2.341352 \times 10^{14} s^{23} + 1.353986 \times 10^{15} s^{22} \text{ (D.27)} \\
& -4.899971 \times 10^{15} s^{21} + 1.244717 \times 10^{16} s^{20} - 2.359727 \times 10^{16} s^{19} \\
& +3.465273 \times 10^{16} s^{18} - 4.038359 \times 10^{16} s^{17} + 3.795706 \times 10^{16} s^{16} \\
& -2.908556 \times 10^{16} s^{15} + 1.829398 \times 10^{16} s^{14} - 9.478927 \times 10^{15} s^{13} \\
& +4.049663 \times 10^{15} s^{12} - 1.424184 \times 10^{15} s^{11} + 4.105361 \times 10^{14} s^{10} \\
& -9.631246 \times 10^{13} s^9 + 1.819663 \times 10^{13} s^8 - 2.727877 \times 10^{12} s^7 \\
& +3.177996 \times 10^{11} s^6 - 2.793456 \times 10^{10} s^5 + 1.773462 \times 10^9 s^4 \\
& -7.587363 \times 10^7 s^3 + 1.930150 \times 10^6 s^2 - 2.167803 \times 10^4 s \\
& +3.295091
\end{aligned}$$

Minimum principal stress σ_2 for gauge 10

$$\begin{aligned}
\sigma_{10,2} = & 2.607051 \times 10^{13} s^{24} - 3.206254 \times 10^{14} s^{23} + 1.855679 \times 10^{15} s^{22} \text{ (D.28)} \\
& -6.720898 \times 10^{15} s^{21} + 1.708589 \times 10^{16} s^{20} - 3.241535 \times 10^{16} s^{19} \\
& +4.763629 \times 10^{16} s^{18} - 5.555293 \times 10^{16} s^{17} + 5.225004 \times 10^{16} s^{16} \\
& -4.006397 \times 10^{16} s^{15} + 2.521494 \times 10^{16} s^{14} - 1.307292 \times 10^{16} s^{13} \\
& +5.588383 \times 10^{15} s^{12} - 1.966425 \times 10^{15} s^{11} + 5.671478 \times 10^{14} s^{10} \\
& -1.331221 \times 10^{14} s^9 + 2.516348 \times 10^{13} s^8 - 3.774025 \times 10^{12} s^7
\end{aligned}$$

$$\begin{aligned} &+4.398673 \times 10^{11} s^6 - 3.867999 \times 10^{10} s^5 + 2.456574 \times 10^9 s^4 \\ &-1.051355 \times 10^8 s^3 + 2.675387 \times 10^6 s^2 - 3.005627 \times 10^4 s \\ &+4.171313 \end{aligned}$$

Appendix E

Natural Frequencies and Damping

E.1 Natural Frequency Variations

The equations obtained for the first eight modes are given below.

For mode 1:

$$\begin{aligned} f_1^* = & -2.050548 \times 10^{11} x^{24} + 2.522161 \times 10^{12} x^{23} - 1.460820 \times 10^{13} x^{22} \text{ (E.1)} \\ & + 5.297771 \times 10^{13} x^{21} - 1.349328 \times 10^{14} x^{20} + 2.566111 \times 10^{14} x^{19} \\ & - 3.782060 \times 10^{14} x^{18} + 4.425622 \times 10^{14} x^{17} - 4.178622 \times 10^{14} x^{16} \\ & + 3.217914 \times 10^{14} x^{15} - 2.034891 \times 10^{14} x^{14} + 1.060482 \times 10^{14} x^{13} \\ & - 4.558763 \times 10^{13} x^{12} + 1.613805 \times 10^{13} x^{11} - 4.684550 \times 10^{12} x^{10} \\ & + 1.107154 \times 10^{12} x^9 - 2.108173 \times 10^{11} x^8 + 3.186489 \times 10^{10} x^7 \\ & - 3.744481 \times 10^9 x^6 + 3.321188 \times 10^8 x^5 - 2.128185 \times 10^7 x^4 \\ & + 9.190837 \times 10^5 x^3 - 2.359530 \times 10^4 x^2 + 2.672685 \times 10^2 x \\ & + 0.9584734 \end{aligned}$$

For mode 2:

$$f_2^* = +1.018073 \times 10^{10} x^{24} - 1.251448 \times 10^{11} x^{23} + 7.245618 \times 10^{11} x^{22} \text{ (E.2)}$$

$$\begin{aligned}
& -2.627358 \times 10^{12} x^{21} + 6.692693 \times 10^{12} x^{20} - 1.273289 \times 10^{13} x^{19} \\
& + 1.877838 \times 10^{13} x^{18} - 2.199336 \times 10^{13} x^{17} + 2.078956 \times 10^{13} x^{16} \\
& - 1.603193 \times 10^{13} x^{15} + 1.015433 \times 10^{13} x^{14} - 5.301594 \times 10^{12} x^{13} \\
& + 2.283653 \times 10^{12} x^{12} - 8.101995 \times 10^{11} x^{11} + 2.357401 \times 10^{11} x^{10} \\
& - 5.585375 \times 10^{10} x^9 + 1.066273 \times 10^{10} x^8 - 1.615897 \times 10^9 x^7 \\
& + 1.903857 \times 10^8 x^6 - 1.693004 \times 10^7 x^5 + 1.087563 \times 10^6 x^4 \\
& - 4.707801 \times 10^4 x^3 + 1.211401 \times 10^3 x^2 - 1.378602 \times 10^1 x \\
& + 1.002069
\end{aligned}$$

For mode 3:

$$\begin{aligned}
f_3^* &= -5.415256 \times 10^9 x^{24} + 7.429460 \times 10^{10} x^{23} - 4.735839 \times 10^{11} x^{22} \quad (\text{E.3}) \\
& + 1.870086 \times 10^{12} x^{21} - 5.141021 \times 10^{12} x^{20} + 1.047582 \times 10^{13} x^{19} \\
& - 1.644012 \times 10^{13} x^{18} + 2.037298 \times 10^{13} x^{17} - 2.027353 \times 10^{13} x^{16} \\
& + 1.638359 \times 10^{13} x^{15} - 1.082928 \times 10^{13} x^{14} + 5.877556 \times 10^{12} x^{13} \\
& - 2.622320 \times 10^{12} x^{12} + 9.603368 \times 10^{11} x^{11} - 2.874935 \times 10^{11} x^{10} \\
& + 6.986620 \times 10^{10} x^9 - 1.364050 \times 10^{10} x^8 + 2.108252 \times 10^9 x^7 \\
& - 2.526799 \times 10^8 x^6 + 2.280308 \times 10^7 x^5 - 1.483422 \times 10^6 x^4 \\
& + 6.490694 \times 10^4 x^3 - 1.684869 \times 10^3 x^2 + 1.918936 \times 10^1 x \\
& + 9.979157e - 1
\end{aligned}$$

For mode 4:

$$\begin{aligned}
f_4^* &= +2.005504 \times 10^{10} x^{24} - 2.295365 \times 10^{11} x^{23} + 1.233207 \times 10^{12} x^{22} \quad (\text{E.4}) \\
& - 4.133632 \times 10^{12} x^{21} + 9.690970 \times 10^{12} x^{20} - 1.688433 \times 10^{13} x^{19}
\end{aligned}$$

$$\begin{aligned}
&+2.267414 \times 10^{13} x^{18} - 2.402347 \times 10^{13} x^{17} + 2.038788 \times 10^{13} x^{16} \\
&-1.399141 \times 10^{13} x^{15} + 7.804800 \times 10^{12} x^{14} - 3.544559 \times 10^{12} x^{13} \\
&+1.308223 \times 10^{12} x^{12} - 3.902908 \times 10^{11} x^{11} + 9.321809 \times 10^{10} x^{10} \\
&-1.755181 \times 10^{10} x^9 + 2.542244 \times 10^9 x^8 - 2.717495 \times 10^8 x^7 \\
&+1.973413 \times 10^7 x^6 - 7.610427 \times 10^5 x^5 - 8.642636 \times 10^3 x^4 \\
&+2.597432 \times 10^3 x^3 - 1.170940 \times 10^2 x^2 + 1.757722 x \\
&+1.001871
\end{aligned}$$

For mode 5:

$$\begin{aligned}
f_5^* &= -2.652155 \times 10^{10} x^{24} + 3.298173 \times 10^{11} x^{23} - 1.930704 \times 10^{12} x^{22} \text{ (E.5)} \\
&+7.074391 \times 10^{12} x^{21} - 1.819946 \times 10^{13} x^{20} + 3.494924 \times 10^{13} x^{19} \\
&-5.199880 \times 10^{13} x^{18} + 6.140820 \times 10^{13} x^{17} - 5.850029 \times 10^{13} x^{16} \\
&+4.544195 \times 10^{13} x^{15} - 2.897765 \times 10^{13} x^{14} + 1.522445 \times 10^{13} x^{13} \\
&-6.595867 \times 10^{12} x^{12} + 2.352476 \times 10^{12} x^{11} - 6.877717 \times 10^{11} x^{10} \\
&+1.636555 \times 10^{11} x^9 - 3.136234 \times 10^{10} x^8 + 4.768891 \times 10^9 x^7 \\
&-5.635255 \times 10^8 x^6 + 5.023868 \times 10^7 x^5 - 3.234281 \times 10^6 x^4 \\
&+1.402638 \times 10^5 x^3 - 3.614468 \times 10^3 x^2 + 4.108672 \times 10^1 x \\
&+9.941499e - 1
\end{aligned}$$

For mode 6:

$$\begin{aligned}
f_6^* &= -5.529646 \times 10^{10} x^{24} + 6.870352 \times 10^{11} x^{23} - 4.018310 \times 10^{12} x^{22} \text{ (E.6)} \\
&+1.471137 \times 10^{13} x^{21} - 3.781577 \times 10^{13} x^{20} + 7.256320 \times 10^{13} x^{19} \\
&-1.078823 \times 10^{14} x^{18} + 1.273141 \times 10^{14} x^{17} - 1.212040 \times 10^{14} x^{16}
\end{aligned}$$

$$\begin{aligned}
&+9.408965 \times 10^{13} x^{15} - 5.996422 \times 10^{13} x^{14} + 3.148725 \times 10^{13} x^{13} \\
&-1.363487 \times 10^{13} x^{12} + 4.860860 \times 10^{12} x^{11} - 1.420580 \times 10^{12} x^{10} \\
&+3.379175 \times 10^{11} x^9 - 6.473999 \times 10^{10} x^8 + 9.842161 \times 10^9 x^7 \\
&-1.162837 \times 10^9 x^6 + 1.036565 \times 10^8 x^5 - 6.672771 \times 10^6 x^4 \\
&+2.893730 \times 10^5 x^3 - 7.456876 \times 10^3 x^2 + 8.478960 \times 10^1 x \\
&+9.878846e - 1
\end{aligned}$$

For mode 7:

$$\begin{aligned}
f_7^* = &+3.004129 \times 10^9 x^{24} - 3.899068 \times 10^9 x^{23} + 2.377297 \times 10^{10} x^{22} \quad (\text{E.7}) \\
&-9.055551 \times 10^{10} x^{21} + 2.417450 \times 10^{11} x^{20} - 4.808809 \times 10^{11} x^{19} \\
&+7.397957 \times 10^{11} x^{18} - 9.016805 \times 10^{11} x^{17} + 8.847815 \times 10^{11} x^{16} \\
&-7.064343 \times 10^{11} x^{15} + 4.619892 \times 10^{11} x^{14} - 2.483181 \times 10^{11} x^{13} \\
&+1.097766 \times 10^{11} x^{12} - 3.984218 \times 10^{10} x^{11} + 1.181961 \times 10^{10} x^{10} \\
&-2.845556 \times 10^9 x^9 + 5.501327 \times 10^8 x^8 - 8.415704 \times 10^7 x^7 \\
&+9.978928 \times 10^6 x^6 - 8.906928 \times 10^5 x^5 + 5.730546 \times 10^4 x^4 \\
&-2.480377 \times 10^3 x^3 + 6.368289 \times 10^1 x^2 - 7.097542e - 1 x \\
&+1.000090
\end{aligned}$$

For mode 8:

$$\begin{aligned}
f_8^* = &-1.516427 \times 10^9 x^{24} + 1.795928 \times 10^{10} x^{23} - 1.001043 \times 10^{11} x^{22} \quad (\text{E.8}) \\
&3.491716 \times 10^{11} x^{21} - 8.548343 \times 10^{11} x^{20} + 1.561610 \times 10^{12} x^{19} \\
&-2.209347 \times 10^{12} x^{18} + 2.480030 \times 10^{12} x^{17} - 2.244847 \times 10^{12} x^{16} \\
&1.656355 \times 10^{12} x^{15} - 1.003110 \times 10^{12} x^{14} + 5.005076 \times 10^{11} x^{13}
\end{aligned}$$

$$\begin{aligned}
& -2.059759 \times 10^{11} x^{12} 6.981623 \times 10^{10} x^{11} - 1.941405 \times 10^{10} x^{10} \\
& 4.399033 \times 10^9 x^9 - 8.040399 \times 10^8 x^8 1.168410 \times 10^8 x^7 \\
& -1.322632 \times 10^7 x^6 1.132671 \times 10^6 x^5 - 7.025769 \times 10^4 x^4 \\
& 2.945075 \times 10^3 x^3 - 7.363191 \times 10^1 x^2 8.230998e - 1 x \\
& 9.997835e - 1
\end{aligned}$$

The curve fitted equations seem to give reasonably correct values between $0.2 < x < 0.8$ for all the modes.

In a similar manner, the non-dimensional frequencies could also be related to the nondimensionalized crack severities.

For mode 1:

$$\begin{aligned}
f_1^* &= -3.151247 \times 10^{14} s^{24} + 2.473037 \times 10^{14} s^{23} + 1.967112 \times 10^{14} s^{22} \text{ (E.9)} \\
& -9.176996 \times 10^{14} s^{21} + 1.504526 \times 10^{15} s^{20} - 1.578466 \times 10^{15} s^{19} \\
& + 1.141041 \times 10^{15} s^{18} - 5.280519 \times 10^{14} s^{17} + 7.422380 \times 10^{13} s^{16} \\
& + 1.153780 \times 10^{14} s^{15} - 1.252063 \times 10^{14} s^{14} + 7.547253 \times 10^{13} s^{13} \\
& - 3.274491 \times 10^{13} s^{12} + 1.092420 \times 10^{13} s^{11} - 2.868373 \times 10^{12} s^{10} \\
& + 5.966818 \times 10^{11} s^9 - 9.806624 \times 10^{10} s^8 + 1.260881 \times 10^{10} s^7 \\
& - 1.246765 \times 10^9 s^6 + 9.235531 \times 10^7 s^5 - 4.922814 \times 10^6 s^4 \\
& + 1.766368 \times 10^5 s^3 - 3.740229 \times 10^3 s^2 + 3.129913 \times 10^1 s \\
& + 1.151107
\end{aligned}$$

For mode 2:

$$f_2^* = +1.513315 \times 10^{14} s^{24} - 1.377753 \times 10^{14} s^{23} - 5.177521 \times 10^{13} s^{22} \text{ (E.10)}$$

$$\begin{aligned}
& 3.978814 \times 10^{14} s^{21} - 7.242848 \times 10^{14} s^{20} + 8.340452 \times 10^{14} s^{19} \\
& - 6.844444 \times 10^{14} s^{18} + 4.040817 \times 10^{14} s^{17} - 1.567508 \times 10^{14} s^{16} \\
& + 1.978422 \times 10^{13} s^{15} + 2.329466 \times 10^{13} s^{14} - 2.191586 \times 10^{13} s^{13} \\
& + 1.132193 \times 10^{13} s^{12} - 4.197771 \times 10^{12} s^{11} + 1.192934 \times 10^{12} s^{10} \\
& - 2.655218 \times 10^{11} s^9 + 4.647834 \times 10^{10} s^8 - 6.357958 \times 10^9 s^7 \\
& + 6.693580 \times 10^8 s^6 - 5.285372 \times 10^7 s^5 + 3.003420 \times 10^6 s^4 \\
& - 1.145465 \times 10^5 s^3 + 2.556907 \times 10^3 s^3 - 2.244886 \times 10^1 s \\
& + 0.9091928
\end{aligned}$$

For mode 3:

$$\begin{aligned}
f_3^* &= -2.049017 \times 10^{14} s^{24} + 1.758522 \times 10^{14} s^{23} + 8.970539 \times 10^{13} s^{22} \text{ (E.11)} \\
& - 5.450891 \times 10^{14} s^{21} + 9.411262 \times 10^{14} s^{20} - 1.029265 \times 10^{15} s^{19} \\
& + 7.869503 \times 10^{14} s^{18} - 4.092397 \times 10^{14} s^{17} + 1.091424 \times 10^{14} s^{16} \\
& + 3.327962 \times 10^{13} s^{15} - 5.900985 \times 10^{13} s^{14} + 3.944191 \times 10^{13} s^{13} \\
& - 1.793937 \times 10^{13} s^{12} + 6.156193 \times 10^{12} s^{11} - 1.648482 \times 10^{12} s^{10} \\
& + 3.481648 \times 10^{11} s^9 - 5.796124 \times 10^{10} s^8 + 7.540892 \times 10^9 s^7 \\
& - 7.544726 \times 10^8 s^6 + 5.659111 \times 10^7 s^5 - 3.058046 \times 10^6 s^4 \\
& + 1.113275 \times 10^5 s^3 - 2.386877 \times 10^3 s^2 + 1.993805 \times 10^1 s \\
& + 1.103724
\end{aligned}$$

For mode 4:

$$\begin{aligned}
f_4^* &= +8.815941 \times 10^{13} s^{24} - 6.995503 \times 10^{13} s^{23} - 5.814424 \times 10^{13} s^{22} \text{ (E.12)} \\
& + 2.744623 \times 10^{14} s^{21} - 4.633179 \times 10^{14} s^{20} + 5.075765 \times 10^{14} s^{19}
\end{aligned}$$

$$\begin{aligned}
& -3.939795 \times 10^{14} s^{18} + 2.123161 \times 10^{14} s^{17} - 6.409554 \times 10^{13} s^{16} \\
& -9.720944 \times 10^{12} s^{15} + 2.613846 \times 10^{13} s^{14} - 1.867276 \times 10^{13} s^{13} \\
& + 8.845767 \times 10^{12} s^{12} - 3.146633 \times 10^{12} s^{11} + 8.738990 \times 10^{11} s^{10} \\
& - 1.919135 \times 10^{11} s^9 + 3.332907 \times 10^{16} s^8 - 4.538068 \times 10^9 s^7 \\
& + 4.763235 \times 10^8 s^6 - 3.751023 \times 10^7 s^5 + 2.124373 \times 10^6 s^4 \\
& - 8.067933 \times 10^4 s^3 + 1.796370 \times 10^3 s^2 - 1.606570 \times 10^1 s \\
& + 9.471387e - 1
\end{aligned}$$

For mode 5:

$$\begin{aligned}
f_5^* &= -1.309029 \times 10^{14} s^{24} + 1.090151 \times 10^{14} s^{23} + 6.751710 \times 10^{13} s^{22} \text{ (E.13)} \\
& - 3.667211 \times 10^{14} s^{21} + 6.248457 \times 10^{14} s^{20} - 6.797694 \times 10^{14} s^{19} \\
& + 5.179544 \times 10^{14} s^{18} - 2.681323 \times 10^{14} s^{17} + 7.022447 \times 10^{13} s^{16} \\
& + 2.340727 \times 10^{13} s^{15} - 3.997155 \times 10^{13} s^{14} + 2.665671 \times 10^{13} s^{13} \\
& - 1.215530 \times 10^{13} s^{12} + 4.191934 \times 10^{12} s^{11} - 1.130155 \times 10^{12} s^{10} \\
& + 2.407349 \times 10^{11} s^9 - 4.048687 \times 10^{10} s^8 + 5.329526 \times 10^9 s^7 \\
& - 5.401827 \times 10^8 s^6 + 4.107545 \times 10^7 s^5 - 2.249841 \times 10^6 s^4 \\
& + 8.292729 \times 10^4 s^3 - 1.798610 \times 10^3 s^2 + 1.539996 \times 10^1 \\
& + 1.068633
\end{aligned}$$

For mode 6:

$$\begin{aligned}
f_6^* &= -2.091404 \times 10^{14} s^{24} + 1.697731 \times 10^{14} s^{23} + 1.196311 \times 10^{14} s^{22} \text{ (E.14)} \\
& - 6.033889 \times 10^{14} s^{21} + 1.014385 \times 10^{15} s^{20} - 1.092966 \times 10^{15} s^{19} \\
& + 8.229132 \times 10^{14} s^{18} - 4.163542 \times 10^{14} s^{17} + 9.914888 \times 10^{13} s^{16}
\end{aligned}$$

$$\begin{aligned}
&+4.718519 \times 10^{13} s^{15} - 6.949309 \times 10^{13} s^{14} + 4.517234 \times 10^{13} s^{13} \\
&-2.038212 \times 10^{13} s^{12} + 6.990131 \times 10^{12} s^{11} - 1.878536 \times 10^{12} s^{10} \\
&+3.994074 \times 10^{11} s^9 - 6.710485 \times 10^{10} s^8 + 8.829213 \times 10^9 s^7 \\
&-8.947219 \times 10^8 s^6 + 6.802355 \times 10^7 s^5 - 3.724597 \times 10^6 s^4 \\
&+1.372029 \times 10^5 s^3 - 2.974867 \times 10^3 s^2 + 2.558487 \times 10^1 s \\
&+1.109270
\end{aligned}$$

For mode 7:

$$\begin{aligned}
f_7^* &= -6.257327 \times 10^{12} s^{24} + 5.057468 \times 10^{12} s^{23} + 3.489445 \times 10^{12} s^{22} \text{ (E.15)} \\
&-1.754236 \times 10^{13} s^{21} + 2.912832 \times 10^{13} s^{20} - 3.080058 \times 10^{13} s^{19} \\
&+2.246801 \times 10^{13} s^{18} - 1.059715 \times 10^{13} s^{17} + 1.719046 \times 10^{12} s^{16} \\
&2.060713 \times 10^{12} s^{15} - 2.334539 \times 10^{12} s^{14} + 1.421371 \times 10^{12} s^{13} \\
&-6.186343 \times 10^{11} s^{12} + 2.064257 \times 10^{11} s^{11} - 5.411081 \times 10^{10} s^{10} \\
&+1.122092 \times 10^{10} s^9 - 1.836039 \times 10^9 s^8 + 2.347503 \times 10^8 s^7 \\
&-2.305973 \times 10^7 s^6 + 1.695777 \times 10^6 s^5 - 8.971599 \times 10^4 s^4 \\
&+3.196326 \times 10^3 s^3 - 6.720912 \times 10^1 s^2 + 5.541918e - 1 s \\
&+1.002964
\end{aligned}$$

For mode 8:

$$\begin{aligned}
f_8^* &= -2.566415 \times 10^{13} s^{24} + 2.170563 \times 10^{13} s^{23} + 1.225784 \times 10^{13} s^{22} \text{ (E.16)} \\
&-7.021319 \times 10^{13} s^{21} + 1.204982 \times 10^{14} s^{20} - 1.315727 \times 10^{14} s^{19} \\
&+1.005986 \times 10^{14} s^{18} - 5.238181 \times 10^{13} s^{17} + 1.403529 \times 10^{13} s^{16} \\
&4.211596 \times 10^{12} s^{15} - 7.545682 \times 10^{12} s^{14} + 5.062734 \times 10^{12} s^{13} \\
&-2.311223 \times 10^{12} s^{12} + 7.964686 \times 10^{11} s^{11} - 2.143244 \times 10^{11} s^{10}
\end{aligned}$$

$$\begin{aligned}
&+4.552675 \times 10^{10} s^9 - 7.629698 \times 10^9 s^8 + 1.000162 \times 10^9 s^7 \\
&-1.009035 \times 10^8 s^6 + 7.635483 \times 10^6 s^5 - 4.162469 \times 10^5 s^4 \\
&+1.527750 \times 10^4 s^3 - 3.300389 \times 10^2 s^2 + 2.799604 s \\
&+1.013301
\end{aligned}$$

E.2 Damping Ratio Variations

Damping ratios for modes 1 and 2 were related to the fatigue crack cycles in Eqns. 5.13 and 5.14; the remainder of the equations obtained for the higher modal damping ratios are given below.

For mode 3:

$$\begin{aligned}
\zeta_3^* = & 1.827458 \times 10^{16} x^{24} - 6.747464 \times 10^{16} x^{23} + 1.411676 \times 10^{17} x^{22} \text{ (E.17)} \\
& -1.969021 \times 10^{17} x^{21} + 1.837391 \times 10^{17} x^{20} - 9.318459 \times 10^{16} x^{19} \\
& -2.600365 \times 10^{16} x^{18} + 1.098199 \times 10^{17} x^{17} - 1.299194 \times 10^{17} x^{16} \\
& +1.027808 \times 10^{17} x^{15} - 6.173331 \times 10^{16} x^{14} + 2.941447 \times 10^{16} x^{13} \\
& -1.132923 \times 10^{16} x^{12} + 3.554181 \times 10^{15} x^{11} - 9.091299 \times 10^{14} x^{10} \\
& +1.888775 \times 10^{14} x^9 - 3.160576 \times 10^{13} x^8 + 4.203413 \times 10^{12} x^7 \\
& -4.357141 \times 10^{11} x^6 + 3.421765 \times 10^{10} x^5 - 1.951464 \times 10^9 x^4 \\
& +7.552855 \times 10^7 x^3 - 1.752369 \times 10^6 x^2 + 1.795534 \times 10^4 x \\
& +8.853209
\end{aligned}$$

For mode 4:

$$\zeta_4^* = -9.638563 \times 10^{14} x^{24} + 3.623038 \times 10^{15} x^{23} - 7.633337 \times 10^{15} x^{22} \text{ (E.18)}$$

$$\begin{aligned}
&+1.070834 \times 10^{16} x^{21} - 1.008360 \times 10^{16} x^{20} + 5.271321 \times 10^{15} x^{19} \\
&+1.125238 \times 10^{15} x^{18} - 5.663584 \times 10^{15} x^{17} + 6.803547 \times 10^{15} x^{16} \\
&-5.409310 \times 10^{15} x^{15} + 3.255528 \times 10^{15} x^{14} - 1.552346 \times 10^{15} x^{13} \\
&+5.979757 \times 10^{14} x^{12} - 1.875591 \times 10^{14} x^{11} + 4.795924 \times 10^{13} x^{10} \\
&-9.959841 \times 10^{12} x^9 + 1.665995 \times 10^{12} x^8 - 2.215019 \times 10^{11} x^7 \\
&+2.295601 \times 10^{10} x^6 - 1.802736 \times 10^9 x^5 + 1.028283 \times 10^8 x^4 \\
&-3.981351 \times 10^6 x^3 + 9.242460 \times 10^4 x^2 - 9.460840 \times 10^2 x \\
&+5.715255e - 1
\end{aligned}$$

For mode 5:

$$\begin{aligned}
\zeta_5^* = &-3.642406 \times 10^{15} x^{24} + 9.669220 \times 10^{15} x^{23} - 1.746770 \times 10^{16} x^{22} \text{(E.19)} \\
&+2.229256 \times 10^{16} x^{21} - 1.944152 \times 10^{16} x^{20} + 9.062952 \times 10^{15} x^{19} \\
&+3.294832 \times 10^{15} x^{18} - 1.137190 \times 10^{16} x^{17} + 1.290972 \times 10^{16} x^{16} \\
&-9.954339 \times 10^{15} x^{15} + 5.864807 \times 10^{15} x^{14} - 2.752084 \times 10^{15} x^{13} \\
&+1.047110 \times 10^{15} x^{12} - 3.253534 \times 10^{14} x^{11} + 8.262224 \times 10^{13} x^{10} \\
&-1.707962 \times 10^{13} x^9 + 2.849856 \times 10^{12} x^8 - 3.787216 \times 10^{11} x^7 \\
&+3.930693 \times 10^{10} x^6 - 3.097203 \times 10^9 x^5 + 1.776294 \times 10^8 x^4 \\
&-6.932957 \times 10^6 x^3 + 1.628799 \times 10^5 x^2 - 1.700022 \times 10^3 x \\
&+7.133746e - 1
\end{aligned}$$

For mode 6:

$$\begin{aligned}
\zeta_6^* = &+5.493108 \times 10^{15} x^{24} - 2.399156 \times 10^{16} x^{23} + 5.291045 \times 10^{16} x^{22} \text{(E.20)} \\
&-7.585840 \times 10^{16} x^{21} + 7.219195 \times 10^{16} x^{20} - 3.754559 \times 10^{16} x^{19}
\end{aligned}$$

$$\begin{aligned}
& -9.372584 \times 10^{15} x^{18} + 4.299653 \times 10^{16} x^{17} - 5.149661 \times 10^{16} x^{16} \\
& + 4.101570 \times 10^{16} x^{15} - 2.475141 \times 10^{16} x^{14} + 1.183536 \times 10^{16} x^{13} \\
& - 4.571023 \times 10^{15} x^{12} + 1.437053 \times 10^{15} x^{11} - 3.681708 \times 10^{14} x^{10} \\
& + 7.657530 \times 10^{13} x^9 - 1.282242 \times 10^{13} x^8 + 1.705770 \times 10^{12} x^7 \\
& - 1.767893 \times 10^{11} x^6 + 1.387571 \times 10^{10} x^5 - 7.905100 \times 10^8 x^4 \\
& + 3.054435 \times 10^7 x^3 - 7.067913 \times 10^5 x^2 + 7.207818 \times 10^3 x \\
& + 4.606382
\end{aligned}$$

For mode 7:

$$\begin{aligned}
\zeta_7^* = & +7.028898 \times 10^{16} x^{24} - 2.417192 \times 10^{17} x^{23} + 4.927007 \times 10^{17} x^{22} \text{(E.21)} \\
& - 6.774495 \times 10^{17} x^{21} + 6.257033 \times 10^{17} x^{20} - 3.134646 \times 10^{17} x^{19} \\
& - 9.134846 \times 10^{16} x^{18} + 3.731189 \times 10^{17} x^{17} - 4.387784 \times 10^{17} x^{16} \\
& + 3.458902 \times 10^{17} x^{15} - 2.072130 \times 10^{17} x^{14} + 9.853256 \times 10^{16} x^{13} \\
& - 3.788997 \times 10^{16} x^{12} + 1.187189 \times 10^{16} x^{11} - 3.033865 \times 10^{15} x^{10} \\
& + 6.298880 \times 10^{14} x^9 - 1.053606 \times 10^{14} x^8 + 1.401053 \times 10^{13} x^7 \\
& - 1.452464 \times 10^{12} x^6 + 1.141091 \times 10^{11} x^5 - 6.512140 \times 10^9 x^4 \\
& + 2.523066 \times 10^8 x^3 - 5.863333 \times 10^6 x^2 + 6.024546 \times 10^4 x \\
& + 2.519049 \times 10^1
\end{aligned}$$

For mode 8:

$$\begin{aligned}
\zeta_8^* = & +4.766570 \times 10^{15} x^{24} - 1.505773 \times 10^{16} x^{23} + 2.966862 \times 10^{16} x^{22} \text{(E.22)} \\
& - 4.008690 \times 10^{16} x^{21} + 3.675545 \times 10^{16} x^{20} - 1.867212 \times 10^{16} x^{19} \\
& - 4.403024 \times 10^{15} x^{18} + 2.032775 \times 10^{16} x^{17} - 2.405102 \times 10^{16} x^{16}
\end{aligned}$$

$$\begin{aligned}
&+1.893880 \times 10^{16} x^{15} - 1.131511 \times 10^{16} x^{14} + 5.364331 \times 10^{15} x^{13} \\
&-2.056993 \times 10^{15} x^{12} + 6.429614 \times 10^{14} x^{11} - 1.640071 \times 10^{14} x^{10} \\
&+3.401048 \times 10^{13} x^9 - 5.686051 \times 10^{12} x^8 + 7.562675 \times 10^{11} x^7 \\
&-7.847210 \times 10^{10} x^6 + 6.174667 \times 10^9 x^5 - 3.531853 \times 10^8 x^4 \\
&+1.372573 \times 10^7 x^3 - 3.202021 \times 10^5 x^2 + 3.294492 \times 10^3 x \\
&+2.156022
\end{aligned}$$

The nondimensional damping ratios ($\zeta^* = \zeta_{cracked}/\zeta_{uncracked}$ with non-dimensional fatigue crack cycles are related by the equations derived below.

For mode 1:

$$\begin{aligned}
\zeta_1^* = &+2.234502 \times 10^{16} x^{24} - 8.847803 \times 10^{16} x^{23} + 1.894852 \times 10^{17} x^{22} \text{ (E.23)} \\
&-2.676179 \times 10^{17} x^{21} + 2.520155 \times 10^{17} x^{20} - 1.293773 \times 10^{17} x^{19} \\
&-3.416873 \times 10^{16} x^{18} + 1.501996 \times 10^{17} x^{17} - 1.787440 \times 10^{17} x^{16} \\
&+1.418582 \times 10^{17} x^{15} - 8.539211 \times 10^{16} x^{14} + 4.075472 \times 10^{16} x^{13} \\
&-1.571723 \times 10^{16} x^{12} + 4.935739 \times 10^{15} x^{11} - 1.263498 \times 10^{15} x^{10} \\
&+2.626496 \times 10^{14} x^9 - 4.396720 \times 10^{13} x^8 + 5.848599 \times 10^{12} x^7 \\
&-6.062596 \times 10^{11} x^6 + 4.760239 \times 10^{10} x^5 - 2.713694 \times 10^9 x^4 \\
&+1.049547 \times 10^8 x^3 - 2.432129 \times 10^6 x^2 + 2.485296 \times 10^4 x \\
&+1.260276 \times 10^1
\end{aligned}$$

For mode 2:

$$\begin{aligned}
\zeta_2^* = &+1.150841 \times 10^{15} x^{24} - 7.693380 \times 10^{15} x^{23} + 1.861831 \times 10^{16} x^{22} \text{ (E.24)} \\
&-2.788172 \times 10^{16} x^{21} + 2.732525 \times 10^{16} x^{20} - 1.472993 \times 10^{16} x^{19}
\end{aligned}$$

$$\begin{aligned}
& -3.073110 \times 10^{15} x^{18} + 1.617947 \times 10^{16} x^{17} - 1.973032 \times 10^{16} x^{16} \\
& + 1.586650 \times 10^{16} x^{15} - 9.638070 \times 10^{15} x^{14} + 4.631271 \times 10^{15} x^{13} \\
& - 1.795393 \times 10^{15} x^{12} + 5.660539 \times 10^{14} x^{11} - 1.453273 \times 10^{14} x^{10} \\
& + 3.026991 \times 10^{13} x^9 - 5.072865 \times 10^{12} x^8 + 6.750182 \times 10^{11} x^7 \\
& - 6.993913 \times 10^{10} x^6 + 5.484539 \times 10^9 x^5 - 3.119868 \times 10^8 x^4 \\
& + 1.202672 \times 10^7 x^3 - 2.772893 \times 10^5 x^2 + 2.809904 \times 10^3 x \\
& + 2.651314
\end{aligned}$$

For mode 3:

$$\begin{aligned}
\zeta_3^* = & -1.107671 \times 10^{15} s^{24} + 1.003935 \times 10^{15} s^{23} + 3.279560 \times 10^{14} s^{22} \text{ (E.25)} \\
& - 2.676877 \times 10^{15} s^{21} + 4.765822 \times 10^{15} s^{20} - 5.287008 \times 10^{15} s^{19} \\
& + 4.086080 \times 10^{15} s^{18} - 2.150999 \times 10^{15} s^{17} + 5.904128 \times 10^{14} s^{16} \\
& + 1.621919 \times 10^{14} s^{15} - 3.057019 \times 10^{14} s^{14} + 2.075114 \times 10^{14} s^{13} \\
& - 9.550817 \times 10^{13} s^{12} + 3.316495 \times 10^{13} s^{11} - 8.995846 \times 10^{12} s^{10} \\
& + 1.927601 \times 10^{12} s^9 - 3.261697 \times 10^{11} s^8 + 4.321317 \times 10^{10} s^7 \\
& - 4.409868 \times 10^9 s^6 + 3.377063 \times 10^8 s^5 - 1.862921 \times 10^7 s^4 \\
& + 6.914068 \times 10^5 s^3 - 1.510779 \times 10^4 s^2 + 1.310075 \times 10^2 s \\
& + 1.526671
\end{aligned}$$

For mode 4:

$$\begin{aligned}
\zeta_4^* = & -9.948718 \times 10^{14} s^{24} + 9.017849 \times 10^{14} s^{23} + 2.953683 \times 10^{14} s^{22} \text{ (E.26)} \\
& - 2.408002 \times 10^{15} s^{21} + 4.288812 \times 10^{15} s^{20} - 4.761022 \times 10^{15} s^{19} \\
& + 3.683664 \times 10^{15} s^{18} - 1.943613 \times 10^{15} s^{17} + 5.381419 \times 10^{14} s^{16}
\end{aligned}$$

$$\begin{aligned}
&+1.414469 \times 10^{14} s^{15} - 2.727472 \times 10^{14} s^{14} + 1.857538 \times 10^{14} s^{13} \\
&-8.561473 \times 10^{13} s^{12} + 2.975438 \times 10^{13} s^{11} - 8.075547 \times 10^{12} s^{10} \\
&+1.731227 \times 10^{12} s^9 - 2.930633 \times 10^{11} s^8 + 3.884214 \times 10^{10} s^7 \\
&-3.965324 \times 10^9 s^6 + 3.037806 \times 10^8 s^5 - 1.676428 \times 10^7 s^4 \\
&+6.224292 \times 10^5 s^3 - 1.360872 \times 10^4 s^2 + 1.196266 \times 10^2 s + 1.475041
\end{aligned}$$

For mode 5:

$$\begin{aligned}
\zeta_5^* = &+1.809306 \times 10^{15} s^{24} - 1.640386 \times 10^{15} s^{23} - 5.407090 \times 10^{14} s^{22} \text{(E.27)} \\
&+4.395566 \times 10^{15} s^{21} - 7.836158 \times 10^{15} s^{20} + 8.712874 \times 10^{15} s^{19} \\
&-6.759133 \times 10^{15} s^{18} + 3.585751 \times 10^{15} s^{17} - 1.013056 \times 10^{15} s^{16} \\
&-2.387324 \times 10^{14} s^{15} + 4.880443 \times 10^{14} s^{14} - 3.350785 \times 10^{14} s^{13} \\
&+1.549688 \times 10^{14} s^{12} - 5.396678 \times 10^{13} s^{11} + 1.466801 \times 10^{13} s^{10} \\
&-3.148124 \times 10^{12} s^9 + 5.334510 \times 10^{11} s^8 - 7.076893 \times 10^{10} s^7 \\
&+7.231302 \times 10^9 s^6 - 5.544977 \times 10^8 s^5 + 3.062886 \times 10^7 s^4 \\
&-1.138248 \times 10^6 s^3 + 2.493887 \times 10^4 s^2 - 2.295692 \times 10^2 s \\
&+1.273097e - 1
\end{aligned}$$

For mode 6:

$$\begin{aligned}
\zeta_6^* = &+1.724814 \times 10^{14} s^{24} - 1.563487 \times 10^{14} s^{23} - 5.126380 \times 10^{13} s^{22} \text{(E.28)} \\
&+4.177325 \times 10^{14} s^{21} - 7.441250 \times 10^{14} s^{20} + 8.262741 \times 10^{14} s^{19} \\
&-6.395796 \times 10^{14} s^{18} + 3.377669 \times 10^{14} s^{17} - 9.383786 \times 10^{13} s^{16} \\
&-2.423201 \times 10^{13} s^{15} + 4.716094 \times 10^{13} s^{14} - 3.216121 \times 10^{13} s^{13} \\
&+1.483156 \times 10^{13} s^{12} - 5.156247 \times 10^{12} s^{11} + 1.399772 \times 10^{12} s^{10}
\end{aligned}$$

$$\begin{aligned}
 & -3.001384 \times 10^{11} s^9 + 5.081603 \times 10^{10} s^8 - 6.736114 \times 10^9 s^7 \\
 & + 6.877819 \times 10^8 s^6 - 5.269853 \times 10^7 s^5 + 2.908644 \times 10^6 s^4 \\
 & - 1.080083 \times 10^5 s^3 + 2.360640 \times 10^3 s^2 - 2.026681 \times 10^1 s \\
 & + 9.175042e - 1
 \end{aligned}$$

For mode 7:

$$\begin{aligned}
 \zeta_7^* = & +6.237558 \times 10^{14} s^{24} - 5.652606 \times 10^{14} s^{23} - 1.839212 \times 10^{14} s^{22} \text{ (E.29)} \\
 & + 1.503924 \times 10^{15} s^{21} - 2.675957 \times 10^{15} s^{20} + 2.965607 \times 10^{15} s^{19} \\
 & - 2.288142 \times 10^{15} s^{18} + 1.200351 \times 10^{15} s^{17} - 3.251146 \times 10^{14} s^{16} \\
 & - 9.529746 \times 10^{13} s^{15} + 1.738575 \times 10^{14} s^{14} - 1.174413 \times 10^{14} s^{13} \\
 & + 5.393989 \times 10^{13} s^{12} - 1.870714 \times 10^{13} s^{11} + 5.069725 \times 10^{12} s^{10} \\
 & - 1.085551 \times 10^{12} s^9 + 1.835719 \times 10^{11} s^8 - 2.430667 \times 10^{10} s^7 \\
 & + 2.479055 \times 10^9 s^6 - 1.897353 \times 10^8 s^5 + 1.046040 \times 10^7 s^4 \\
 & - 3.880073 \times 10^5 s^3 + 8.473030 \times 10^3 s^2 - 7.339531 \times 10^1 s \\
 & + 7.052958e - 1
 \end{aligned}$$

For mode 8:

$$\begin{aligned}
 \zeta_8^* = & +8.207956 \times 10^{14} s^{24} - 7.436002 \times 10^{14} s^{23} - 2.398948 \times 10^{14} s^{22} \text{ (E.30)} \\
 & + 1.969224 \times 10^{15} s^{21} - 3.499439 \times 10^{15} s^{20} + 3.869822 \times 10^{15} s^{19} \\
 & - 2.975004 \times 10^{15} s^{18} + 1.548911 \times 10^{15} s^{17} - 4.071899 \times 10^{14} s^{16} \\
 & - 1.365067 \times 10^{14} s^{15} + 2.335679 \times 10^{14} s^{14} - 1.561839 \times 10^{14} s^{13} \\
 & + 7.141889 \times 10^{13} s^{12} - 2.470390 \times 10^{13} s^{11} + 6.682281 \times 10^{12} s^{10} \\
 & - 1.428674 \times 10^{12} s^9 + 2.412750 \times 10^{11} s^8 - 3.190735 \times 10^{10} s^7
 \end{aligned}$$

$$\begin{aligned} &+3.250268 \times 10^9 s^6 - 2.484517 \times 10^8 s^5 + 1.368028 \times 10^7 s^4 \\ &-5.068240 \times 10^5 s^3 + 1.105644 \times 10^4 s^2 - 9.552891 \times 10^1 s \\ &+6.174606e - 1 \end{aligned}$$

Appendix F

Equations Derived by Piecewise Cubic Spline Approach

F.1 Static Strains

The equations relating the normalized strains to the normalized crack area parameter s , are given below:

For channel 7:

$$\epsilon_7^* = \begin{cases} 1.62 - .80 s - 14.97 s^2 + 23.56 s^3 & 0 < s < .44 \\ 6.74 - 36.03 s + 65.85 s^2 - 38.23 s^3 & .44 < s < .84 \\ -365.34 + 1287.07 s - 1502.44 s^2 + 581.41 s^3 & .84 < s < .90 \\ 215.04 - 649.53 s + 651.54 s^2 - 217.18 s^3 & \text{other} \end{cases}$$

For channel 8:

$$\epsilon_8^* = \begin{cases} 1.74 - 2.17s - 9.23s^2 + 14.54s^3 & 0 < s < .44 \\ 4.40 - 20.45s + 32.68s^2 - 17.51s^3 & .44 < s < .84 \\ -153.88 + 542.35s - 634.42s^2 + 246.06s^3 & .84 < s < .90 \\ 95.19 - 288.74s + 289.97s^2 - 96.66s^3 & \text{other} \end{cases}$$

For channel 9:

$$\epsilon_9^* = \begin{cases} 1.34 - 1.23s - 2.55s^2 + 4.01s^3 & 0 < s < .44 \\ 1.67 - 3.55s + 2.79s^2 - .07s^3 & .44 < s < .84 \\ 61.44 - 216.08s + 254.71s^2 - 99.60s^3 & .84 < s < .90 \\ -44.43 + 137.178s - 138.21s^2 + 46.07s^3 & \text{other} \end{cases}$$

For channel 9:

$$\epsilon_9^* = \begin{cases} 1.34 - 1.23s - 2.55s^2 + 4.01s^3 & 0 < s < .44 \\ 1.68 - 3.55s + 2.79s^2 - .07s^3 & .44 < s < .84 \\ 61.44 - 216.08s + 254.71s^2 - 99.60s^3 & .84 < s < .90 \\ -44.43 + 137.18s - 138.21s^2 + 46.07s^3 & \text{other} \end{cases}$$

For channel 16:

$$\epsilon_{i6}^* = \begin{cases} 1.44 + .14s - 15.58s^2 + 24.52s^3 & 0 < s < .44 \\ 7.37 - 40.67s + 78.03s^2 - 47.05s^3 & .44 < s < .84 \\ -484.49 + 1708.34s - 1995.09s^2 + 772.05s^3 & .84 < s < .90 \\ 286.19 - 863.23s + 865.12s^2 - 288.37s^3 & \text{other} \end{cases}$$

For channel 17:

$$\epsilon_{i7}^* = \begin{cases} 1.33 - .073s - 10.54s^2 + 16.60s^3 & 0 < s < .44 \\ 5.31 - 27.48s + 52.31s^2 - 31.47s^3 & .44 < s < .84 \\ -324.08 + 1143.84s - 1336.06s^2 + 517.09s^3 & .84 < s < .90 \\ 192.50 - 579.87s + 581.13s^2 - 193.71s^3 & \text{other} \end{cases}$$

For channel 18:

$$\epsilon_{i8}^* = \begin{cases} 1.33 - .07s - 10.54s^2 + 16.60s^3 & 0 < s < .44 \\ 5.31 - 27.48s + 52.31s^2 - 31.47s^3 & .44 < s < .84 \\ -324.08 + 1143.84s - 1336.06s^2 + 517.07s^3 & .84 < s < .90 \\ 192.50 - 579.87s + 581.13s^2 - 193.71s^3 & \text{other} \end{cases}$$

For channel 22:

$$\epsilon_{22}^* = \begin{cases} 1.06 + 1.00s - 9.10s^2 + 14.33s^3 & 0 < s < .44 \\ 5.18 - 27.35s + 55.92s^2 - 35.39s^3 & .44 < s < .84 \\ -417.29 + 1474.94s - 1724.76s^2 + 668.17s^3 & .84 < s < .90 \\ 254.20 - 765.67s + 767.35s^2 - 255.78s^3 & \text{other} \end{cases}$$

For channel 23:

$$\epsilon_{23}^* = \begin{cases} .99 + 1.15s - 7.79s^2 + 12.27s^3 & 0 < s < .44 \\ 4.57 - 23.49s + 48.72s^2 - 30.94s^3 & .44 < s < .84 \\ -327.78 + 1158.33s - 1352.10s^2 + 522.53s^3 & .84 < s < .90 \\ 189.48 - 567.62s + 567.58s^2 - 189.19s^3 & \text{other} \end{cases}$$

For channel 24:

$$\epsilon_{24}^* = \begin{cases} .89 + 1.06 s - 3.76 s^2 + 5.916 s^3 & 0 < s < .44 \\ 2.81 - 12.16 s + 26.58 s^2 - 17.28 s^3 & .44 < s < .84 \\ -179.16 + 634.90 s - 740.40 s^2 + 285.76 s^3 & .84 < s < .90 \\ 101.38 - 301.19 s + 300.76 s^2 - 100.25 s^3 & \text{other} \end{cases}$$

F.2 Static Principal Stresses

The equations relating the normalized principal stresses to the normalized crack area parameter s , are given below:

Maximum principal stress for gauge 1:

$$\sigma_{1,1}^* = \begin{cases} 1.45 - 1.06 s - 7.37 s^2 + 11.61 s^3 & 0 < s < .44 \\ 3.42 - 14.66 s + 23.82 s^2 - 12.24 s^3 & .44 < s < .84 \\ -40.36 + 141.04 s - 160.73 s^2 + 60.67 s^3 & .84 < s < .90 \\ 10.74 - 29.49 s + 28.94 s^2 - 9.65 s^3 & \text{other} \end{cases}$$

Minimum principal stress for gauge 1:

$$\sigma_{1,2}^* = \begin{cases} 1.49 - .99s - 9.28s^2 + 14.60s^3 & 0 < s < .44 \\ 4.77 - 23.59s + 42.57s^2 - 25.04s^3 & .44 < s < .84 \\ -273.53 + 966.01s - 1130.42s^2 + 438.41s^3 & .84 < s < .90 \\ 170.12 - 514.32s + 516.08s^2 - 172.03s^3 & \text{other} \end{cases}$$

Maximum principal stress for gauge 4:

$$\sigma_{4,1}^* = \begin{cases} 1.25 + .24s - 10.20s^2 + 16.05s^3 & 0 < s < .44 \\ 4.91 - 24.91s + 47.50s^2 - 28.06s^3 & .44 < s < .84 \\ -236.04 + 831.89s - 968.08s^2 + 373.20s^3 & .84 < s < .90 \\ 127.66 - 381.68s + 381.71s^2 - 127.24s^3 & \text{other} \end{cases}$$

Minimum principal stress for gauge 4:

$$\sigma_{4,2}^* = \begin{cases} 1.53 - .23s - 16.06s^2 + 25.28s^3 & 0 < s < .44 \\ 7.87 - 43.84s + 83.95s^2 - 51.20s^3 & .44 < s < .84 \\ -588.90 + 2078.22s - 2431.35s^2 + 942.61s^3 & .84 < s < .90 \\ 362.86 - 1097.56s + 1100.90s^2 - 366.97s^3 & \text{other} \end{cases}$$

Maximum principal stress for gauge 10:

$$\sigma_{10,1}^* = \begin{cases} .98 + .95 s - 6.11 s^2 + 9.62 s^3 & 0 < s < .44 \\ 3.84 - 18.73 s + 39.02 s^2 - 24.89 s^3 & .44 < s < .84 \\ -278.87 + 986.59 s - 1152.59 s^2 + 445.92 s^3 & .84 < s < .90 \\ 165.63 - 496.62 s + 497.11 s^2 - 165.70 s^3 & \text{other} \end{cases}$$

Minimum principal stress for gauge 10:

$$\sigma_{10,2}^* = \begin{cases} .96 + 1.18 s - 7.16 s^2 + 11.27 s^3 & 0 < s < .44 \\ 4.35 - 22.09 s + 46.21 s^2 - 29.54 s^3 & .44 < s < .84 \\ -341.02 + 1206.00 s - 1409.46 s^2 + 545.60 s^3 & .84 < s < .90 \\ 204.75 - 615.07 s + 616.01 s^2 - 205.34 s^3 & \text{other} \end{cases}$$

F.3 Natural Frequencies

The equations relating the normalized natural frequencies to crack severities are given below:

For mode 1:

$$f_1^* = \begin{cases} 1.02 + .06 s - 1.05 s^2 + 1.65 s^3 & 0 < s < .44 \\ 1.46 - 2.96 s + 5.90 s^2 - 3.66 s^3 & .44 < s < .84 \\ -34.02 + 123.20 s - 143.64 s^2 + 55.42 s^3 & .84 < s < .90 \\ 20.28 - 58.00 s + 57.90 s^2 - 19.30 s^3 & \text{other} \end{cases}$$

For mode 2:

$$f_2^* = \begin{cases} 1.00 + .05s - .38s^2 + .60s^3 & 0 < s < .44 \\ 1.17 - 1.08s + 2.22s^2 - 1.39s^3 & .44 < s < .84 \\ -9.60 + 37.18s - 43.14s^2 + 16.53s^3 & .84 < s < .90 \\ 5.91 - 14.54s + 14.39s^2 - 4.80s^3 & \text{other} \end{cases}$$

For mode 3:

$$f_3^* = \begin{cases} 1.00 + .002s - .17s^2 + .27s^3 & 0 < s < .44 \\ 1.07 - .48s + .93s^2 - .57s^3 & .44 < s < .84 \\ -3.91 + 17.25s - 20.08s^2 + 7.73s^3 & .84 < s < .90 \\ 3.54 - 7.62s + 7.58s^2 - 2.53s^3 & \text{other} \end{cases}$$

For mode 4:

$$f_4^* = \begin{cases} 1.00 - .01s + .03s^2 - .05s^3 & 0 < s < .44 \\ .99 + .07s - .16s^2 + .09s^3 & .44 < s < .84 \\ 3.83 - 10.08s + 11.88s^2 - 4.66s^3 & .84 < s < .90 \\ -1.22 + 6.81s - 6.91s^2 + 2.30s^3 & \text{other} \end{cases}$$

For mode 5:

$$f_5^* = \begin{cases} 1.00 + .01s - .14s^2 + .22s^3 & 0 < s < .44 \\ 1.06 - .38s + .75s^2 - .46s^3 & .44 < s < .84 \\ -3.54 + 15.98s - 18.64s^2 + 7.20s^3 & .84 < s < .90 \\ 3.55 - 7.68s + 7.68s^2 - 2.56s^3 & \text{other} \end{cases}$$

For mode 6:

$$f_6^* = \begin{cases} 1.00 + .03s - .34s^2 + .54s^3 & 0 < s < .44 \\ 1.15 - .95s + 1.90s^2 - 1.17s^3 & .44 < s < .84 \\ -10.88 + 41.81s - 48.79s^2 + 18.85s^3 & .84 < s < .90 \\ 7.77 - 20.43s + 20.43s^2 - 6.81s^3 & \text{other} \end{cases}$$

For mode 7:

$$f_7^* = \begin{cases} 1.00 + .002s - .018s^2 + .03s^3 & 0 < s < .44 \\ 1.01 - .049s + .10s^2 - .06s^3 & .44 < s < .84 \\ .41 + 2.07s - 2.41s^2 + .93s^3 & .84 < s < .90 \\ 1.32 - .96s + .96s^2 - .32s^3 & \text{other} \end{cases}$$

For mode 8:

$$f_s^* = \begin{cases} 1.00 + .001 s - .02 s^2 + .04 s^3 & 0 < s < .44 \\ 1.01 - .07 s + .13 s^2 - .08 s^3 & .44 < s < .84 \\ .084 + 3.23 s - 3.77 s^2 + 1.46 s^3 & .84 < s < .90 \\ 1.56 - 1.68 s + 1.67 s^2 - .56 s^3 & \text{other} \end{cases}$$



